Analysis

Non-Linear Dynamic Analysis of Geared Systems

Rajendra Singh, Donald R. Houser,
and Ahmet Kahraman
Ohio State University
Columbus, Ohio

NASA

National Aeronautics and
Space Administration

Office of Management

Scientific and Technical
Information Division

1990

NON-LINEAR DYNAMIC ANALYSES OF GEARED SYSTEMS

Rajendra Singh, Donald R. Houser, and Ahmet Kahraman
Ohio State University
Department of Mechanical Engineering
Columbus, Ohio 43210

Under the driving conditions, a typical geared system may be subjected to large dynamic loads. Also, the vibration level of the geared system is directly related to the noise radiated from the gear box. Accordingly, a good understanding of the steady state dynamic behavior of the system is required in order to design reliable and quiet transmissions. It is the main focus of this study with the scope limited to a system containing a spur gear pair with backlash and periodically time-varying mesh stiffness, and rolling element bearings with clearance type non-linearities. The internal static transmission error excitation at the gear mesh, which is of importance from high frequency noise and vibration control view point, is considered in the formulation in sinusoidal or periodic form.

A dynamic finite element model of the linear time-invariant (LTI) system is developed. Effects of several system parameters, such as torsional and transverse flexibilities of the shafts and prime mover/load inertias, on free and forced vibration characteristics are investigated. Several reduced order LTI models are developed and validated by comparing their eigen solutions with the finite element model results. Using the reduced order formulations, a three-degree of freedom dynamic model is developed which includes non-linearities associated with radial clearances in the radial rolling element bearings, backlash between a spur gear pair and periodically varying gear meshing stiffness. As a limiting case, a single degree of freedom model of the spur gear pair with backlash is considered and mathematical conditions for tooth

separation and back collision are defined. Both digital simulation technique and analytical methods such as method of harmonic balance and the method of multiple scales have been used to develop the steady state frequency response characteristics for various non-linear and/or time-varying cases. Difficulties associated with the determination of the multiple solutions at a given frequency in the digital simulation technique have been resolved. The proposed formulation has been validated by comparing the predictions with the results of two benchmark experiments reported in the literature. Several key system parameters such as mean load and damping ratio are identified and their effects on the non-linear frequency response are evaluated quantitatively. Other fundamental issues such as the dynamic coupling between non-linear modes, dynamic interactions between component non-linearities and time-varying mesh stiffness, and the existence of subharmonic and chaotic solutions including routes to chaos have also been examined in depth.

ACKNOWLEDGEMENTS

TABLE OF CONTENTS

LIST OF SYMBOLS

b	backlash
c, C	viscous damping coefficient
d	diameter
e	static transmission error
f	non-linear displacement function
F	force
g, h	non-linear functions
H	total number of rolling elements in contact
I	rotary inertia
j	imaginary number
k, K	stiffness
L	length
m, M	mass
n	power of non-linear bearing function
N, N^*	describing functions
p	relative displacement
q	displacement
t	time
T	torque
U	mass unbalance of the gear
u	relative displacement
v	gear ratio
w	displacement vector
X	coordinate axis at the direction perpendicular to the line of action
Y	coordinate axis at the direction parallel to the line of action
x	relative displacement
y	transverse displacement
Z	number of rolling elements
α	angular position of the rolling element in contact

β	dynamic compliance
δ	Kronecker delta
ε	geometric eccentricity of the gear
φ	phase angle
φ	an angle
κ	dimensionless stiffness
θ	rotational displacement
σ	stress
ω	natural frequency
Ω	excitation frequency
ζ	damping ratio
ψ	mode shape

Subscripts:

a	alternating component
b	bearing
c, c1	reference quantities
d	dynamic
e	external
g1	pinion
g2	gear
h	gear mesh
i	internal
j	an index
L	load or left
m	mean component
n	natural
P	prime mover
p	period
R	right
r	mode index or response
S	stress

s1	driving shaft
s2	driven shaft
s	static or modal index
t	inner contact
T	torque
X	coordinate axis at the direction perpendicular to the line of action
Y	coordinate axis at the direction parallel to the line of action
I, II, III	modal index

Supercripts:

T	matrix transpose
—	dimensional quantities[†]
~	amplitude of a harmonic function
·	derivative with respect to time
^	stiffness or force ratio

† All dimensionless quantities are without any superscript.

CHAPTER I

INTRODUCTION

1.1. PROBLEM FORMULATION

Dynamic analysis of geared systems is an essential step in design due to two reasons. First, under the driving conditions, a typical geared system is subject to dynamic forces which can be large. Therefore, the prediction of dynamic loads, motions or stresses is needed in developing reliable gear trains. Second, the vibration level of the geared system is directly related to the noise radiated from the gear box. An attempt in designing quiet gears requires a good understanding of the dynamic behavior of the system and the gear mesh source. Accordingly, the main objective of this study is to develop accurate mathematical models of a generic geared rotor-bearing system shown in Figure 1.1a. Of interest here is to investigate several key modelling issues which have not been addressed in the literature, such as system non-linearities and time-varying mesh stiffness.

The generic geared system shown in Figure 1.1a consists of a single spur gear mesh of ratio $v_g = d_{g2}/d_{g1}$, rolling element bearings, a prime mover driving the system at Ω_{s1} speed and a typical inertial load. The system also includes other elements such as couplings and flywheel. A discrete model of the system is shown in Figure 1.1b. Here, shafts are represented by discrete translational springs k_{s1} and k_{s2}, translational dampers c_{s1} and c_{s2}, and torsional springs K_{s1} and K_{s2}. The gear mesh is represented by a time-varying mesh stiffness $k_h(t)$ and a non-linear displacement function f_h

(a)

(b)
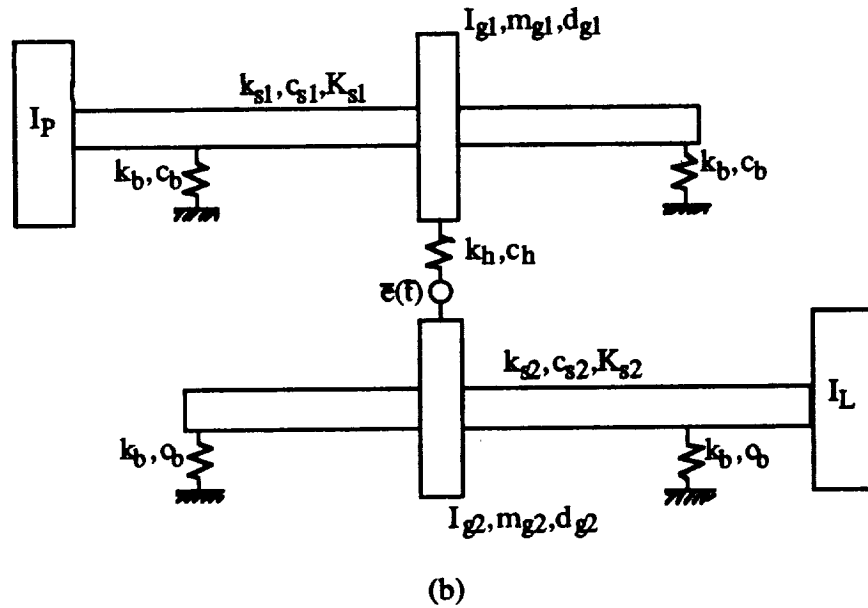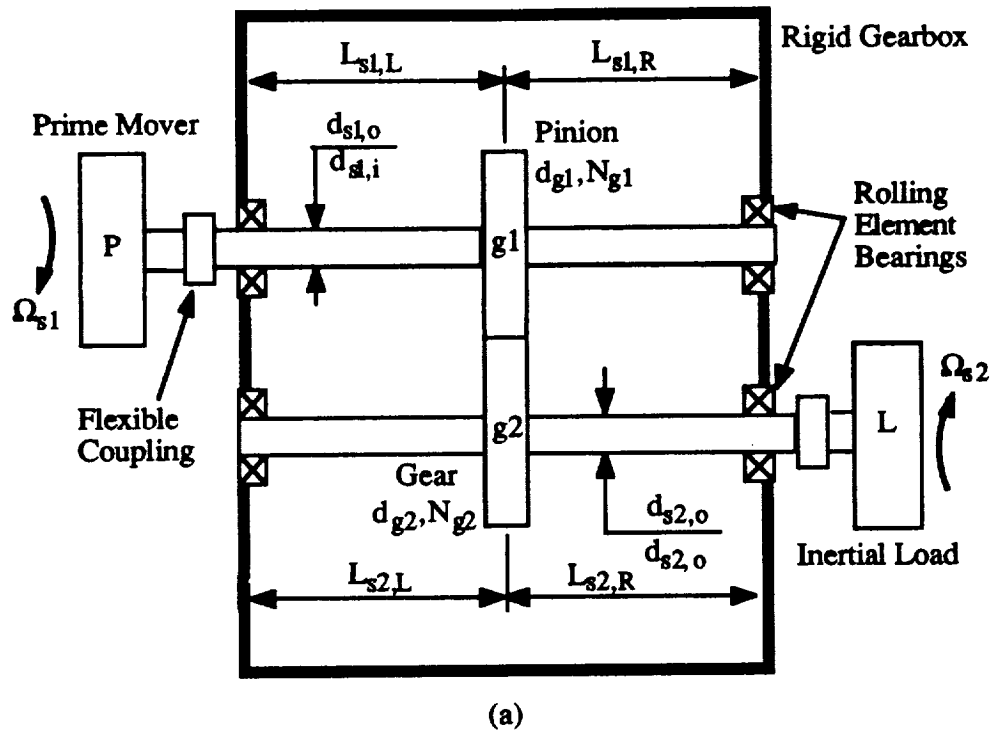
Figure 1.1.   a) A generic geared rotating system, b) discrete model of geared rotating system.

2

which includes gear backlash. Further, linear time-invariant (LTI) mesh damping c_h is considered here. The rolling element bearings are defined by a time-invariant radial stiffness k_b subject to a non-linear displacement function f_b, and an LTI damping coefficient c_b. The prime mover and load are modeled as purely torsional elements of inertias I_p and I_L, respectively. The mean rotational speeds Ω_{s1} and Ω_{s2} and the geometric end conditions are such that gyroscopic effects are not seen.

The generalized displacement vector $\{\bar{q}(\bar{t})\}$, associated with the inertia elements, consists of angular displacements θ and transverse displacements $\bar{x}$ and $\bar{y}$. The governing equation of motion for the non-linear, time-varying multi-degree of freedom model can be given in the general form as

$$\left[\overline{M}\right]\{\bar{q}''(\bar{t})\} + \left[\overline{C}\right]\{\bar{q}'(\bar{t})\} + \left[\overline{K}(\bar{t})\right]\{f(\bar{q}(\bar{t}))\} = \{\overline{F}(\bar{t})\} \tag{1.1}$$

where $\left[\overline{M}\right]$ is the time-invariant mass matrix and $\{\bar{q}(\bar{t})\}$ is the displacement vector. Here, damping matrix $\left[\overline{C}\right]$ is assumed to be LTI type, as the effect of the tooth separation and time-varying mesh properties on mesh damping are considered negligible; validity of this assumption will be examined later. The stiffness matrix $\left[\overline{K}(\bar{t})\right]$ is considered to be time-varying, given by a periodically time varying matrix $\left[\overline{K}(\bar{t})\right] = \left[\overline{K}(\bar{t} + 2\pi / \overline{\Omega}_h)\right]$ where $\overline{\Omega}_h$ is the fundamental gear mesh frequency. The non-linear displacement vector $\{f(\bar{q}(\bar{t}))\}$ includes the radial clearances in bearings and the gear backlash, and the forcing vector $\{\overline{F}(\bar{t})\}$ consists of both external excitations due to torque fluctuations, mass unbalances and geometric eccentricities, and an internal static transmission error excitation.

3

1.2. OBJECTIVES

Specific objectives of this study are given as follows; each chapter, written in the journal paper style, deals with one major objective.

First, a dynamic finite element model of the linear time-invariant (LTI) system given in Figure 1.1a is developed. Effects of several system parameters, such as torsional and transverse flexibilities of the shafts and prime mover/load inertias, on free and forced vibration characteristics are investigated. Three different reduced order LTI models will be derived and the conditions under which these are valid will be determined by comparing the eigen solutions with the finite element model results. Development and verification of such a reduced order (with a very few degrees of freedom) linear model is an essential step before the non-linear dynamic behavior is analyzed [Chapter I].

Second, non-linear frequency response characteristics of a spur gear pair with backlash are examined for both external and internal excitations. The internal excitation is of importance from the high frequency noise and vibration control viewpoint and it represents the overall kinematic or static transmission error. Such problems may be significantly different from the rattle problems associated with external, low frequency torque excitation. Two solution methods, namely the digital simulation technique and the method of harmonic balance have been used to develop the steady state solutions for the internal sinusoidal excitation. Difficulties associated with the determination of the multiple solutions at a given frequency in the digital simulation technique have been resolved as one must search the entire initial conditions map. Such solutions and the transition frequencies for various impact situations are found by the method of harmonic balance. Further, the principle of superposition can be employed to analyze the periodic transmission error excitation and/or combined excitation problems

4

provided the excitation frequencies are sufficiently apart from each other. Predictions are compared with the limited experimental data available in the literature [Chapter II].

Third, non-linear frequency response characteristics of a geared rotor-bearing system are examined. A three degree of freedom dynamic model is developed which includes non-linearities associated with radial clearances in the radial rolling element bearings and backlash between a spur gear pair; time-invariant gear meshing stiffness is assumed. The bearing non-linear stiffness function is approximated for convenience sake by a simple model which is identical to that used for the gear mesh. This approximate bearing model has been verified by comparing steady state frequency spectra. The applicability of both analytical and numerical solution techniques to the multi degree of freedom non-linear problem is investigated. Proposed theory is validated by comparing the results with available experimental data. Several key issues such as non-linear modal interactions and differences between internal static transmission error excitation and external torque excitation are discussed. Additionally, parametric studies are performed to understand the effect of system parameters such as bearing stiffness to gear mesh stiffness ratio, alternating to mean force ratio and radial bearing preload to mean force ratio on the non-linear dynamic behavior. A criterion used to classify the steady state solutions is presented and the conditions for chaotic, quasi-periodic and subharmonic steady state solutions are determined. Two typical routes to chaos observed in this geared system are also identified [Chapter III].

Fourth, this study extends the non-linear single degree of freedom spur gear pair model of Chapter II and multi-degree of freedom geared rotor-bearing system model of Chapter III by including time-varying mesh stiffness $k_h(\bar{t})$, and investigates the effect of $k_h(\bar{t})$ on the frequency response of lightly and heavily loaded geared systems. Interactions between mesh stiffness variation and system non-linearities associated with

5

gear backlash and radial clearances in rolling element bearings are also considered. Resonances of the corresponding linear time-varying (LTV) system associated with the parametric and external excitations are identified using the method of multiple scales. Theoretical results are validated by available experimental results [Chapter IV].

1.3. DEVELOPMENT OF LINEAR TIME-INVARIANT MODELS

1.3.1. Literature Review

The study of geared rotor dynamics requires that the coupling between torsional and transverse vibrations be included in the model. Although several modeling and solution techniques such as lumped mass models and the use of the transfer matrix method have been applied to rotor dynamic problems, the finite element method (FEM) seems to be a highly efficient and accurate method for linear modeling. In one of the early examples of FEM applied to a single rotor, Nelson and McVaugh [1] used a Rayleigh beam finite element including the effects of translational and rotary inertia, gyroscopic moments and axial load. Zorzi and Nelson [2] extended this by including internal damping. Later, Nelson [3] developed a Timoshenko beam by adding shear deformation to the Rayleigh beam theory. This model was further extended by Ozguven and Ozkan [4] to include all possible effects such as transverse and rotary inertia, gyroscopic moments, axial load, internal hysteretic and viscous damping and shear deformations in a single model. However, none of the rotor dynamics models described above can handle geared rotor systems, although they are capable of determining the dynamic behavior of rotors which consist of shafts supported at several points and carrying rigid disks at several locations.

Gear dynamics studies, on the other hand, have usually neglected the lateral vibrations of the shafts and bearings, and have typically represented the system with a

6

linear torsional model. Although neglecting transverse vibrations might be a good approximation for systems having stiff shafts, it has been observed experimentally [5] that the dynamic coupling between the transverse and torsional vibrations due to the gear mesh affects the system behavior considerably when the shafts are compliant. This fact directed the attention of investigators to the inclusion of transverse vibrations of the shafts and the bearings in mathematical models. Lund [6] developed influence coefficients at each gear mesh for both torsional and lateral vibrations, obtained critical speeds and a forced vibration response. Hamad and Seireg [7] studied the whirling of geared rotor systems supported on hydrodynamic bearings; torsional vibrations were not considered in this model and the shaft was assumed to be rigid. Iida, et al. [8] considered the same problem by taking one of the shafts to be rigid and neglecting the compliance of the gear mesh, and obtained a three degree of freedom model to determine the first three vibration modes and the forced vibration response due to the unbalance and the geometric eccentricity of one of the gears. Later, Iida, et al. [9,10,11] applied their model to a larger system which consists of three shafts coupled by two gear meshes. Hagiwara, Iida, and Kikuchi [12] developed a simple model that included the transverse flexibilities of the shafts by using discrete stiffness values, and studied the forced response of geared shafts due to unbalances and runout errors. They included the damping and compliances of the journal bearings and assumed a constant mesh stiffness. Although most of these gear dynamics studies have discussed several aspects of the problem, none of them has been able to represent a geared rotor-bearing system completely since almost all of them have used one or more simplifying assumptions such as rigid shafts, rigid bearings, rigid gear mesh etc. which may not be applicable to a real system. In addition, these studies proposed lower order lumped mass linear models.

Neriya, et al. [13] employed a dynamic finite element model which eliminates many of the simplifying assumptions. They found the forced vibration response of the system at the shaft frequency, excited by mass unbalances and runout errors of the gears by using the modal summation. But they did not consider the high frequency, internal, static transmission error excitation which has the major role in noise generation. An extensive survey of linear mathematical models used in gear dynamics analyses is given in a recent paper by Ozguven and Houser [14].

1.3.2. Mathematical Model

Here, we assume linear bearings and no tooth separations with time-invariant mesh stiffness, i.e. $[\overline{K}] \neq [\overline{K}(\bar{t})]$ and $\{f(\overline{q}(\bar{t}))\} = \{\overline{q}(\bar{t})\}$. Then the corresponding LTI form of equation (1.1) is:

$$[\overline{M}]\{\overline{q}''(\bar{t})\} + [\overline{C}]\{\overline{q}'(\bar{t})\} + [\overline{K}]\{\overline{q}(\bar{t})\} = \{\overline{F}(\bar{t})\}$$

(1.2)

Since many investigators have modeled the generic system shown in Figure 1.1a as a single degree of freedom model, our analysis uses it as a reference model to transform the governing equation into the dimensionless form. Focusing only on the gear pair as shown in Figure 1.2, the equation of motion of the semi-definite system is given in terms of the relative translational displacement $\overline{u}(\bar{t}) = \left(d_{g1}\theta_{g1} - d_{g2}\theta_{g2}\right)/2$

$$m_{c1}\frac{d^2\overline{u}(\bar{t})}{d\bar{t}^2} + c_h\frac{d\overline{u}(\bar{t})}{d\bar{t}} + k_h\overline{u}(\bar{t}) = \overline{F}(\bar{t})$$

(1.3a)

where m_{c1} is the equivalent gear pair mass defined as

8
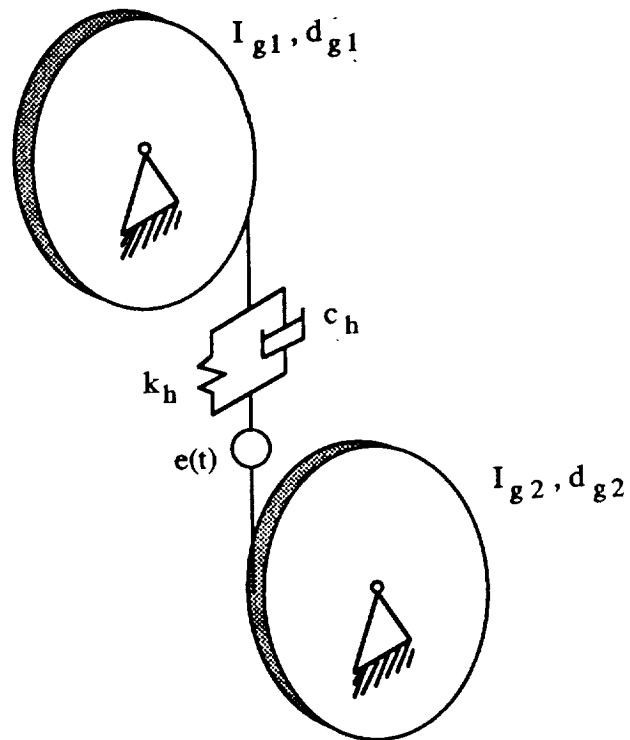
Figure 1.2.   A single degree of freedom dynamic model.

$$m_{c1} = \frac{1}{\left(\dfrac{d_{g1}^2}{4I_{g1}} + \dfrac{d_{g2}^2}{4I_{g2}} \right)}; \qquad \omega_n = \sqrt{\frac{k_h}{m_{c1}}} \qquad\qquad (1.3b,c)$$

First, we establish the dimensionless time t as $t = \omega_n \bar{t}$. Second, we use the base circle diameter of the pinion d_{g1} and the equivalent mass m_{c1} as characteristic length and mass parameters, respectively, to obtain the governing equations in the dimensionless form as

$$[M]\{\ddot{q}(t)\} + [C]\{\dot{q}(t)\} + [K]\{q(t)\} = \{F_m\} + \{F_{ah}(t)\} + \{F_{aT}(t)\}. \qquad (1.4)$$

where an overdot means derivative with respect to time t, and the dimensionless forcing vector consists of a mean force vector $\{F_m\}$ and two time-varying components: a) high frequency excitation due to the kinematic gear transmission error $\{F_{ah}(t)\}$ and, b) other excitations due to mass unbalance U_{gi}, geometric eccentricities (run-out errors) ε_{gi} and prime mover and load torque pulsations $T_{gia}(t)$, typically at low frequencies, are combined into a single term $\{F_{aT}(t)\}$.

1.3.3. Gear Mesh Formulation

The gear mesh is represented by a pair of rigid disks connected by a translational, viscously damped spring along the pressure line which is tangent to the base circles of the gears as shown in Figure 1.3. By choosing the Y axis on the pressure line and the X axis perpendicular to the pressure line, the transverse vibrations in the X direction

10

Figure 1.3. Model of gear mesh used in FEM.

are uncoupled from both the torsional vibrations and transverse vibrations in the Y direction. The dynamic mesh force $\overline{F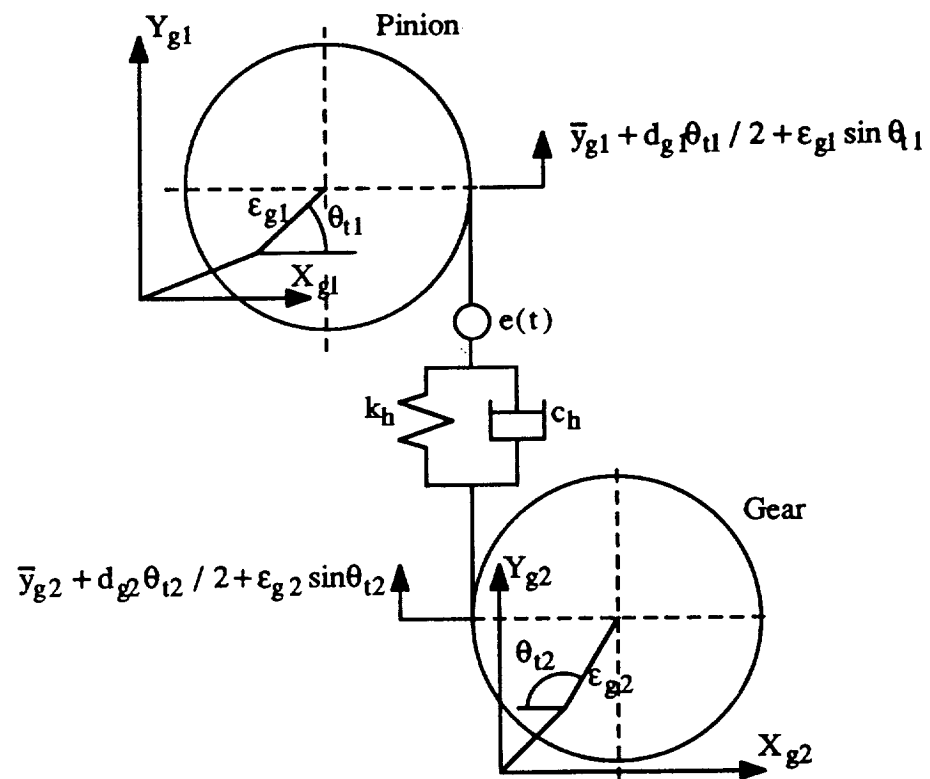}_{hY}$ at the mesh point in the Y direction can be written in terms of the symbols given in Figure 1.3 from the rigid body dynamics

$$\overline{F}_{hY}(\bar{t}) = c_h(\dot{\overline{y}}_{g1} + \frac{d_{g1}}{2}\dot{\theta}_{t1} + \varepsilon_{g1}\Omega_{s1}\cos\theta_{t1} - \dot{\overline{y}}_{g2} - \frac{d_{g2}}{2}\dot{\theta}_{t2}$$

$$-\varepsilon_{g2}\Omega_{s2}\cos\theta_{t2} - \tilde{e}N_{g1}\Omega_{s1}\cos(N_{g1}\theta_{t1})) + k_h(\overline{y}_{g1} + \frac{d_{g1}}{2}\theta_{t1}$$

$$+\varepsilon_{g1}\sin\theta_{t1} - \overline{y}_{g2} - \frac{d_{g2}}{2}\theta_{t2} - \varepsilon_{g2}\sin\theta_{t2} - \tilde{e}_1\sin(N_{g1}\theta_{t1})) \qquad (1.5)$$

Here, only the fundamental component of the static transmission error $\overline{e}(\bar{t})$ is considered, i.e. $\overline{e}(\bar{t}) = \tilde{e}\sin(N_{g1}\Omega_{s1}\bar{t})$ where N_{g1} is the number of teeth of gear g1. Dynamic mesh force $\overline{F}_{hY}$ also introduces moments $\overline{T}_{hg1}$ and $\overline{T}_{hg2}$ about instantaneous centers of the gears:

$$\overline{T}_{hg1}(\bar{t}) = \overline{F}_{hY}(\bar{t})\left(\frac{d_{g1}}{2} + \varepsilon_{g1}\cos\theta_{t1}\right) \qquad (1.6a)$$

$$\overline{T}_{hg2}(\bar{t}) = -\overline{F}_{hY}(\bar{t})\left(\frac{d_{g2}}{2} + \varepsilon_{g2}\cos\theta_{t2}\right) \qquad (1.6b)$$

The total angular rotation θ_{ti} of the i-th gear is $\theta_{ti}(t) = \Omega_{si}\bar{t} + \theta_{gi}(\bar{t})$, i=1,2. The displacement vector can be decomposed into two parts as $\{\overline{q}\} = \{\overline{q}_s\} + \{\overline{q}_h\}$ where $\{\overline{q}_s\} = \left[\overline{x}_1, \overline{y}_1, \theta_1, ..., \overline{x}_j, \overline{y}_j, \theta_j, ..., \overline{x}_n, \overline{y}_n, \theta_n\right]$, j = 1 to n, j ≠ g1, j ≠ g2 (excluding the degrees of freedom of the nodes where the gear and pinion are mounted) and

12

$\{\bar{q}_h\} = \left[\bar{x}_{g1}, \bar{y}_{g1}, \theta_{g1}, \bar{x}_{g2}, \bar{y}_{g2}, \theta_{g2}\right]$, i=1,2. The coupling effect due to gear mesh is only seen in the terms governed by $\{\bar{q}_h\}$ and the mesh stiffness $\left[\bar{K}_h\right]$, which represents this dynamic coupling due to gear mesh is obtained from equations (1.5) and (1.6) as

$$
[\bar{K}_h] = k_h
\begin{bmatrix}
0 & 0 & 0 & 0 & 0 & 0 \\
0 & 1 & \dfrac{d_{g1}}{2} & 0 & -1 & -\dfrac{d_{g2}}{2} \\
0 & \dfrac{d_{g1}}{2} & \dfrac{d_{g1}^2}{4} & 0 & -\dfrac{d_{g1}}{2} & -\dfrac{d_{g1}d_{g2}}{4} \\
0 & 0 & 0 & 0 & 0 & 0 \\
0 & -1 & -\dfrac{d_{g1}}{2} & 0 & 1 & \dfrac{d_{g2}}{2} \\
0 & -\dfrac{d_{g2}}{2} & -\dfrac{d_{g1}d_{g2}}{4} & 0 & \dfrac{d_{g2}}{2} & \dfrac{d_{g2}^2}{4}
\end{bmatrix}
\tag{1.7a}
$$

Since mesh viscous damping is proportional to the mesh stiffness,

$$
[\bar{C}_h] = \frac{c_h}{k_h}[\bar{K}_h].
\tag{1.7b}
$$

In the overall force vector, non-zero terms correspond to displacements $\{\bar{q}_h\}$ and are given in the following form:

13

$$\{\bar{F}_{ah}(\bar{t})\} + \{\bar{F}_{aT}(\bar{t})\} = \left\{ \begin{array}{c} U_{g1}\Omega_{s1}^2 \sin\Omega_{s1}\bar{t} + \bar{F}(\bar{t})_1 \\[2mm] U_{g1}\Omega_{s1}^2 \cos\Omega_{s1}\bar{t} \\[2mm] -\dfrac{2T_{g1m}}{d_{g1}}\varepsilon_{g1}\cos\Omega_{s1}\bar{t} + \dfrac{d_{g1}}{2}\bar{F}_1(\bar{t}) + \bar{T}_{g1a}(t) \\[2mm] U_{g2}\Omega_{s2}^2 \sin\Omega_{s2}\bar{t} - \bar{F}_1(\bar{t}) \\[2mm] U_{g2}\Omega_{s2}^2 \cos\Omega_{s2}\bar{t} \\[2mm] \dfrac{2T_{g1m}}{d_{g1}}\varepsilon_{g2}\Omega_{s2}^2 \cos\Omega_{s2}\bar{t} - \dfrac{d_{g2}}{2}\bar{F}_1(\bar{t}) - \bar{T}_{g2a}(\bar{t}) \end{array} \right\} \qquad (1.8a)$$

$$\bar{F}_1(\bar{t}) = c_h(\varepsilon_{g2}\Omega_{s2}\cos\Omega_{s2}\bar{t} - \varepsilon_{g1}\Omega_{s1}\cos\Omega_{s1}\bar{t} + \tilde{e}N_{g1}\Omega_{s1}\cos(N_{g1}\Omega_{s1}\bar{t}))$$

$$+k_h(\varepsilon_{g2}\sin\Omega_{s2}\bar{t} - \varepsilon_{g1}\sin\Omega_{s1}\bar{t} + \tilde{e}\sin(N_{g1}\Omega_{s1}\bar{t})) \qquad (1.8b)$$

where $\bar{T}_{g1m}$ is the mean input torque.

1.3.4. Finite Element Formulation and Eigen-Value Problem

The finite element method has been employed in obtaining stiffness and mass matrices of the system of equations (1.4). The shafts are discretized and five degrees of freedom are defined at each node, only the axial motion being excluded. The stiffness and mass matrices of each finite rotor element are derived by using the variational principle [3,4,15]. The system overall matrices are obtained by combining element matrices, dynamic coupling matrices due to gear mesh defined by equation (1.7), assumed bearing damping values and stiffnesses, and the inertias of the gears and other lumped inertia elements. Here, [M] is diagonal and positive definite and [K] is symmetric and positive semi-definite. The equation describing the undamped free vibration of the system is obtained from equation (1.4) as

$$[M]\{\ddot{q}(t)\} + [K]\{q(t)\} = \{0\}. \tag{1.9}$$

The assumed form of the solution $\{q(t)\} = \{q_a\}\cos(\omega t + \phi)$ is substituted into equation (1.9) to obtain the standard eigen-value problem:

$$[K]\{q_a\} = \omega^2[M]\{q_a\}. \tag{1.10}$$

The solution of equation (1.10) yield the eigen-vectors or modes $\{\psi_r\}$ and associated eigen-values or natural frequencies ω_r. Here, a torsional rigid body mode at $\omega=0$ exists since $[K]$ is semi-definite.

1.3.5. Forced Vibration Response

The excitation given by equation (1.8) (for no torque pulsations, i.e. $\overline{T}_{g1a}(\overline{t}) = \overline{T}_{g2a}(\overline{t}) = 0$) is the sum of three sinusoidal terms at frequencies Ω_{s1}, Ω_{s2} and gear mesh frequency $N_{g1}\Omega_{s1}$

$$\{\overline{F}(\overline{t})\} = \sum_{i=1}^{2} \{\overline{F}_{gi}\}\sin(\Omega_{si}\overline{t} + \phi_{si}) + \{\overline{F}_h\}\sin(N_{g1}\Omega_{s1}\overline{t} + \phi_h) \tag{1.11}$$

The steady state displacement response of the system due to this excitation is assumed to be

$$\{\overline{q}(\overline{t})\} = \sum_{i=1}^{2} [\beta_{gi}]\{\overline{F}_{gi}\}\sin(\Omega_{si}\overline{t} + \phi_{si}) + [\beta_h]\{\overline{F}_h\}\sin(N_{g1}\Omega_{s1}\overline{t} + \phi_h) \tag{1.12}$$

15

where $[\beta_{gi}]$ i=1, 2 and $[\beta_h]$ are the dynamic compliance matrices in the frequency domain corresponding to the excitation frequencies, Ω_{s1}, Ω_{s2} and $N_{g1}\Omega_{s1}$, respectively.

$$\left[\beta_{gi}\right] = \sum_{r=1}^{n} \frac{\{\psi_r\}\{\psi_r\}^T}{\left[\left(\omega_r^2 - \Omega_{si}^2\right) + 2j\zeta_r\Omega_{si}\omega_r\right]}, \qquad i=1, 2; \tag{1.13a}$$

$$\left[\beta_h\right] = \sum_{r=1}^{n} \frac{\{\psi_r\}\{\psi_r\}^T}{\left[\left(\omega_r^2 - \left(N_{g1}\Omega_{si}\right)^2\right) + 2j\zeta_r N_{g1}\Omega_{si}\omega_r\right]}. \tag{1.13b}$$

$\{\psi_r\}$ represents the r-th mass matrix-normalized modal vector, n is the total number of degrees of freedom of the system, $j = \sqrt{-1}$, and ζ_r is the damping ratio for r-th mode. See Appendix A for the computer code GRD which uses the theory given here.

1.4. PARAMETRIC STUDIES

1.4.1. Modes of Interest

The generic system shown in Figure 1.1 is modeled by FEM to examine the natural modes of a general linear geared rotor-bearing system and to study the effects of several system parameters on the dynamics of the system. Two numerical data sets as listed in Table 1.1 are used. Predicted natural frequencies and modes for Set A are presented in Table 1.2. The response of the system to $\bar{e}(t)$ is also computed; Figures 1.4, 1.5 and 1.6 display the response in the Y and torsional directions at the pinion location and the dynamic load to static load ratio at the mesh point $d_{g1}\bar{F}_{hY} / 2\bar{T}_{mg1}$, respectively. The system has no peak responses at the modes corresponding to motion in the X direction since the excitation is applied in the Y (pressure line) direction, and

16

Table 1.1 Numerical data sets of the system used for calculations.

Parameters	Set A[†]	Set B
I_{g1}, I_{g2} (kg-m^2)	0.0018, 0.0018	0.0097, 0.0097
m_{g1}, m_{g2} (kg)	1.84, 1.84	3.45, 3.45
d_{g1}, d_{g2} (m)	0.089, 0.089	0.135, 0.135
N_{g1}	28	30
k_h	1.0×10^8	1.0×10^8
k_b (N/m)	variable	rigid
L_{s1L}, L_{s1R} (m)	0.127, 0.127	variable
L_{s2L}, L_{s2R} (m)	0.127, 0.127	variable
K_1, K_2 (N-m/rad)	--	variable
I_P, I_L (kg-m^2)	--	variable
$d_{s1,o}, d_{s2,o}$ (m)	0.037, 0.037	0.04, 0.04
$d_{s1,i}, d_{s2,i}$ (m)	0., 0.01	--
$\tilde{e}$ (m)	9.3×10^{-6}	--

[†] NASA Lewis Research Center gear test rig.

Table 1.2. First 10 natural frequencies for set A of Table 1.1 ($k_t/k_b=10$).

Modal Index	Modes of Interest	Natural Frequency ω_r Hz.	Natural Mode Description
0		0	torsional rigid body
1	ψ_I	581	first transverse-torsional coupled
2		687	X direction, transverse (driving shaft)
3	ψ_{II}	689	Y direction, transverse
4		691	X direction, transverse (driven shaft)
5	ψ_{III}	2524	second transverse-torsional coupled
6		3387	Y direction, transverse
7		3387	X direction, transverse (driving shaft)
8		3421	X direction, transverse (driven shaft)
9		3421	Y direction, transverse
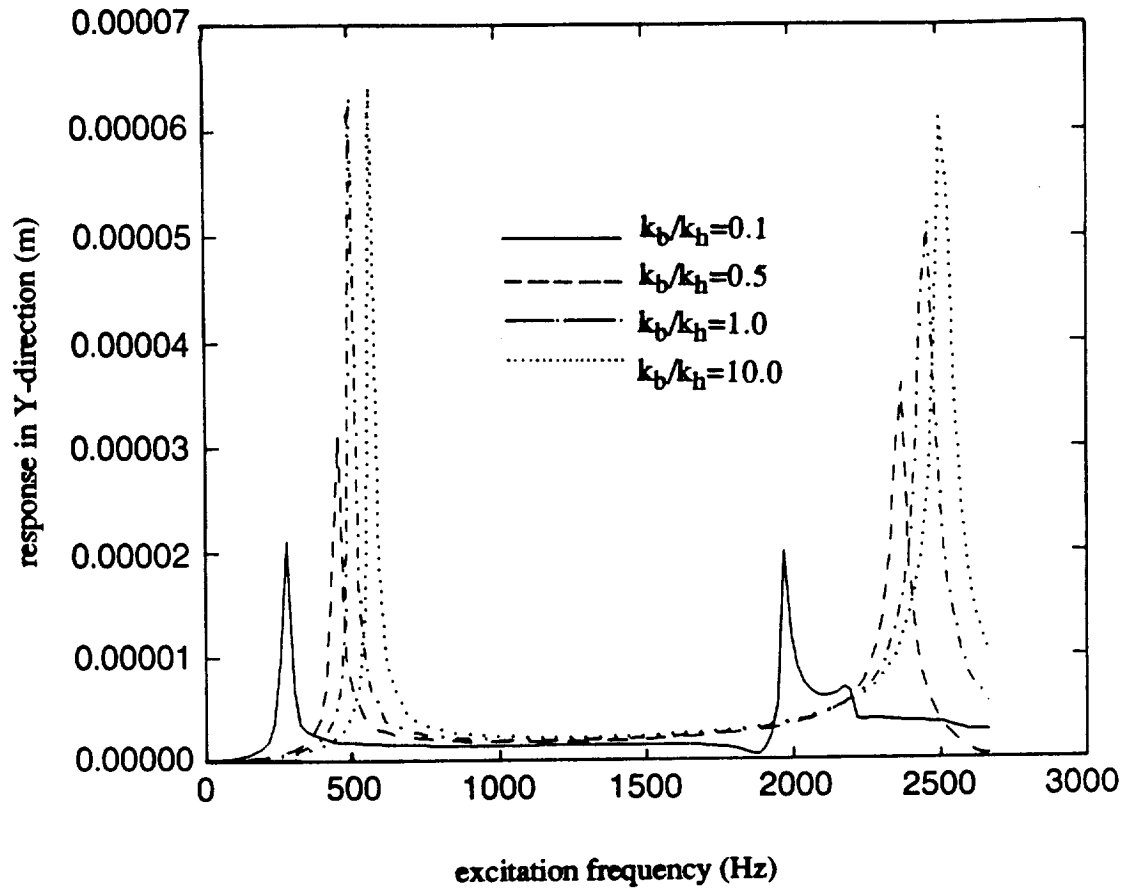
Figure 1.4. Forced response of the system with dataset A (Table 1.1) to the displacement excitation in the direction of pressure line (at pinion location) for four different bearing stiffnesses k_b.

19
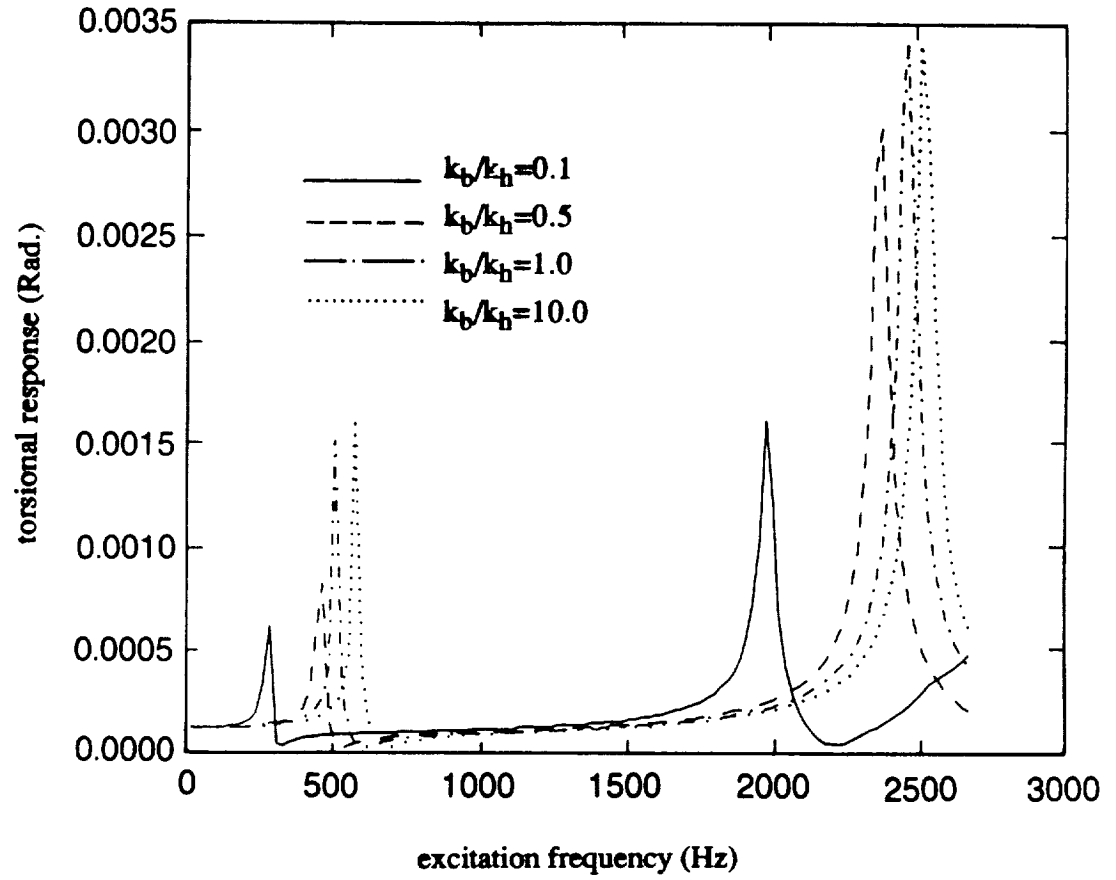
Figure 1.5.   Forced torsional response of the system with dataset A (Table 1.1) to
the displacement excitation at pinion location for four different bearing
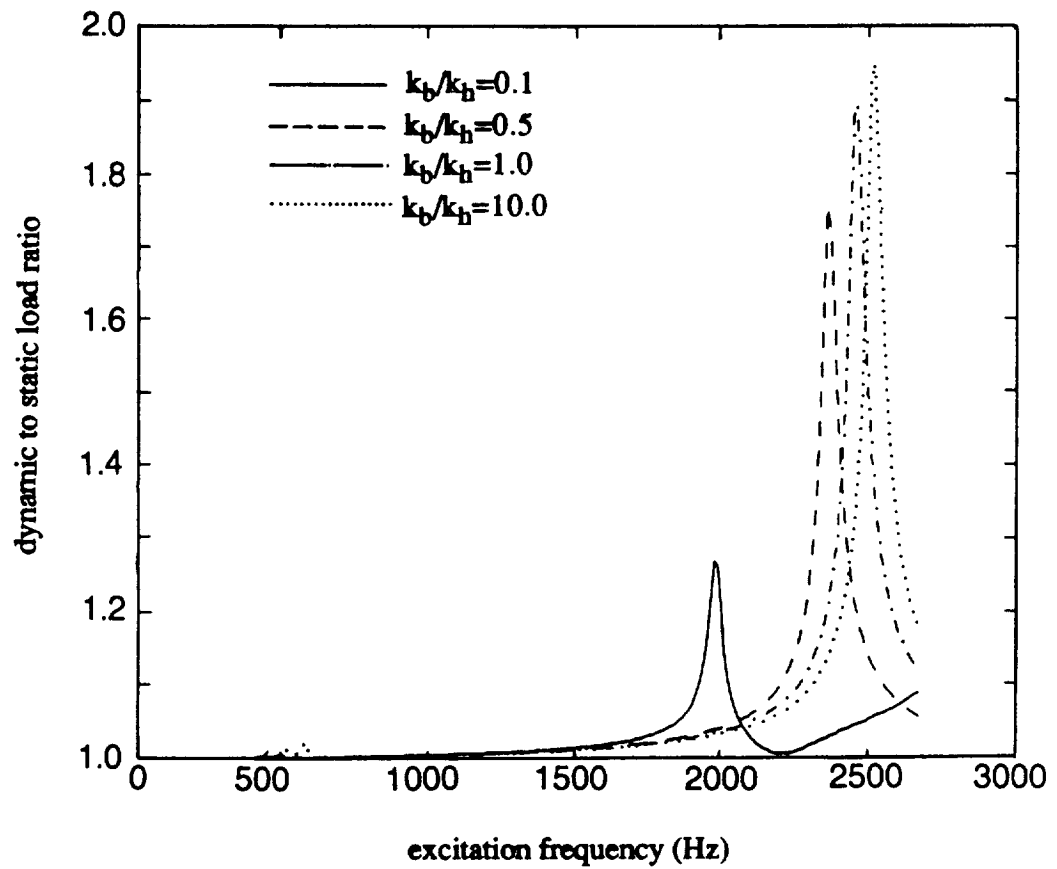stiffnesses k_b.

20

Figure 1.6   Dynamic to static load ratio for dataset A (Table 1.1) due to the static transmission error excitation for four different bearing stiffnesses k_b.

the vibration in the X direction is dynamically uncoupled from the vibrations in the Y and torsional motions, as described in the previous section. Therefore, the natural modes corresponding to motions in the X direction can be eliminated when only $\bar{e}(\bar{t})$ excites the system. Accordingly, the following three typical modes are of special importance:
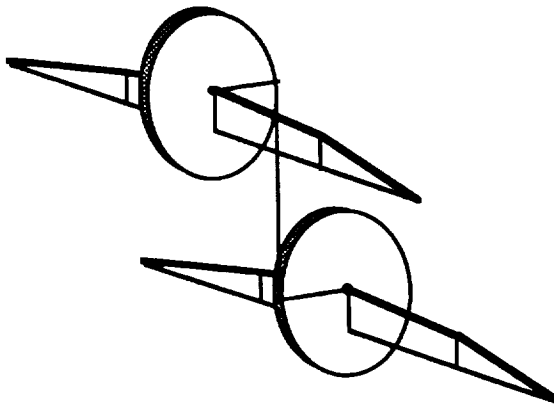
I. First Transverse-Torsional Coupled Mode ψ_I: This is the second mode listed in Table 1.2 at ω_I (581 Hz for the system considered). This mode corresponds to the first peak in Figures 1.4 and 1.5 and its schematic shape is shown in Figure 1.7a. Here, shafts move in opposite directions, gears vibrate in opposite directions also; but transverse and torsional vibrations combine to yield small relative motion at the gear mesh point. Therefore, dynamic loads at the mesh point are not large, resulting in no peak in Figure 1.6 at ω_I while Figures 1.4 and 1.5 have peaks governed by this mode.

II. Purely Transverse Mode ψ_{II}: At this mode with natural frequency ω_{II} (689 Hz in Table 1.2), there is no torsional vibration and both shafts vibrate in phase in the pressure line direction as shown in Figure 1.7b schematically. The relative displacement at mesh point is zero since the gear ratio $v_g=1$. Therefore, $\bar{e}(\bar{t})$ cannot excite this mode as no peaks are observed in Figures 1.4, 1.5 and 1.6 at frequency ω_{II}.

III. Second Transverse-Torsional Coupled Mode ψ_{III}: The second and the highest peak seen in Figures 1.4, 1.5 and 1.6 corresponds to this mode at ω_{III} . As seen from the mode shape illustrated in Figure 1.7c, both shafts and gears vibrate in opposite directions, and transverse and torsional vibrations are additive at the mesh point. Thus a large relative displacement at the mesh point is obtained, which results in
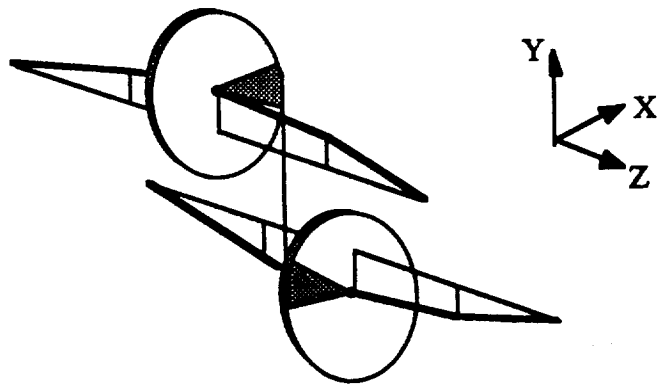
a) first transverse-torsional coupled mode, Ψ_I

b) purely transverse mode, Ψ_{II}
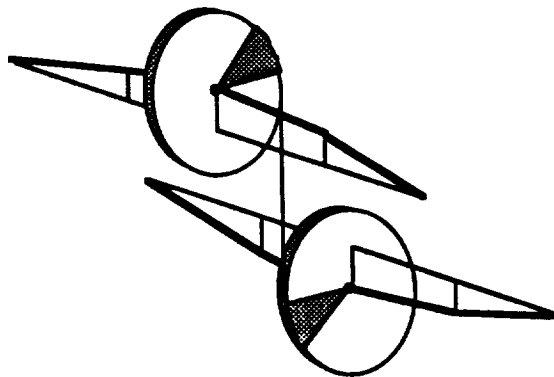
c) second transverse-torsional coupled mode, Ψ_{III}

Figure 1.7.   Typical natural modes of interest; see Table 1.2 for further details..

23

a large peak in Figures 1.4, 1.5 and 1.6. This is the mode at which the coupling between transverse and torsional vibrations is very strong.

These three modes are observed in all geared rotor systems and they play an important role in governing dynamic response of the system excited by $\bar{e}(\bar{t})$. Therefore, any accurate mathematical model of the geared rotor-bearing systems must be able to predict these modes.

1.4.2. Effect of Bearing Compliances

In most cases, radial stiffness of a typical rolling element bearings k_b is roughly of the same order of magnitude as the gear mesh stiffness k_h; in general it lies in the range $0.1k_h<k_b<100k_h$. Therefore, bearing flexibility should be included in the analysis. A parametric study for data set A of Table 1.1 has been conducted to demonstrate the effect of k_b on the natural frequencies and the frequency response of the system excited by $\bar{e}(\bar{t})$. Figures 1.4, 1.5 and 1.6 show the response in the Y and torsional directions and the dynamic mesh load respectively for k_b values ranging from $0.1k_h$ to $10k_h$, shaft stiffnesses are being kept the same. An increase in bearing stiffness results in an increase in both natural frequencies and the peak amplitudes. Above the range of k_b, the bearing becomes very rigid when compared to the shaft compliances and its effect on the system can be ignored.

1.4.3. Effect of Shaft Compliance

Data set B of Table 1.1 has been used to study the effect of shaft compliance on the natural modes. The shaft length is varied and the corresponding ω_r values are predicted by FEM; Figure 1.8 displays this result. The first natural frequency ω_I does not change considerably with varying shaft length, whereas ω_{II} and ω_{III} are strongly
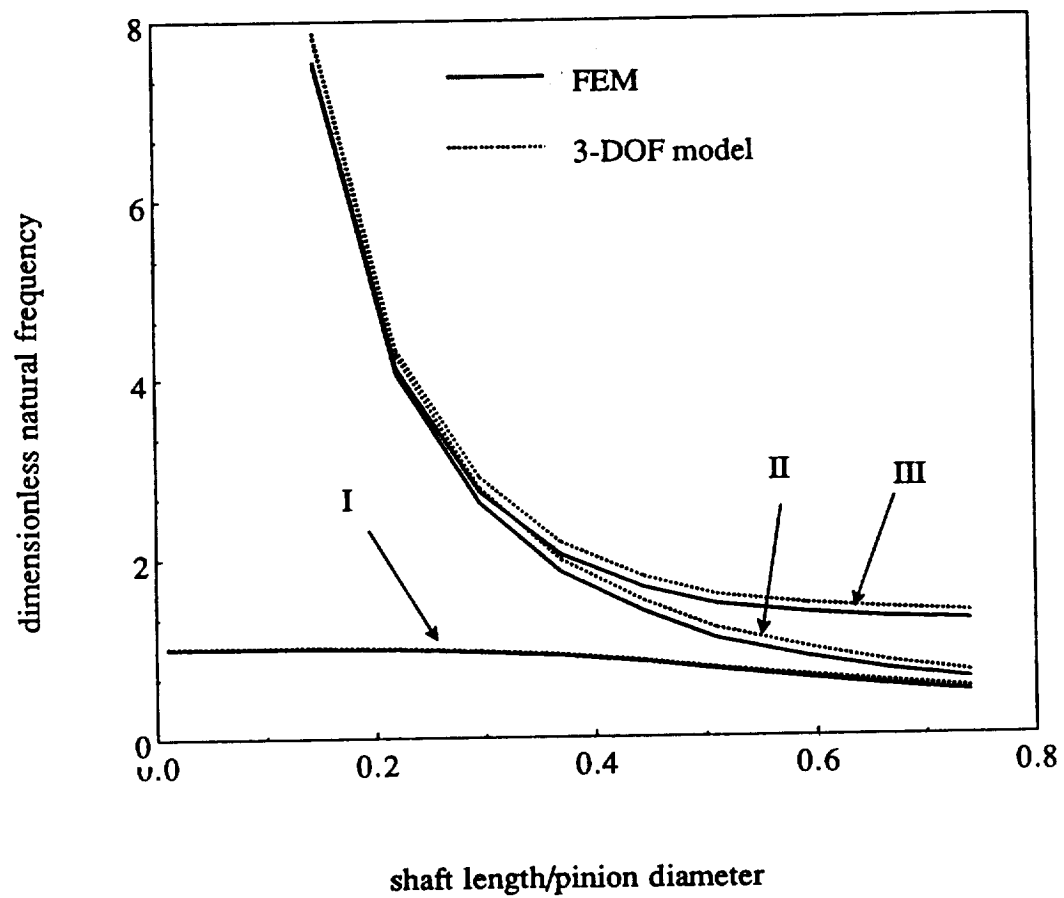
24

Figure 1.8.   Effect of the shaft length on the typical natural frequencies.

dependent on the shaft length, especially at smaller lengths. Another observation from Figure 1.8 is that ω_{II} and ω_{III} become very large for smaller shaft lengths and clearly move beyond the range of the operational speed of most geared rotor systems. In this case, the first coupled transverse-torsional mode ψ_I can be assumed to be uncoupled from these two modes.

1.4.4. Effect of Load and Prime Mover Rotary Inertias

As shown in Figure 1.1, the shafts are connected to a prime mover and a load at either end through flexible torsional couplings. The following parameters need to be considered: motor and load rotary inertias, torsional compliances of the flexible couplings, and stiffnesses of the driving and driven shafts.

First, the motor and load are assumed to be connected to the shafts without considering any torsional couplings in between. Figure 1.9 displays the variation in ω_I, ω_{II} and ω_{III} with a variation in the prime mover inertia. Here, data set B of Table 1.1 with L_{si}=0.04 m is used. ω_{II} and ω_{III} are not affected and therefore, the inertias of motor and load can be disregarded if the major concern is to predict these two modes. However, ω_I is strongly dependent on prime mover and load inertias.

Second, the load and prime mover inertias are fixed (I_p=5I_{g1}) and the torsional springs K_1 and K_2, which represent flexible couplings and shafts are varied. Figure 1.10 shows the variation in ω_r with changing K_1 and K_2. Here ω_{II} and ω_{III} are again not affected, as expected. On the other hand, ω_I is almost constant (which is nearly equal to the value yielded by zero prime mover and load inertias) up to a point and, it starts increasing with increasing K. This indicates that the motor and load are isolated from the geared rotor system when the in-between torsional elements are compliant
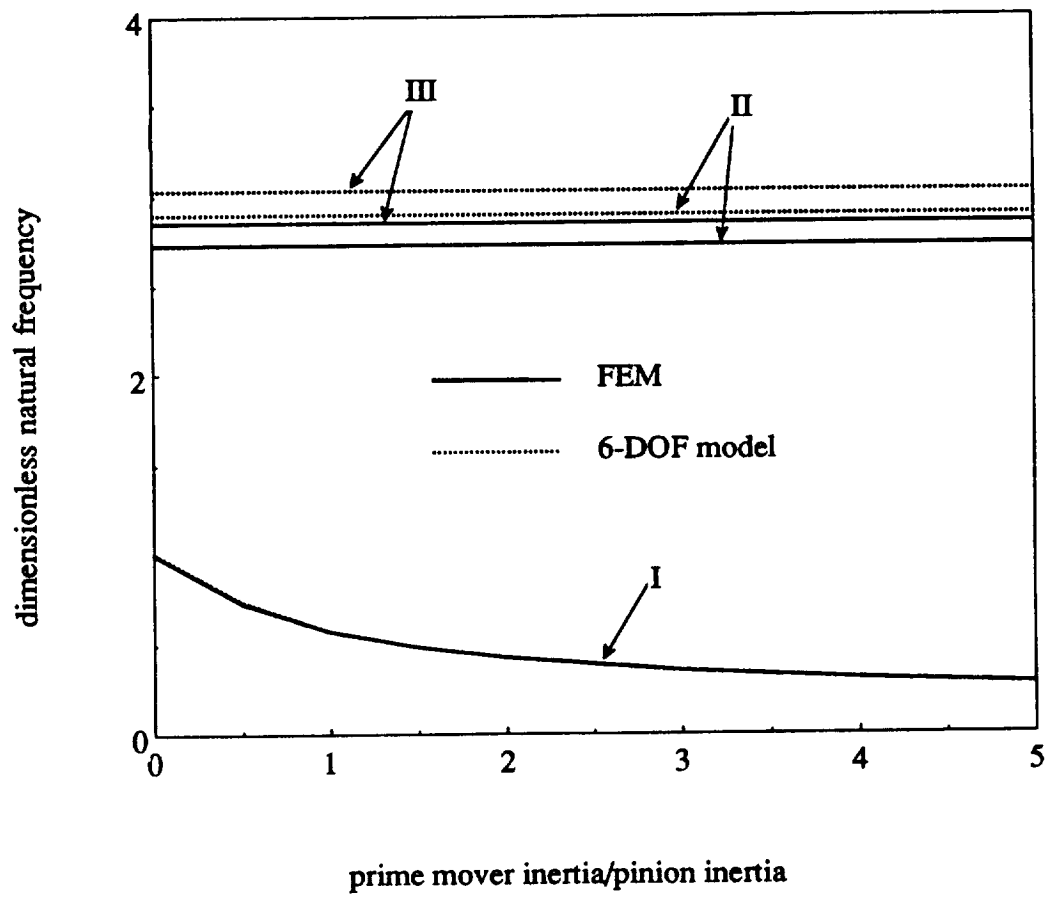
26

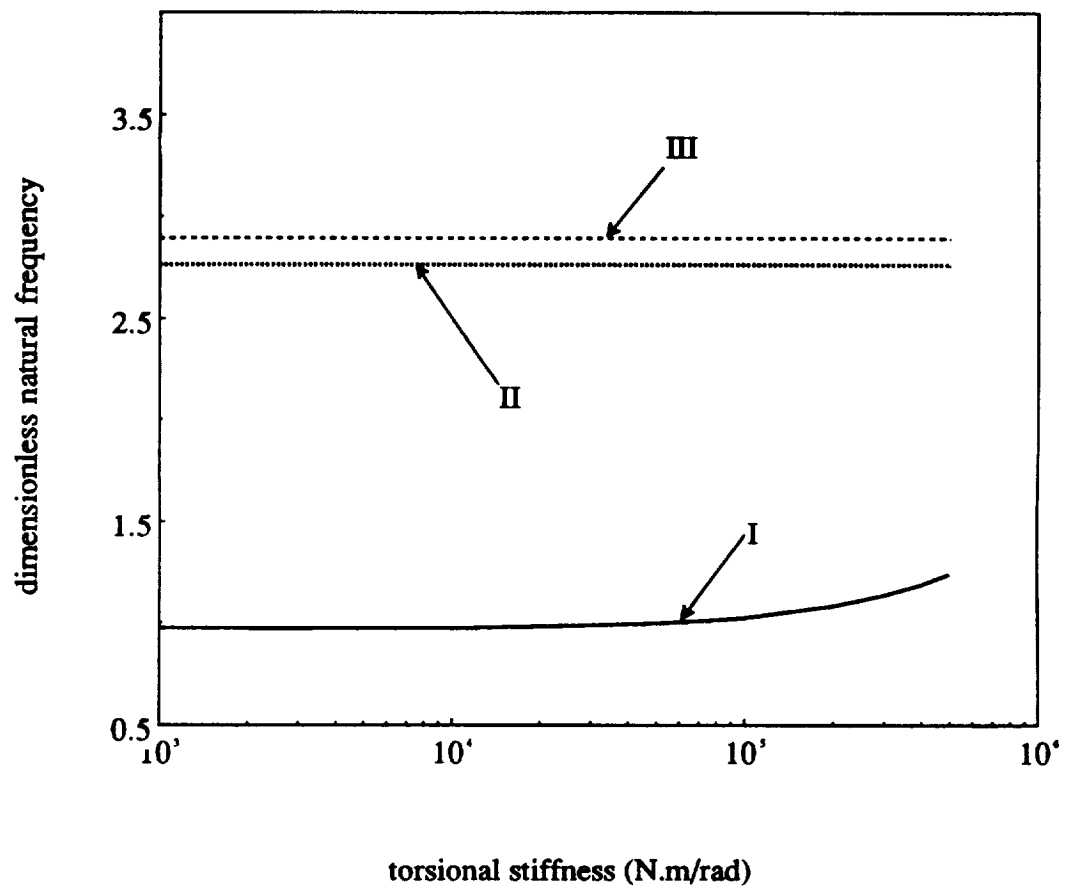Figure 1.9.   Effect of the prime mover inertia on the natural frequencies.

Figure 1.10. Effect of the torsional stiffness K of the transmission elements in between the gear box and the prime mover & load inertias on the natural frequencies.

enough, which is the case in most practical systems. Under these circumstances, motor and load inertias can be neglected in the analysis.

1.5. REDUCED ORDER LINEAR TIME-INVARIANT MODELS

In this section, three different reduced order analytical models of the geared rotor-bearing systems shown in Figure 1.1 will be developed and the conditions and system parameters at which these simple models can predict the dynamics of the system accurately, will be discussed. The finite element model of Section 1.3 will be employed as a reference model to check the validity.

1.5.1. Single Degree of Freedom Torsional Model of Gear Pair

As the simplest model, a single degree of freedom (SDOF) model of geared rotor systems shown in Figure 1.2 is considered. The shaft and bearing flexibilities and the motor and load inertias are not considered in this model. This model can only predict a single mode at a frequency ω_n as defined in equation (1.3c) which corresponds to the first transverse-torsional mode at ω_I. Here, $\omega_I \rightarrow \omega_n$ when shaft lengths $L_{si} \rightarrow 0$ and bearings are very stiff. And, ω_{II} and ω_{III} are sufficiently beyond the operational speed range and the variation in ω_I is assumed to be negligible with shaft length as shown in Figure 1.8. Therefore, in some cases, the SDOF model of Figure 1.2 can be used to represent the system provided these conditions are met. For instance, for data set B of Table 1.1 with $L_{si}=5$ cm, a SDOF model can be utilized up to an operational rotational speed of 6000 rpm which corresponds to the excitation frequency at 3000 Hz for $N_{g1}=30$ teeth. As it is seen in Figure 1.8, only the first mode is observed and its variation is not significant within $0 \leq \Omega \leq 3000$ Hz and $0 \leq L_{si} \leq 5$ cm.

1.5.2. Three Degree of Freedom Model

The SDOF model of Figure 1.2 is not adequate when the shafts and bearings are compliant. To overcome this deficiency, a three degree of freedom (3-DOF) transverse-torsional model as shown in Figure 1.11a is developed. Equation 1.4 gives the equations of motion with dimensionless mass [M], damping [C] and stiffness [K] matrices and displacement vector {q} given as follows:

$$[M] = \begin{bmatrix} 1 & 0 & 0 \\ 0 & m_{g1}/m_{c1} & 0 \\ 0 & 0 & m_{g2}/m_{c1} \end{bmatrix}; \quad (1.14a)$$

$$[C] = \frac{c_h}{\sqrt{k_h m_{c1}}} \begin{bmatrix} 1 & 1 & -1 \\ 1 & (1+c_{bs1}/c_h) & -1 \\ -1 & -1 & (1+c_{bs2}/c_h) \end{bmatrix}; \quad (1.14b)$$

$$[K] = \begin{bmatrix} 1 & 1 & -1 \\ 1 & (1+k_{bs1}/k_h) & -1 \\ -1 & -1 & (1+k_{bs2}/k_h) \end{bmatrix}; \quad (1.14c)$$

$$\{q\} = \begin{bmatrix} u, & y_{g1}, & y_{g2} \end{bmatrix} \quad (1.14d)$$

$$u = \frac{\theta_{g1}}{2} - \frac{d_{g2}\theta_{g2}}{2d_{g1}}; \quad y_{gi} = \frac{\bar{y}_{gi}}{d_{g1}}, \quad i = 1, 2. \quad (1.14e,f)$$

Here, k_{bs1} and k_{bs2} are equivalent lateral stiffnesses representing shaft and bearing flexibilities, and c_{bs1} and c_{bs2} are equivalent viscous damping values. This model can
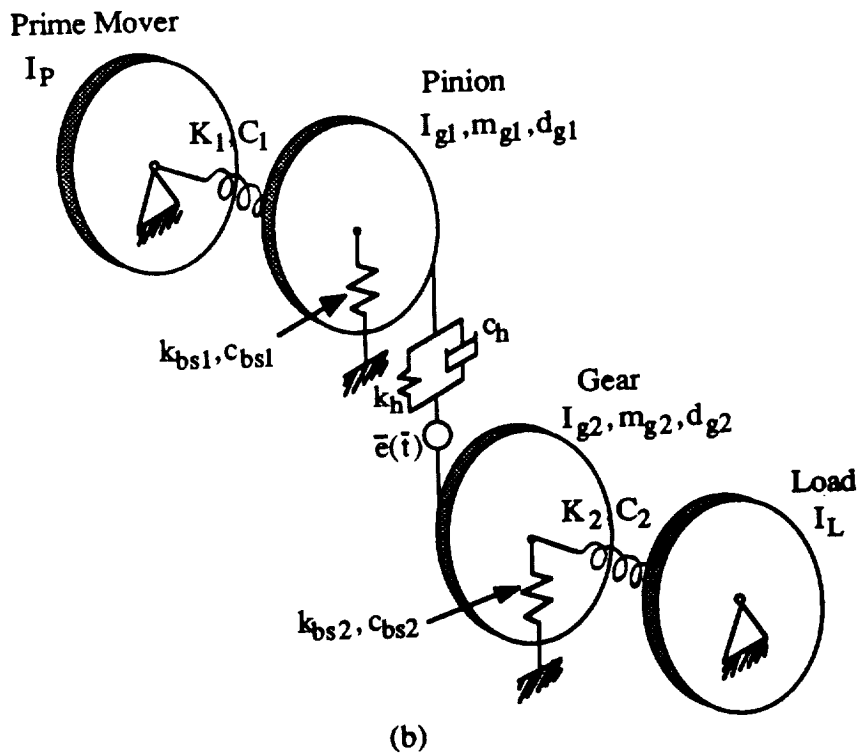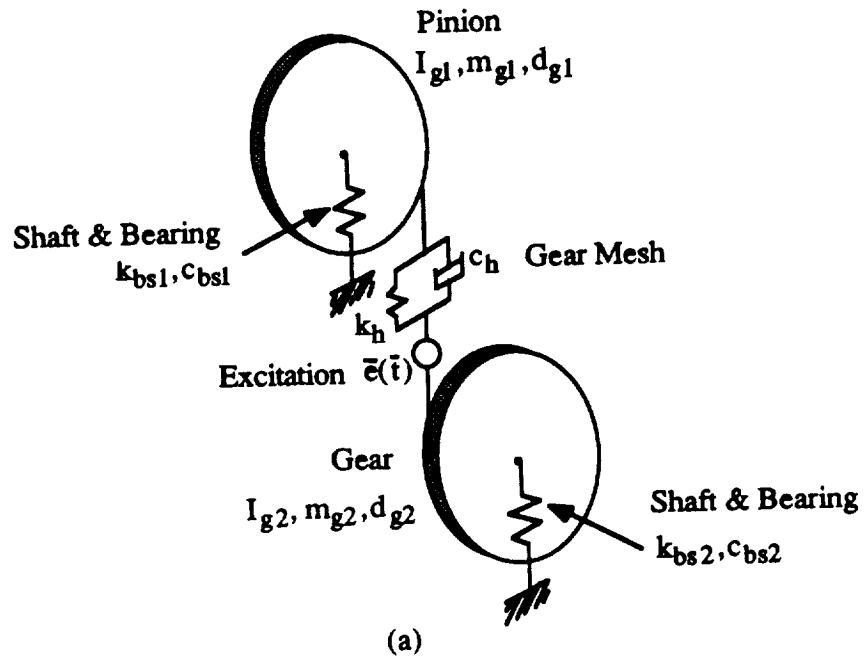
30

Figure 1.11. Reduced order analytical models of Figure 1.1; a) three degree of freedom model, b) six degree of freedom model.

31

accurately predict all three modes of interest as evident from Figure 2.8 and Table 1.3 where its predictions are compared with the results of FEM.

When the system is connected to the motor and load inertias, then the in between torsional stiffnesses K_1 and K_2 should be compliant enough to be able to neglect the effects of the motor and load inertias, as it is discussed earlier in Section 1.4.4. In summary, the 3-DOF model shown in Figure 1.11a can be used to describe the dynamics of the geared rotor system when: a) the shafts and bearings are compliant and provided the shafts are short such that higher order bending modes of the shafts are out of the frequency range considered, and b) the torsional stiffnesses of the connections in between the motor and load inertias and the gear box are sufficiently compliant.

1.5.3. Six Degree of Freedom Model

A six degree of freedom (6-DOF) model as shown in Figure 1.11b can be employed to represent the geared rotor-bearing system when the effects of the motor and load are not negligible as mentioned in Section 1.4.4. Equations of motion are still given by equation (1.4) and the dimensionless system matrices are defined as

$$[M] = \frac{1}{m_{c1}} \begin{bmatrix} I_P/d_{g1}^2 & 0 & 0 & 0 & 0 & 0 \\ 0 & I_{g1}/d_{g1}^2 & 0 & 0 & 0 & 0 \\ 0 & 0 & I_{g2}/d_{g1}^2 & 0 & 0 & 0 \\ 0 & 0 & 0 & I_L/d_{g1}^2 & 0 & 0 \\ 0 & 0 & 0 & 0 & m_{g1} & 0 \\ 0 & 0 & 0 & 0 & 0 & m_{g2} \end{bmatrix}; \qquad (1.15a)$$

Table 1.3. Comparison of typical modes obtained by FEM and 3-DOF models for set B of Table 1.1; L_{si}/d_{g1}=0.3.

| Displacement | Mode ψ | | |
	ψ_I FEM/3-DOF	ψ_{II} FEM/3-DOF	ψ_{III} FEM/3-DOF
θ_{g1}	-0.012/-0.011	-0.001/0.0	-0.210/-0.246
θ_{g2}	0.012/0.011	-0.001/0.0	0.210/0.246
y_{g1}	1.0/1.0	1.0/1.0	-1.0/-1.0
y_{g2}	-1.0/-1.0	1.0/1.0	1.0/1.0

$$[C] = \frac{1}{\sqrt{k_h m_{c1}}} \begin{bmatrix} \dfrac{C_1}{d_{g1}^2} & -\dfrac{C_1}{d_{g1}^2} & 0 & 0 & 0 & 0 \\[2mm] & \left(\dfrac{C_1}{d_{g1}^2}+\dfrac{c_h}{4}\right) & -\dfrac{c_h v_g}{4} & 0 & \dfrac{c_h}{2} & -\dfrac{c_h}{2} \\[2mm] & & \left(\dfrac{C_2}{d_{g1}^2}+\dfrac{c_h v_g}{4}\right) & -\dfrac{C_2}{d_{g1}^2} & -\dfrac{c_h v_g}{2} & \dfrac{c_h v_g}{2} \\[2mm] & & & \dfrac{C_2}{d_{g1}^2} & 0 & 0 \\[2mm] & -\text{symmetric}- & & & (c_h+c_{bs1}) & -c_h \\[2mm] & & & & & (c_h+c_{bs2}) \end{bmatrix}$$

$$(1.15b)$$

$$[K] = \frac{1}{k_h} \begin{bmatrix} \dfrac{K_1}{d_{g1}^2} & -\dfrac{K_1}{d_{g1}^2} & 0 & 0 & 0 & 0 \\[2mm] & \left(\dfrac{K_1}{d_{g1}^2}+\dfrac{k_h}{4}\right) & -\dfrac{k_h v_g}{4} & 0 & \dfrac{k_h}{2} & -\dfrac{k_h}{2} \\[2mm] & & \left(\dfrac{K_2}{d_{g1}^2}+\dfrac{k_h v_g}{4}\right) & -\dfrac{K_2}{d_{g1}^2} & -\dfrac{k_h v_g}{2} & \dfrac{k_h v_g}{2} \\[2mm] & & & \dfrac{K_2}{d_{g1}^2} & 0 & 0 \\[2mm] & -\text{symmetric}- & & & (k_h+k_{bs1}) & -k_h \\[2mm] & & & & & (k_h+k_{bs2}) \end{bmatrix}$$

$$(1.15c)$$

$$\{q\} = \left[\theta_P, \theta_{g1}, \theta_{g2}, \theta_L, y_{g1}, y_{g2}\right]$$

$$(1.15d)$$

For data set B of Table 1.1 predictions yielded by the 6-DOF model are compared with those by FEM as shown in Figure 2.9 and Table 1.4. Based on these results, it can be concluded that the 6-DOF model is accurate enough to predict the natural modes of the system. Accordingly, 6-DOF model must be employed when the effects of the motor and load are not negligible.

Table 1.4. Comparison of typical modes obtained by FEM and 6-DOF models for set B of Table 1.1; $L_{si}/d_{g1}=0.3$, $I_p/I_{g1}=5$.

Displacement	Mode ψ		
	ψ_I FEM/6-DOF	ψ_{II} FEM/6-DOF	ψ_{III} FEM/6-DOF
θ_P	0.079/0.079	0.002/0.0	-0.018/-0.013
θ_{g1}	-1.0/-1.0	-0.005/0.0	1.0/1.0
θ_{g2}	1.0/1.0	-0.005/0.0	-1.0/-1.0
θ_L	-0.079/-0.079	-0.002/0.0	0.018/0.013
y_{g1}	0.006/0.006	1.0/1.0	0.391/0.451
y_{g2}	-0.006/-0.006	1.0/1.0	-0.391/-0.451

35

1.6. CONCLUSION

In this chapter, a finite element model to investigate the dynamic behavior of linear time-invariant geared rotor systems has been developed. The transverse vibration of the system associated with shaft and bearing flexibilities and the dynamic coupling between the transverse and torsional vibrations due to gear mesh have been considered. Natural modes of the system have been identified and forced vibration response due to both low frequency external and high frequency internal excitations have been determined. Reduced order analytical models of the geared rotor bearing system have also been developed. Three different linear time-invariant models (SDOF, 3-DOF and 6-DOF) have been suggested to represent the geared system. By comparing results with FEM predictions, it has been shown that such reduced order linear models are reasonably accurate. Therefore these models will be extended in Chapters II, III and IV in analyzing the effects of system non-linearities and time-varying mesh stiffness.

CHAPTER II

NON-LINEAR DYNAMIC ANALYSIS OF
A SPUR GEAR PAIR

2.1. INTRODUCTION

2.1.1. Excitation Types and Backlash

The focus of this chapter is on the backlash non-linearity as excited primarily by the transmission error between the spur gear pair. A gear pair is bound to have some backlash which may be designed to provide adequate lubrication and eliminate interference due to manufacturing errors. Backlash-induced torsional vibrations may cause tooth separation and impacts in unloaded or lightly loaded geared drives. Such impacts result in intense vibration and noise problems and large dynamic loads, which may affect reliability and life of the gear drive [16,17]. Excitation mechanisms can be grouped as follows:

A. External Excitations: This group includes excitations due to rotating mass unbalances, geometric eccentricities, and prime mover and/or load torque fluctuations [18]. Although mass unbalances and geometric eccentricities can be reduced through improved design and manufacturing, torque fluctuations are not easy to eliminate since they are determined by the characteristics of the prime mover (piston engines, dc motors etc.) and load [19]. Such excitations are typically at low frequencies $\bar{\Omega}_T$ which are the first few multiples of the input shaft speed $\bar{\Omega}_s$. Practical examples include rattle problems in lightly loaded automotive transmissions and machine tools [19,20].

37

This group includes high frequency $\bar{\Omega}_h$ excitations caused by the manufacturing related profile and spacing errors, and the elastic deformation of teeth, shafts and bearings. Under the static conditions, all such mechanisms can be combined to yield an overall kinematic error function known as "the static transmission error" $\bar{e}(\bar{t})$ [17,18]. This error is defined as the difference between the actual angular position of the driven gear and where it would be if the gears were perfectly conjugate [17,18,21-23]. In gear dynamic models, $\bar{e}(\bar{t})$ is modeled as a periodic displacement excitation at the mesh point along the line of action [15,24-26] and its period is given by the fundamental meshing frequency $\bar{\Omega}_h = N \bar{\Omega}_s$ where N is the number of teeth on the pinion. Practical examples include steady state noise and vibration problems in automotive, aerospace, industrial, marine and appliance geared systems.

2.1.2. Literature Review

Experimental studies on the dynamic behavior of a spur gear pair with backlash started almost 30 years ago and still continue [27-29]. As one of the better examples of such experiments, Munro [27] developed a lightly damped (damping ratio $\zeta \approx 0.02$) four-square test rig to measure the dynamic transmission error of a spur gear pair. He used high precision gears with rigid shafts and bearings, and showed experimentally that the tooth separation takes place when the mean load is less than the design load. Dynamic transmission error versus speed curves were plotted to illustrate the steady state response and the jump phenomenon. Kubo [28] measured the dynamic tooth stresses using a similar set-up in order to calculate the dynamic

factors. He also observed a jump in the frequency response of the gear pair with backlash even though the test set-up was heavily damped ($\zeta \approx 0.1$).

Such experimental studies, though limited in scope, have clearly shown that the gear pair dynamics can not be predicted with a linear model - see Ozguven and Houser [14] for a detailed review of the linear gear dynamic models as available in the literature. Although most of the non-linear mathematical models used to describe the dynamic behavior of a gear pair are somewhat similar to each other, they differ in terms of the excitation mechanisms considered and the solution technique used. For instance, a large number of studies have focused on the rattle problem in lightly loaded geared drives which are excited by the low frequency external torque excitations [30-35]. A few investigators have included the static transmission error excitation in the non-linear models [24,35-37].

The gear backlash non-linearity is essentially a discontinuous and non-differentiable function and it represents a strong non-linear interaction in the governing differential equation. This issue has been discussed by Comparin and Singh [33] and they have concluded that most of the solution techniques available in the literature can not be directly applied to examine this problem. Most of the gear dynamic researchers recognized this problem implicitly, and therefore employed either digital or analog simulation techniques [19,24,29,35-38]. For instance, Umezawa et.al [29], Yang and Lin [32] and Ozguven and Houser [24] have solved a one degree of freedom torsional model of the gear pair using numerical techniques. Lin et.al. [38] included motor and load inertias in a three degree of freedom torsional model. Kucukay [35] has developed an eight degrees of freedom model to include the rocking and axial motions of the rigid shafts. In most of these studies, with the exception of Umezawa's analysis [29] which did not include any backlash, a

39

discontinuity has been seen in the frequency response characteristics. But many investigators have typically joined two discrete points to show a broad jump in the frequency response curve [24,35,38]. Some of these problems have been due to the numerical simulation techniques which may not work or may result in misleading answers if not employed properly. Such difficulties have been found by Comparin and Singh [33], Singh et al. [34] and Gear [39-40] but are yet to be resolved or addressed by the gear dynamics researchers. Accordingly, one of the major objectives of this chapter is to examine whether numerical simulation techniques can, in fact, be used to predict the dynamic response completely, and what precautions one must take to develop such a mathematical model. Since Comparin and Singh [33] and Singh et al. [34] have examined the external excitation problem, in this chapter we focus mainly on the internal excitation and see whether the numerical simulation technique can be made to work for the prediction of the non-linear frequency response characteristics.

A few researchers have attempted to obtain the analytical solutions for a gear pair problem, based on the piece-wise linear techniques which divided the non-linear regime into several linear regimes [41-43]. For instance, Wang [41,42] has used two and three degree of freedom torsional models with backlash, and assumed that the gear teeth are rigid and the driven gear has an infinite inertia. The governing equations have been solved using the piece-wise linear technique. It should be noted that the piece-wise linear technique gives only solutions for the equivalent linear systems and one typically may have difficulties in combining such solutions [43]. Comparin and Singh [33] overcame these problems by employing the harmonic balance method (HBM) and constructed analytical solutions for the non-linear frequency response characteristics of a gear pair with backlash as excited by the

external torque. In this chapter, we will use the same technique to examine the internal excitation problem, and compare results with digital simulation and experimental studies. Further literature review is included in subsequent sections.

2.2. PROBLEM FORMULATION

2.2.1. Physical Model

A two degree of freedom semi-definite model of the spur gear pair with rotary inertias I_{g1} and I_{g2} and base circle diameters d_{g1} and d_{g2} as shown in Figure 2.1 is considered here. The shafts and bearings are assumed to be rigid. The gear mesh is described by backlash of 2b and by a time invariant mesh stiffness $k_h \neq k_h(\bar{t})$ when in contact and viscous damping c_h. The equations of torsional motion of the gear pair as shown in Figure 2.1 are

$$I_{g1}\frac{d^2\theta_{g1}}{d\bar{t}^2} + \frac{d_{g1}c_h}{2}\left(\frac{d_{g1}}{2}\frac{d\theta_{g1}}{d\bar{t}} - \frac{d_{g2}}{2}\frac{d\theta_{g2}}{d\bar{t}} - \frac{d\bar{e}}{d\bar{t}}\right)$$

$$+ \frac{d_{g1}}{2}\bar{f}\left(\frac{d_{g1}}{2}\theta_{g1} - \frac{d_{g2}}{2}\theta_{g2} - \bar{e}(\bar{t})\right) = \bar{T}_{g1}(\bar{t}) \qquad (2.1a)$$

$$I_{g2}\frac{d^2\theta_{g2}}{d\bar{t}^2} - \frac{d_{g2}c_h}{2}\left(\frac{d_{g1}}{2}\frac{d\theta_{g1}}{d\bar{t}} - \frac{d_{g2}}{2}\frac{d\theta_{g2}}{d\bar{t}} - \frac{d\bar{e}}{d\bar{t}}\right)$$

$$- \frac{d_{g2}}{2}\bar{f}\left(\frac{d_{g1}}{2}\theta_{g1} - \frac{d_{g2}}{2}\theta_{g2} - \bar{e}(\bar{t})\right) = -\bar{T}_{g2}(\bar{t}) \qquad (2.1b)$$
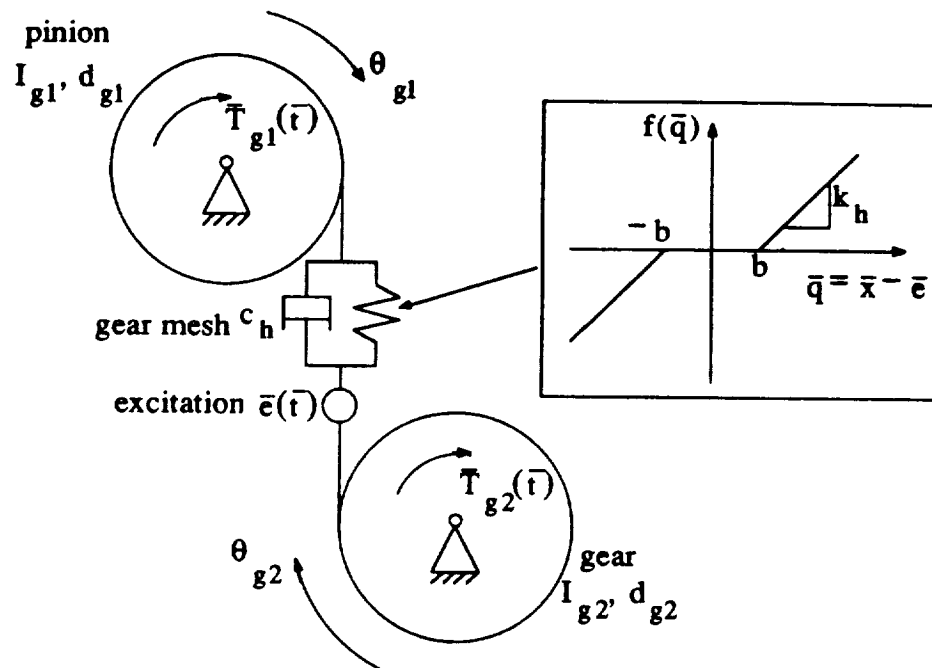
41

Figure 2.1.   Gear pair model.

where $\bar{T}_{g1}(\bar{t}) = \bar{T}_{g1m} + \bar{T}_{g1a}(\bar{t})$ and $\bar{T}_{g2}(\bar{t}) = \bar{T}_{g2m} + \bar{T}_{g2a}(\bar{t})$ are torques on pinion and gear and $\bar{f}$ is a non-analytical function essentially describing the mesh elastic force as shown in Figure 2.1. Here, output torque fluctuation $\bar{T}_{g2a}(\bar{t})$ will be neglected to simplify the dynamic problem, i.e. $\bar{T}_{g2}(\bar{t}) = \bar{T}_{g2m}$. Equations (2.1a) and (2.1b) can be reduced to one equation in terms of $\bar{q}(\bar{t})$ which is defined as the difference between the dynamic transmission error $\bar{x}(\bar{t})$ and the static transmission error $\bar{e}(\bar{t})$.

$$m_{c1}\frac{d^2\bar{q}}{d\bar{t}^2} + c_h\frac{d\bar{q}}{d\bar{t}} + k_h f(\bar{q}(\bar{t})) = \bar{F}_m + \bar{F}_{aT}(\bar{t}) - m_c\frac{d^2\bar{e}}{d\bar{t}^2} \; ; \qquad (2.2a)$$

$$\bar{q}(\bar{t}) = \bar{x}(\bar{t}) - \bar{e}(\bar{t}) = \frac{d_{g1}}{2}\theta_{g1}(\bar{t}) - \frac{d_{g2}}{2}\theta_{g2}(\bar{t}) - \bar{e}(\bar{t}) \; ; \qquad (2.2b)$$

$$m_{c1} = \frac{1}{\left(\dfrac{d_{g1}^2}{4I_{g1}} + \dfrac{d_{g2}^2}{4I_{g2}}\right)} \; ; \qquad m_{c2} = \frac{4I_{g1}}{d_{g1}} \; ; \qquad (2.2c,d)$$

$$\bar{F}_m = \frac{2\bar{T}_{g1m}}{d_{g1}} = \frac{2\bar{T}_{g2m}}{d_{g2}} \; ; \qquad \bar{F}_{aT}(\bar{t}) = \frac{2m_c\bar{T}_{g1a}(\bar{t})}{m_{c2}d_{g1}} \; ; \qquad (2.2e,f)$$

$$f(\bar{q}(\bar{t})) = \frac{\bar{f}(\bar{q}(\bar{t}))}{k_h} . = \begin{cases} \bar{q}(\bar{t}) - b; & \bar{q}(\bar{t}) > b \\ 0; & -b < \bar{q}(\bar{t}) < b \\ \bar{q}(\bar{t}) + b; & \bar{q}(\bar{t}) < -b \end{cases} . \qquad (2.2g)$$

43

where m_{cl} is the equivalent gear pair mass, $\bar{F}_m$ is the average force transmitted through the gear pair, $\bar{F}_{aT}(\bar{t})$ is the fluctuating force related to the external input torque excitation and $f(\bar{q}(\bar{t}))$ is the nonlinear displacement function. Equation (2.2a) is nondimensionalized by letting $q(\bar{t}) = \bar{q}(\bar{t}) / b$, $\omega_n = \sqrt{k_h / m_{cl}}$, $t = \omega_n \bar{t}$ and $\zeta = c_h / (2 m_{cl} \omega_n)$. Now, consider harmonic excitation for both $\bar{e}(\bar{t})$ and $\bar{F}_{aT}(\bar{t})$ as $\bar{e}(\bar{t}) = \tilde{e} \sin(\bar{\Omega}_h \bar{t} + \phi_h)$, $\bar{F}_{aT}(\bar{t}) = \tilde{F}_{aT} \sin(\bar{\Omega}_T \bar{t} + \phi_T)$ where $\bar{\Omega}_h$ and $\bar{\Omega}_T$ are the fundamental excitation frequencies of internal displacement and external torque fluctuations, respectively. Further, define dimensionless excitation frequencies $\Omega_h = \bar{\Omega}_h / \omega_n$ and $\Omega_T = \bar{\Omega}_T / \omega_n$, dimensionless external mean load $F_m = \bar{F}_m / bk_h$, amplitudes of the dimensionless internal $(F_i(t))$ and external alternating forces $(F_e(t))$ $F_{aT} = \tilde{F}_{aT} / bk_h$ and $F_{ah} = \tilde{e} / b$ and nonlinear displacement function $f(q(t))$ to yield the following governing equation of motion.

$$\ddot{q}(t) + 2\zeta\dot{q}(t) + f(q(t)) = F(t) \tag{2.3a}$$

$$F(t) = F_m + F_{aT} \sin(\Omega_T t + \phi_T) + F_{ah}\Omega_h^2 \sin(\Omega_h t + \phi_h) \tag{2.3b}$$

$$f(q(t)) = \frac{f(\bar{q}(t))}{b} = \begin{cases} q(t) - 1; & q(t) > 1 \\ 0; & -1 < q(t) < 1 \\ q(t) + 1; & q(t) < -1 \end{cases} \tag{2.3c}$$

2.2.2. Scope and Objectives

When only external forces excite the system, i.e. $F_i(t)=0$, equation (2.3a) reduces to

$$\ddot{q}(t) + 2\zeta\dot{q}(t) + f(q(t)) = F_m + F_e(t) = F_m + F_{aT}\sin(\Omega_T t + \phi_T) \qquad (2.4)$$

This equation has been solved both analytically and numerically by Comparin and Singh [33]. Conversely, no analytical solution is available when the system is excited by internal static transmission error at the mesh frequency Ω_h which is considerably higher than Ω_T. The governing equation is given by substituting $F_e(t)=0$ in equation (2.3a); note that the external mean load F_m is not equal to zero.

$$\ddot{q}(t) + 2\zeta\dot{q}(t) + f(q(t)) = F_m + F_i(t) = F_m + F_{ah}\Omega_h^2\sin(\Omega_h t + \phi_h) \qquad (2.5)$$

Both equations (2.4) and (2.5) include the clearance non-linearity. While equation (2.4) represents the conventional representation of the vibro-impact problem [33,34], equation (2.5) is more applicable to the clearance problems in built-up assemblies where the excitation is generated by the kinematic errors. This chapter focuses on the steady frequency response characteristics of equation (2.5) which represents a gear pair with backlash as excited harmonically by the static transmission error excitation $\bar{e}(\bar{t})$ or F_{ah}. Specific objectives of this chapter are as follows:

1. Solve equation (2.5) numerically to resolve various modeling issues such as the existence of multiple solutions, subharmonic resonances and chaos.

45

2. Construct analytical solutions to equation (2.5) using the harmonic balance method (HBM) which has been applied successfully to solve equation (2.4) by Comparin and Singh [33].

3. Compare digital simulation and harmonic balance techniques and establish the premises under which the jump phenomenon can be predicted.

4. Perform parametric studies in order to understand the effects of F_m, F_{ah} and ζ on the frequency response. Vary the force ratio $\hat{F} = F_m/F_{ah}$ which is a measure of the load on the gear pair and compare the dynamic behavior for lightly and heavily loaded gears.

5. Validate analytical and numerical solution techniques by comparing these with previous experimental studies [27,28].

6. Compare the frequency response characteristics of equations (2.4) and (2.5), and also examine the possibility of finding overall response when both external and internal excitations are applied simultaneously.

7. Consider the periodic static transmission error excitation case, i.e. $F(t) = F_m + F_i(t) = F_m + \sum_{j=1}^{k} (j\Omega_h)^2 F_{ahj} \sin(j\Omega_h t + \phi_{hj})$; only the first three (k=3) harmonics are included.

2.3. DIGITAL SIMULATION

Clearance or vibro-impact problems in single degree of freedom systems have been examined by a number of investigators whose formulations are similar to equation (4) - see Comparin and Singh [33] for a detailed review. Moreover, Shaw and Holmes [43] and Moon and Shaw [44] have considered an elastic beam with one sided amplitude constraint subject to a periodic displacement excitation, and have

46

shown experimentally and numerically that the chaotic and subharmonic resonance regimes exist. Whiston [45-47] has investigated the non-linear response of a mechanical oscillator preloaded against a stop. He has solved the system equation for harmonic excitation by digital simulation and studied the existence and stability of the subharmonic and chaotic responses and the effect of preload on chaos. Similarly, Ueda [48] has solved the Duffing's equation, $\ddot{q} + 2\zeta\dot{q} + q^3 = F \sin t$, numerically and defined the regions of different solutions on a ζ versus F map. According to him, the existence of harmonic, subharmonic and chaotic responses depends on values of ζ and F, and multiple steady state solutions typically exist. Thompson and Stewart [49] have reviewed the available literature, with focus on the Duffing's equation. It should be noted that equation (2.5) is different from the non-linear differential equations considered by the above mentioned studies. Therefore, equation (2.5) must be studied in depth as the results of the other non-linear equations may not be directly applicable to our case.

First, we solve the governing non-linear differential equation (2.5) numerically using a 5th-6th order, variable step Runge-Kutta numerical integration routine (DVERK of IMSL [50]) which is suitable for a strongly non-linear equation [33,39,40]. Second, we investigate the existence of chaos and subharmonic resonances. Since the steady state response of the system due to the sinusoidal excitation is of major interest, it is necessary to run the numerical program for a sufficient length of time. The number of cycles of the forcing function required to reach the steady state depends on ζ.

A lightly loaded system ($\hat{F} = F_m/F_{ah} = 0.5$) with low damping ($\zeta = 0.02$) is considered as the first example case. For $F_m = 0.1$ and $F_{ah} = 0.2$, the response q(t) is computed over the frequency range $0 < \Omega_h < 1.5$. Figure 2.2 shows phase plane

47

plots $\dot{q}(t)$ vs. $q(t)$ for different Ω_h values. For $\Omega_h=0.3$, all transients converge to one periodic solution at the fundamental frequency Ω_h of the forcing function irrespective of the initial conditions $q(0)$ and $\dot{q}(0)$. Therefore, it is called a "period-one, t_p" attractor where $t_p=2\pi/\Omega_h$. But, in the case of $\Omega_h=0.5$, three coexisting period-one attractors have been found as shown in Figure 2.2. Here, $q(0)$ and $\dot{q}(0)$ define three steady state limit cycle solutions. For all initial conditions given by $-2 < q(0) < 2$ and $-2 < \dot{q}(0) < 2$, a map of the domains of attraction for each steady state solution is obtained in the map in Figure 2.3. If a smaller increment is used for the initial conditions, a finer resolution will be obtained. Hence each phase plane plot shown in Figure 2.2 is strictly governed by a subset of the initial conditions. Similarly, two period-one attractors are found at $\Omega_h=0.6$. At $\Omega_h=0.7$, besides two period-one t_p attractors, two more solutions of period $3t_p$ exist, i.e. period-three attractors. But only a period-two $2t_p$ attractor is seen when $\Omega_h=0.8$. Within the range $1.0 \le \Omega_h \le 1.5$, non-periodic, steady state or chaotic response is observed. Figure 2.4 shows the chaotic time history and the Poincare map (strange attractor) at $\Omega_h=1.0$. These results are qualitatively, but not quantitatively, similar to the studies reported on the Duffing's equation [48,49] and clearance non-linearity (equation (2.4) type) [33].

It is concluded that the subharmonic response of period nt_p provided $n \ne 1$ and the chaotic response ($t_p \rightarrow \infty$) are seen in the gear pair only for a certain set of parameters F_m, $\hat{F}$, ζ and Ω_h. It must also be noted that the multi-solution regions are strongly dependent on the choice of $q(0)$ and $\dot{q}(0)$. Only one steady state solution can be found via digital simulation when only one set of initial conditions is chosen at a given Ω_h, and the rest of the steady state solutions are not predicted. This
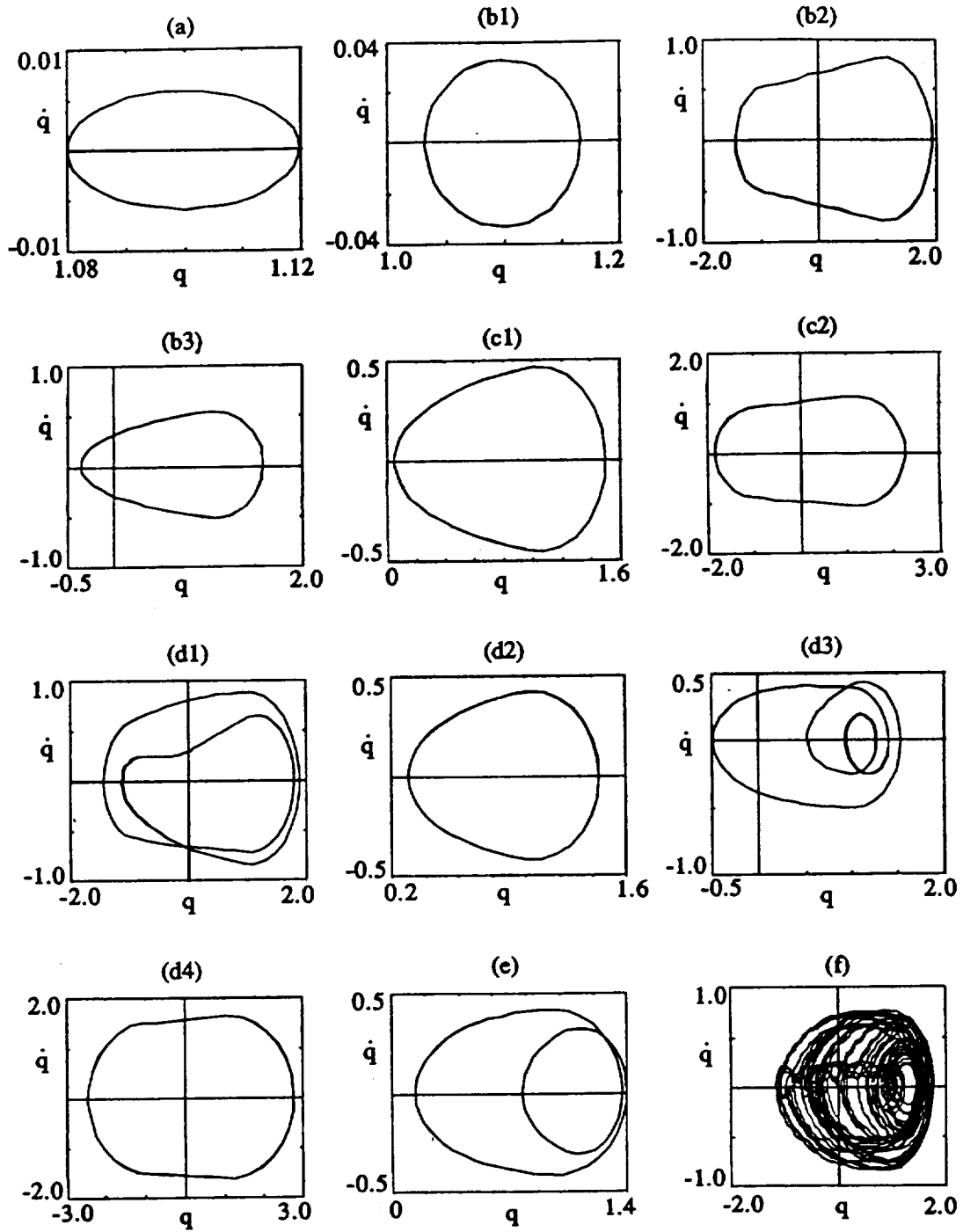
Figure 2.2. Phase plane plots of steady state solution q(t) for $\hat{F}=0.5$, $F_m=0.1$, $\zeta=0.02$ and for different Ω_h values; a) $\Omega_h=0.3$, b) $\Omega_h=0.5$, c) $\Omega_h=0.6$, d) $\Omega_h=0.7$, e) $\Omega_h=0.8$, f) $\Omega_h=1.0$.
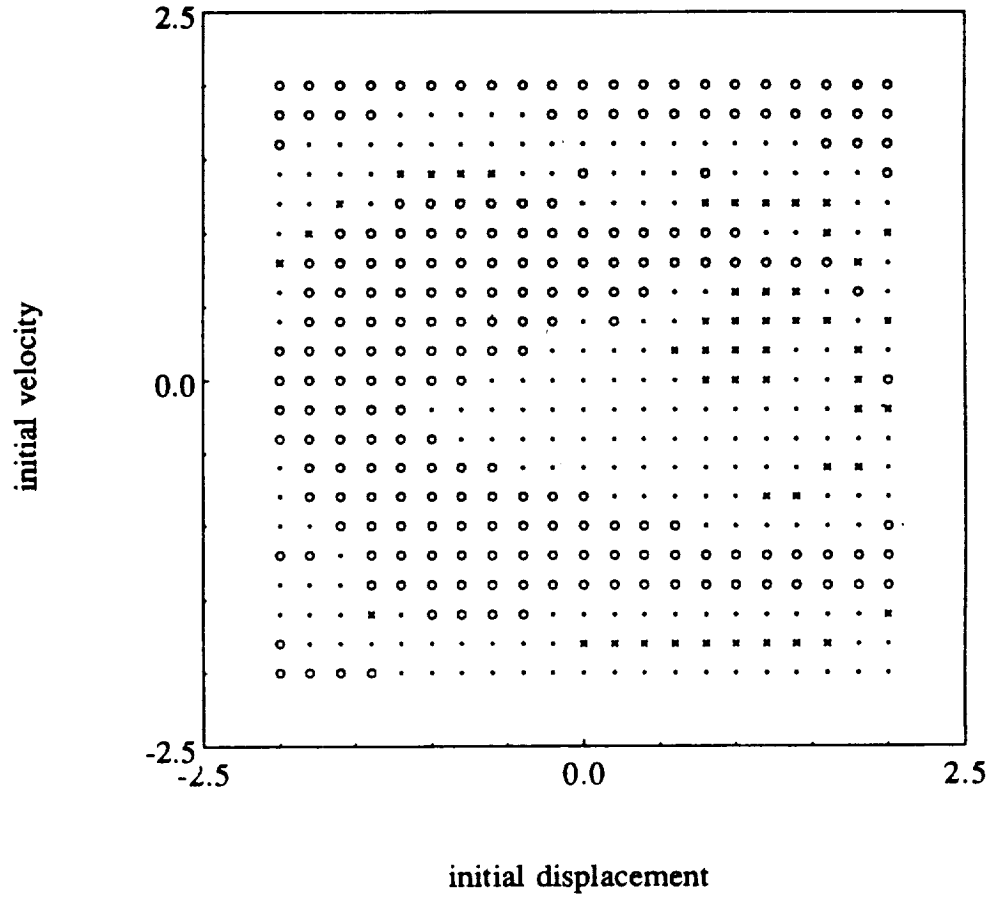
Figure 2.3. Domains of attraction for three attractors; x no impact (Figure 2.2b1), •
single sided impact (Figure 2.2b3), ○ double sided impact (Figure 2.2b2);
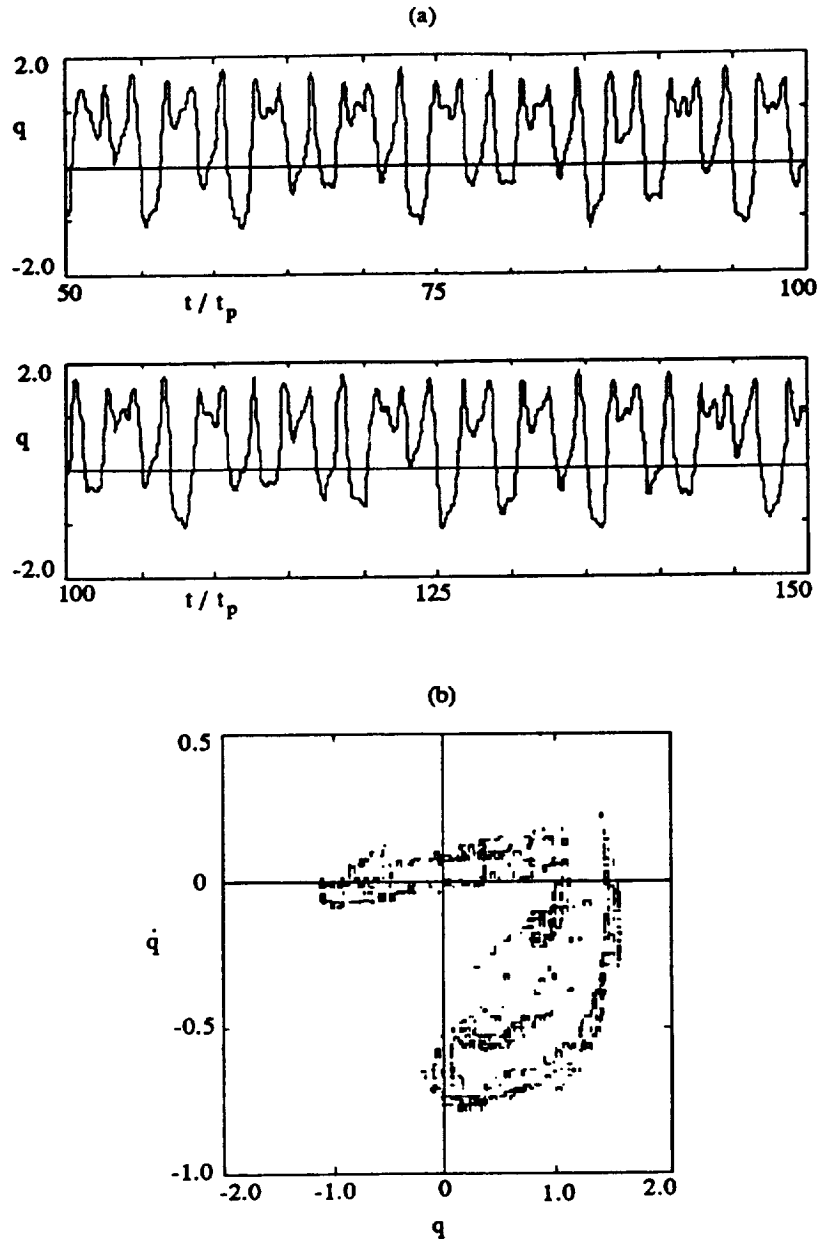$\hat{F}$=0.5, F_m=0.1, ζ=0.02 and Ω_h=0.5.

Figure 2.4. Chaotic response of a gear pair; $\hat{F}=0.5$, $F_m=0.1$, $\zeta=0.02$ and $\Omega_h=1.0$; a) time history, b) Poincare map.

51

results in an incomplete frequency response description. These issues will be discussed further in Section 2.5.

A heavily loaded system with $\hat{F}=2$, $F_m=0.1$ and the same amount of damping $\zeta=0.02$ is considered as the second example case. Figure 2.5 shows the phase plane plots for the same values of Ω_h which are used in the first example case. Unlike the first example case, no chaotic responses are found here. All of the solutions are period-one t_p type for all $\Omega_h<1.0$ and Figure 2.6 shows the typical domains of attraction at $\Omega_h=0.6$. However, within the range $1.0 \le \Omega_h \le 1.5$, one period-two attractor co-exists with the period-one orbit. Hence the force ratio $\hat{F}$ determines the existence of the chaotic and subharmonic responses. To illustrate this point, consider chaos shown in Figure 2.4. As $\hat{F}$ and ζ are increased, significant changes in the response are observed in Figures 2.7 and 2.8. A transition from the chaos to a period-two, and then to a period-one steady state solution is seen when $\hat{F}$ is increased from 0.75 to 1.0 and then to 1.5. Similarly, an increase in ζ to 0.05 reduces chaos to a period-eight attractor, which then bifurcates to a period-two orbit at $\zeta=0.1$ as shown in Figure 2.8. Since most real geared systems are heavily loaded with a high $\hat{F}$, chaotic and subharmonic responses should not be seen under the normal driving conditions. This issue will be discussed again in section 2.6.

2.4. ANALYTICAL SOLUTION

An approximate solution for equation (2.5) is constructed using the harmonic balance method (HBM). Assume that $q(t) = q_m + q_a \sin(\Omega_h t + \phi_r)$ where q_m and q_a are mean and alternating components of the steady state response, and ϕ_r is the phase angle. Here, higher harmonics of the response are not included in the analysis.
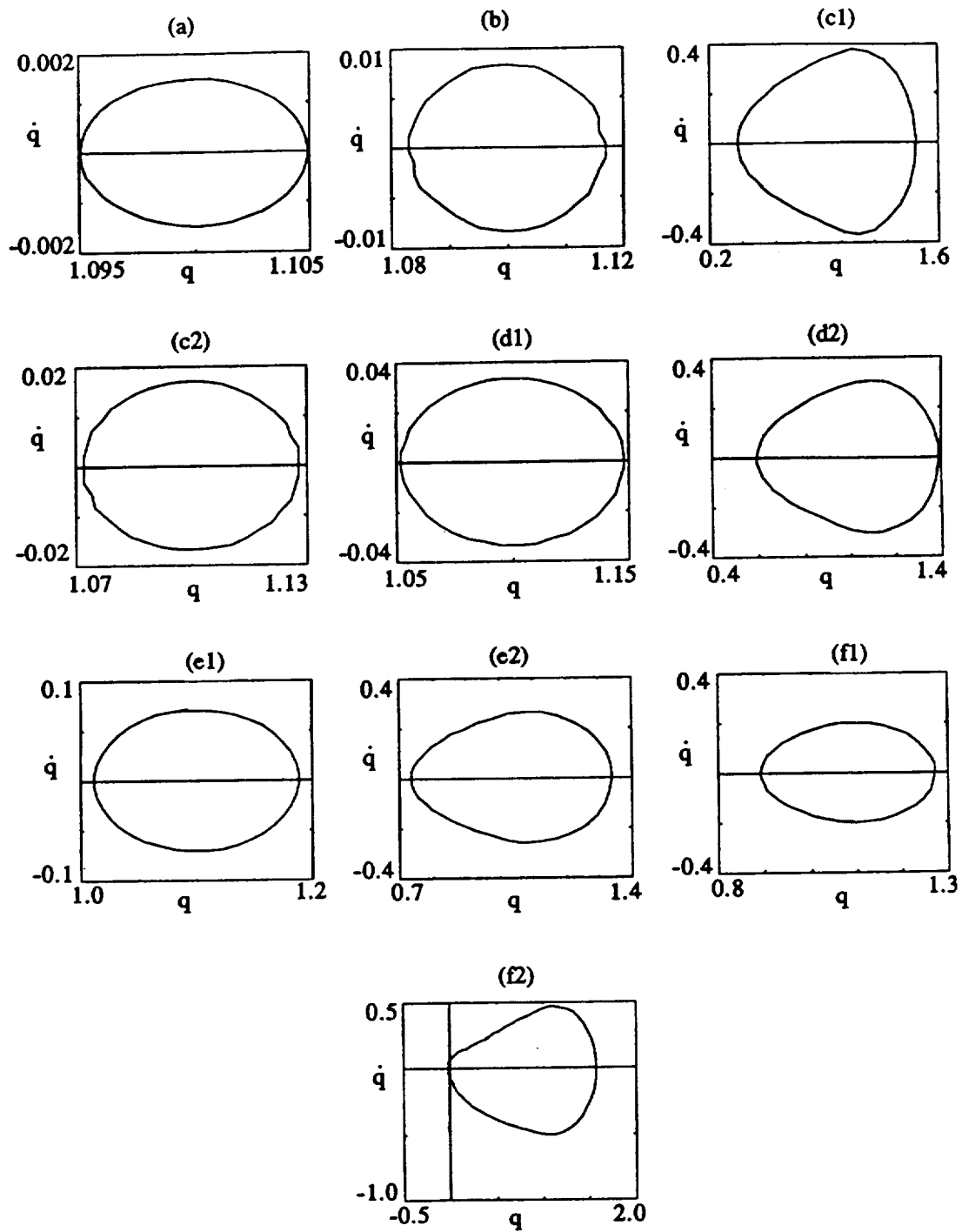
Figure 2.5. Phase plane plots of steady state solution q(t) for $\hat{F} = 2$, $F_m = 0.1$, $\zeta = 0.02$ and for different Ω_h values; a) $\Omega_h = 0.3$, b) $\Omega_h = 0.5$, c) $\Omega_h = 0.6$, d) $\Omega_h = 0.7$, e) $\Omega_h = 0.8$, f) $\Omega_h = 1.0$.
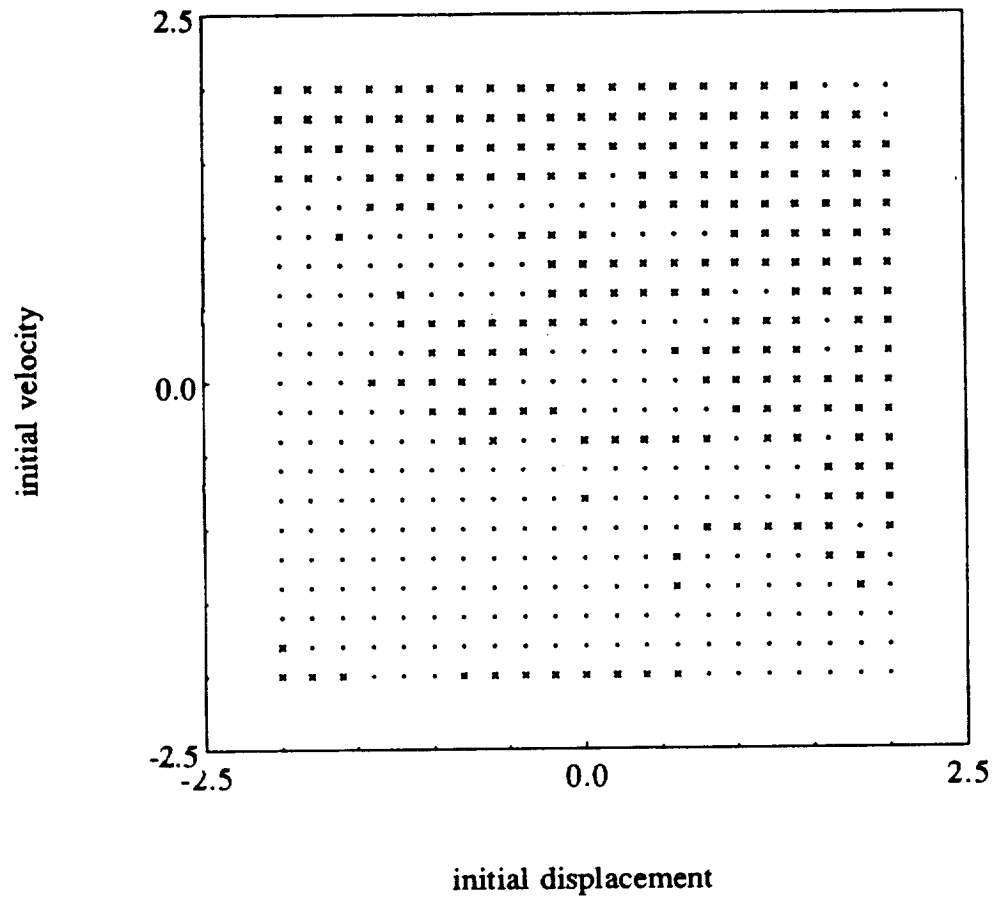
53

Figure 2.6. Domains of attraction for two attractors; x no impact (Figure 2.5c2), • single sided impact (Figure 2.5c1); $\hat{F}=2$, $F_m=0.1$, $\zeta=0.02$ and $\Omega_b=0.6$.
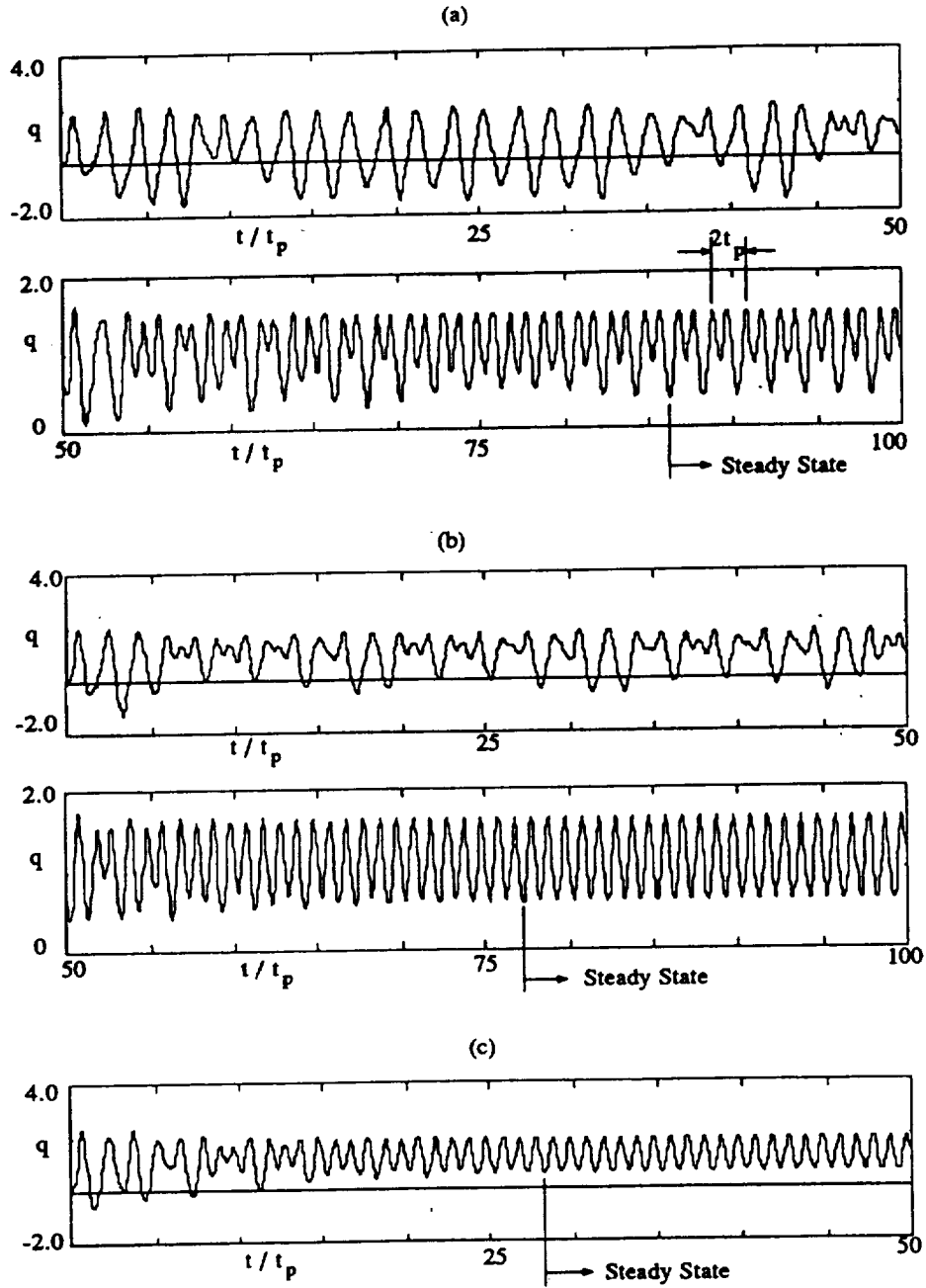
Figure 2.7. Time histories of q(t) for $F_{ah}=0.2$, $\zeta=0.02$ and a) $\hat{F}=0.75$, b) $\hat{F}=1$, c) $\hat{F}=1.5$.
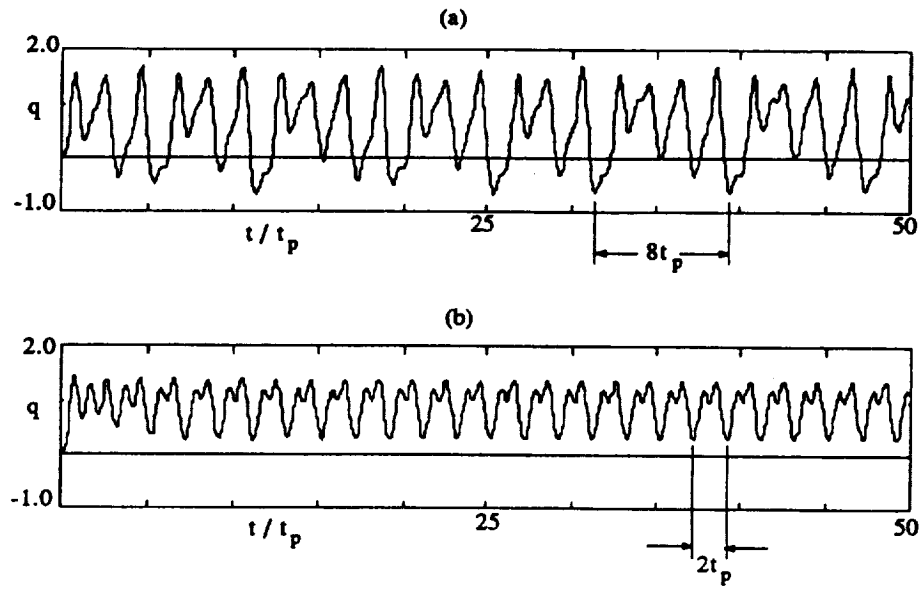
55

Figure 2.8. Time histories of q(t) for F_m=0.1, $\hat{F}$=0.5 and a) ζ=0.05, b) ζ=0.1.

56

The quasilinear approximation to the nonlinear function f(q) with the excitation

$$F(t) = F_m + F_i(t) = F_m + F_{ah}\Omega_h^2 \sin(\Omega_h t + \phi_h) \text{ is in the form [33,51]}$$

$$f(q) = N_m q_m + N_a q_a \sin(\Omega_h t + \phi_r) + N_a^* q_a \cos(\Omega_h t + \phi_r) \qquad (2.6)$$

where the describing functions N_m, N_a and N_a^* are defined as:

$$N_m = \frac{1}{2\pi q_m} \int_0^{2\pi} f(q_m + q_a \sin \varphi) d\varphi ; \qquad (2.7a)$$

$$N_a = \frac{1}{\pi q_a} \int_0^{2\pi} f(q_m + q_a \sin \varphi) \sin \varphi d\varphi ; \qquad (2.7b)$$

$$N_a^* = \frac{1}{\pi q_a} \int_0^{2\pi} f(q_m + q_a \sin \varphi) \cos \varphi d\varphi ; \quad \varphi = \Omega_h t + \phi_r . \qquad (2.7c,d)$$

Equation (2.3b) is substituted into equations (2.7a), (2.7b) and (2.7c) to obtain

$$N_m = 1 - \frac{q_a}{2q_m}[g(\gamma_+) - g(\gamma_-)] ; \quad N_a = 1 - \frac{1}{2}[h(\gamma_+) + h(\gamma_-)] ; \quad (2.8a,b)$$

$$N_a^* = 0 ; \quad \gamma_{\pm} = \frac{1 \pm q_m}{q_a} \qquad (2.8c,d)$$

where

$$g(\gamma) = \begin{cases} \frac{2}{\pi}\left(\gamma \sin^{-1}\gamma + \sqrt{1-\gamma^2}\right) \; ; & |\gamma| \le 1 \\ |\gamma| \; ; & |\gamma| > 1 \end{cases} ; \qquad (2.8e)$$

$$h(\gamma) = \begin{cases} \frac{2}{\pi}\left(\sin^{-1}\gamma + \gamma\sqrt{1-\gamma^2}\right) \; ; & |\gamma| \le 1 \\ -1 \; ; & \gamma < -1 \\ 1 \; ; & \gamma > 1 \end{cases} \qquad (2.8f)$$

Comparin and Singh [33] used truncated series expansions for functions $g(\gamma)$ and $h(\gamma)$ given by equations (2.8e) and (2.8f). They stated that the error involved in using truncated series is within 6 percent when only the first two terms are considered with the coefficient of the second term adjusted to yield the actual value for $\gamma = 1$. Using the same approach, one gets

$$g(\gamma) \cong \frac{2}{\pi}\left(1 + \left(\frac{\pi - 2}{2}\right)\gamma^2\right) ; \quad h(\gamma) \cong \frac{4}{\pi}\left(\gamma - \left(\frac{4-\pi}{4}\right)\gamma^3\right) ; \quad |\gamma| \le 1 \qquad (2.9a,b)$$

and obtains the following frequency response by substituting equations (2.6) into equation (2.5) and equating the coefficients of like harmonics:

$$q_a = \frac{F_{ah}\Omega_h^2}{\sqrt{\left(N_a - \Omega_h^2\right)^2 + (2\zeta\Omega_h)^2}} ; \quad q_m = \frac{F_m}{N_m} ; \qquad (2.10a,b)$$

$$\phi_r = \phi_h - \tan^{-1}\left(\frac{2\zeta\Omega_h}{N_a - \Omega_h^2}\right) . \qquad (2.10c)$$

58

Depending on the damping ratio ζ and the parameters F_m, F_{ah} and Ω which define the excitation, there are three cases at which different solutions are obtained: (a) no impact (no tooth separation), (b) single sided impacts (tooth separation, but no back collision), and (c) two sided impacts (back collision).

Case I: No Impact : The tooth separation (impact) is not observed in a geared system if the displacement q(t) lies in the region q(t)>1 all the time. This condition, shown in Figure 2.9 as case I, can be described mathematically as

$$\left|q_m + q_a\right| > 1 \quad \underline{and} \quad \left|q_m - q_a\right| > 1 \qquad (2.11)$$

Then, for no impact region in which the conditions defined by equation (2.11) are satisfied, the describing functions are given by

$$N_m = 1 - \frac{1}{q_m} ; \qquad N_a = 1 . \qquad (2.12a,b)$$

Substitution of equations (2.12) into equations (2.9) yields the following governing equations for no impact case

$$q_{aI} = \frac{F_{ah}\Omega_h^2}{\sqrt{\left(1 - \Omega_h^2\right)^2 + (2\zeta\Omega_h)^2}} ; \quad q_{mI} = F_m + 1 ; \qquad (2.13a,b)$$

$$\phi_{hI} = \phi_p - \tan^{-1}\left(\frac{2\zeta\Omega_h}{1 - \Omega_h^2}\right) . \qquad (2.13c)$$

59

Figure 2.9. Illustration of different impact regimes.

Hence, when there is no tooth separation, the system is linear and the mean and alternating components of the response, q_m and q_a, are uncoupled from each other. The transition frequencies from the no impact (linear) regime to the other non-linear regimes where tooth separation occurs are found by substituting $q_a = |q_m - 1|$ into the equations (2.13a) and (2.13c) as

$$\Omega_{t2, t1} = \sqrt{\frac{\left(1 - 2\zeta^2\right) \pm \sqrt{\left(1 - 2\zeta^2\right)^2 - \left(1 - \left(\frac{F_{ah}}{F_m}\right)^2\right)}}{\left(1 - \left(\frac{F_{ah}}{F_m}\right)^2\right)}} \qquad (2.14)$$

where Ω_{t1} and Ω_{t2} are the transition frequencies from no impact to single sided impact regimes below and above resonance, respectively.

Case II: Single Sided Impact : Mathematically, the single sided impacts (tooth separation without back collision) are observed if

$$q_m + q_a > 1 \quad \underline{and} \quad |q_m - q_a| < 1 . \qquad (2.15)$$

As illustrated in Figure 2.9 as case II, the solution remains in the region $q(t) > -1$. The describing functions satisfying equation (2.15) are in the form

$$N_m = 1 - \frac{q_{all}}{2q_{mII}} [\gamma_+ - g(\gamma_-)] ; \quad N_a = 1 - \frac{1}{2} [1 + h(\gamma_-)] . \qquad (2.16a,b)$$

61

Substitution of equations (2.10a) and (2.10b) into equations (2.16a) and (2.16b) gives the describing functions for the single sided impact case:

$$N_m = 1 + \frac{q_{all}}{2q_{mII}} \left\{ \frac{2}{\pi} \left[1 + \left(\frac{\pi - 2}{2} \right)(\gamma_-)^2 \right] - (\gamma_+) \right\} ; \qquad (2.17a)$$

$$N_a = \frac{1}{2} - \frac{2(1 - q_{mII})}{\pi q_{all}} \left[1 - \left(\frac{4 - \pi}{4} \right)(\gamma_-)^2 \right]. \qquad (2.17b)$$

Then equations (2.9a), (2.9b) and (2.9c) with the describing functions given by equations (2.17a) and (2.17b) define the response of the system in the single sided impact region. In this case, it is hard to find closed form expressions for transition frequencies from single sided to double sided impact regions. The validity of the solutions, obtained by solving equations (2.9) and (2.17) iteratively, should be checked. If the solution does not satisfy equation (2.15), then single sided impacts are not seen at that particular frequency.

Case III: Double Sided Impact : The double sided impact case exists if q_m and q_a are such that the following conditions are satisfied:

$$q_a > |1 - q_m| \quad \underline{and} \quad q_a > |1 + q_m| \qquad (2.18)$$

Figure 2.9 (case III) shows the double sided impact case at which q_a is large enough when compared to q_m so that back collision is observed. The describing functions

62

for this case are obtained from equations (2.8a) and (2.8b) under the condition given by equations (2.19):

$$N_m = 1 - \frac{2(\pi - 2)}{\pi\, q_{aIII}} \quad ; \quad N_a = 1 - \frac{4}{\pi}\left[\frac{1}{q_{aIII}} - \left(\frac{4 - \pi}{4}\right)\left(\frac{1 + 3q_{mIII}^2}{q_{aIII}^3}\right)\right] \quad (2.19a,b)$$

The solution for the double sided impact case is obtained by solving equations (2.9) and (2.19) numerically. The validity of the solution, again, should be examined by using the conditions defined by equation (2.18), as it is done in the single sided impact case.

The solutions of all three regimes are combined to obtain the overall frequency response of the gear pair. Figure 2.10 illustrates typical q_a versus Ω_h and q_m versus Ω_h plots. All three impact regimes are shown on these plots. Also we note the frequency region where multiple steady state solutions are obtained.

2.5. COMPARISON OF TWO SOLUTION METHODS

First, we validate the approximate analytical solutions of equation (2.5) by comparing predictions with the results obtained by digital simulation. Again, two example cases (a heavily loaded system and a lightly loaded system) are considered and the frequency response curves q_a versus Ω_h and q_m versus Ω_h are generated. Figure 2.11 shows the frequency response for the heavily loaded system with $\hat{F} = 2$, $F_m = 0.1$ and $\zeta = 0.05$. Numerical and analytical results agree very well as both predict amplitudes and the transition frequencies for case I (no impact) and case II (single sided impact) regimes, and both show that the double sided impact solutions do not exist. These results demonstrate that the analytical solutions are indeed correct for the
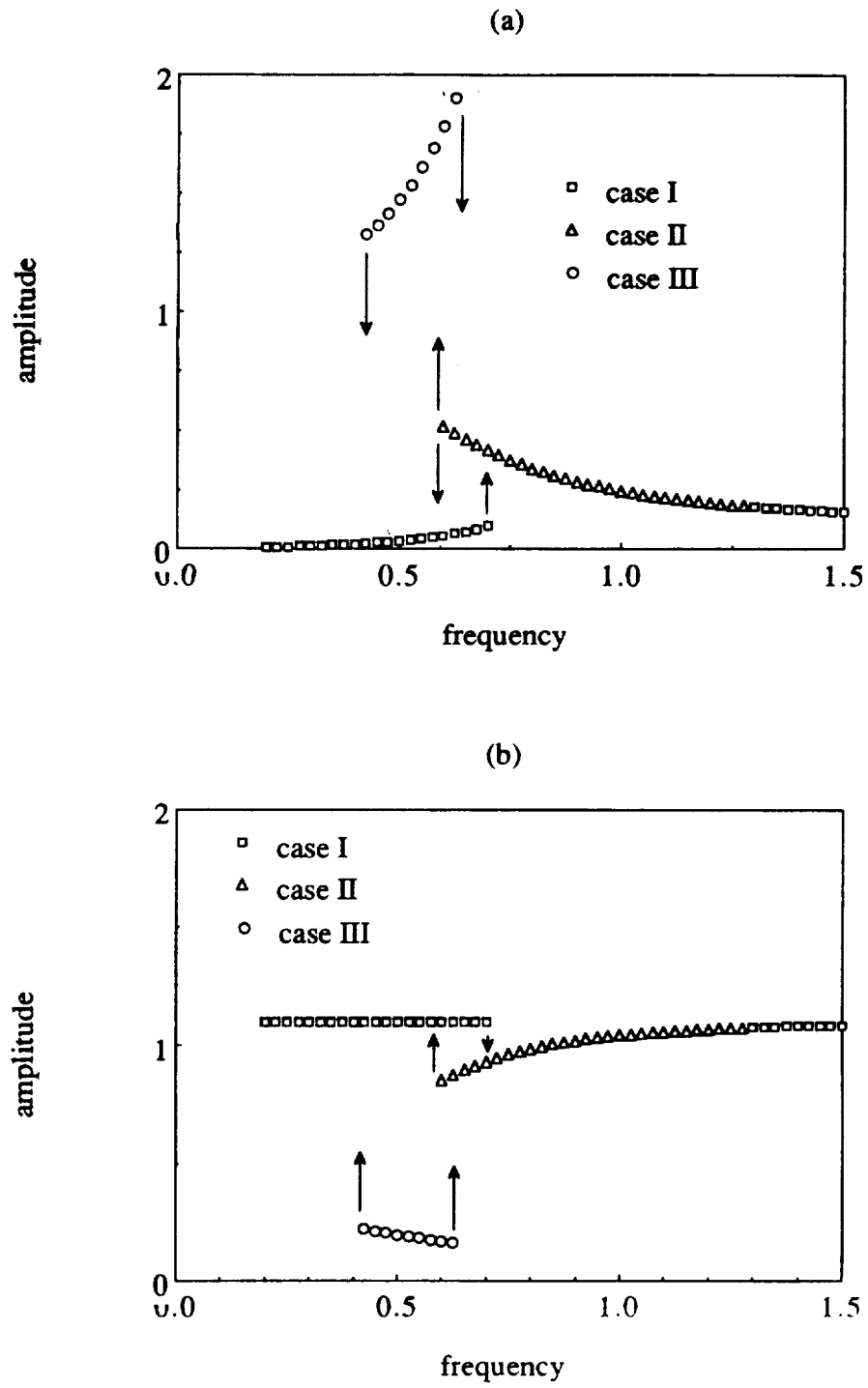
63

(a)

(b)

Figure 2.10.   Typical frequency response plots for a gear pair; a) q_a versus Ω_h, b) q_m versus Ω_h.

heavily loaded system. Now consider the lightly loaded system as the second example case with $\hat{F}=0.5$, $F_m=0.1$ and $\zeta=0.05$. From Figure 2.12 we note that while case I and case II solutions as yielded by both solution techniques are very close to each other, case III regime is predicted only by the analytical expressions. Why is case III not predicted by the digital simulation? To answer this consider the following:

a) In digital simulation, several sets of q(0) and $\dot{q}(0)$ must be tried to find all of the steady state solutions within a multi-valued region, for instance $0.6 \leq \Omega_h \leq 0.7$ in Figure 2.11 and $0.4 \leq \Omega_h \leq 0.7$ in Figure 2.12. When q(0) and $\dot{q}(0)$ are kept constant for each Ω_h or if the steady state solution of the previous frequency is used as the basis for the initial conditions for the next frequency considered, only one of the solutions can be found while missing the other(s). Figure 2.13 illustrates this point as the steady state solution of the previous frequency is used here for the initial conditions at each Ω_h. Using this procedure, case II solutions within the multi-valued regions are missed. Therefore, whenever digital simulation is used to solve the equation of motion, dependence of the steady state solutions on q(0) and $\dot{q}(0)$ must be taken into account to avoid the risk of obtaining an incomplete frequency response description.

b) In the case of Figure 2.12, no initial conditions governed by case III are found by the digital simulation within the range of initial conditions $-2 < q(0) < 2$ and $-2 < \dot{q}(0) < 2$ we have considered. Conversely, the analytical method predicts this regime as the issue of initial conditions is irrelevant here. To illustrate

this, first we consider the case of Figure 2.3 with $\hat{F}=0.5$, $F_m=0.1$, $\zeta=0.02$ and $\Omega_h=0.5$. Figure 2.14a shows the domain of attraction governed by case III within the range $-2 < q(0) < 2$ and $-2 < \dot{q}(0) < 2$ with a q(0) or $\dot{q}(0)$ increment of 0.2. Here, almost half of the initial conditions considered define case III solutions. Therefore the chance of having a double sided impact solution at $\Omega_h=0.5$ is considerably high. Now, increase the damping to $\zeta=0.03$. Once again a case III regime is predicted analytically, but the number of initial conditions corresponding to case III is not sufficiently high like the case of $\zeta=0.02$. In the digital simulation, the transient solution will converge to case I or case II solution unless the initial condition corresponds to one of those shown in Figure 2.14b for case III. And the limiting case is reached when $\zeta=0.04$, while holding the other parameters the same; now no initial conditions corresponding to case III are found. Obviously there might be initial conditions, out of the range considered, which correspond to the analytical results. Therefore the existence of case III solutions should be checked numerically by searching the entire range of initial conditions as defined by the physical considerations of the system.

2.6. PARAMETRIC STUDIES

Frequency response amplitudes, transition frequencies and the existence of various impact regimes depend on F_m, $\hat{F}$ and ζ. Therefore, a set of parametric studies using analytical solutions of section 2.4 will be presented here; same results can be duplicated by the digital simulation technique. First we examine the effect of F_m and $\hat{F}$ while holding the damping ratio ζ equal to 0.05. Figures 2.15 and 2.16 compare results for four different $\hat{F}$ values obtained by varying F_{ah} for a given $F_m=0.1$. Both gears maintain complete contact with each other when $\hat{F}$ is very
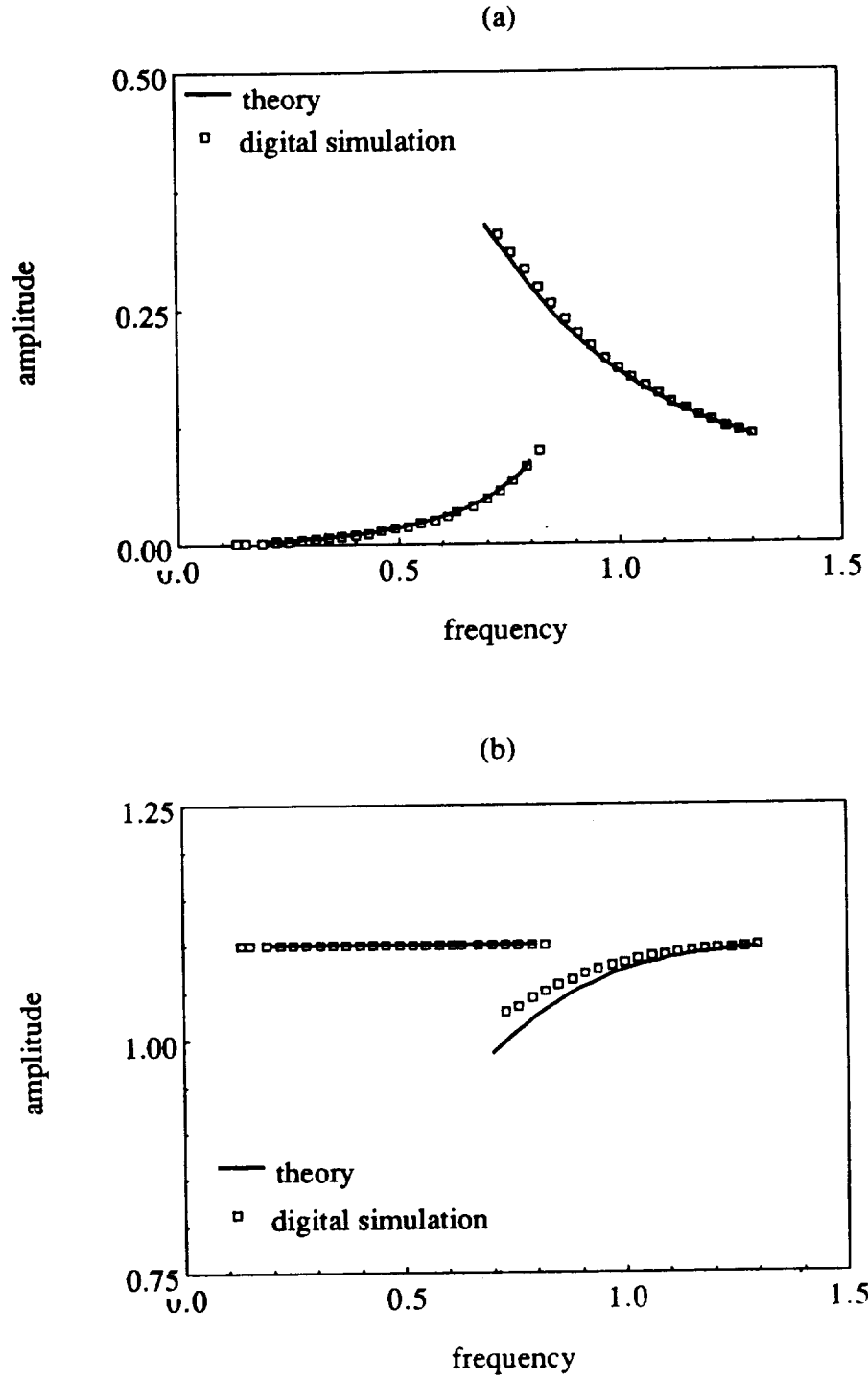
66

(a)

(b)

Figure 2.11.   Comparison of theory with numerical simulation; F_m=0.1, $\hat{F}$=2, ζ=0.05;
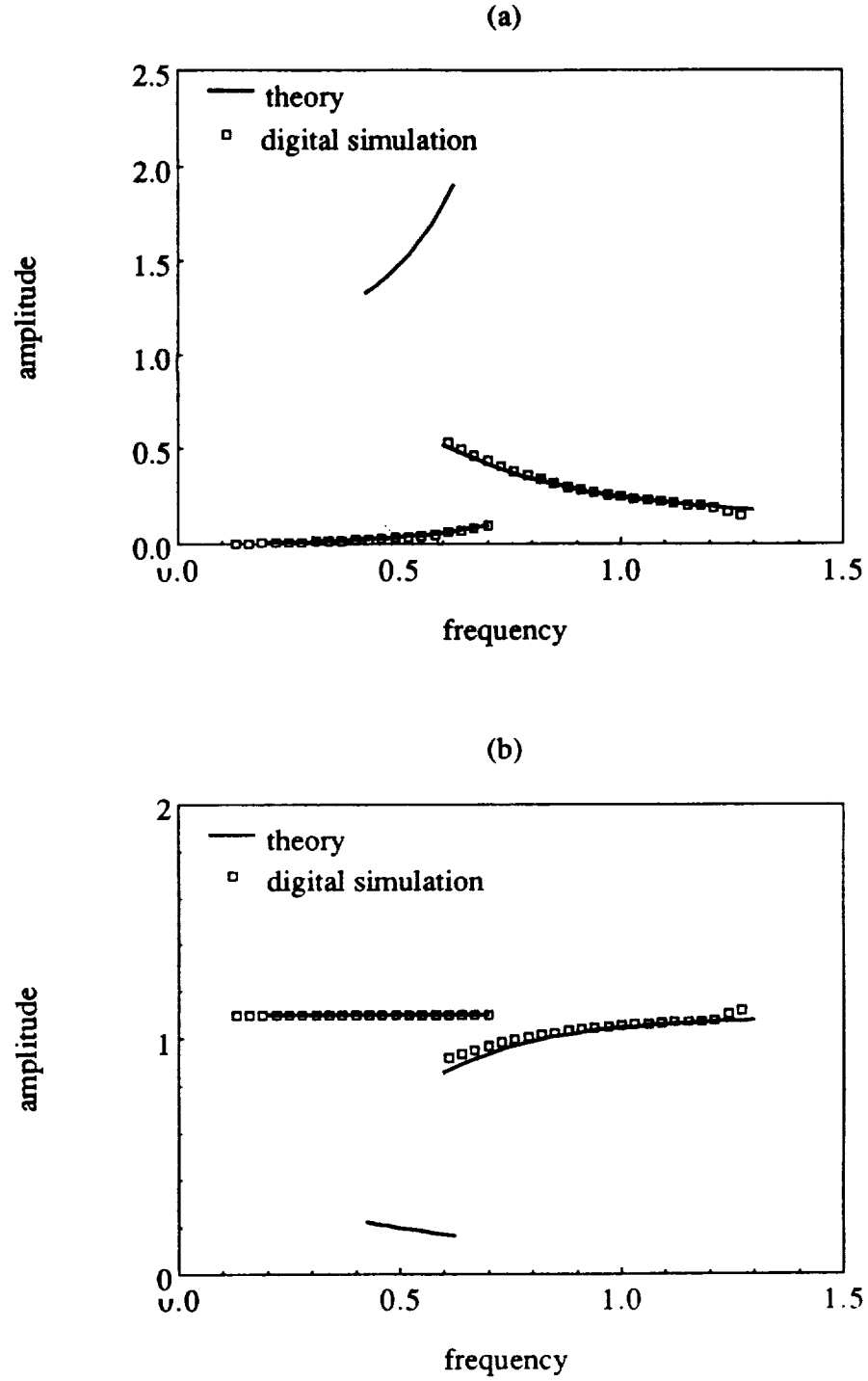a)q_a versus Ω_b, b) q_m versus Ω_b.

Figure 2.12.   Comparison of theory with numerical simulation; F_m=0.1, $\hat{F}$=0.5, ζ=0.05;
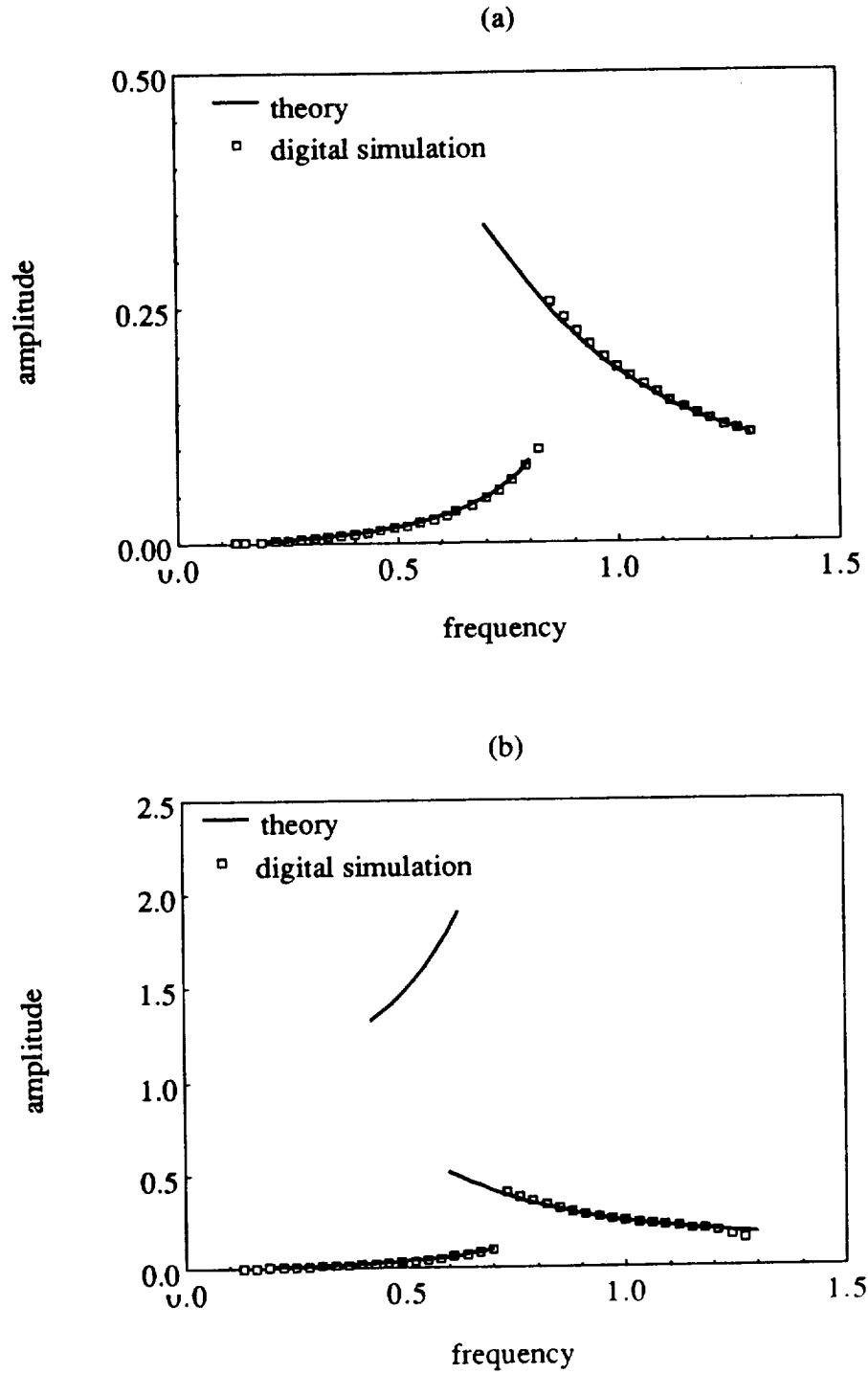a) q_a versus Ω_h, b) q_m versus Ω_h.

(a)

(b)

Figure 2.13. Comparison of theory with numerical simulation when initial conditions are kept constant; F_m=0.1, ζ=0.05; a) $\hat{F}$=2, b) $\hat{F}$=0.5.
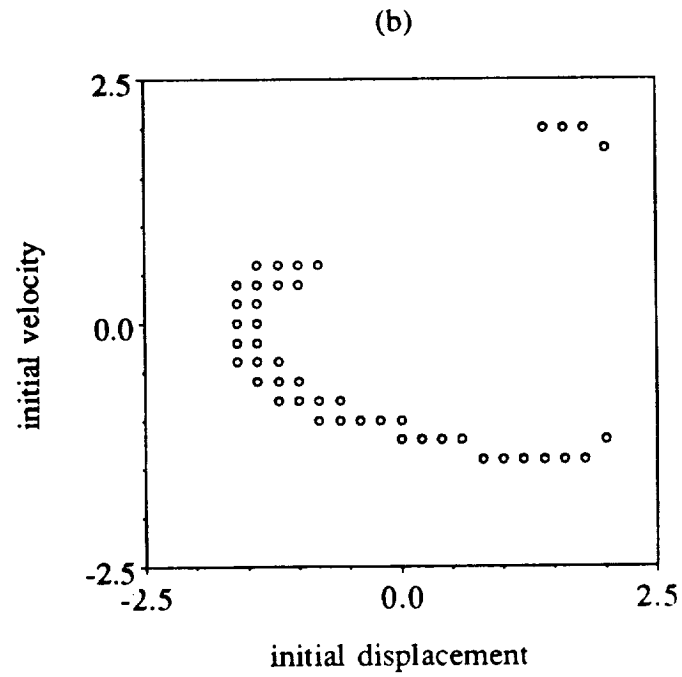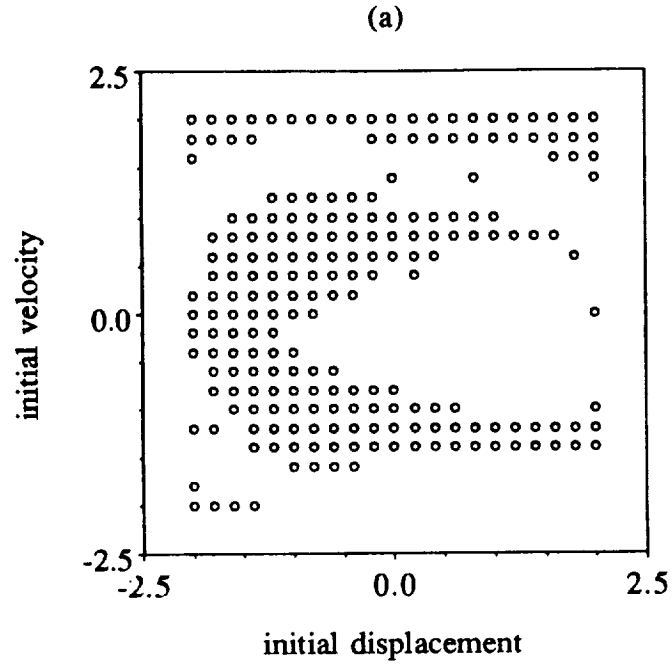
69

Figure 2.14.   Domains of attraction for case III solutions for F_m=0.1, $\hat{F}$=0.5, Ω_h=0.5; a)ζ=0.02, b) ζ=0.03.

large, say $\hat{F}=10$ in Figures 2.15a and 2.16a. Consequently the dynamic system is linear and the mean q_m and alternating q_a components of the torsional motion are uncoupled as expected. However, for $\hat{F}=2$, no-impact regime (case I) can not cover the whole frequency range and a region around the resonant frequency is dictated by the single sided impacts (case II). Away from the resonance, over the range given by $\Omega_h>0.8$ and $\Omega_h<0.7$, solutions are single-valued, whether case I or case II solutions. Conversely, near the resonance given by $0.7<\Omega_h<0.8$ dual-valued solutions are seen in Figures 2.15b and 2.16b. And sudden discontinuities are observed, i.e. a jump up at $\Omega_h=0.8$ and a jump down at $\Omega_h=0.7$. When $\hat{F}$ is reduced further, double sided impact (case III) solutions start to appear in Figures 2.15c and 2.16c. Now, the frequency range of interest can be divided into the following four regions: i) case I, $\Omega_h<0.4$; ii) case I and case III , $0.4<\Omega_h<0.6$; iii) all three cases, $0.6<\Omega_h<0.625$; and iv) only case II, $\Omega_h>0.625$. Region (ii) disappears at $\hat{F}>0.5$.

Next, we vary $\hat{F}$ by changing F_m for a given $F_{ah}=0.05$. This set of parameters does not yield any double sided impacts (Case III). Again, the tooth pair does not lose contact when $\hat{F}$ is large enough, say $\hat{F}\geq10$ and only the linear solutions exist as shown in Figure 2.17a. But when $\hat{F}$ is lowered to $\hat{F}=4$, 2 and 1, the response is non-linear which is composed of cases I and II as shown in Figures 2.17b-d.

Next we examine the role of damping ratio ζ on the frequency response in Figure 2.18, given $F_m=0.1$ and $F_{ah}=2$. Double-sided impacts are found at a low damping value $\zeta=0.025$ as shown in Figure 2.18a. When ζ is increased to 0.05, case III solutions no longer exist and case I and case II solutions define the frequency response completely. The jump-up and jump-down transition frequencies in Figure 2.18b are distinctly apart. With an increase in ζ, transition frequencies approach each
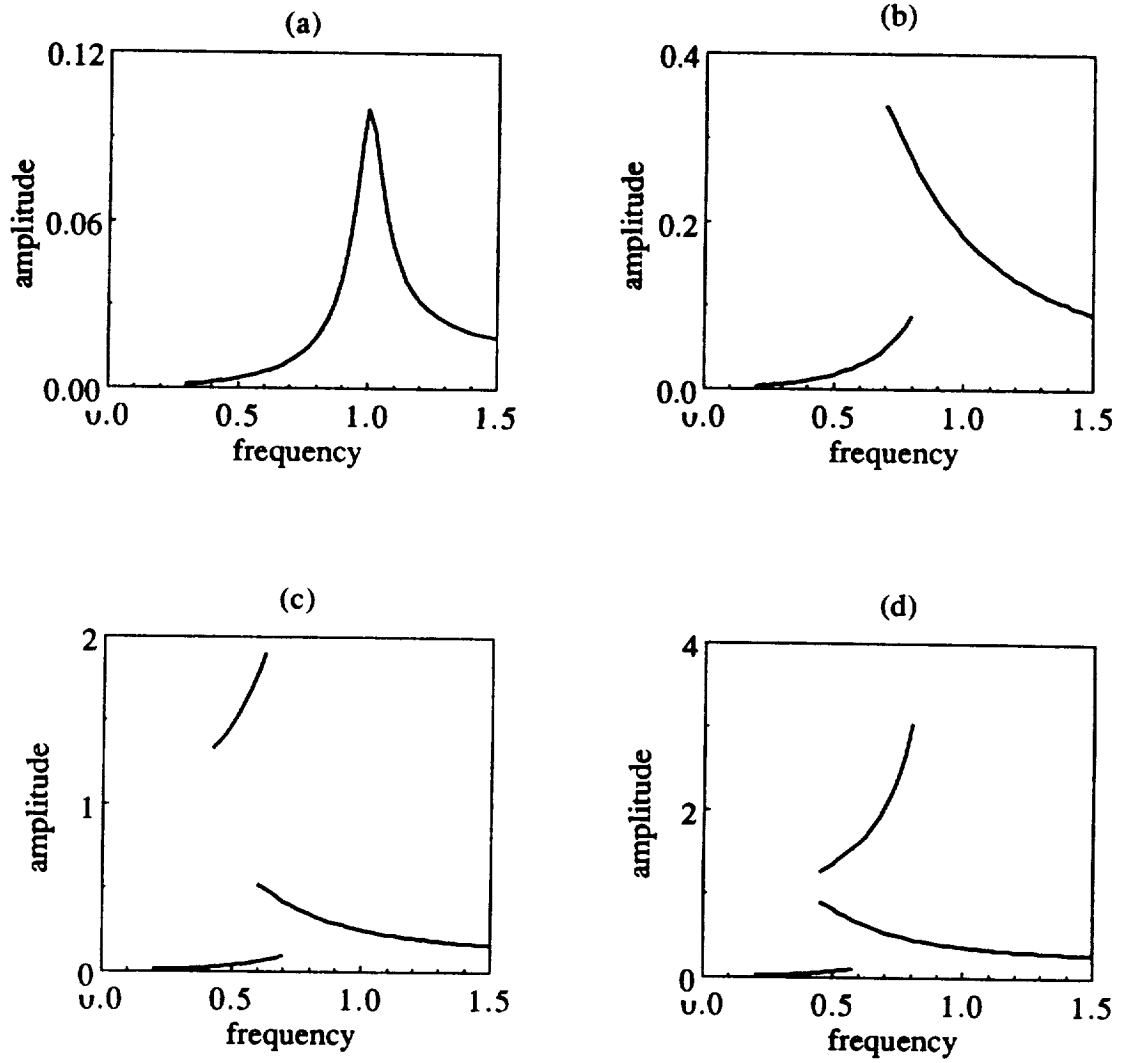
Figure 2.15. Frequency response q_a for different alternating loads; $F_m=0.1$, $\zeta=0.05$, a) $\hat{F}=10$, b) $\hat{F}=2$, c) $\hat{F}=1$, d) $\hat{F}=0.5$.
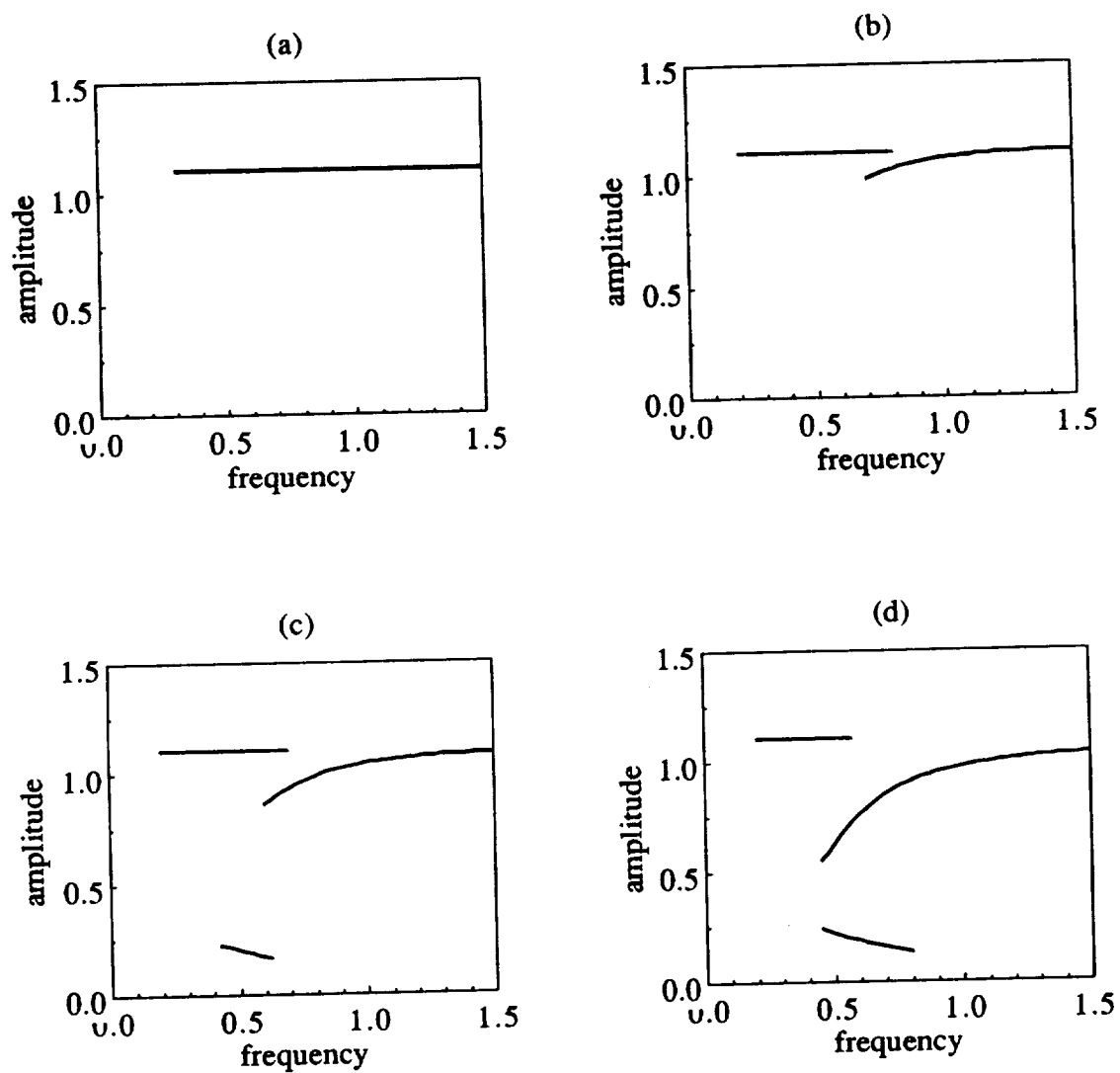
Figure 2.16.   Frequency response q_m for different alternating loads; F_m=0.1, ζ=0.05, a) $\hat{F}$=10, b) $\hat{F}$=2, c) $\hat{F}$=1, d) $\hat{F}$=0.5.
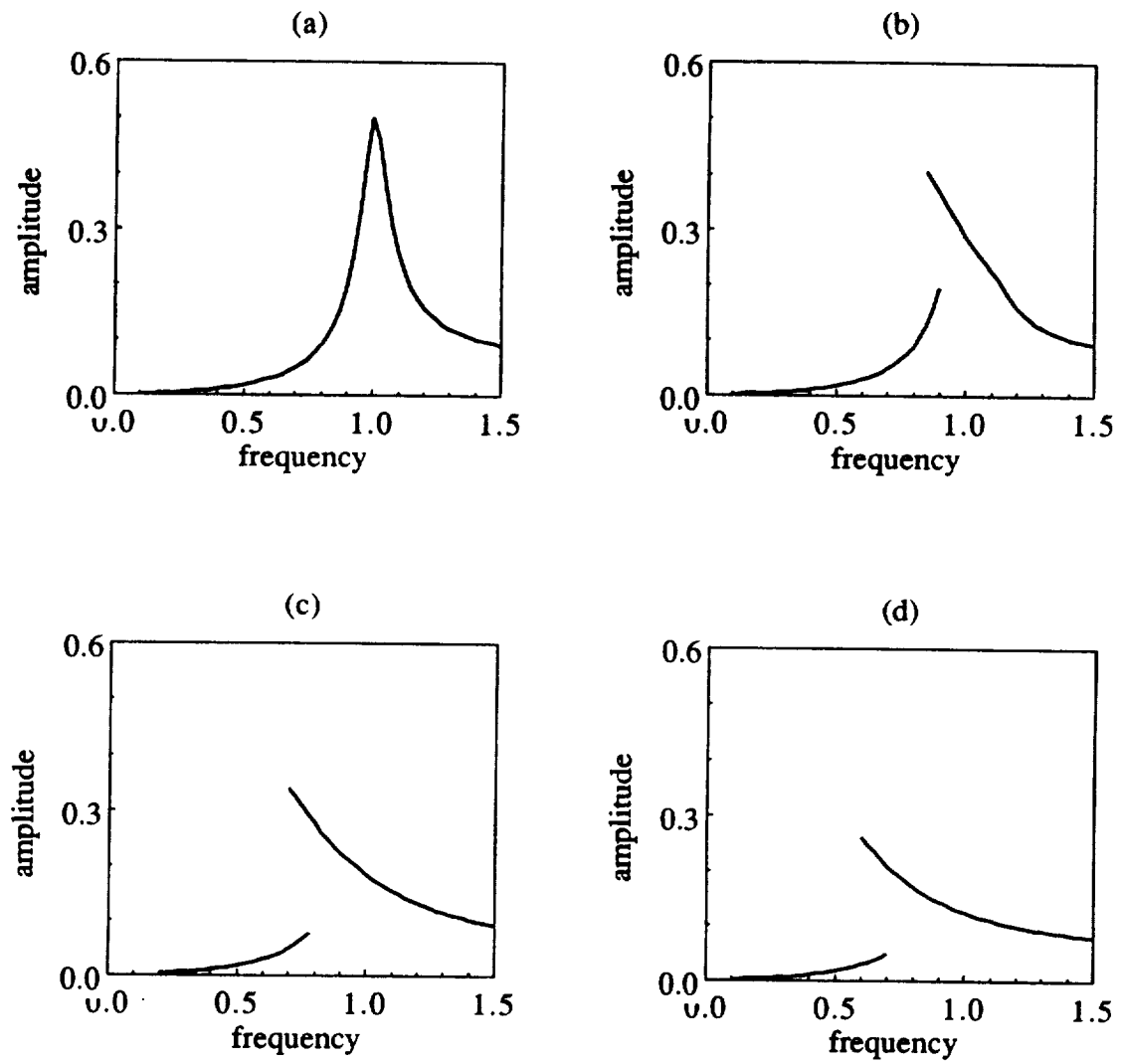
73

Figure 2.17. Frequency response q_a for different mean loads; $F_{ah}=0.05$, $\zeta=0.05$, a) $\hat{F}=10$, b) $\hat{F}=4$, c) $\hat{F}=2$, d) $\hat{F}=1$.
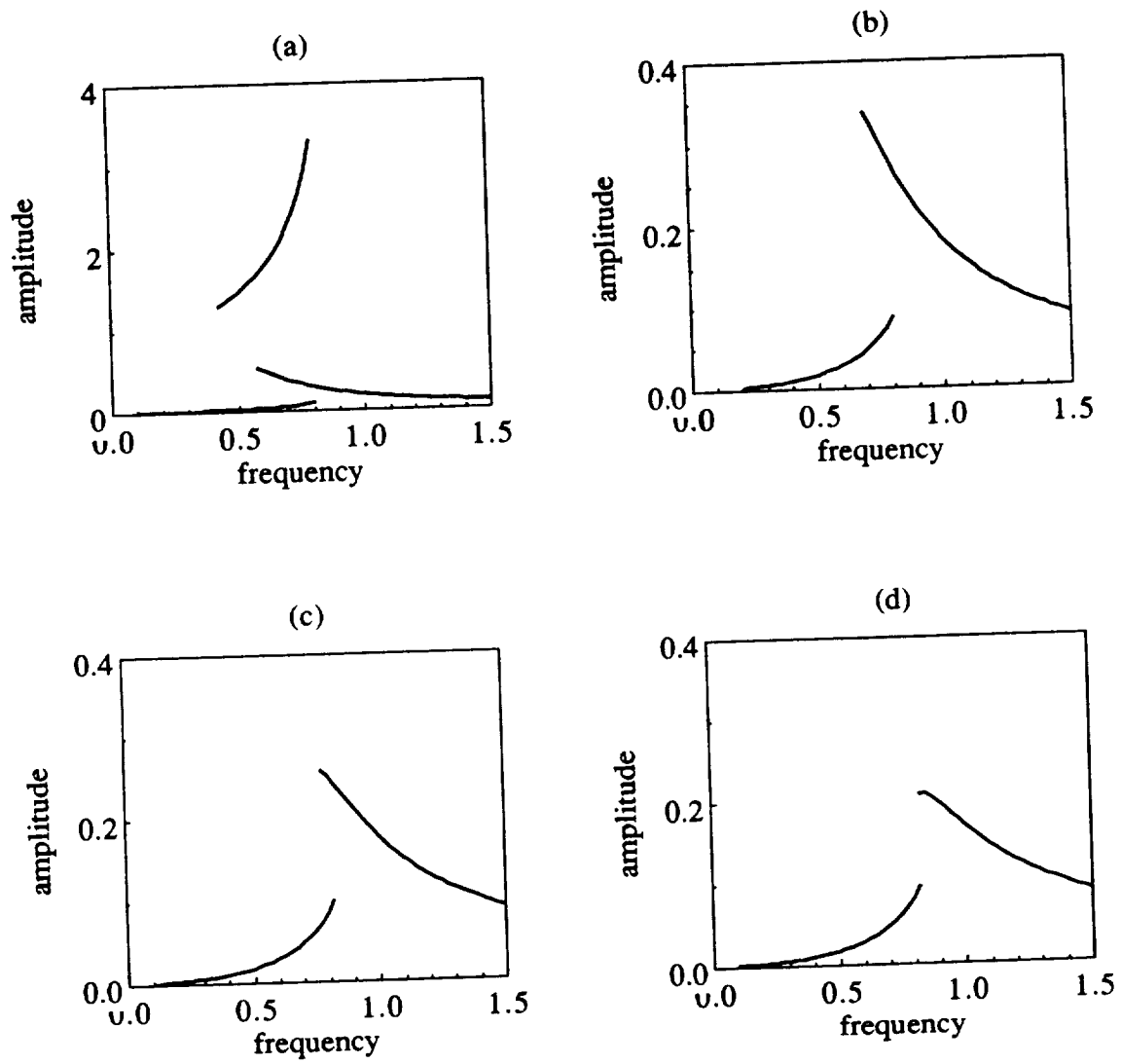
Figure 2.18. Frequency response q_a for different damping values; $F_m=0.1$, $\hat{F}=2$, and a)$\zeta=0.025$, b) $\zeta=0.05$, c) $\zeta=0.075$, d) $\zeta=0.1$.

other which narrows the dual-valued solution region. At $\zeta=0.1$, the frequency response is single valued and the jump-up and jump-down transitions in Figure 2.18d take place almost at the same frequency. Finally, like the linear systems, the damping ratio also lowers the amplitudes in the non-linear resonance regime.

2.7. EXPERIMENTAL VALIDATION

Our analytical solutions of Section 2.4 will be compared with the experimental results of Munro [27] who used a four-square test rig to measure the dynamic transmission error $\bar{x}(\bar{t})$ of a spur gear pair. High precision spur gears with manufacturing errors much smaller than tooth deflections were selected. Pinion and gear were identical with 32 teeth, face width of 12.7 mm and diametral pitch of 4. Tooth profile modifications were applied to obtain a minimum (but not zero) $\bar{e}(\bar{t})$ at the design load of 3780 N. Other components of the set-up including shafts, bearings and casing were made as rigid as possible in order to simulate the configuration shown in Figure 2.1. $\bar{x}(\bar{t})$ was measured for a range of gear mesh excitation frequencies under different mean loads $\bar{F}_m$. Some of the key parameters were not specified by Munro [27]. For example, it was stated that some additional inertias were added to the gears to shift the primary resonant frequency within the operational speed range, but the specific values of such inertias were not given. It was also reported that the damping ratio ζ varies with load "in a random manner". Also, backlash was not measured or reported. Therefore, in our study, we estimate the damping ratio ($\zeta=0.0175$) and the resonant frequency ω_n by considering the design load case at which only linear behavior is seen; time-invariant mesh stiffness is assumed in the model. The same value of ζ is used at each discrete load $\bar{F}_m$ and a backlash value of $2b=0.1$ mm is assumed in our model.

76

Figures 2.19 to 2.22 compare measured and predicted frequency response of the dynamic transmission error $\bar{x}(\bar{t})$, on a peak to peak basis, at the design load and at 1/4, 1/2 and 3/4 of the design load, respectively. As shown in Figure 2.19, both analytical and experimental results indicate that teeth maintain contact at the design load and hence the system behaves as a linear system in spite of the backlash. This is because the static transmission error $\bar{e}(\bar{t})$ is minimum at the design load which results in a large force ratio F_m/F_a, say 50. However, when the mean load $\bar{F}_m$ is lowered to 3/4 of the design load which corresponds to a larger static transmission error $\bar{e}(\bar{t})$, tooth separation takes place. Consequently we note a jump in the frequency response as shown in Figure 2.20 for both analysis and experiment. This jump phenomenon is more noticeable at 1/2 and 1/4 of the design loads as shown in Figures 2.21 and 2.22, respectively. Our theory matches very well with Munro's experimental results [27] in spite of the lack of knowledge of some relevant parameters.

As the second example case, the experimental results of Kubo [28] are considered and compared with our theory. Experimental results and the relevant system parameters are extracted from a recent paper by Ozguven and Houser [24] and the excitation $\bar{e}(\bar{t})$ is calculated using a spur gear elastic model [21]. Kubo designed a four-square spur gear test rig which was heavily damped ($\zeta \approx 0.1$). He measured dynamic root stresses σ_d and then estimated the dynamic factor D_S as $D_S = \sigma_d/\sigma_s$ where σ_s is the static tooth root stress. However, in several other studies [16] the dynamic factor is defined as the ratio of the dynamic mesh load $\bar{F}_d$ to static mesh load $\bar{F}_m$, given by $D_L = \bar{F}_d / \bar{F}_m = F_d / F_m = (2\zeta \dot{q}(t) + f(q(t))) / F_m$. Note that D_L is equal to D_S when the change of the moment arm due to a change in contact point is neglected. Figure 2.23 shows the envelope of dynamic factor D_S
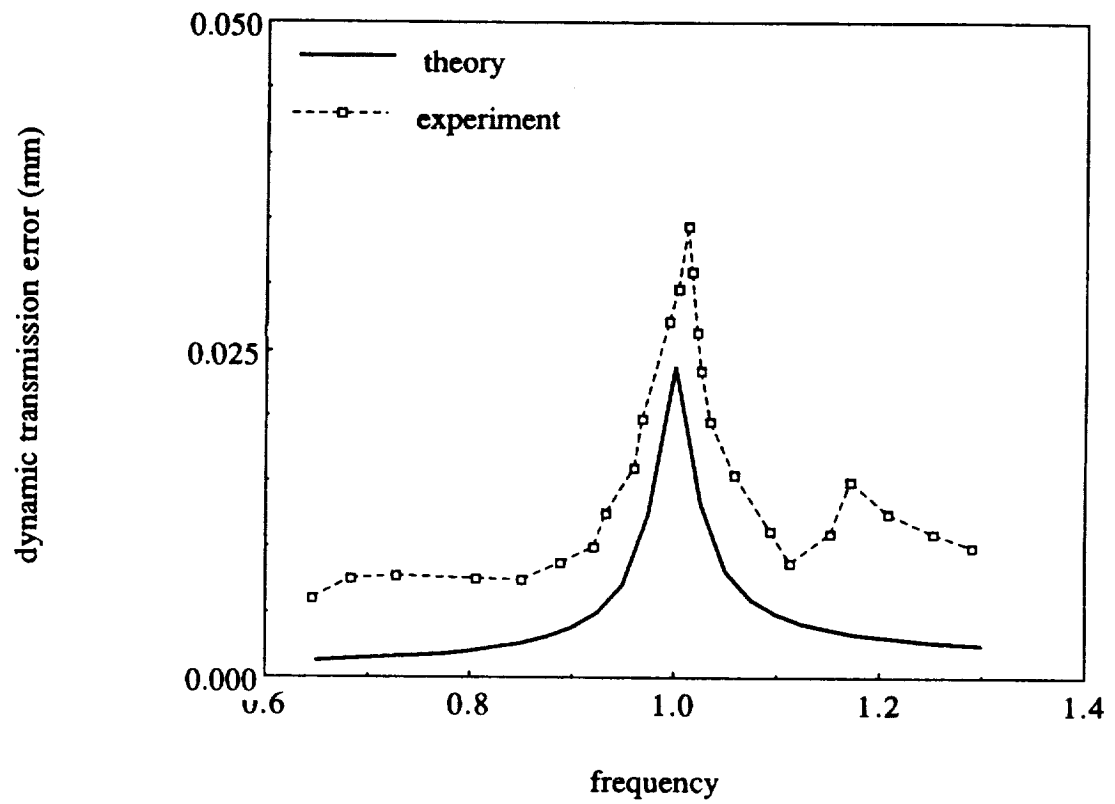
Figure 2.19. Comparison of the theory with Munro's [27] experiments at design load.
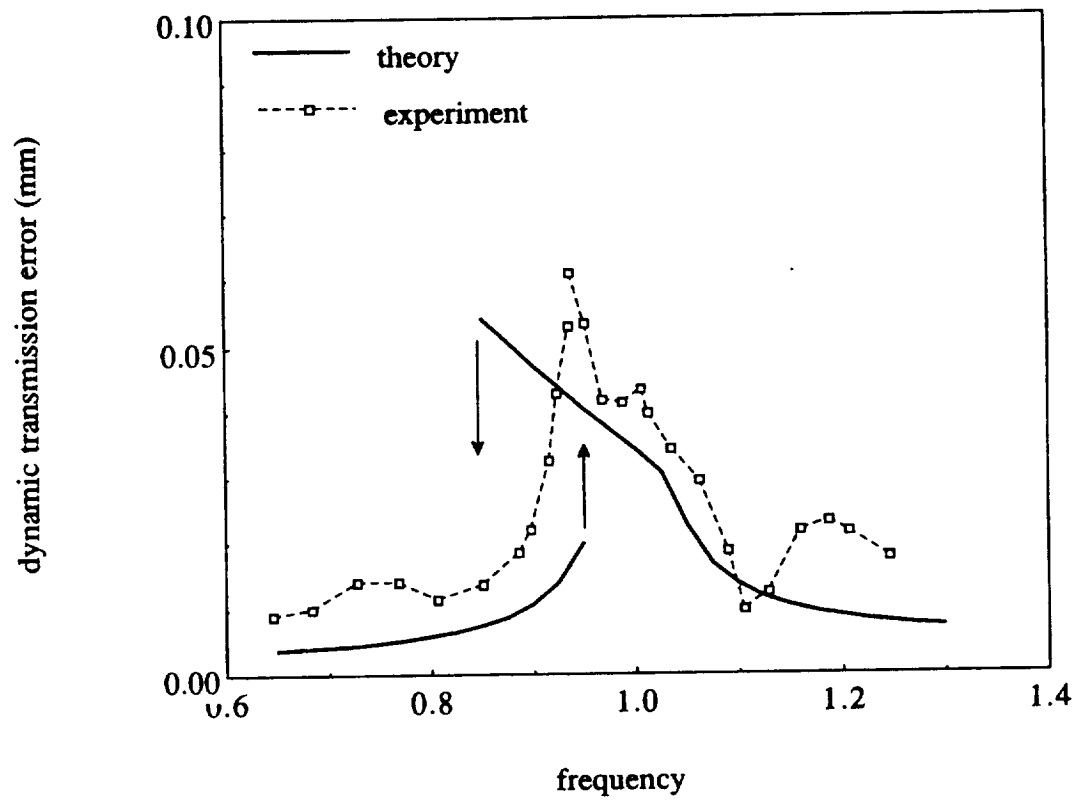
78

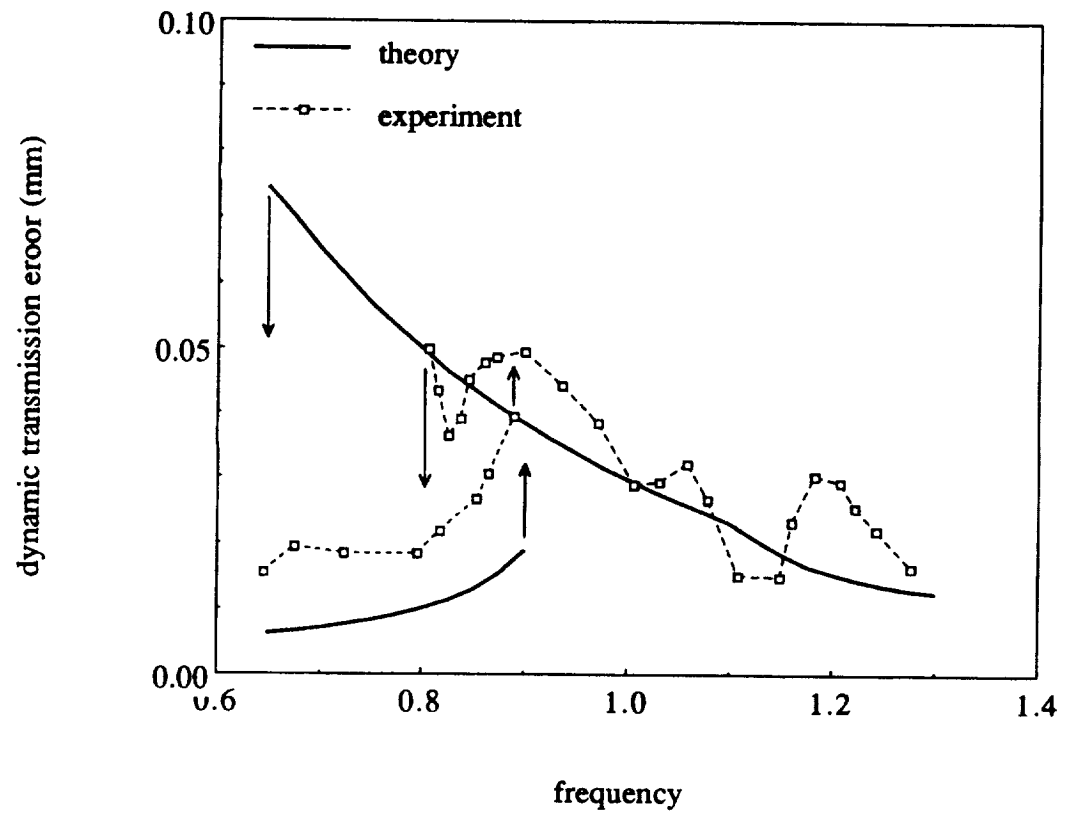Figure 2.20. Comparison of theory with Munro's [27] experiments at 3/4 of design load.

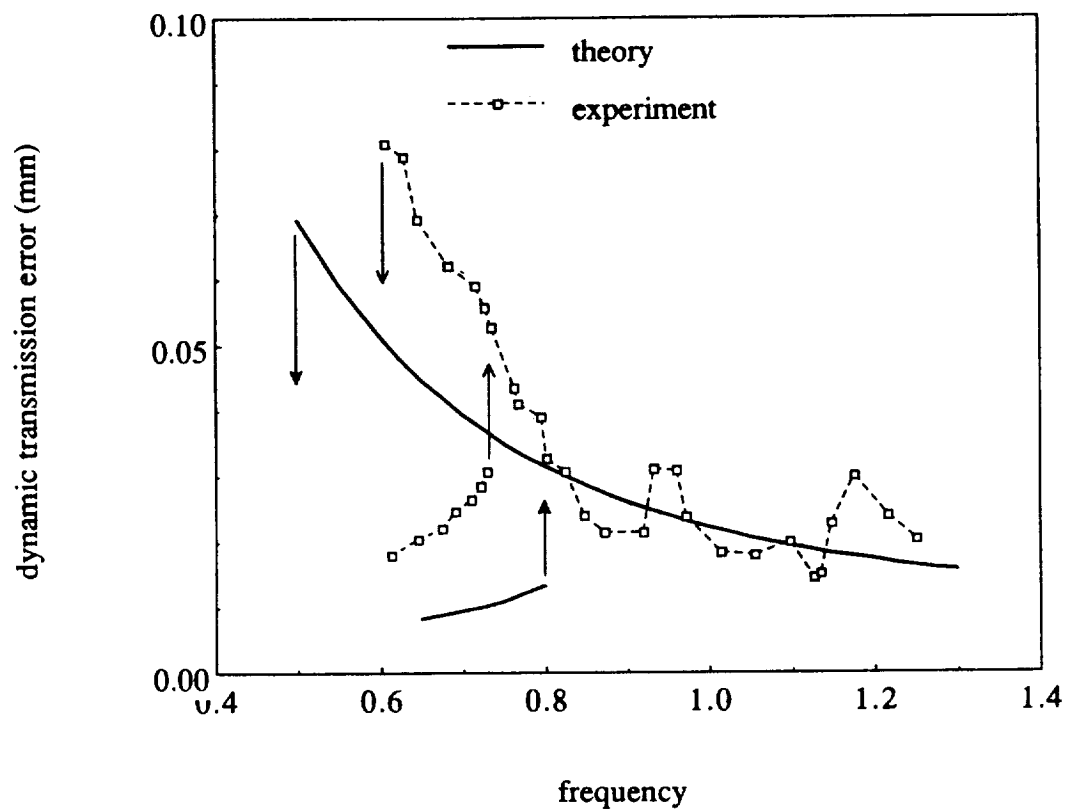Figure 2.21. Comparison of theory with Munro's [27] experiments at 1/2 of design load.

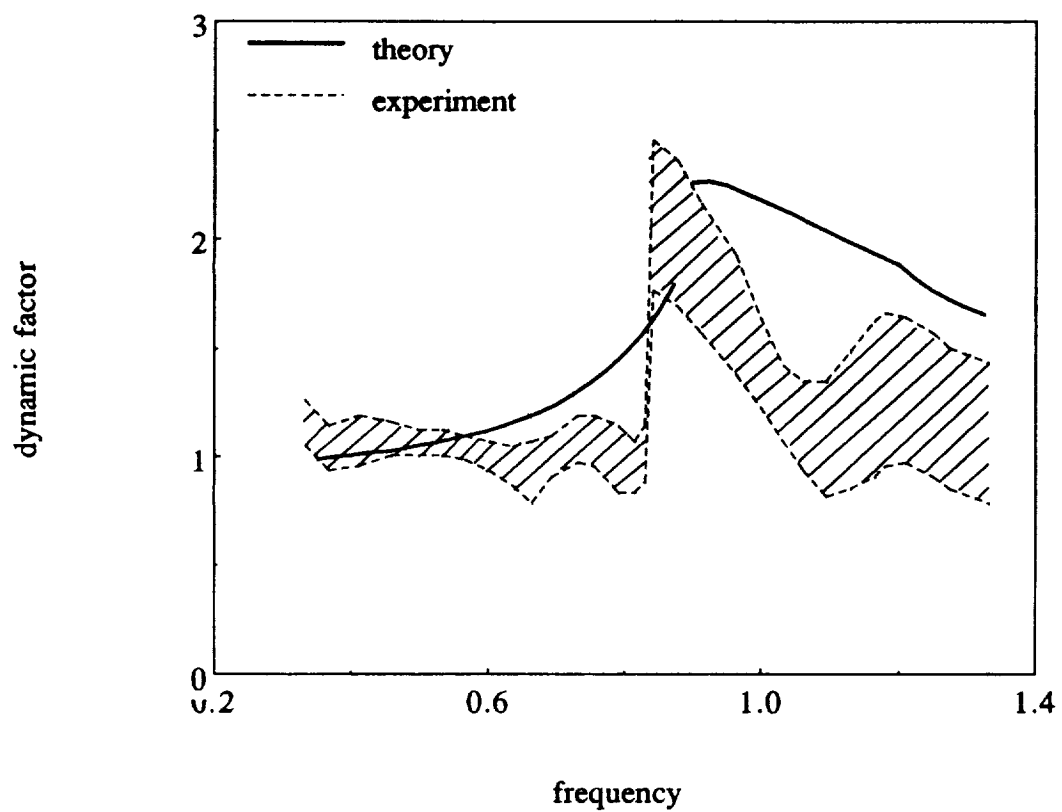Figure 2.22. Comparison of theory with Munro's [27] experiments at 1/4 of design load.

Figure 2.23. Comparison of theory with experimental results of Kubo (extracted from reference [24]).

measured for eight different teeth pairs and D_L spectrum computed using the analytical solutions of Section 2.4. Here, at most of the frequencies, our predictions are not within the measured envelope, but the transition frequency and the amplitude at the jump discontinuity are predicted accurately. There might be several reasons for the discrepancy including the usage of D_L instead of D_S, the validity of the computer model used to calculate $\bar{e}(\bar{t})$, insufficient knowledge of some system parameters such as profile modifications, and the assumptions made in developing our theory such as the time invariant mesh stiffness. Therefore the experimental data is not exactly analogous to our analytical predictions even though a satisfactory agreement is found. Obviously our theory should be refined in order to obtain a better agreement with Kubo's data; for instance, time-varying mesh stiffness may be included.

2.8. COMPARISON OF EXCITATIONS

2.8.1. Internal versus External Excitation

First, we assume that only one type of excitation exists at a time and compare the frequency response characteristics of the system due to the internal static transmission error sinusiodal excitation $F_i(t)$ given by equation (2.5) with the external sinusoidal excitation $F_e(t)$ given by equation (2.4). The comparison is based on the analytical solutions which are constructed in Section 2.4 for equation (2.5) and in Reference [33] for equation (2.4). In the case of internal excitation, the amplitude of the alternating force has a Ω_h^2 term which makes the alternating force amplitude frequency dependent. This amplitude $F_{ah}\Omega_h^2$ is smaller than F_{ah} for $\Omega_h < 1$ and greater than F_{ah} when $\Omega_h > 1$. Hence the overall alternating force amplitude ratio

83

$F_m / F_{ah} \Omega_h^2$ varies with Ω_h even though $\hat{F} = F_m / F_{ah}$ is kept constant. In the case of external excitation, the force amplitude ratio $\hat{F} = F_m/F_{aT}$ is frequency independent.

Figures 2.24 and 2.25 compare the frequency responses for four values of $\hat{F}$ given $F_m = 0.1$, $\Omega_h = \Omega_T = \Omega$ and $\zeta = 0.05$. When $\hat{F}$ is sufficiently large, say $\hat{F} \geq 10$, only case I solutions corresponding to the no-impact (case I) exist. Accordingly both excitations result in the linear system responses which are close to each other for $\Omega < 1$; but for $\Omega > 1$ there is a difference which grows with increasing frequency Ω as shown in Figure 2.24a. When $\hat{F}$ is reduced to 2, both case I and case II regimes exist; the difference between two excitations is again significant at higher Ω as shown in Figure 2.24b. The transition frequencies also differ, and a larger range of dual-valued solutions is seen for equation (2.5). Case III solutions are witnessed at lower values of $\hat{F}$ (1 and 0.5) as shown in Figures 2.25a and 2.25b. While equation (2.5) always has a case I regime at low Ω, equation (2.4) does not produce case I at $\hat{F} = 0.5$. Another important observation from Figures 2.24 and 2.25 is that up to two steady state solutions are seen in the external torque excitation case; conversely as many as three solutions are found for the geared system excited by the static transmission error.

2.8.2. Periodic or Combined Excitation

The approximate analytical solutions given in Section 2.4 are constructed only for a single harmonic internal excitation term $\bar{e}(\bar{t})$ or $F_i(t)$. However, in the real geared systems, $\bar{e}(\bar{t})$ or $F_i(t)$ is a periodic which can be represented by a fourier series of the fundamental frequency Ω_h. Therefore, it is necessary to consider the

84

(a)

(b)

Figure 2.24.   Comparison of the frequency response due to the external torque excitation given by Comparin and Singh [33] and the static transmission error excitation; $\zeta=0.05$, $F_m=0.1$, $\Omega_h=\Omega_T$ and a) $\hat{F}=10$, b) $\hat{F}=2$.
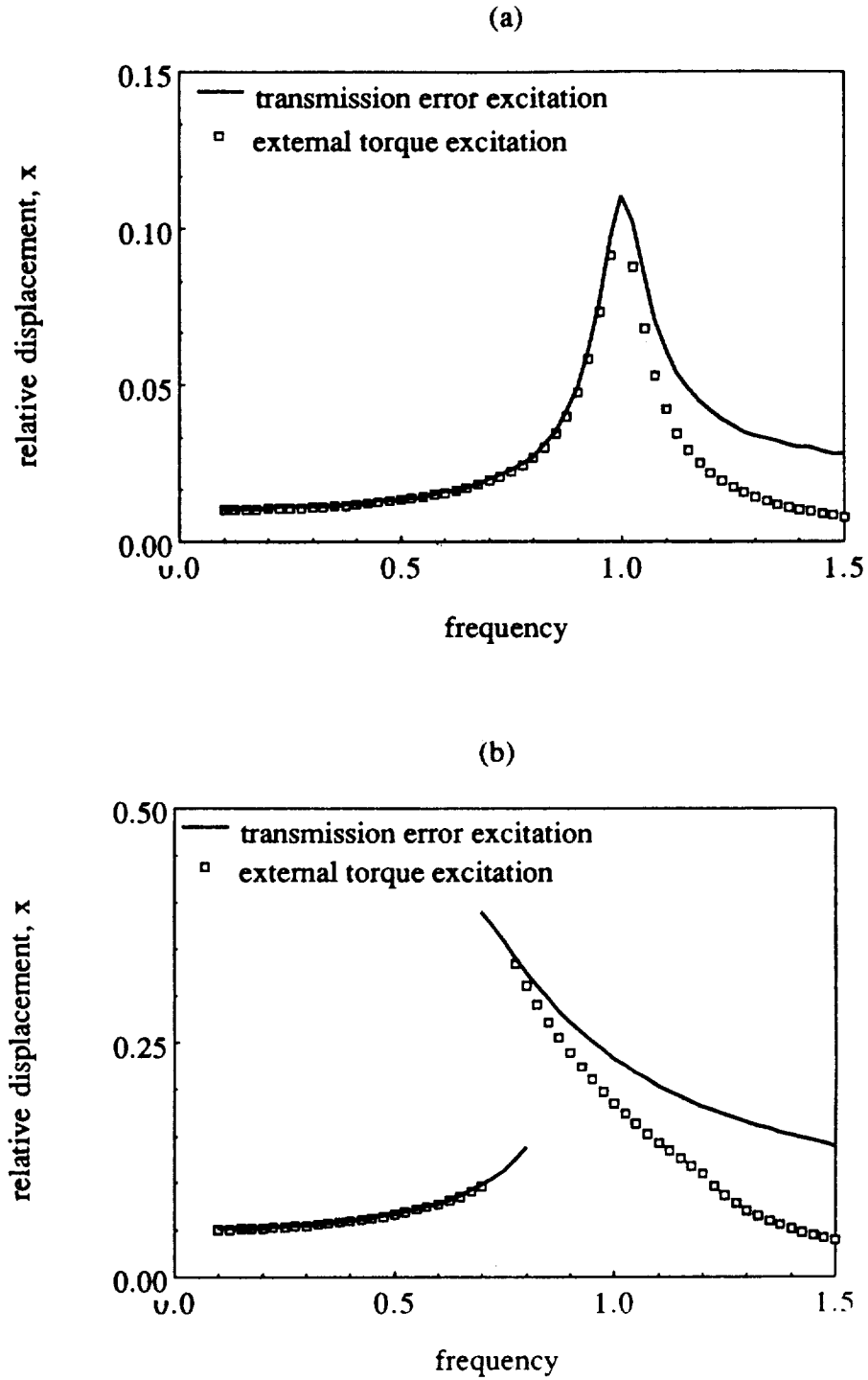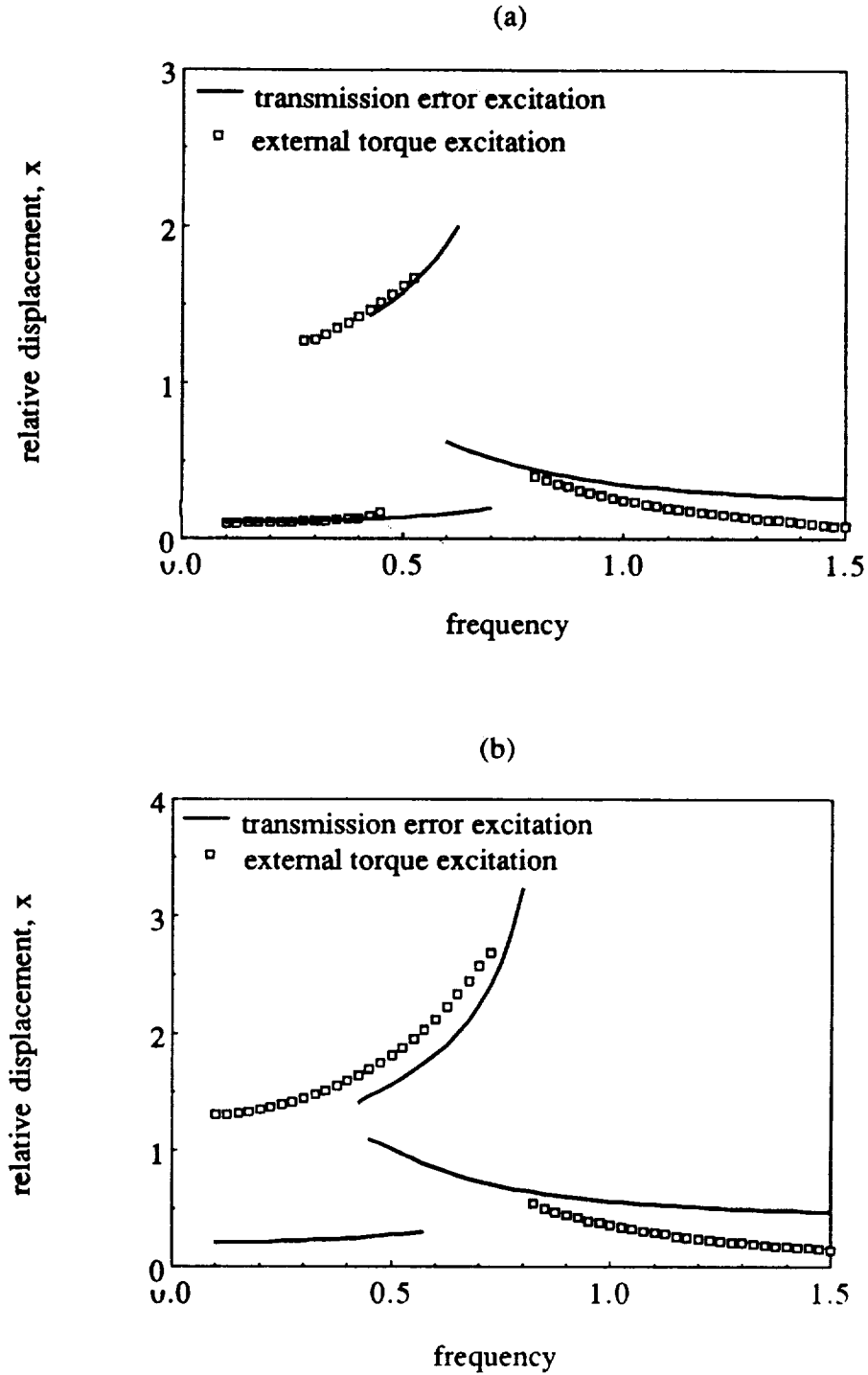
(a)

(b)

Figure 2.25. Comparison of the frequency response due to the external torque excitation given by Comparin and Singh [33] and the static transmission error excitation; $\zeta=0.05$, $F_m=0.1$, $\Omega_h=\Omega_T$ and a) $\hat{F}=1$, b) $\hat{F}=0.5$.

86

higher harmonics of $F_i(t)$ besides the fundamental component which is already included in the analysis. On the other hand, both external $F_e(t)$ and internal $F_i(t)$ excitations may exist simultaneously. These two cases require that $F(t)$ in equation (2.3) be reformulated as follows

$$F(t) = F_m + F_e(t) + F_i(t) = F_m + \sum_{j=1}^{k} F_{aTj} \sin(j\Omega_T t + \phi_{Tj})$$

$$+ \sum_{j=1}^{k} (j\Omega_h)^2 F_{ahj} \sin(j\Omega_h t + \phi_{hj}) \qquad (2.20)$$

In order to construct analytical solutions of this equation, we must investigate the applicability of the principle of superposition, which would consider first each excitation separately and then superimpose the corresponding responses to generate the overall frequency response. Two cases are considered and the analytical results based on the principle of superposition are verified through digital simulation.

Consider only the static transmission error excitation $F_i(t)$ in equation (2.20) with 3 harmonics, i.e. $F_e(t)$ and $F(t) = F_m + \sum_{j=1}^{3} (j\Omega_h)^2 F_{ahj} \sin(j\Omega_h t + \phi_{hj})$. The amplitudes of the harmonics are selected to be $F_{ah1}=0.05$, $F_{ah2}=0.02$ and $F_{ah3}=0.01$, and the mean force $F_m=0.1$. First each excitation component is considered separately without paying any attention to the phase angles and the frequency responses are obtained using digital simulation as shown in Figure 2.26. Second, all there excitations are included simultaneously and the overall response is compared with the previous solutions in Figure 2.26. The frequency response due to each harmonic of

87

the excitation is very close to the overall solution around the resonance peaks governed by that harmonic. When all of the solutions corresponding to each harmonic are added algebraically by also considering the phase angles, the overall response improves as shown in Figure 2.27. This response is in the form

$$q_a(t) = \sum_{j=1}^{3} q_{aj} \sin\left(\Omega_h t + \phi_{hj}\right)$$ where q_{aj} is the alternating displacement when only

the j-th harmonic is considered. Figure 2.27 suggests that the principle of superposition can be applied to a gear pair with backlash provided that the excitation frequencies are sufficiently far apart from each other. In the case of periodic static transmission excitation, this is valid as all excitation frequencies are at least Ω_h apart.

Now, the principle of superposition, which has been already verified by digital simulation, can be used to obtain the approximate analytical solutions per Section 2.4 when the periodic forcing function is considered. Figure 2.28 shows the analytical frequency response curve for $F_m=0.1$, $F_{ah1}=0.05$, $F_{ah2}=0.02$, $F_{ah3}=0.01$ and $\zeta=0.05$. Here the jump discontinuity is seen only at the peak Ω_{h1} governed by F_{ah1} since F_m/F_{ah2} and F_m/F_{ah3} are both sufficiently high so that no tooth separation occurs at Ω_{h2} and Ω_{h3}, respectively. However, the jump phenomenon can also be seen at the higher harmonics depending on the force ratios F_m/F_{ahj}, $j \neq 1$ and ζ in accordance with the results of Section 2.6. The same concept can be applied to the superharmonic components of the external torque excitation of equation (2.20) provided $F_{ahj}=0$.

The principle of superposition is now extended to the case where both internal $F_i(t)$ and external $F_e(t)$ sinusoidal excitations exist simultaneously as given by equation (2.3) provided that the excitation frequencies Ω_h and Ω_T are not close to each other. In a real geared system, Ω_h is much higher than Ω_T which implies that
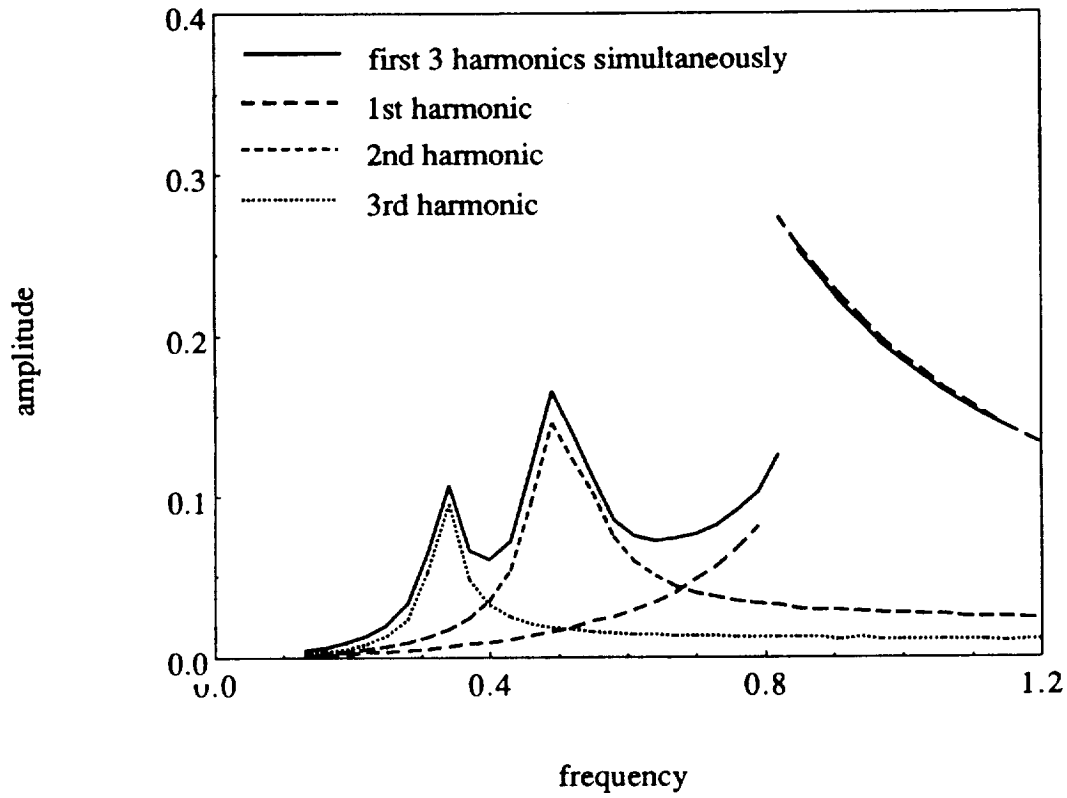
Figure 2.26. Comparison of the frequency response q_a due to first there harmonics of the static trancmission error for the cases when the harmonics are considered simultaneously and separately; $F_m=0.1$, $\zeta=0.05$, $F_{ah1}=0.05$, $F_{ah2}=0.02$ and $F_{ah3}=0.01$. These results are obtained using digital simulation.
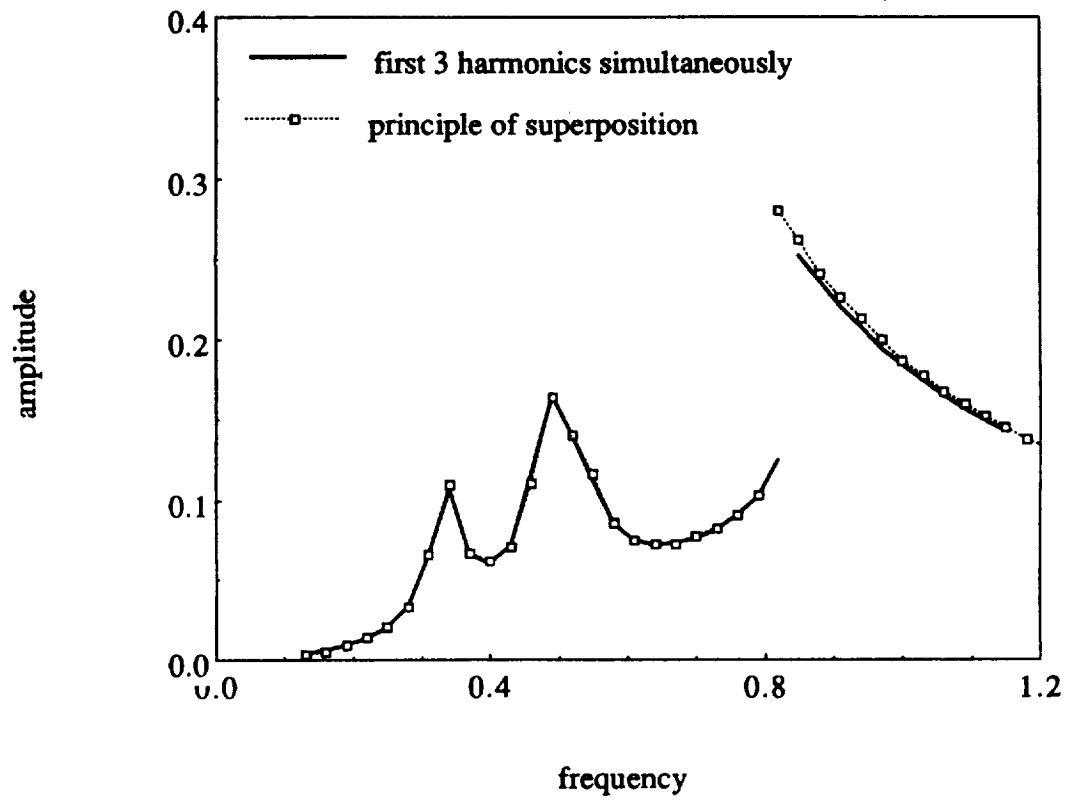
89

Figure 2.27. Comparison of digital simulation results obtained by using the principle of superposition and by considering all three harmonic excitations applied simultaneously; F_m=0.1, ζ=0.05, F_{ah1}=0.05, F_{ah2}=0.02 and F_{ah3}=0.01. In this case, phase angles are included in the superposition.
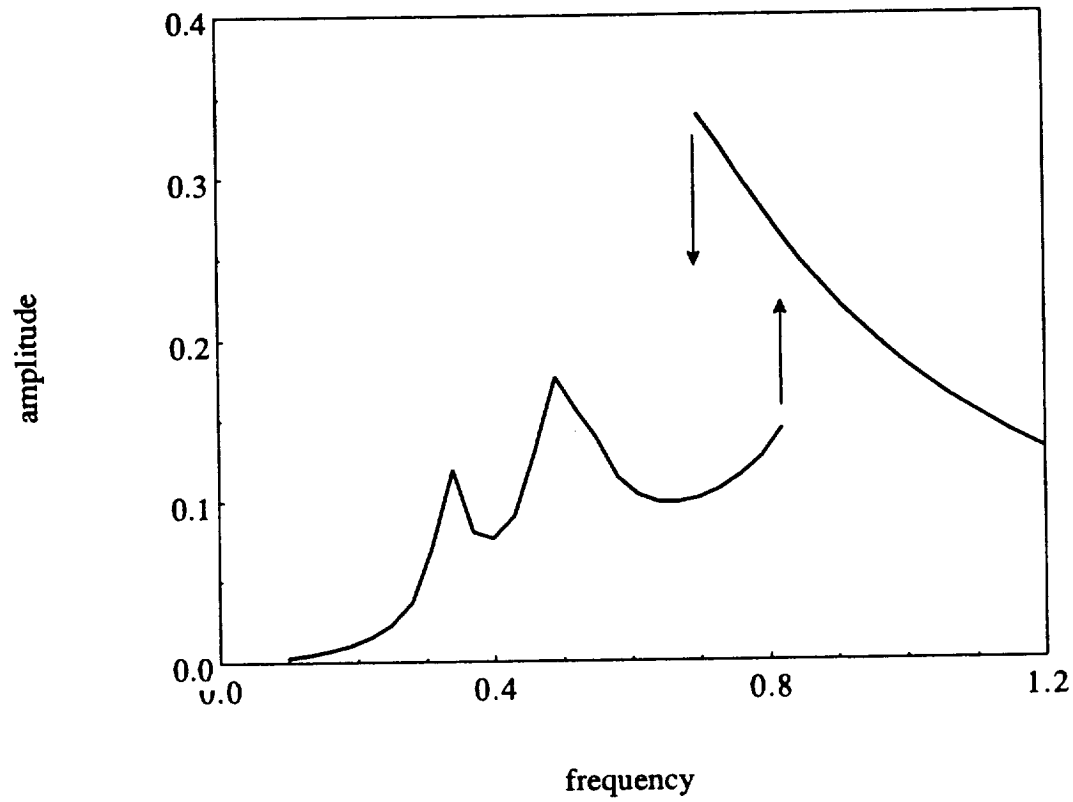
90

Figure 2.28. Comparison of the frequency response q_a due to first three harmonics of the static transmission error. This curve is based on the principle of superposition applied to the analytical solutions which have been constructed by the method of harmonic balance; $F_m=0.1$, $\zeta=0.05$, $F_{ah1}=0.05$, $F_{ah2}=0.02$ and $F_{ah3}=0.01$.
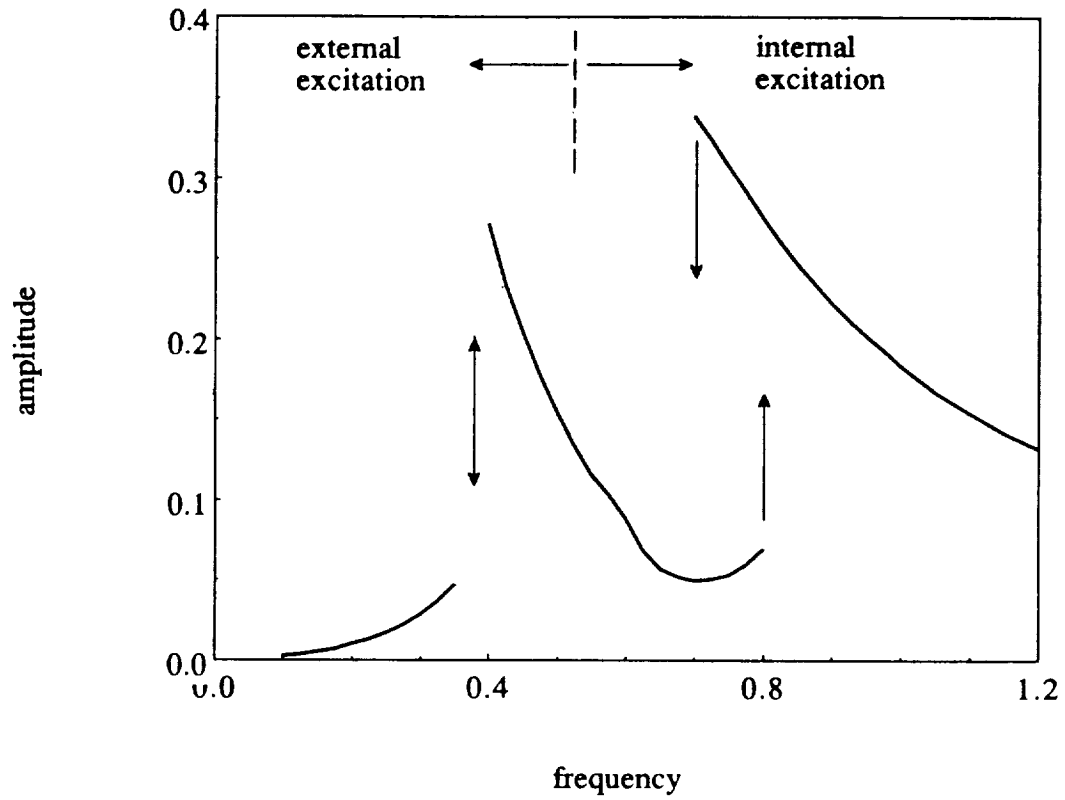
91

Figure 2.29. Frequency response q_a due to both the external torque and the static transmission error excitations. This curve is based on the principle of superposition applied to the analytical solutions which have been constructed by the method of harmonic balance; $F_m=0.1$, $\zeta=0.05$, $F_{ah}=0.05$, $F_{aT}=0.05$, $\Omega_h=2\Omega_T$.

the principle of superposition should be suitable for this case. Figure 2.29 illustrates the frequency response solutions due to the fundamental harmonic component of both excitations for $F_m=0.1$, $F_{ah1}=F_{aT1}=0.05$, $\zeta=0.05$ and by assuming that $\Omega_h=2\Omega_T$. Here, the jump discontinuity is seen at two frequencies. However, when $\Omega_h \approx \Omega_T$ or when one of the superharmonic peaks of $F_i(t)$ coincides with the resonant peak governed by $F_e(t)$, the principle of superposition will no longer be applicable. In such cases, we will use the digital simulation as the analytical interpretation of these cases is yet to be explored.

2.9. CONCLUSION

This analytical study on the non-linear dynamics of a spur gear pair with backlash as excited by the static transmission error has made a number of contributions to the state of the art. First, difficulties associated with the digital simulation technique have been resolved as multiple steady state solutions at a given frequency can be found provided the entire initial condition map is searched. Second, new frequency response solutions for the gear pair have been constructed using the method of harmonic balance. Third, our mathematical models have been validated as these compare well with two previous experimental studies and the key parameters such as the mean load, mean to alternating force ratio, damping and backlash have been identified. Forth, the chaotic and subharmonic resonances are observed if the mean load is too small for a lightly damped system. Fifth, mathematical conditions for tooth separation and back collision have been established which are compatible with available measured data. Sixth, the periodic transmission error excitation case has been analyzed using the method of harmonic balance in conjunction with the principle of superposition. Finally, on a more fundamental note, our study enriches

the current literature on the clearance non-linearity or vibro-impact systems as the governing non-linear differential equation is different from the conventional single degree of freedom system formulation.

CHAPTER III

NON-LINEAR DYNAMIC ANALYSIS A GEARED ROTOR-BEARING SYSTEM WITH MULTIPLE CLEARANCES

3.1. INTRODUCTION

Mathematical modeling of geared rotor-bearing systems, being an essential step in designing quiet and reliable power transmissions, has been the subject of numerous studies over the past few decades. Most proposed dynamic models, as reviewed by Ozguven and Houser [14], are essentially linear. However in several cases, it has been experimentally shown that the geared systems exhibit non-linear behavior [27-29,35]. For instance, vibro-impacts are observed in a lightly loaded transmission with gear backlash or loose bearings [30,31,34]. Accordingly, we must develop non-linear mathematical model of the geared system - this is main focus of this chapter with emphasis on the clearance type non-linearity in gears and rolling element bearings. In Chapter II we had considered the single degree of freedom non-linear model of a spur gear pair with backlash and investigated the effects of system parameters on the vibrations and chaos excited by the static transmission error. Applicability of the harmonic balance method and digital simulation technique to the solution of the steady state response has been demonstrated, and difficulties associated with the digital simulation technique when applied to such systems governed by stiff non-linear differential equations have also been resolved in Chapter II.

Although there is a vast body of literature which considers a single degree of freedom system with clearances, as reviewed earlier in Chapter II, studies on the multi

degree of freedom vibro-impact systems are very limited. For example, Galhoud et.al. [52] considered a two degree of freedom translational system with a gap and found the forced harmonic response using the piecewise linear technique. Winter and Kojima [53] also used the same technique to study the geared systems with backlash. However, it should be noted that the piecewise linear technique can not predict several non-linear phenomena such as subharmonic and chaotic responses since it employs the assumption that both impact and no-impact regimes "are repeated in an identical manner once every period of excitation" [52]. Kucukay [35] developed an eight degree of freedom model of a helical gear pair with backlash to include the rocking and axial motions of rigid shafts and radial deflections of linear bearings. Lin et.al. [38] included motor and load inertias in a three degree of freedom torsional model. Both of these studies employed the digital simulation technique, but did not consider a number of issues of primary concern in non-linear system such as the existence of multiple steady state solutions, their dependence on initial conditions, subharmonic, quasi-periodic and chaotic responses, etc. A few of these issues have been addressed by Singh et.al [34] on the gear rattle problem. Comparin and Singh [54] have also used the digital simulation, analog simulation and harmonic balance method to analyze coupled impact pairs assuming that the modes are "weakly coupled", which allows the system to be represented by a combination of single impact pairs. They included only the low frequency external torque excitation and found the steady state frequency response at the primary resonance. This solution has then been used to analyze the neutral gear problem in more detail [55].

The other two groups of studies which consider multi-degree of freedom systems with continuous non-linearities [56-61] and periodic excitations due to mesh stiffness variations [29,62], will not be addressed here since their responses are significantly

different from the clearance non-linearities as discussed by Comparin and Singh [33]. The literature on chaotic vibrations and rolling element bearings will be discussed later.

3.2. PROBLEM FORMULATION

3.2.1. Scope

Figure 3.1 shows the generic geared system considered in this study. It consists of a spur gear pair mounted on flexible shafts which are supported by rolling element bearings assembled in a rigid gear box. Since the shafts and bearings are compliant, our single degree of freedom model of spur gear pair which assumes fixed gear centers is obviously not suitable. Instead, a three degree of freedom non-linear model as shown in Figure 3.2a is considered. It includes equivalent stiffness and damping elements representing the shaft and the bearings. The corresponding linear model has been found to be sufficiently accurate when compared with a finite element model for eigen solutions provided that the gear dynamic response (mesh force, dynamic transmission error, etc.) is of major concern. Gear backlash and radial clearances in bearings are defined analytically. An approximate non-linear bearing model is also proposed. Applicability of both analytical and numerical solution techniques to this problem is investigated. Several key issues such as non-linear modal interactions and differences between internal static transmission error excitation and external torque excitation are discussed. Parametric studies are conducted to understand the effect of system parameters such as bearing stiffness k_{bi} to mesh stiffness k_h ratio $\hat{k} = k_{bi} / k_h$, alternating to mean force ratio F_a/F_m and radial bearing preload to mean force ratio F_b/F_m on the non-linear frequency response. A criterion is used to classify the steady state solutions, and the conditions for chaotic, quasi-periodic and subharmonic steady state solutions are determined. Two typical routes to chaos
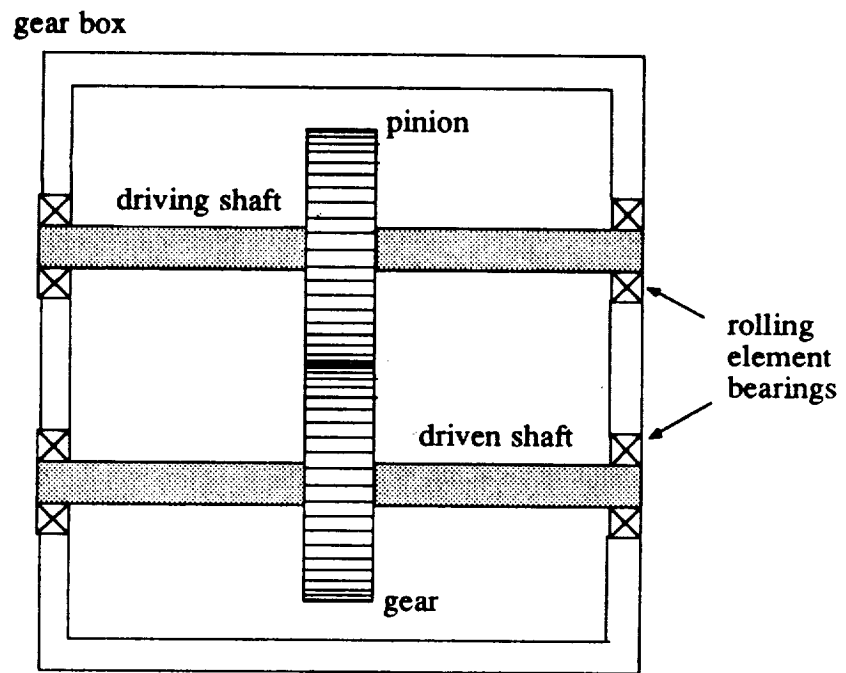
Figure 3.1.   Generic geared rotor-bearing system.

observed on a geared system are also identified. Finally, our formulation is verified by comparing predictions with measurements [27].

3.2.2. Physical Model and Assumptions

The three degree of freedom non-linear model of the geared rotor system with gear inertias I_{g1} and I_{g2}, gear masses m_{g1} and m_{g2}, and base circle diameters d_{g1} and d_{g2}, as shown in Figure 3.2a, is considered here. The gear mesh is described by a non-linear displacement function f_h and viscous damping c_h. Friction forces at the mesh point are assumed to be negligible [18]. Thus the transverse vibrations in the pressure line direction are uncoupled from the vibrations in the direction perpendicular to the pressure line. Bearings and the shafts that support the gears are modeled by equivalent elements with viscous damping coefficients c_{b1} and c_{b2} and non-linear springs defined by force-displacement functions f_{b1} and f_{b2}. The effects of the prime mover and the load inertias are not considered assuming that these inertial elements are connected to the gear box through soft torsional couplings. Further, we assume that the system is symmetric about the plane of the gears and the axial motion (parallel to the shafts) is negligible. Like the spur gear pair model of Chapter II, both low frequency external excitation due to torque fluctuations and high frequency internal excitations due to the static transmission error $\bar{e}(\bar{t})$ are considered in the formulation. Input torque fluctuation is included, but the output torque is assumed to be constant, i.e. $\bar{T}_{g1}(\bar{t}) = \bar{T}_{g1m} + \bar{T}_{g1a}(\bar{t})$ and $\bar{T}_{g2}(\bar{t}) = \bar{T}_{g2m}$. External radial preloads $\bar{F}_{b1}$ and $\bar{F}_{b2}$ are also applied to both rolling element bearings.

3.2.3. Equations of Motion

Equations of coupled transverse-torsional motion of the non-linear geared rotor-bearing system shown in Figure 3.2a are

$$m_{g1}\,\bar{y}_{g1}'' + c_{b1}\,\bar{y}_{g1}' + c_h\left(\bar{x}' + \bar{y}_{g1}' - \bar{y}_{g2}' - \bar{e}'\right) + k_{b1}f_{b1}\left(\bar{y}_{g1}\right)$$

$$+ k_h f_h\left(\bar{x} + \bar{y}_{g1} - \bar{y}_{g2} - \bar{e}\right) = -\bar{F}_{b1} \qquad (3.1a)$$

$$m_{g2}\,\bar{y}_{g2}'' + c_{b2}\,\bar{y}_{g2}' - c_h\left(\bar{x}' + \bar{y}_{g1}' - \bar{y}_{g2}' - \bar{e}'\right) + k_{b2}f_{b2}\left(\bar{y}_{g2}\right)$$

$$- k_h f_h\left(\bar{x} + \bar{y}_{g1} - \bar{y}_{g2} - \bar{e}\right) = \bar{F}_{b2} \qquad (3.1b)$$

$$m_{c1}\,\bar{x}'' + c_h\left(\bar{x}' + \bar{y}_{g1}' - \bar{y}_{g2}' - \bar{e}'\right) + k_h f_h\left(\bar{x} + \bar{y}_{g1} - \bar{y}_{g2} - \bar{e}\right) = \bar{F}_m + \bar{F}_{aT}(\bar{t}) \qquad (3.1c)$$

$$\bar{x}(\bar{t}) = \frac{d_{g1}}{2}\theta_{g1}(\bar{t}) - \frac{d_{g2}}{2}\theta_{g2}(\bar{t}) \; ; \quad m_{c1} = \cfrac{1}{\left(\cfrac{d_{g1}^2}{4I_{g1}} + \cfrac{d_{g2}^2}{4I_{g2}}\right)} \; ; \qquad (3.1d,e)$$

$$\bar{F}_m = \frac{2\bar{T}_{g1m}}{d_{g1}} = \frac{2\bar{T}_{g2m}}{d_{g2}} \; ; \quad \bar{F}_{aT}(\bar{t}) = \frac{m_{c1}\bar{T}_{g1a}(\bar{t})}{2I_{g1}} \; . \qquad (3.1f,g)$$

Here, $(\ )'$ means derivative with respect to time $\bar{t}$, y_{gi} and θ_{gi} are the transverse and torsional displacements of the i-th gear (i=1,2), m_{c1} is the equivalent gear pair mass, $\bar{F}_m$ is the average force transmitted through the gear mesh and $\bar{F}_{aT}(t)$ is the fluctuating force related to the external input torque excitation. Equations (3.1a), (3.1b) and (3.1c) are simplified further by defining below a new variable $\bar{p}(\bar{t})$ which is the difference between the dynamic transmission error and the static transmission error $\bar{e}(\bar{t})$.
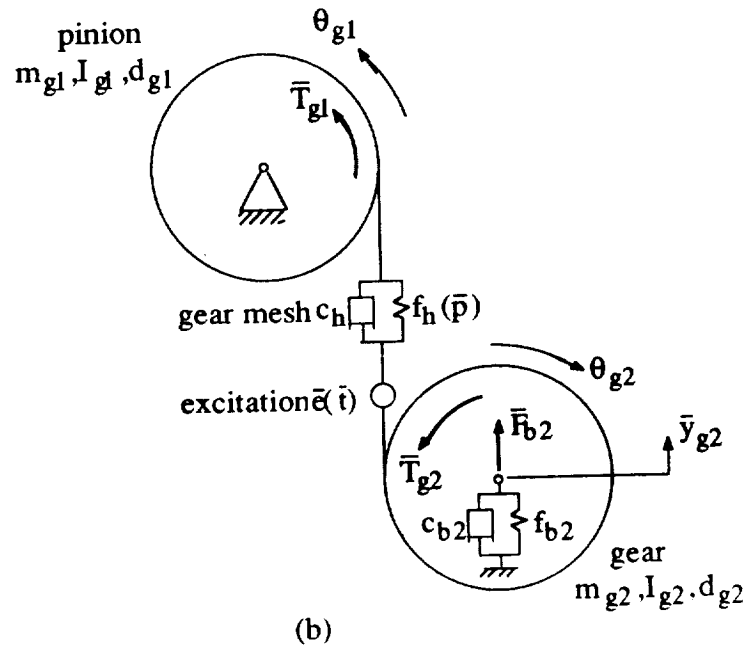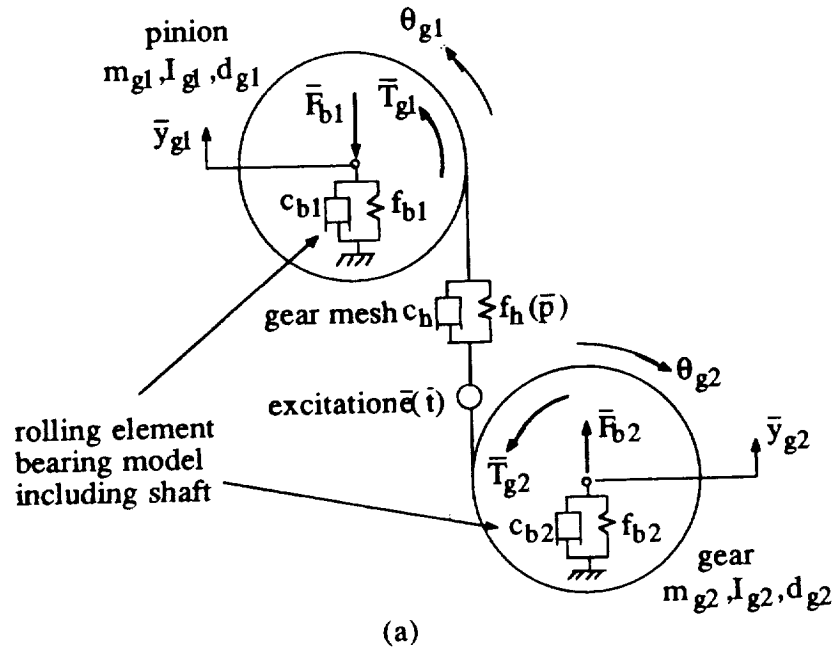
100

Figure 3.2.   Non-linear models of the geared rotor-bearing system; a) three degree of freedom model, b) two degree of freedom model.

101

$$\bar{p}(\bar{t}) = \bar{x}(\bar{t}) + \bar{y}_{g1}(\bar{t}) - \bar{y}_{g2}(\bar{t}) - \bar{e}(\bar{t}) ; \tag{3.2a}$$

$$\begin{bmatrix} m_{g1} & 0 & 0 \\ 0 & m_{g2} & 0 \\ -m_{c1} & m_{c1} & m_{c1} \end{bmatrix} \begin{Bmatrix} \bar{y}_{g1}''(\bar{t}) \\ \bar{y}_{g2}''(\bar{t}) \\ \bar{p}''(\bar{t}) \end{Bmatrix} + \begin{bmatrix} c_{b1} & 0 & c_h \\ 0 & c_{b2} & -c_h \\ 0 & 0 & c_h \end{bmatrix} \begin{Bmatrix} \bar{y}_{g1}'(\bar{t}) \\ \bar{y}_{g2}'(\bar{t}) \\ \bar{p}'(\bar{t}) \end{Bmatrix}$$

$$+ \begin{bmatrix} k_{b1} & 0 & k_h \\ 0 & k_{b2} & -k_h \\ 0 & 0 & k_h \end{bmatrix} \begin{Bmatrix} f_{b1}(\bar{y}_{g1}) \\ f_{b2}(\bar{y}_{g2}) \\ f_h(\bar{p}) \end{Bmatrix} = \begin{Bmatrix} -\bar{F}_{b1} \\ \bar{F}_{b2} \\ \bar{F}_m - m_{c1}\bar{e}''(\bar{t}) + \bar{F}_{aT}(\bar{t}) \end{Bmatrix}. \tag{3.2b}$$

A dimensionless form of equation (3.2b) is obtained by letting $y_{gi}(\bar{t}) = \bar{y}_{gi}(\bar{t})/b_c$, $p(\bar{t}) = \bar{p}(\bar{t})/b_c$, $\omega_n = \sqrt{k_h/m_{c1}}$, $\omega_{bi} = \sqrt{k_{bi}/m_{gi}}$ (i=1,2) and $t = \omega_n \bar{t}$ where b_c is the characteristic length. Here, we consider harmonic excitation for both $\bar{e}(\bar{t})$ and $\bar{F}_{aT}(\bar{t})$ as $\bar{e}(\bar{t}) = \tilde{e}\sin(\bar{\Omega}_h\bar{t} + \phi_h)$, $\bar{F}_{aT}(\bar{t}) = \tilde{F}_{aT}\sin(\bar{\Omega}_T\bar{t} + \phi_T)$ where $\bar{\Omega}_h$ and $\bar{\Omega}_T$ are the fundamental excitation frequencies of internal displacement and external torque fluctuations, respectively. Further, define dimensionless excitation frequencies $\Omega_h = \bar{\Omega}_h/\omega_n$ and $\Omega_T = \bar{\Omega}_T/\omega_n$ to yield the following dimensionless governing equation of motion.

$$\begin{bmatrix} 1 & 0 & 0 \\ 0 & 1 & 0 \\ -1 & 1 & 1 \end{bmatrix} \begin{Bmatrix} \ddot{y}_{g1}(t) \\ \ddot{y}_{g2}(t) \\ \ddot{p}(t) \end{Bmatrix} + 2\begin{bmatrix} \zeta_{11} & 0 & \zeta_{13} \\ 0 & \zeta_{22} & -\zeta_{23} \\ 0 & 0 & \zeta_{33} \end{bmatrix} \begin{Bmatrix} \dot{y}_{g1}(t) \\ \dot{y}_{g2}(t) \\ \dot{p}(t) \end{Bmatrix}$$

$$+ \begin{bmatrix} \kappa_{11} & 0 & \kappa_{13} \\ 0 & \kappa_{22} & -\kappa_{23} \\ 0 & 0 & 1 \end{bmatrix} \begin{Bmatrix} f_{b1}(y_{g1}) \\ f_{b2}(y_{g2}) \\ f_h(p) \end{Bmatrix} = \{F(t)\}; \tag{3.3a}$$

$$\{F(t)\} = \{F\}_m + \{F(t)\}_i + \{F(t)\}_e$$

$$= \begin{Bmatrix} -F_{b1} \\ F_{b2} \\ F_m \end{Bmatrix} + \begin{Bmatrix} 0 \\ 0 \\ F_{ah}\Omega_h^2 \end{Bmatrix} \sin(\Omega_h t + \phi_h) + \begin{Bmatrix} 0 \\ 0 \\ F_{aT} \end{Bmatrix} \sin(\Omega_T t + \phi_T); (3.3b)$$

$$\zeta_{ii} = \frac{c_{bi}}{2m_{gi}\omega_n}; \quad \zeta_{i3} = \frac{c_h}{2m_{gi}\omega_n}, \ i=1,2; \quad \zeta_{33} = \frac{c_h}{2m_{cl}\omega_n}; \qquad (3.3c,d,e)$$

$$\kappa_{ii} = \frac{\omega_{bi}^2}{\omega_n^2}; \quad \kappa_{i3} = \frac{m_{cl}}{m_{gi}}; \quad F_{bi} = \frac{\overline{F}_{bi}}{m_{gi}b_c\omega_n^2}, \ i=1,2; \qquad (3.3f,g,h)$$

$$F_m = \frac{\overline{F}_m}{m_{cl}b_c\omega_n^2}; \quad F_{ah} = \frac{\tilde{e}}{b_c}; \quad F_{aT} = \frac{\tilde{F}_{aT}}{m_{cl}b_c\omega_n^2}; \qquad (3.3i,j,k)$$

where F_{bi} (i=1,2) and F_m, are the dimensionless components of the mean force vector $\{F\}_m$, and F_{aT} and F_{ah} pertain to the alternating external excitation $\{F(t)\}_e$ and internal excitation $\{F(t)\}_i$ force vectors, respectively.

3.2.4. Modeling of Non-linearities

The non-linear displacement functions $f_{bi}(y_{gi})$, i=1, 2 and $f_h(p)$ in equation (3.3a), which represent the bearing radial and gear mesh stiffnesses, respectively, should be defined explicitly before solving the non-linear equations. Here, $f_h(p)$ is, defined as a clearance type dead space function with a backlash $2b_h$ and linear time-invariant mesh stiffness of one, in the dimensionless form

103

$$f_h(p) = \begin{cases} p - \dfrac{b_h}{b_c}, & p > \dfrac{b_h}{b_c} \\[2mm] 0; & -\dfrac{b_h}{b_c} < p < \dfrac{b_h}{b_c} \\[2mm] p + \dfrac{b_h}{b_c}, & p < -\dfrac{b_h}{b_c} \end{cases} \tag{3.4}$$

For the i-th rolling element bearing, radial force $\bar{F}_{yi}$ versus displacement $\bar{y}_{gi}$ relationship under the static loading condition is defined as [63-65]

$$\bar{F}_{yi}(\bar{y}_{gi}) = \begin{cases} k_{ti} \sum_{r=1}^{H} \left(\bar{y}_{gi} \cos\alpha_r - b_{bi} \right)^n \cos\alpha_r; & \bar{y}_{gi} > b_{bi} \\[2mm] 0; & -b_{bi} < \bar{y}_{gi} < b_{bi} \\[2mm] -k_{ti} \sum_{r=1}^{H} \left(|\bar{y}_{gi}| \cos\alpha_r - b_{bi} \right)^n \cos\alpha_r & \bar{y}_{gi} < -b_{bi} \end{cases} \tag{3.5}$$

where k_{ti} is the inner contact stiffness, α_r is the angular position of the r-th rolling element in contact, $2b_{bi}$ is the radial clearance of the i-th bearing, n is the power of the non-linear force displacement relationship (n=1.5 for ball bearings and n=10/9 for roller bearings) and H is the total number of rolling elements in contact under loaded conditions. Now the dimensionless bearing displacement function $f_{bi}(y_{gi})$ of equation (3.3a) is obtained from equation (3.5) as

$$f_{bi}(y_{gi}) = \frac{\bar{F}_{yi}}{k_{ti}b_c^n} = \begin{cases} \sum\limits_{r=1}^{H}\left(y_{gi}\cos\alpha_r - \dfrac{b_{bi}}{b_c}\right)^n \cos\alpha_r; & y_{gi} > \dfrac{b_{bi}}{b_c} \\[3ex] 0; & -\dfrac{b_{bi}}{b_c} < y_{gi} < \dfrac{b_{bi}}{b_c} \\[3ex] -\sum\limits_{r=1}^{H}\left(|y_{gi}|\cos\alpha_r - \dfrac{b_{bi}}{b_c}\right)^n \cos\alpha_r; & y_{gi} < -\dfrac{b_{bi}}{b_c} \end{cases} \qquad (3.6)$$

Figure 3.3 shows the non-linear function $f_{gi}(y_{gi})$ for a roller bearing with $n=10/9$, $k_t=1 \times 10^8$ N/m$^{10/9}$, total number of rollers $Z=15$ and $b_b=0.01$ mm. In Figure 3.3, we note almost a linear relationship for large displacements, say $y_{gi} > 3b_{bi}/b_c$. Since the degree of non-linearity is not very significant, equation (3.6) can be approximated by a piece-wise linear function, similar to $f_h(p)$ given by equation (3.4), in order to simplify the analysis considerably. Figure 3.3 also illustrates two linear approximations A and B beyond the clearance for $f_{bi}(y_{gi})$ in the form

$$f_{bi}(y_{gi}) = \begin{cases} y_{gi} - \dfrac{b_{bi}}{b_c}; & y_{gi} > \dfrac{b_{bi}}{b_c} \\[3ex] 0; & -\dfrac{b_{bi}}{b_c} < y_{gi} < \dfrac{b_{bi}}{b_c} \\[3ex] y_{gi} + \dfrac{b_{bi}}{b_c}; & y_{gi} < -\dfrac{b_{bi}}{b_c} \end{cases} \qquad (3.7)$$

Note that both approximations A and B differ in clearances b_{bi_A} and b_{bi_B} but have the same slope as the exact bearing stiffness curve for $y_{gi} > 3b_{bi}/b_c$, $i=1,2$, which is unity in the dimensionless form. The validity of these approximations will be given later.
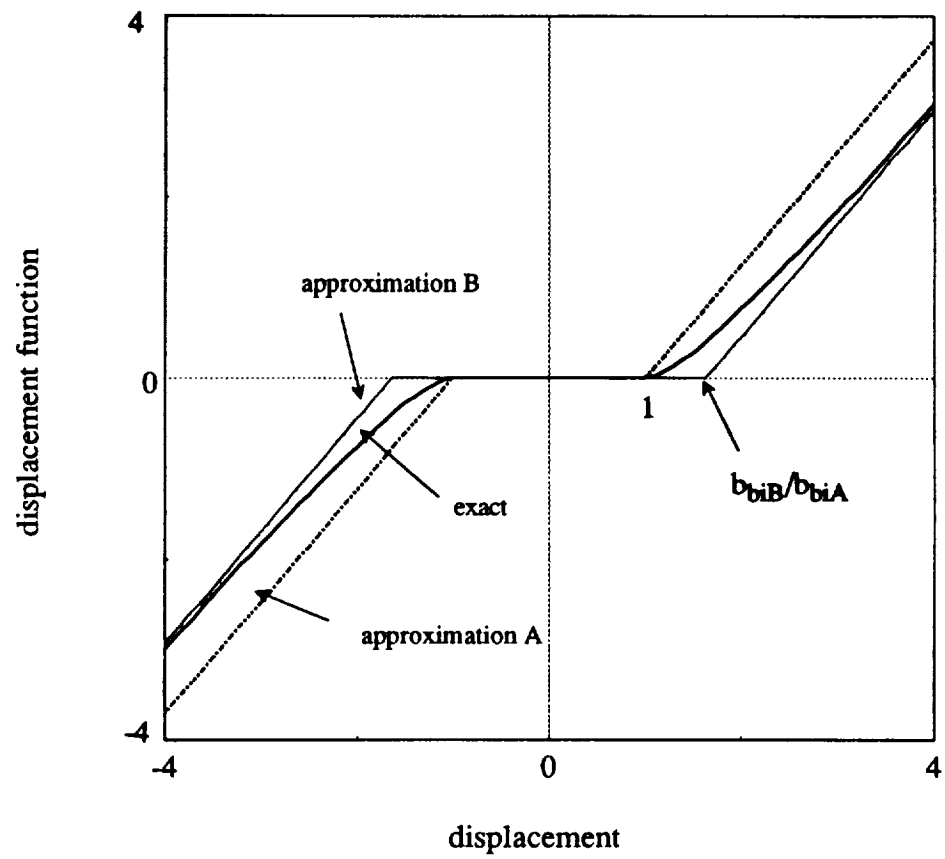
105

Figure 3.3. Exact and approximate bearing deflection functions.

3.3. CORRESPONDING LINEAR MODEL

As a limiting case, equations of motion of the corresponding linear system are obtained by substituting $f_{bi}(y_{gi}) = y_{gi}$, for i=1 and 2, and $f_h(p) = p$ in equation (3.3a)

$$\begin{bmatrix} 1 & 0 & 0 \\ 0 & 1 & 0 \\ -1 & 1 & 1 \end{bmatrix} \begin{Bmatrix} \ddot{y}_{g1}(t) \\ \ddot{y}_{g2}(t) \\ \ddot{p}(t) \end{Bmatrix} + 2 \begin{bmatrix} \zeta_{11} & 0 & \zeta_{13} \\ 0 & \zeta_{22} & -\zeta_{23} \\ 0 & 0 & \zeta_{33} \end{bmatrix} \begin{Bmatrix} \dot{y}_{g1}(t) \\ \dot{y}_{g2}(t) \\ \dot{p}(t) \end{Bmatrix}$$

$$+ \begin{bmatrix} \kappa_{11} & 0 & \kappa_{13} \\ 0 & \kappa_{22} & -\kappa_{23} \\ 0 & 0 & \kappa_{33} \end{bmatrix} \begin{Bmatrix} y_{g1}(t) \\ y_{g2}(t) \\ p(t) \end{Bmatrix} = \{F(t)\} \qquad (3.8a)$$

or in the matrix form with $\{q(t)\}$ as the displacement vector

$$[M]\{\ddot{q}(t)\} + [C]\{\dot{q}(t)\} + [K]\{q(t)\} = \{F(t)\} \qquad (3.8b)$$

where the mass [M], damping [C] and stiffness [K] matrices are all positive definite. These matrices are asymmetric due to $\ddot{y}_{g1}$ and $\ddot{y}_{g2}$ terms in the last row of matrix equation (3.8a). For this linear system, the mean and alternating components of the motion can be separated by letting $y_{gi}(t) = y_{gim} + y_{gia}(t)$, i=1,2 and $p(t) = p_m + p_a(t)$. Hence, equation (3.8a) is rearranged in terms of the alternating motion as

$$[M]\{\ddot{q}_a(t)\} + [C]\{\dot{q}_a(t)\} + [K]\{q_a(t)\} = \{F(t)\}_i + \{F(t)\}_e \qquad (3.9)$$

The natural frequencies ω_r and the modes $\{\psi_r\}$ are calculated by considering the corresponding eigen-value problem. The forced harmonic vibration response is then

107

obtained by the modal expansion technique in the following form

$$\{q_a(t)\} = \sum_{r=1}^{3} \frac{\{\psi_r\}\{\psi_r\}^T}{\left[(\omega_r^2 - \Omega_h^2) + j\Omega_h c_r\right]} F_{ah}\Omega_h^2 \sin(\Omega_h t + \phi_h)$$

$$+ \sum_{r=1}^{3} \frac{\{\psi_r\}\{\psi_r\}^T}{\left[(\omega_r^2 - \Omega_T^2) + j\Omega_T c_r\right]} F_{aT}\Omega_T^2 \sin(\Omega_T t + \phi_T); \quad j = \sqrt{-1} \quad (3.10a)$$

$$c_r = \frac{1}{\delta_{rs}}\{\psi^r\}^T[C]\{\psi^s\}; \quad \delta_{rs} = \begin{cases} 1; & r = s \\ 0; & r \neq s \end{cases} \quad (3.10b)$$

Table 3.1 shows the natural frequencies of the three degree of freedom linear system given by equation (3.9) and the ones found by finite element method for three different $\hat{k} = k_{bi}/k_h$ values with $m_{gi}=1$ kg, $I_{gi}=0.0008$ kg/m^2, $d_{gi}=0.08$ m, $\zeta_{ii}=0.01$, $\zeta_{i3}=0.0125$, $\zeta_{33}=0.05$, i=1, 2 and $k_h=2 \times 10^8$ N/m. As evident from Table 3.1, the three degree of freedom and finite element models [15] result in virtually the same natural frequencies. This concludes that the three degree of freedom model is indeed suitable for the geared-rotor bearing system. The first ψ_I and third ψ_{III} natural modes are coupled transverse-torsional modes while ψ_{II} is purely transverse type [15]. The second natural mode ψ_{II} is not excited by $\bar{e}(\bar{t})$ in this particular case, since the gear ratio $v_g=d_{g2}/d_{g1}$ is one for a symmetric pair. Therefore only two peaks should exist in the frequency response spectrum which will be presented in Section 3.5.

108

Table 3.1   Natural frequencies of the corresponding three degree of freedom (3-DOF) linear model.

Ψ_r	ω_r	$\hat{k}=k_{bi}/k_h$		
		1	5	10
		3-DOF/FEM[†]	3-DOF/FEM	3-DOF/FEM
first transverse-torsional coupled	ω_I	0.396/0.402	0.500/0.512	1.262/1.275
purely transverse	ω_{II}	0.758/0.795	1.118/1.157	1.475/1.560
second transverse-torsional coupled	ω_{III}	0.880/0.930	1.581/1.692	1.796/1.868

†   Finite Element Method (FEM) from Reference [15].

3.4. TWO DEGREE OF FREEDOM SYSTEM STUDIES

3.4.1. Equations of Motion

As a first example, we reduce the three degree of freedom transverse-torsional semi-definite model to a two degree of freedom non-linear model. This is obtained by clamping one of the gear centers as shown in Figure 3.2b, i.e. one of the transverse displacements is assumed to be zero, say $y_{g1}=0$ which physically corresponds to a system with one gear g1 mounted on a rigid shaft which is supported by very stiff bearings while the other gear g2 is assembled with compliant lumped shaft and bearings. Equations of motion of the reduced order system are obtained from equation (3.3a) by letting $y_{g1}=0$.

$$\begin{bmatrix} 1 & 0 \\ 1 & 1 \end{bmatrix} \begin{Bmatrix} \ddot{y}_{g2}(t) \\ \ddot{p}(t) \end{Bmatrix} + 2\begin{bmatrix} \zeta_{22} & -\zeta_{23} \\ 0 & \zeta_{33} \end{bmatrix} \begin{Bmatrix} \dot{y}_{g2}(t) \\ \dot{p}(t) \end{Bmatrix}$$

$$+ \begin{bmatrix} \kappa_{22} & -\kappa_{23} \\ 0 & 1 \end{bmatrix} \begin{Bmatrix} f_{b2}(y_{g2}) \\ f_h(p) \end{Bmatrix} = \{F(t)\}. \qquad (3.11)$$

The intent here is to simplify the physical system in order to investigate several key issues in depth. Specifically, the objectives are to: a) justify using approximate bearing models proposed in Section 3.2.4 by comparing the frequency responses excited by $\bar{e}(t)$, b) show applicability of the harmonic balance method (HBM) to solve non-linear system equations and compare its predictions with the results yielded by the digital simulation technique, c) study interactions between system non-linearities for both weakly and strongly coupled modes, and d) compare the steady state frequency response spectra due to internal static transmission error excitation $\{F(t)\}_i$ and external torque excitation $\{F(t)\}_e$.

110

3.4.2. Solution

Both analytical and numerical solution techniques which we have used successfully for the spur gear pair problem are employed again to solve equation (3.11). First, approximate analytical solutions are constructed using the harmonic balance method [33,51] with only the bearing non-linearity assuming no gear backlash, i.e. $b_h=0$ or $f_h(p)=p$. For the harmonic excitation given by equation (3.3), we assume

$$p(t) = p_m + p_a \sin(\Omega_h t + \phi_p) \; ; \quad y_{g2}(t) = y_{g2m} + y_{g2a} \sin(\Omega_h t + \phi_{g2}) \quad (3.12a,b)$$

where subscripts m and a represent mean and alternating components of the steady state response, and ϕ_p and ϕ_{g2} are the phase angles. The non-linear bearing function is approximated as

$$f_{b2}(y_{g2}) = N_m y_{g2m} + N_a y_{g2a} \sin(\Omega_h t + \phi_{g2}). \quad (3.13)$$

where $N_m=N_m(y_{g2m},y_{g2a})$ and $N_a=N_a(y_{g2m},y_{g2a})$ are the describing functions which are given in Chapter II; these need to be defined for each impact regime (no impact, single sided impact, double sided impact). Governing frequency response equations are obtained by substituting equations (3.12) and (3.13) into equation (3.11) and equating the coefficients of like harmonics:

$$p_a = \frac{\left[\Lambda_1^2 + (2\zeta_{22}\Omega_h)^2\right]\Omega_h^2 F_{ah}}{\sqrt{\Lambda}} \; ; \quad (3.14a)$$

$$\Lambda = (-\Omega_h^3 \kappa_{23} \Lambda_1 + 4\Omega_h^4 \zeta_{22} \zeta_{23} + \Lambda_2 \Lambda_1^2 + 4\Omega_h^4 \zeta_{22}^2 \Lambda_2)^2$$

$$+(-2\Omega_h^3 \zeta_{22} \kappa_{23} - 2\Omega_h^3 \zeta_{23} \Lambda_1 + 2\Omega_h \zeta_{33} \Lambda_1^2 + 8\Omega_h^3 \zeta_{22}^2 \zeta_{33})^2 \ ; \qquad (3.14b)$$

$$\Lambda_1 = \kappa_{22} N_a - \Omega_h^2; \qquad \Lambda_2 = 1 - \Omega_h^2 \ ; \qquad P_m = F_m \ ; \qquad (3.14c,d,e)$$

$$y_{g2a} = \left[\frac{\kappa_{23}^2 + (2\Omega_h \zeta_{23})^2}{(\kappa_{23} \Lambda_1 - 4\Omega_h^2 \zeta_{22} \zeta_{23})^2 + (2\Omega_h \zeta_{22} \kappa_{23} + 2\Omega_h \zeta_{23} \Lambda_1)^2} \right]^{1/2} \ ; \qquad (3.14f)$$

$$y_{g2m} = \frac{F_{b2} + \kappa_{23} P_m}{\kappa_{22} N_m} \qquad (3.14g)$$

The overall frequency response is obtained by solving equation (3.14) numerically for each impact regime separately.

Second, the digital simulation technique is used to solve equation (3.11) for no gear backlash. A 5th-6th order variable step size Runge Kutta numerical integration algorithm [50], which has already been employed successfully in solving similar problems, is used here. Figure 3.4 compares frequency response spectra obtained using the harmonic balance method and digital simulation. Although both methods are in a very close agreement for the case considered in Figure 3.4, one should be aware of the following: (i) several problems may exist in the application of the numerical integration method to the clearance type problems, hence caution must be exercised, and (ii) the harmonic balance method is incapable of predicting chaotic and subharmonic responses. Accordingly for further analysis, we will use only the digital simulation technique.
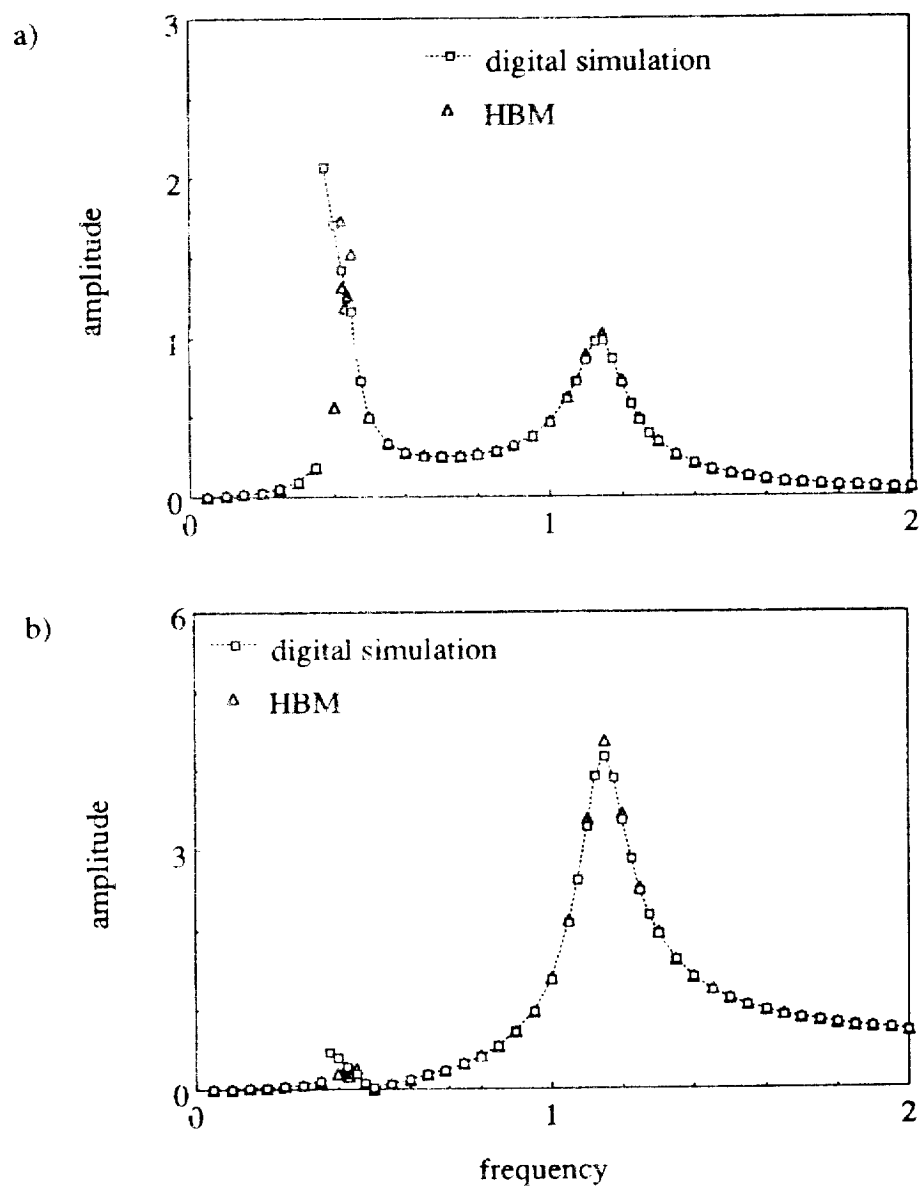
112

Figure 3.4. Comparison of harmonic balance method and digital simulation technique; $F_m=1.0$, $F_{ah}=0.5$, $F_{b2}=0$, $b_h=0$, $b_{b2}=b_c$, $\zeta_{33}=0.05$, $\zeta_{23}=0.0125$, $\zeta_{22}=0.01$, $\hat{k}=1$; a) y_{g2a} versus Ω_h, b) p_a versus Ω_h.

113

3.4.3. Validation of Non-linear Bearing Model

We examine the validity of two approximations for $f_{bi}(y_{gi})$, as suggested in Section 3.2.4 and shown in Figure 3.3, by assuming $b_h=0$ and $F_{aT}=0$. Equation (3.11) is solved using the digital simulation technique, given $F_m=1.0$, $F_{ah}=0.05$, $F_{b2}=0$, $\zeta_{22}=0.01$, $\zeta_{33}=0.05$, $\zeta_{23}=0.0125$ and $\kappa_{22}=\kappa_{23}=0.25$, for three bearing models (exact, approximations A: $b_{b2_A}=b_{b2}=b_c$, approximation B: $b_{b2_B}=1.63b_{b2}=1.63b_c$). Figures 3.5a and 3.5b compare y_{g2a} versus Ω_h and p_a versus Ω_h spectra for all three bearing models. Both approximations are in a very close agreement with the exact bearing model over the entire frequency range. The frequency and the amplitude of the jump at the first peak is predicted accurately by both approximate models. Hence we conclude that the approximate piecewise linear model can be used for a bearing without losing any accuracy and the dynamic behavior is not sensitive to the minor variations in bearing clearances b_{bi}.

3.4.4. Non-linear Modal Interactions

Although both natural modes of the corresponding linear model are transverse-torsional coupled modes, first mode ψ_I is more dependent on transverse vibrations than the second peak. Accordingly, it is expected that bearing non-linearities should affect the first peak directly while gear backlash should dominate the second peak in Figure 3.4. The validity of this claim depends on the nature of non-linearities and system parameter values, as illustrated below.

First, a set of parameters is selected so that natural frequencies ω_I and ω_{II} of the corresponding linear system are far away from each other: $\omega_I=0.437$ and $\omega_{II}=1.144$ for $\kappa_{22}=0.25$, $\kappa_{23}=0.25$, $\zeta_{22}=0.01$, $\zeta_{23}=0.0125$, and $\zeta_{33}=0.05$. Frequency response characteristics of the system with a forcing function, $F_m=1.0$ and $F_{ah}=0.5$ are evaluated
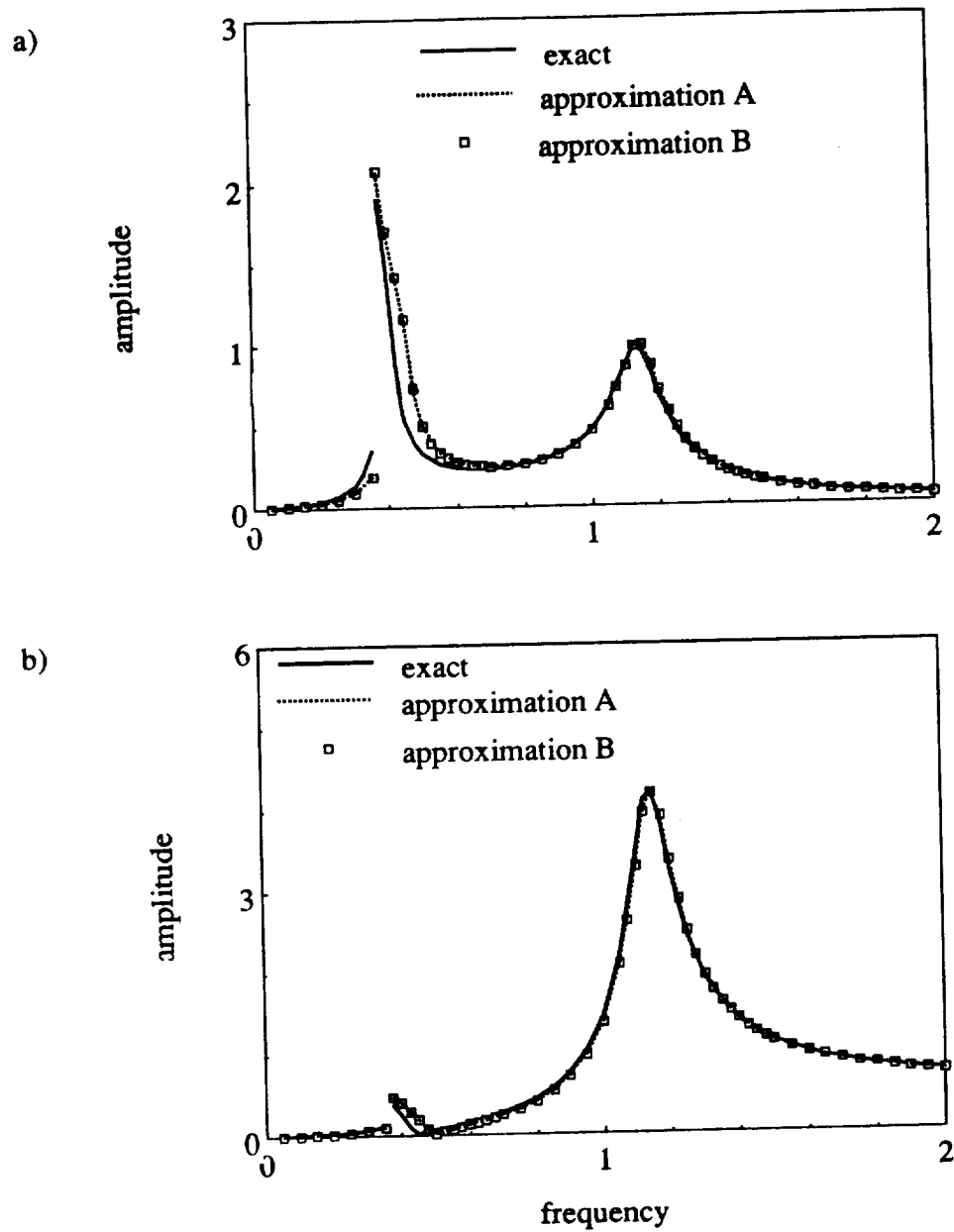
114

Figure 3.5.   Comparison of frequency responses obtained by using the exact and approximate bearing displacement functions given in Figure 3.3; $F_m=1.0$, $F_{ah}=0.5$, $F_{b2}=0$, $b_h=0$, $b_{b2}=b_c$, $\zeta_{33}=0.05$, $\zeta_{23}=0.0125$, $\zeta_{22}=0.01$, $\hat{k}=1$; a) y_{g2a} versus Ω_h, b) p_a versus Ω_h.

for the following three cases: a) no gear backlash, $b_h=0$, non-linear bearing, $b_{b2}=b_c$; b) gear backlash, $b_h=10b_c$, linear bearing, $b_{b2}=0$; and c) gear backlash and non-linear bearing with $b_h=10b_{b2}=10b_c$. In the last two cases, gear backlash is taken to be 10 times the bearing clearance as it is a typical order of magnitude value for many geared rotor systems supported by roller bearings. Figures 3.6 and 3.7 show the frequency responses, y_{g2a} versus Ω_h and p_a versus Ω_h respectively, for all three cases given above; also superimposed is the linear frequency response curve for comparison purposes. As shown in Figure 3.6a and 3.7a, a jump discontinuity is observed at the first peak only for case a. In the case with only gear backlash non-linearity, jump is seen at the second peak while the first peak is continuous as shown in Figures 3.6b and 3.7b; this supports the claim of torsional mode dominance of the second peak. Finally, when both non-linearities are included simultaneously, both peaks become non-linear as shown in Figures 3.6c and 3.7c. For such a system, natural modes are essentially "uncoupled" and the interactions between component non-linearities are negligible. In summary, for case a of Figures 3.6a and 3.7a, a linear model can be used to predict the frequency response beyond ω_I, say $\Omega_h > 0.6$. Similarly, a linear model could be suitable for case b for $\Omega_h < 0.8$ as shown in Figures 3.6b and 3.7c. But for case c, a linear model is suitable only far away from the resonances.

Second, choose a dataset, say $\kappa_{22}=0.64$, $\kappa_{23}=0.10$, $\zeta_{22}=0.01$, $\zeta_{23}=0.0125$, and $\zeta_{33}=0.05$, such that two natural frequencies for the corresponding linear system are brought closer to each other: $\omega_I=0.720$, $\omega_{II}=1.101$. We again consider the same cases a, b and c and compare the frequency response for $F_m=2.0$ and $F_{ah}=0.5$ in Figures 3.8 and 3.9. Here, each non-linearity affects both modes, resulting in jumps at each peak. Therefore, for this set of parameters, modes are considered to be "coupled" because of dynamic interactions. Accordingly both non-linearities must be included
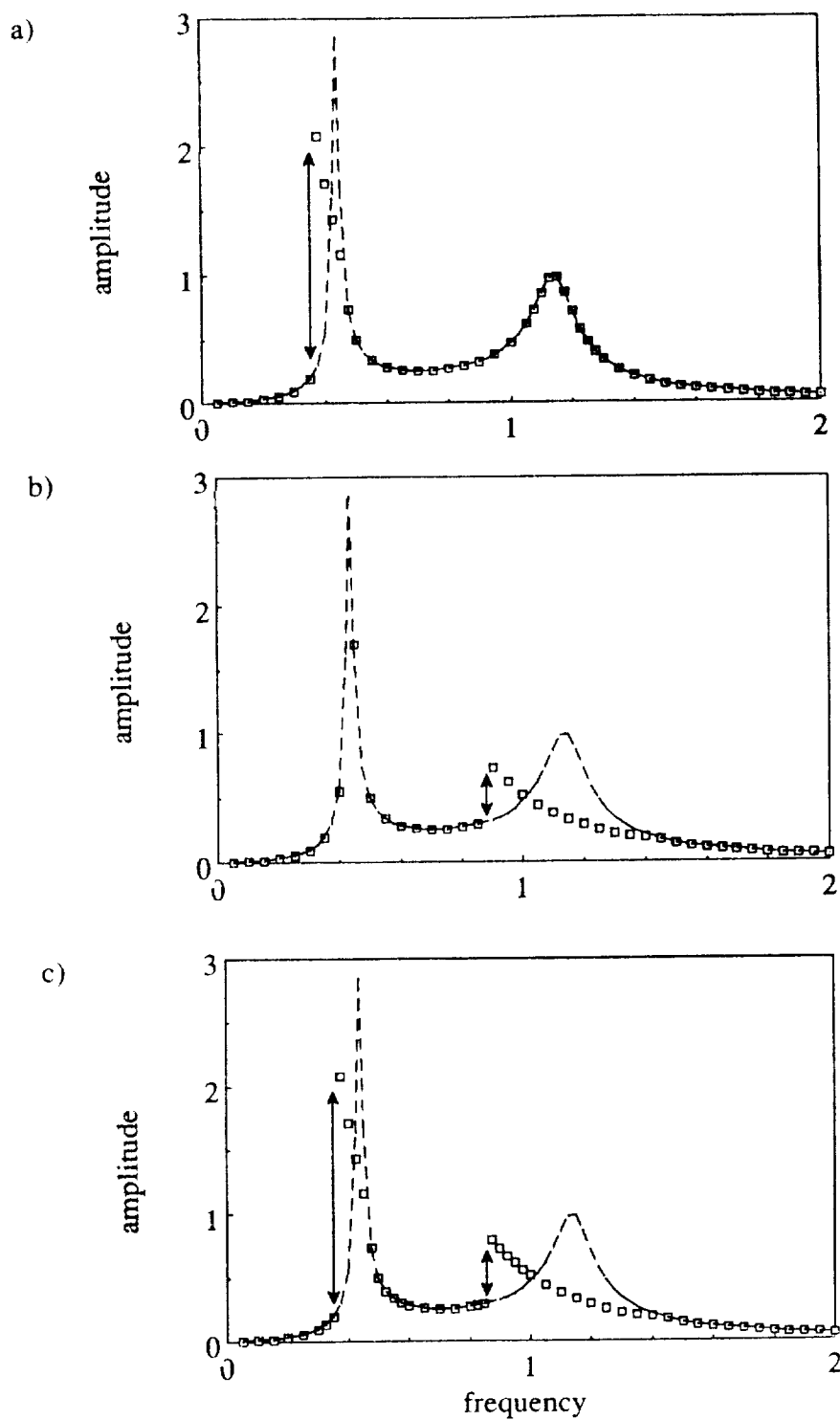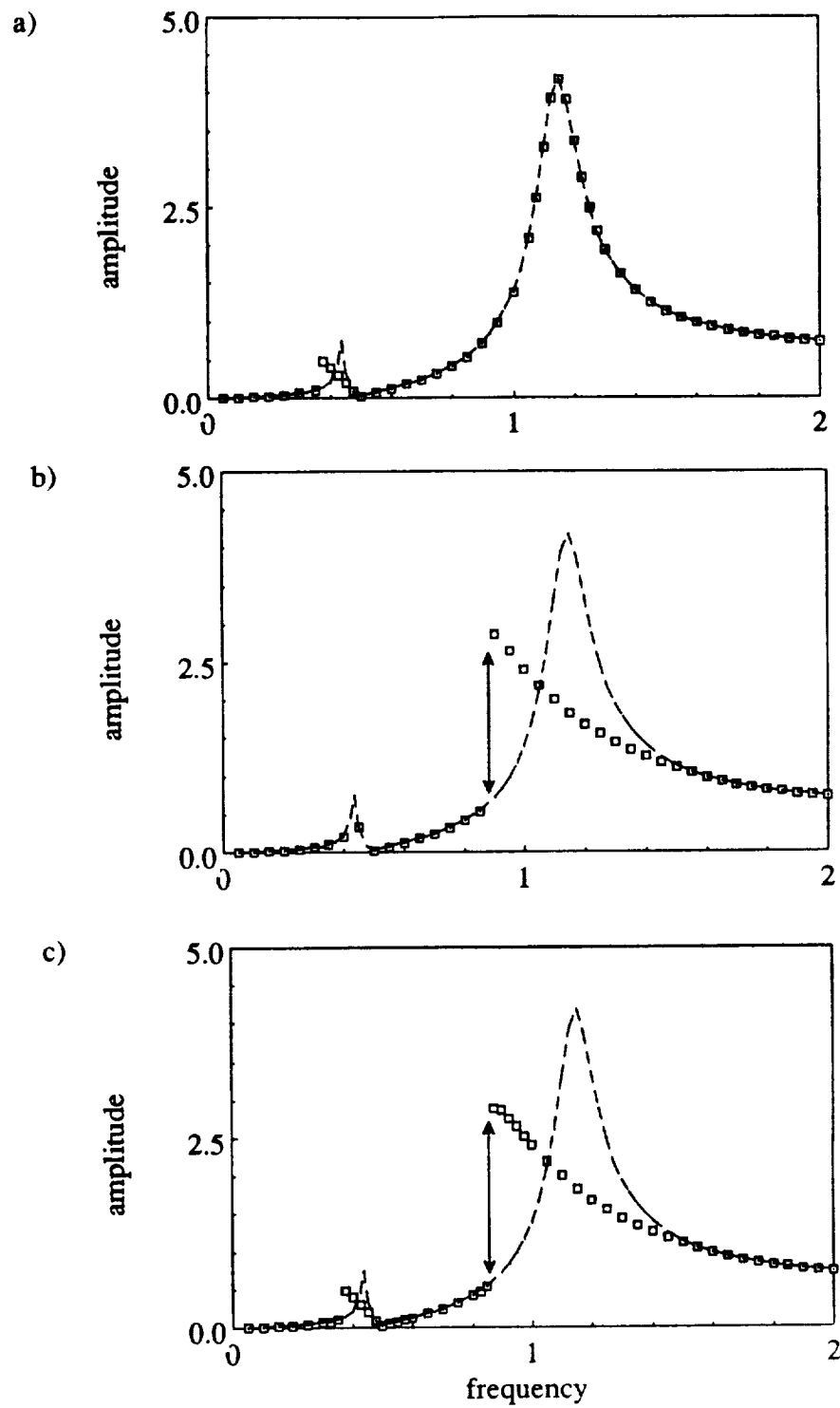
Figure 3.6. y_{g2a} versus Ω_h plots for the case of uncoupled modes; a) no backlash, non-linear bearings, b) backlash, linear bearings, c) backlash, non-linear bearings; — — — — corresponding linear response.
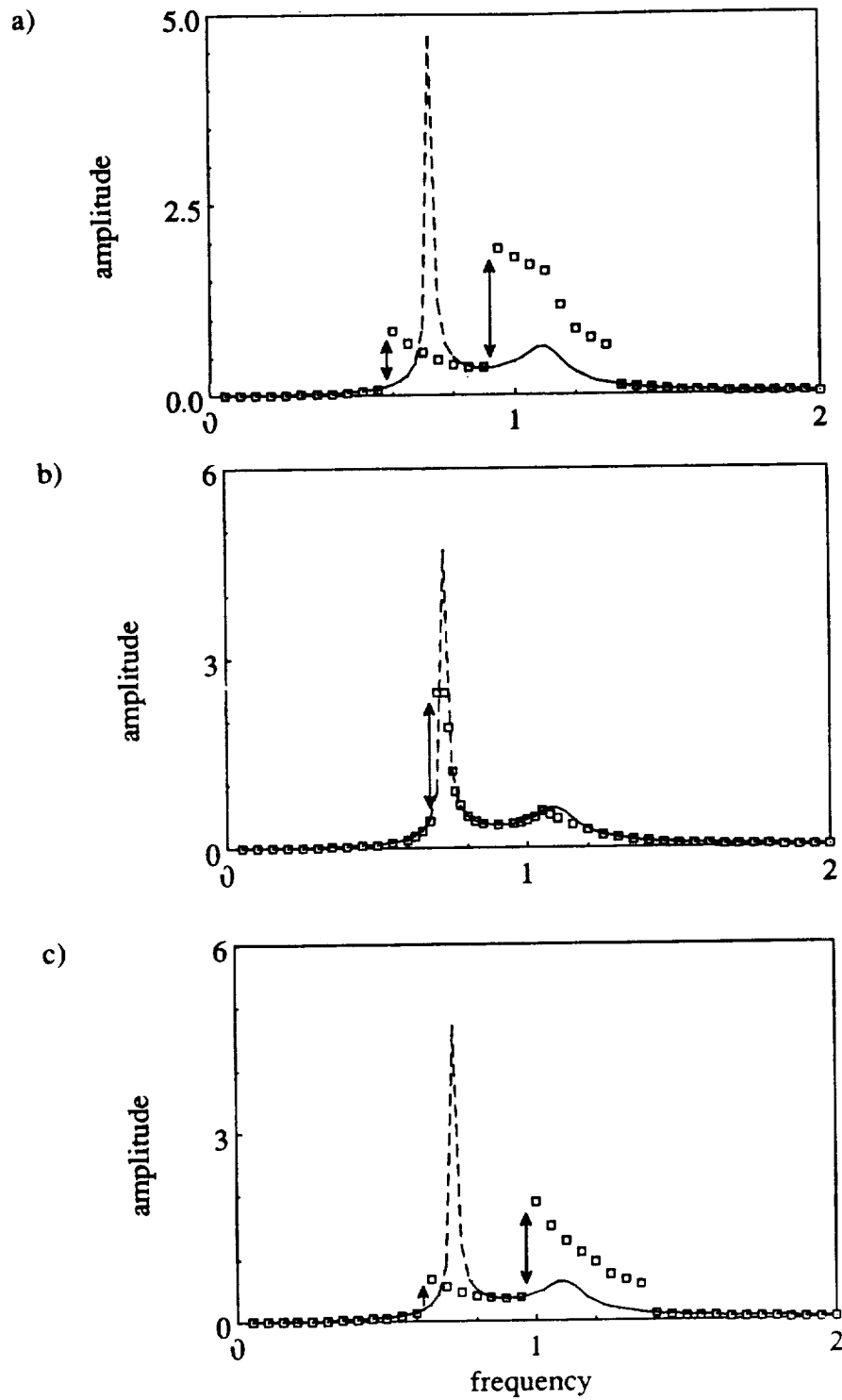
Figure 3.7. p_a versus Ω_h plots for the case of uncoupled modes; a) no backlash, non-linear bearings, b) backlash, linear bearings, c) backlash, non-linear bearings; — — — — corresponding linear response.

118

Figure 3.8. y_{g2a} versus Ω_h plots for the case of coupled modes: a) no backlash, non-linear bearings, b) backlash, linear bearings, c) backlash, non-linear bearings; — — — — corresponding linear response.
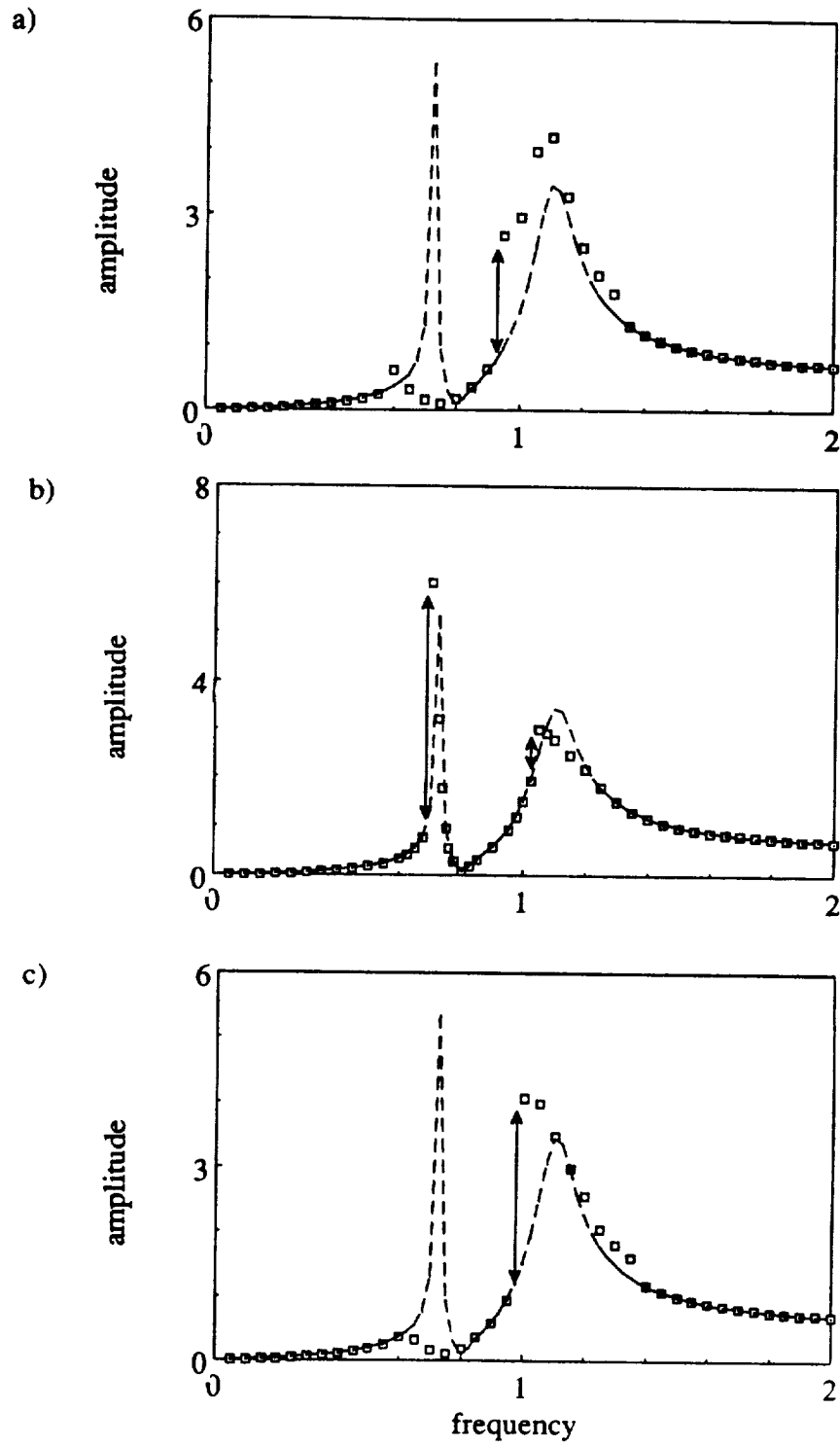
119

Figure 3.9. p_a versus Ω_h plots for the case of coupled modes: a) no backlash, non-
linear bearings, b) backlash, linear bearings, c) backlash, non-linear
bearings; — — — — corresponding linear response.

120

simultaneously in the dynamic model.

3.4.5. Internal versus External Excitation

Here we will apply only one type of excitation at a time and compare frequency response characteristics of the system due to sinusoidal excitations $\{F(t)\}_i$ and $\{F(t)\}_e$ in equation (3.3a). Here, only the bearing non-linearity will be considered assuming no tooth separation, $b_h=0$. In the case of internal excitation, amplitude of alternating component is dependent on Ω_h^2. Conversely, the amplitude of alternating external force is frequency independent. Therefore, for a constant force ratio F_{ai}/F_m, i=h,T, the overall amplitude ratio $\Omega_h^2 F_{ah}/F_m$ for internal excitation varies with excitation frequency whereas the overall amplitude ratio F_{aT}/F_m for external excitation remains constant similar to the single degree of freedom model of Chapter II.

Figures 3.10a and 3.10b compare y_{g2a} versus Ω and p_a versus Ω spectra for $\Omega_t=\Omega_h=\Omega$, $F_m=1.0$, $F_{aT}=F_{ah}=0.5$, $F_{b2}=0$, $\zeta_{22}=0.01$, $\zeta_{23}=0.0125$, $\zeta_{33}=0.05$ and $\kappa_{22}=\kappa_{23}=0.25$. As shown Figures 3.10a and 3.10b, both excitations yield the same values at $\Omega=1.0$ since $F_m/F_{aT}=F_m/\Omega^2 F_{ah}$ at $\Omega=1.0$. For $\Omega>1$ the internal excitation gives larger amplitudes than the external excitation, but the converse is true for $\Omega<1$. Another important difference is that for increasing Ω, there are two jumps (a jump-up from the no-impact regime to the double sided impact regime at $\Omega=0.3$ and a jump-down from the double sided to the single sided impact regimes at $\Omega=0.4$) for the external excitation; but the double sided impact regime is not seen in the internal excitation case and only one jump from the no-impact to the single sided impact is found at $\Omega=0.35$.
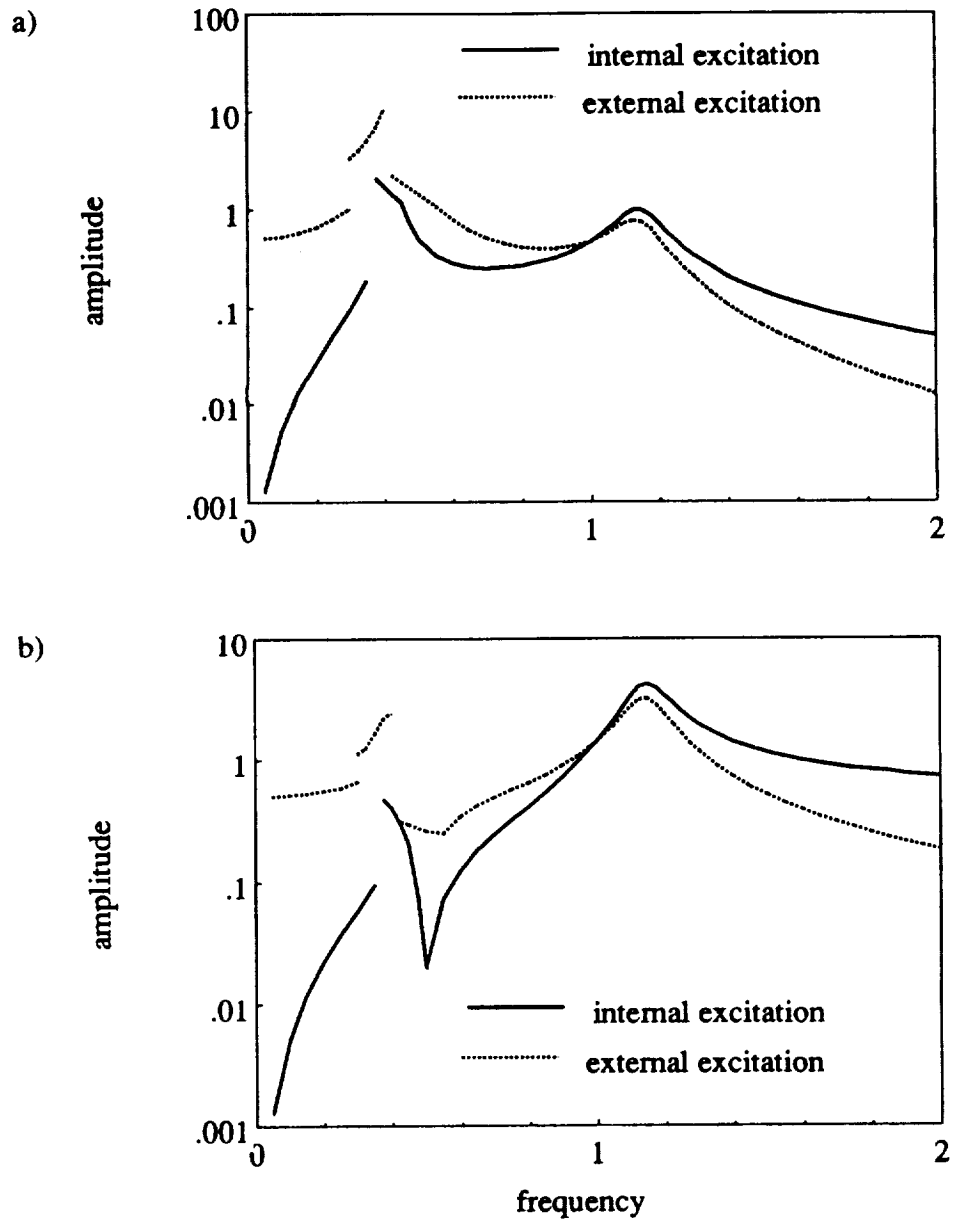
Figure 3.10. Comparison of frequency responses due to internal static transmission error and external torque excitation; $F_m=1.0$, $F_{ah}=0.5$, $F_{b2}=0$, $b_h=0$, $b_{b2}=b_c$, $\zeta_{33}=0.05$, $\zeta_{23}=0.0125$, $\zeta_{22}=0.01$, $\hat{k}=1$; a) y_{g2a} versus Ω_h, b) p_a versus Ω_h.

3.5. THREE DEGREE OF FREEDOM SYSTEM STUDIES

3.5.1. Classification of Steady State Solutions

The steady state response results excited by internal force $\{F(t)\}_i$ at each frequency Ω_h have been categorized into the following five groups: (i) harmonic or nearly harmonic solution at the same period $t_p=2\pi/\Omega_h$ as that of forcing function (period-one), (ii) non-harmonic period-one solution, (iii) subharmonic solution with period nt_p, $n>1$, (iv) quasi-periodic solution, and (v) chaotic solution (non-periodic, $n \rightarrow \infty$). The solution classification criteria are based on time histories, phase plane plots, Poincare maps and Fourier spectra [66-71]. Figures 3.11 through 3.15 illustrate different types of steady state solutions obtained from the three degree of freedom non-linear model of Figure 3.2a. As shown in Figure 3.11, period-one, non-harmonic solutions have a non-circular (non-elliptic) phase plane plot and repeat themselves at t_p. Figure 3.12 shows the time histories, phase plane plots and Poincare maps for a $2t_p$ subharmonic solution. In this case, the Poincare map consists of two discrete points. Similarly, the $6t_p$ (ultra)subharmonic response has six points on the Poincare map as shown in Figure 3.13. Figure 3.14 illustrates a typical quasi-periodic response (combination oscillations) which consists of two or more "incommensurate" frequencies [66,67]. Quasi-periodic solutions result in closed orbits on the Poincare map as shown in Figure 3.14c. The chaotic responses which are defined by a non-periodic time history and as many points as the number of cycles considered in the analysis on the Poincare map are illustrated in Figure 3.15. Figures 3.16a-e show the FFT spectra corresponding to the time histories given in Figures 3.11 to 3.15. For period-one non-harmonic solution of Figure 3.11, corresponding spectrum has peaks at $m\omega$ where ω is the fundamental frequency and m is a positive integer, as shown in Figure 3.16a. The nt_p subharmonic solutions contain peaks at the frequencies $m\omega/n$.

123

For instance, spectra of the $2t_p$ and $6t_p$ solutions of Figures 3.12 and 3.13 have peaks at frequencies $m\omega/2$ and $m\omega/6$ respectively in Figures 3.16b and 3.17a. The quasi-periodic solution of Figure 3.14 consists of two fundamental frequencies ω_1 and ω_2 at a ratio $\omega_1/\omega_2 \approx 8$ (an irrational number) and there are peaks at the combination frequencies $m\omega_1 + r\omega_2$, $m,r = 0, \pm 1, \pm 2....$. Finally, a characteristic broad band spectrum is obtained in Figure 3.18 when the solution as shown in Figure 3.15 is chaotic.

3.5.2. Routes to Chaos

In Chapter II, we had investigated the effect of mean load F_m and damping ζ on chaotic response of a gear pair. It has been shown that chaos typically exists in lightly damped and lightly loaded gear pairs. Now, two different routes to chaos for the three degree of freedom system are illustrated.

A. Period-Doubling Route to Chaos : This consists of a sequence of bifurcations of the periodic response to another periodic response with twice the period of the original response due to a change in one of the system parameters [66, 68-70]. Figures 3.19 to 3.23 demonstrates this with a change in excitation frequency Ω_h given $F_m=0.1$, $F_{ah}=0.05$, $F_{bi}=0$ $i=1,2$, $\zeta_{11}=\zeta_{22}=0.01$, $\zeta_{13}=\zeta_{23}=0.0125$, $\zeta_{33}=0.05$, $\kappa_{11}=\kappa_{22}=1.25$, $\kappa_{13}=\kappa_{23}=0.25$, $b_c=b_h$ and $b_{bi}=0$, $i=1,2$. At $\Omega_h=1.500$, with zero initial conditions, we note a t_p harmonic solution in Figure 3.19. This t_p solution bifurcates to $2t_p$ subharmonic solution in Figure 3.20 when Ω_h is reduced to $\Omega_h=1.48$. Furthermore at $\Omega_h=1.44$ a $4t_p$ solution is obtained which is further transformed to a $8t_p$ response at $\Omega_h=1.402$ as shown in Figures 3.21 and 3.22 respectively. At $\Omega_h=1.4$, however the steady state solution becomes chaotic as evident from Figure 3.23. Also note from
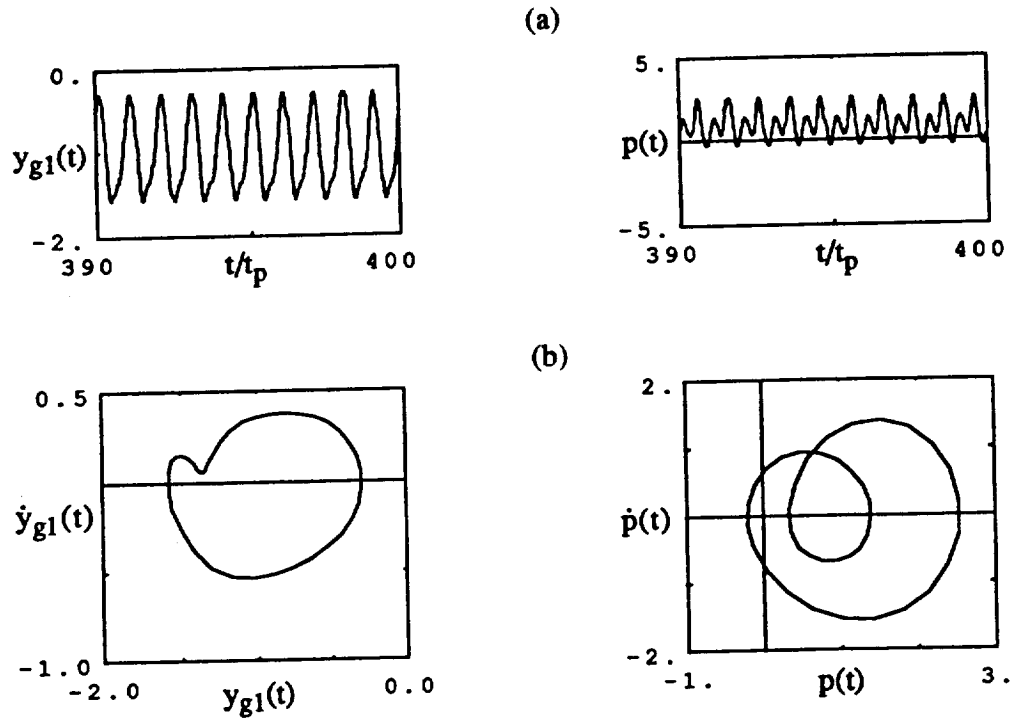
124

(a)

(b)

Figure 3.11. A non-harmonic period-one response; $F_m=1.0$, $F_{ah}=0.5$, $F_{b2}=0$, $b_h=0$, $b_{b2}=b_c$, $\zeta_{33}=0.05$, $\zeta_{13}=\zeta_{23}=0.0125$, $\zeta_{11}=\zeta_{22}=0.01$, $\hat{k}=5$, $\Omega_h=0.6$; a) time histories, b) phase plane plots.
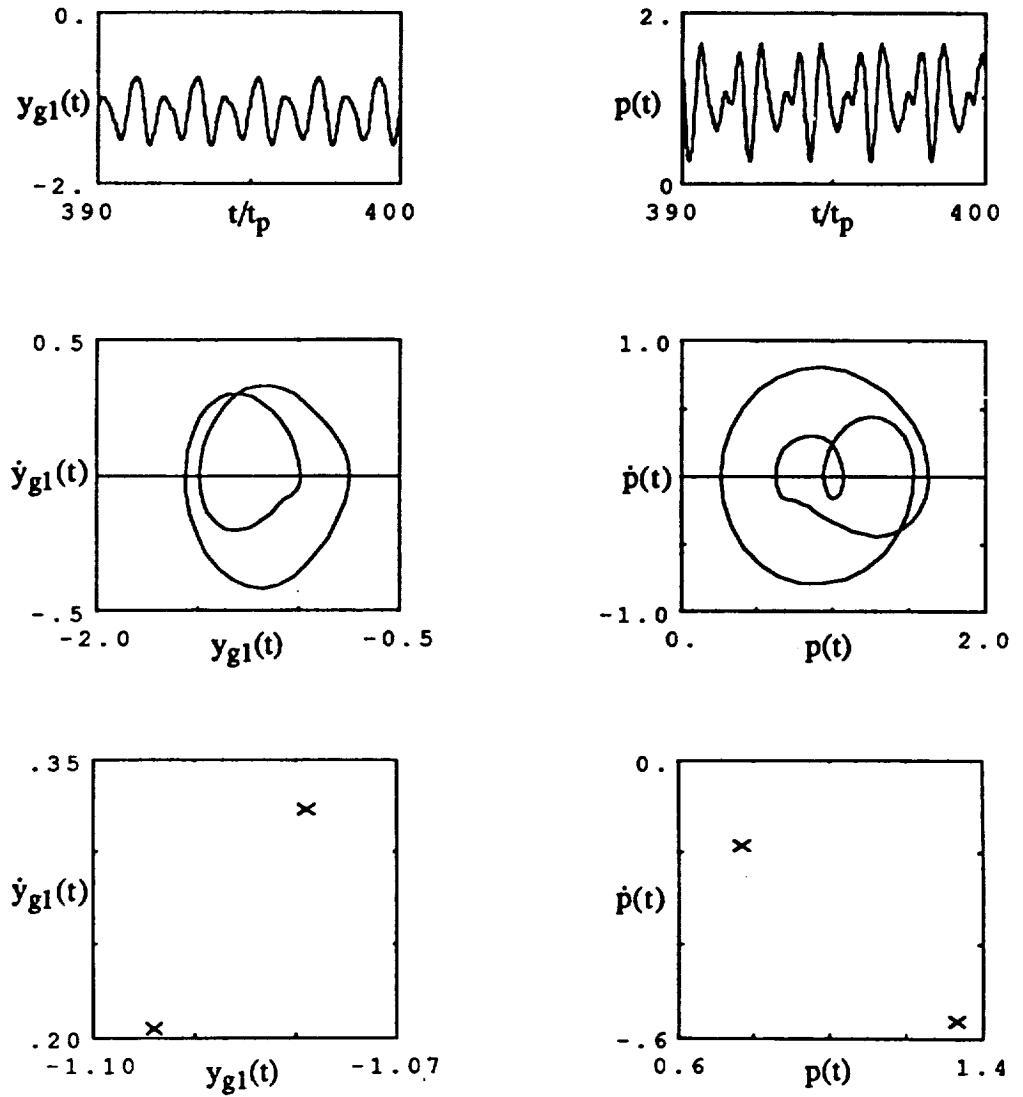
Figure 3.12.   A period-two subharmonic response; $F_m=1.0$, $F_{ah}=0.5$, $F_{b2}=0$, $b_h=0$, $b_{b2}=b_c$, $\zeta_{33}=0.05$, $\zeta_{13}=\zeta_{23}=0.0125$, $\zeta_{11}=\zeta_{22}=0.01$, $\hat{k}=5$, $\Omega_h=0.85$.
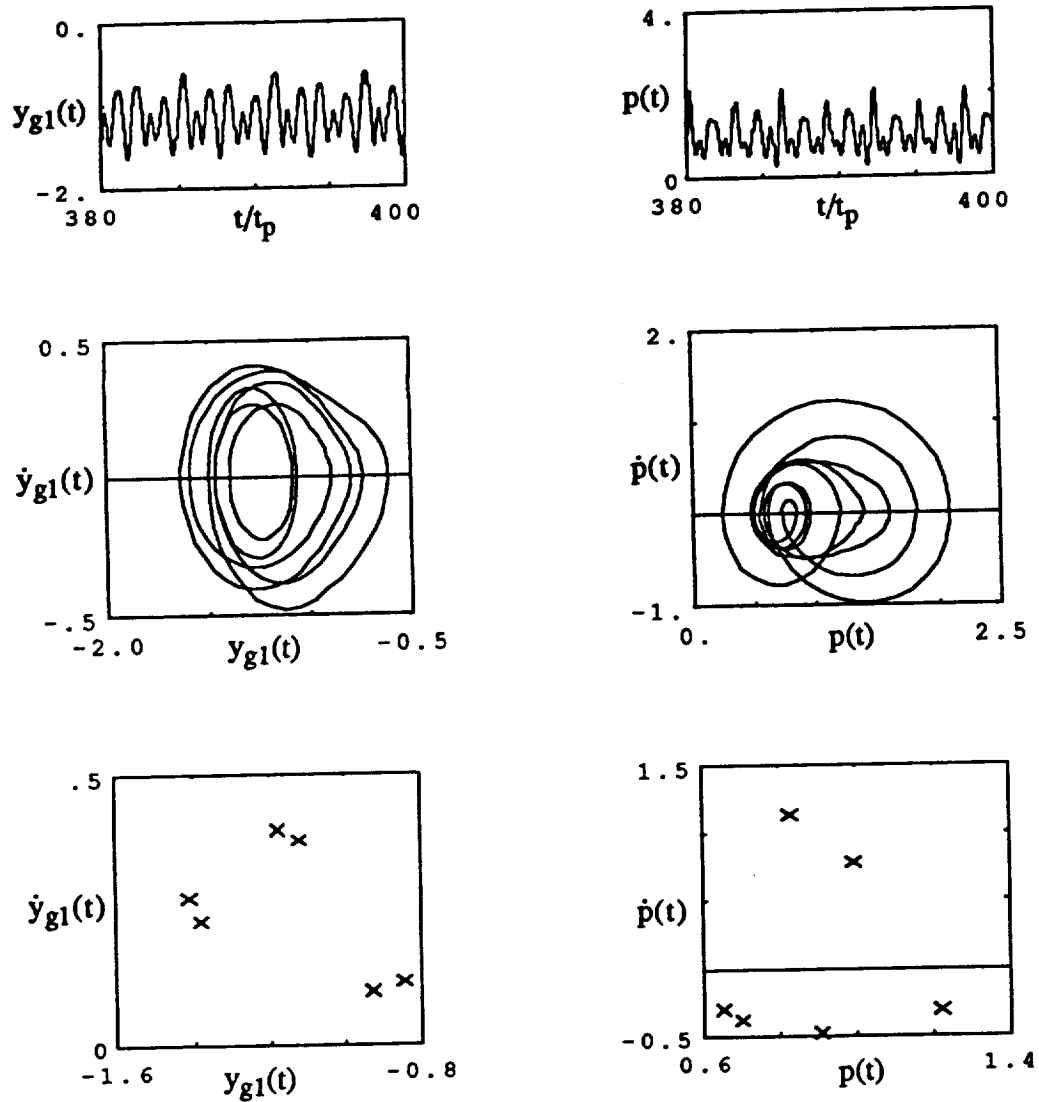
Figure 3.13.   A period-six (ultra)subharmonic response; F_m=1.0, F_{ah}=0.5, F_{b2}=0, b_h=0, b_{b2}=b_c, ζ_{33}=0.05, ζ_{13}=ζ_{23}=0.0125, ζ_{11}=ζ_{22}=0.01, $\hat{k}$=5, Ω_h=1.0.
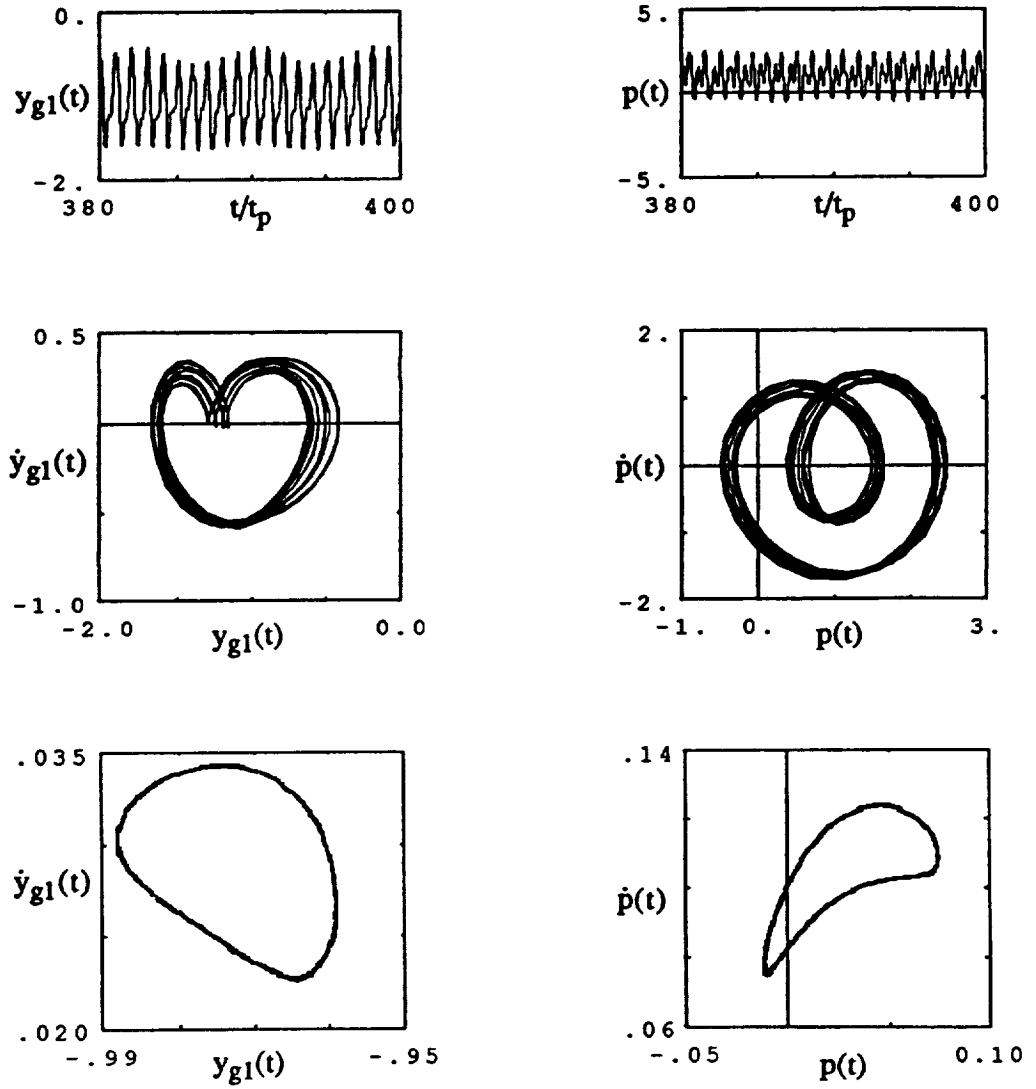
Figure 3.14. A quasi-periodic response; $F_m=1.0$, $F_{ah}=0.5$, $F_{b2}=0$, $b_h=0$, $b_{b2}=b_c$, $\zeta_{33}=0.05$, $\zeta_{13}=\zeta_{23}=0.0125$, $\zeta_{11}=\zeta_{22}=0.01$, $\hat{k}=5$, $\Omega_h=0.65$.

Figure 3.15. A chaotic response; $F_m=1.0$, $F_{ah}=0.5$, $F_{b2}=0$, $b_h=0$, $b_{b2}=b_c$, $\zeta_{33}=0.05$, $\zeta_{13}=\zeta_{23}=0.0125$, $\zeta_{11}=\zeta_{22}=0.01$, $\hat{k}=5$, $\Omega_h=0.85$.
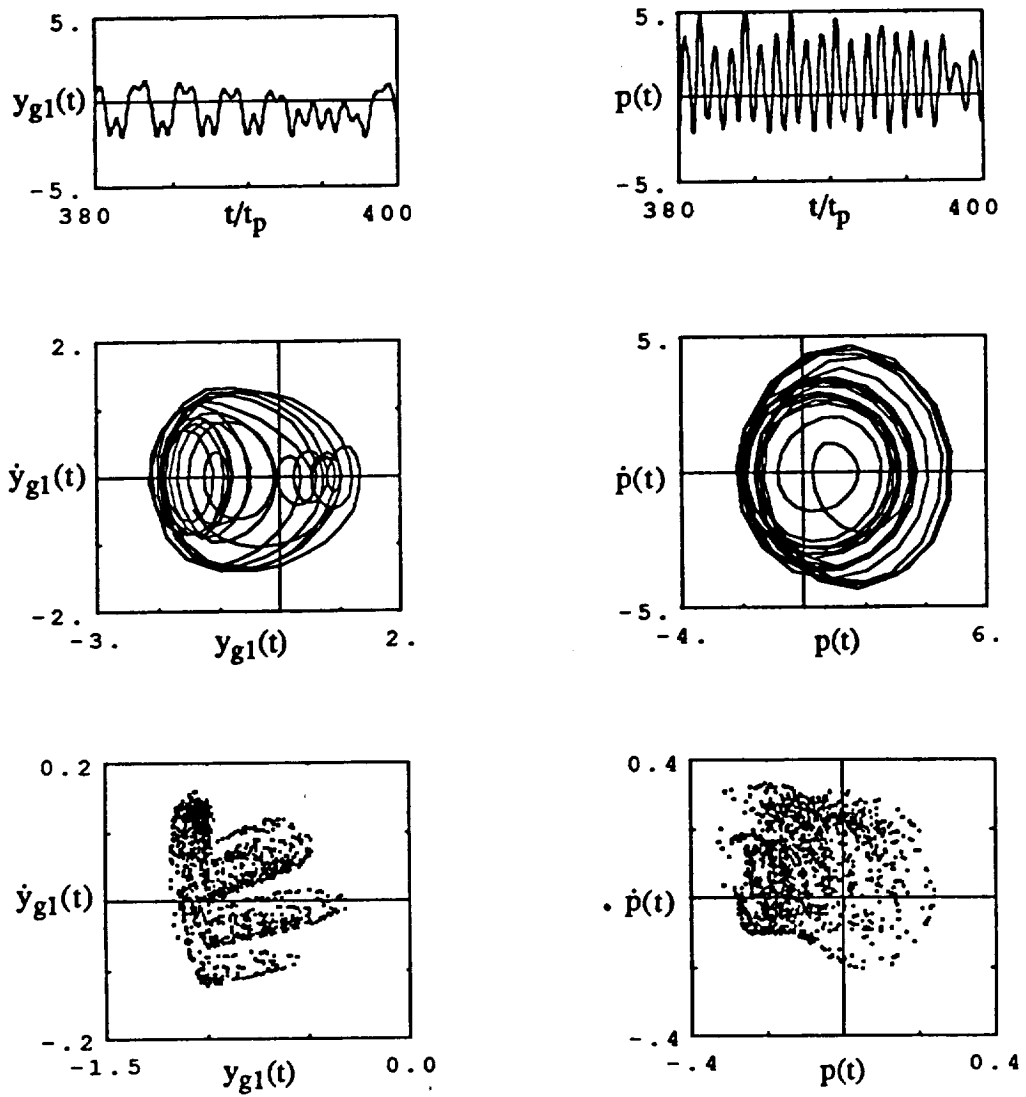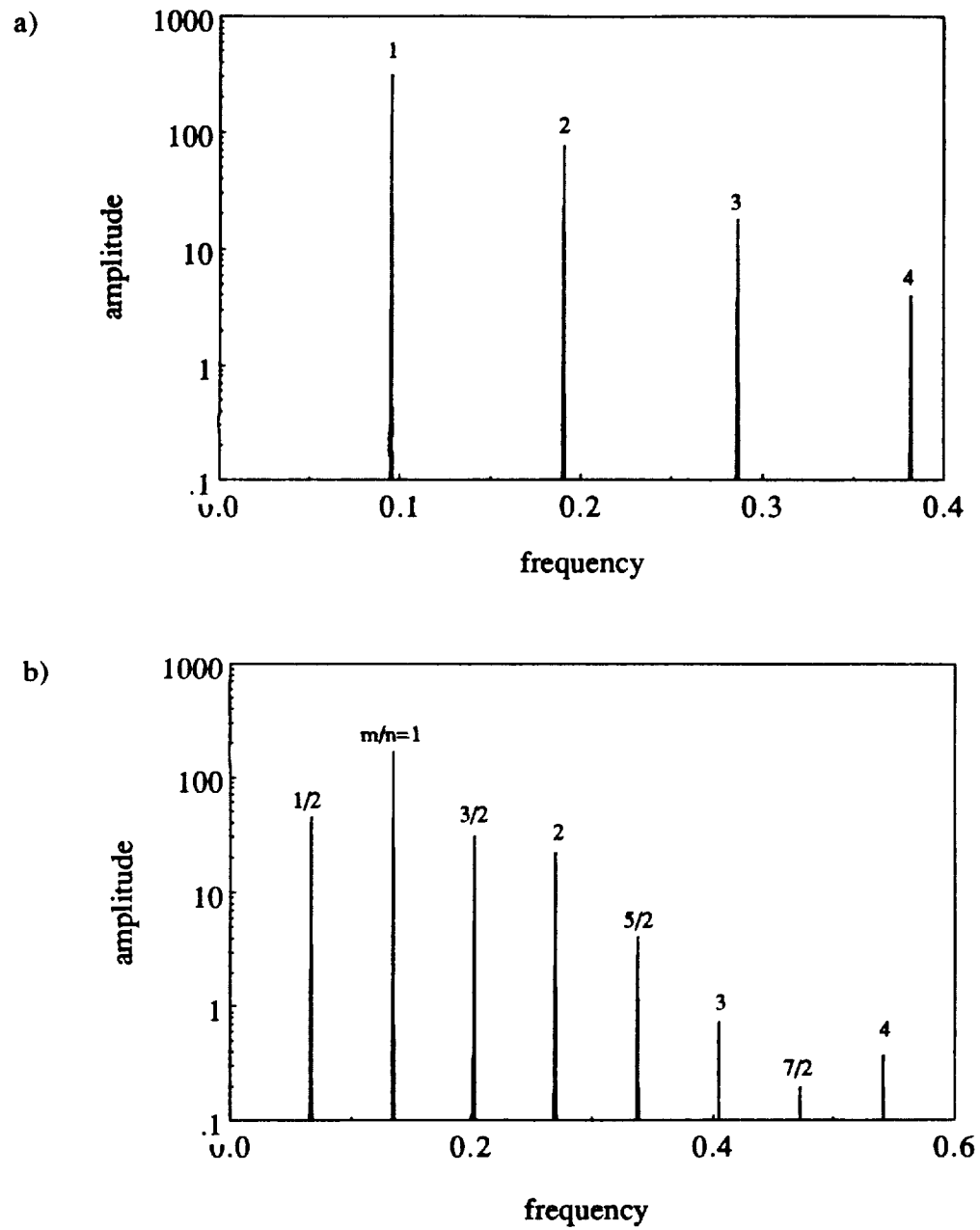
Figure 3.16. FFT spectra of $y_{g2}(t)$ for the responses given in Figures 3.11 to 3.12 a) period-one, b) period -two.
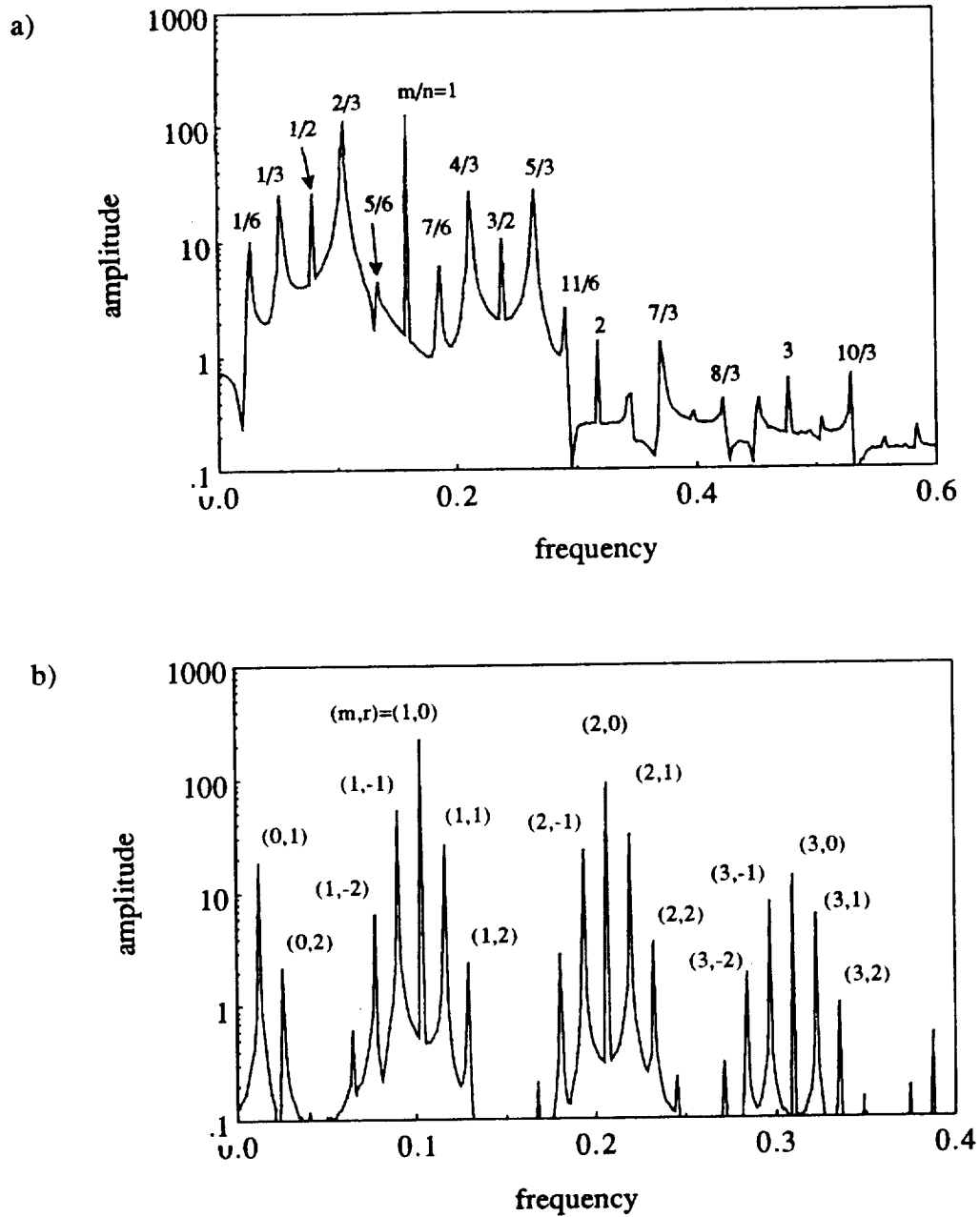
130

Figure 3.17. FFT spectra of $y_{g2}(t)$ for the responses given in Figures 3.13 to 3.14 a) period-six, b) quasi-linear.
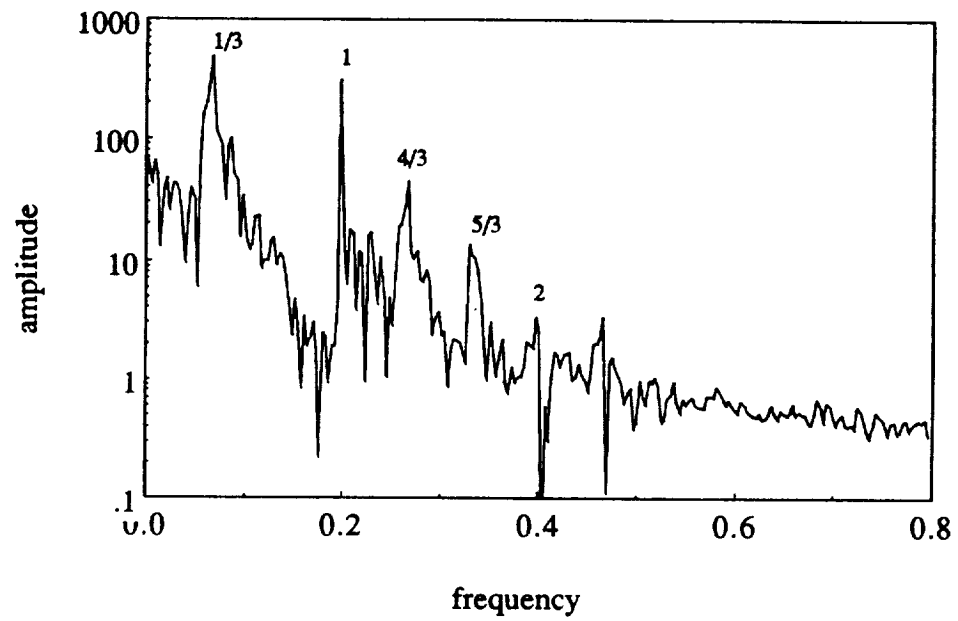
131

Figure 3.18. FFT spectra of $y_{g2}(t)$ for the chaotic response given in Figure 3.15

132

spectra of Figures 3.19 to 3.23 that the single peak spectrum is transformed to a broad band spectrum corresponding to chaos through period-doubling.

B. Quasi-periodic Route to Chaos: In this case, instead of going through the period doubling, the response undergoes a sequence of Hopf bifurcations with a change in a system parameter. First a quasi-periodic response and finally a chaotic response are obtained [66,71]; Figures 3.24-3.27 shows such a route to chaos. $3t_p$ solution at $\Omega_h=1.1$ bifurcates to a quasi-periodic solution when Ω_h is increased to 1.2 as shown in Figure 3.24 and 3.25. A further increase in Ω_h to 1.3 yields a deformed closed orbit Poincare map as shown in Figure 3.26. It is then transformed to a chaotic strange attractor at $\Omega_h=1.4$ in Figure 3.27. Similar observations are evident from the Fourier spectra shown in Figures 3.25-3.27; the spectrum consists of combination frequencies for the quasi-periodic solution, but it finally changes to a broad band spectrum characteristic of chaos.

3.5.3. Parametric Studies

The three degree of freedom non-linear model of Figure 3.2a is used to study the effect of several system parameters such as the stiffness ratio, $\hat{k} = k_{bi} / k_h$ $i = 1,2$, radial bearing preload to mean load ratio, F_{bi}/F_m (i=1,2) and alternating load to mean load ratio F_{ab}/F_m on the non-linear dynamic behavior. A geared rotor-bearing system of one-to-one gear ratio ($v_g=1$) with $m_{gi}=1$ kg, $I_{gi}=0.0008$ kg/m^2, $d_{gi}=0.08$ m, i=1,2, and mesh stiffness $k_h=2 \times 10^8$ N/m is selected. Five percent mesh damping and one percent bearing damping values, which are somewhat realistic [72,73], are used, i.e. $\zeta_{11}=\zeta_{22}=0.01$, $\zeta_{13}=\zeta_{23}=0.0125$ and $\zeta_{33}=0.05$. Both non-linearities are considered separately in this parametric study. The case when both bearing non-linearities and
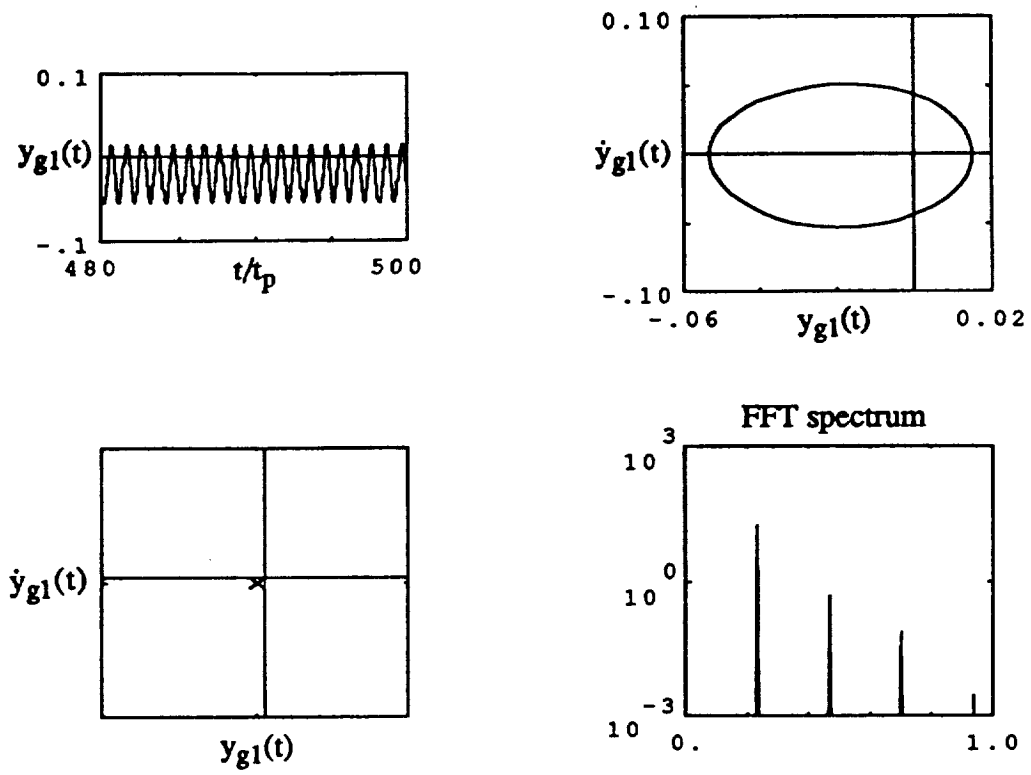
Figure 3.19. Frequency doubling route to chaos; $F_m=0.1$, $F_{ah}=0.05$, $F_{b2}=0$, $b_h=b_c$, $b_{b2}=0$, $\zeta_{33}=0.05$, $\zeta_{13}=\zeta_{23}=0.0125$, $\zeta_{11}=\zeta_{22}=0.01$, $\hat{k}=5$; period-one response at $\Omega_h=1.5$.

Figure 3.20.   Frequency doubling route to chaos; $F_m=0.1$, $F_{ah}=0.05$, $F_{b2}=0$, $b_h=b_c$, $b_{b2}=0$, $\zeta_{33}=0.05$, $\zeta_{13}=\zeta_{23}=0.0125$, $\zeta_{11}=\zeta_{22}=0.01$, $\hat{k}=5$; period-two response at $\Omega_h=1.48$.

Figure 3.21. Frequency doubling route to chaos; F_m=0.1, F_{ah}=0.05, F_{b2}=0, b_h=b_c, b_{b2}=0, ζ_{33}=0.05, ζ_{13}=ζ_{23}=0.0125, ζ_{11}=ζ_{22}=0.01, $\hat{k}$=5; period-four response at Ω_h=1.44.
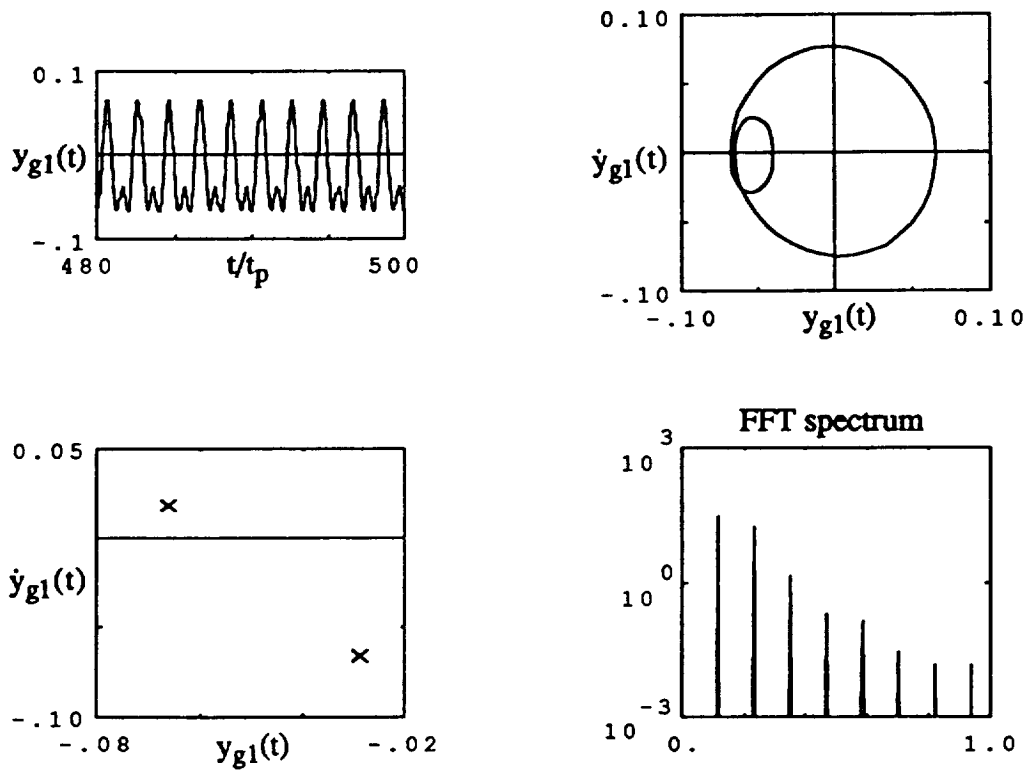
136

Figure 3.22.   Frequency doubling route to chaos; F_m=0.1, F_{ah}=0.05, F_{b2}=0, b_h=b_c, b_{b2}=0, ζ_{33}=0.05, ζ_{13}=ζ_{23}=0.0125, ζ_{11}=ζ_{22}=0.01, $\hat{k}$=5; period-eight response at Ω_h=1.402.

137

Figure 3.23.   Frequency doubling route to chaos; F_m=0.1, F_{ah}=0.05, F_{b2}=0, b_h=b_c, b_{b2}=0, ζ_{33}=0.05, ζ_{13}=ζ_{23}=0.0125, ζ_{11}=ζ_{22}=0.01, $\hat{k}$=5; chaos at Ω_h=1.4.

Figure 3.24. Quasi-periodic route to chaos; $F_m=0.1$, $F_{ah}=0.05$, $F_{b2}=0$, $b_h=b_c=0.1$, $b_{b2}=0$, $\zeta_{33}=0.05$, $\zeta_{13}=\zeta_{23}=0.0125$, $\zeta_{11}=\zeta_{22}=0.01$, $\hat{k}=1$; period three response at $\Omega_h=1.1$.
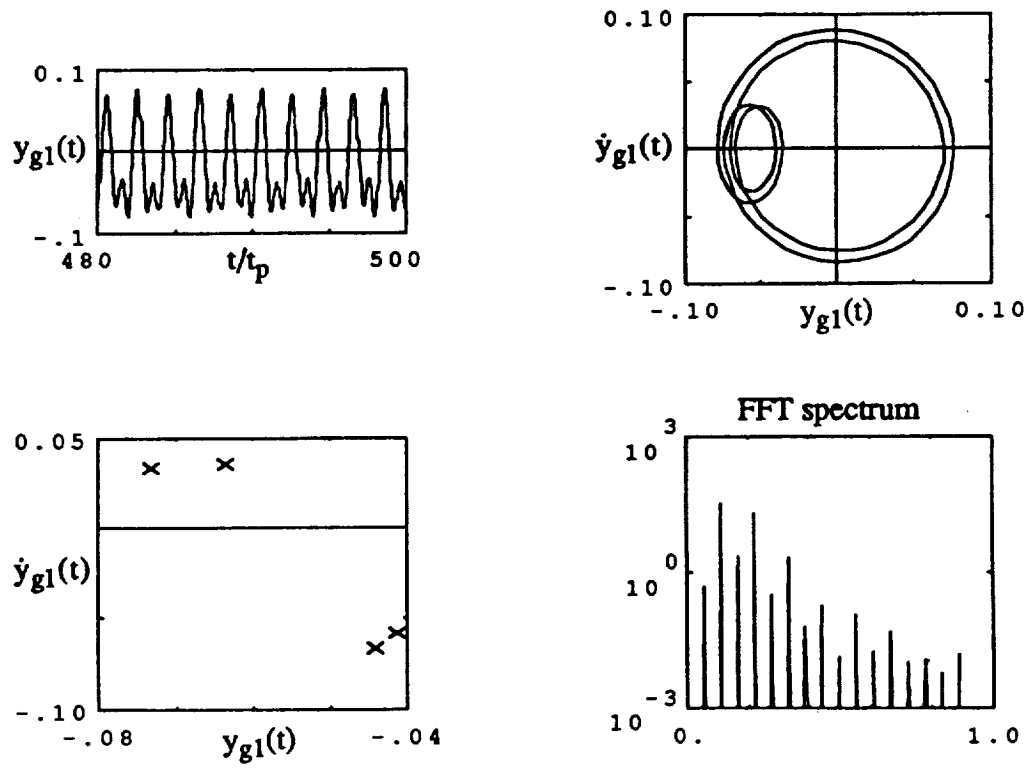
139
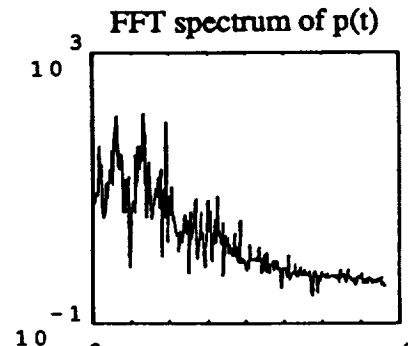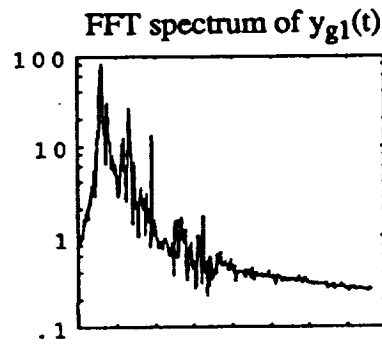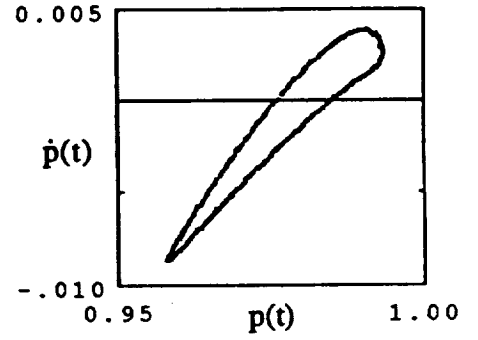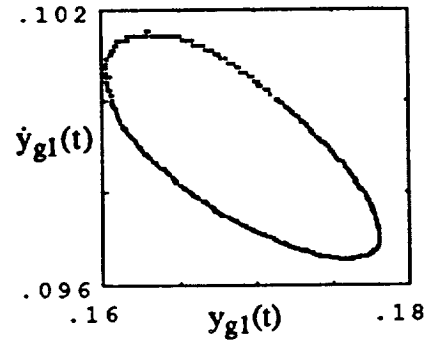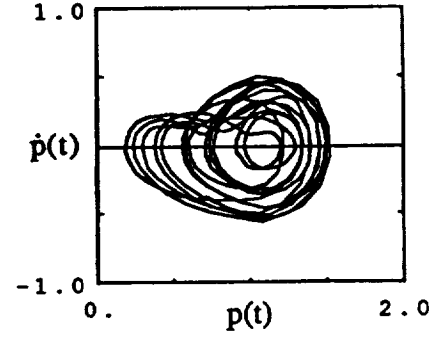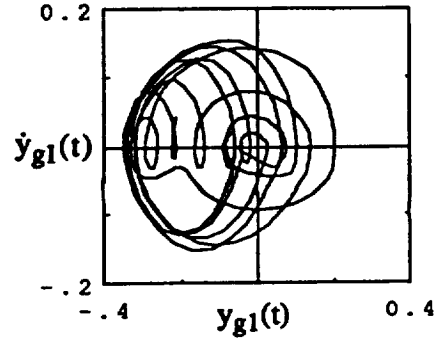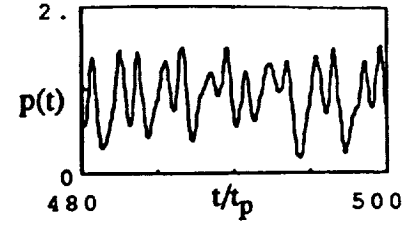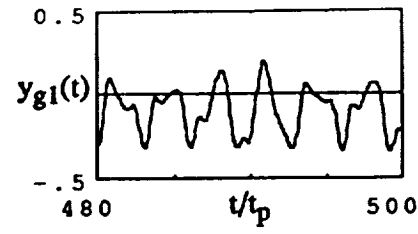
Figure 3.25. Quasi-periodic route to chaos; $F_m=0.1$, $F_{ah}=0.05$, $F_{b2}=0$, $b_h=b_c=0.1$, $b_{b2}=0$, $\zeta_{33}=0.05$, $\zeta_{13}=\zeta_{23}=0.0125$, $\zeta_{11}=\zeta_{22}=0.01$, $\hat{k}=1$; quasi-periodic response at $\Omega_h=1.2$.
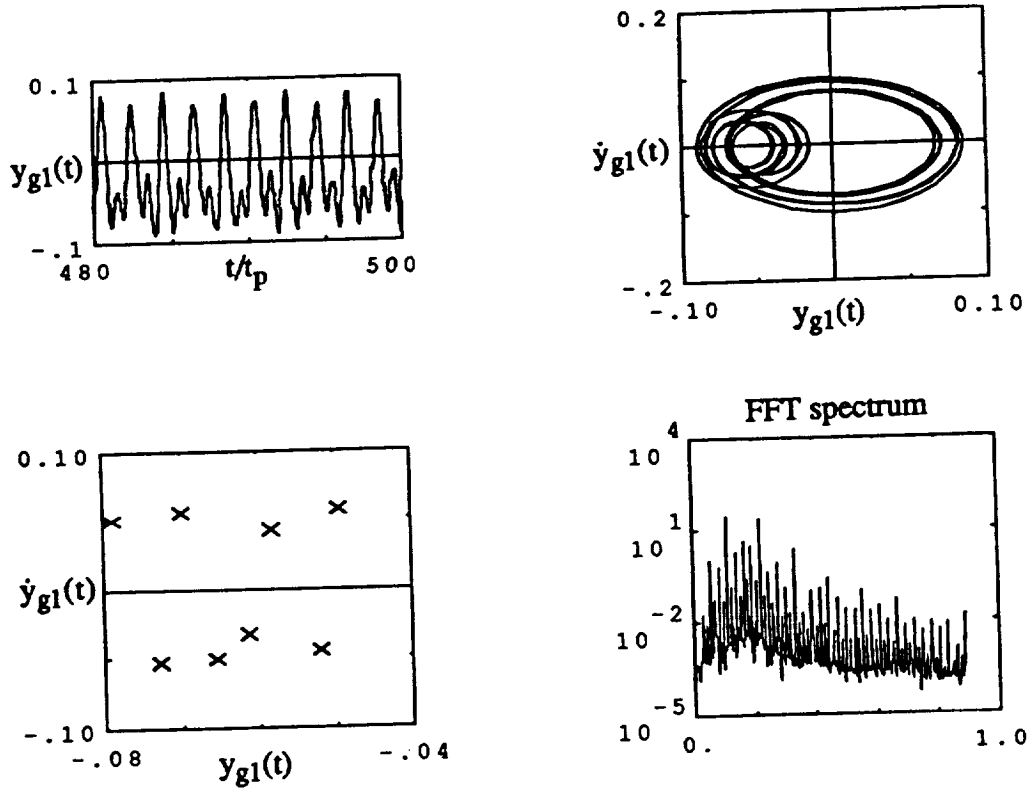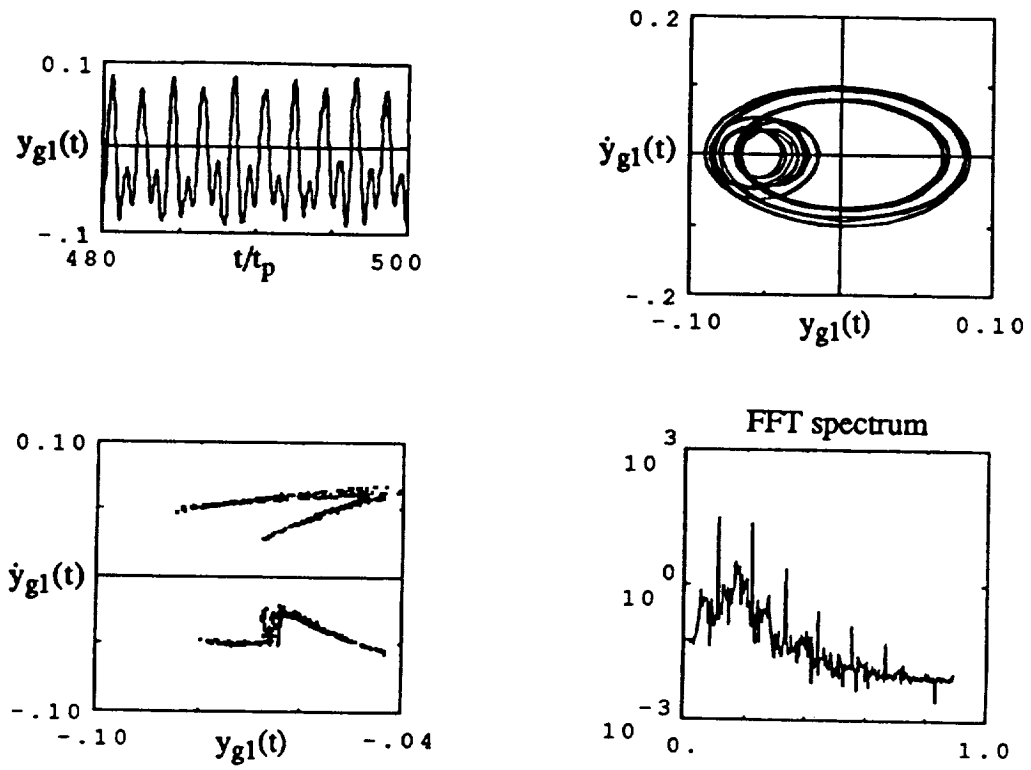
140
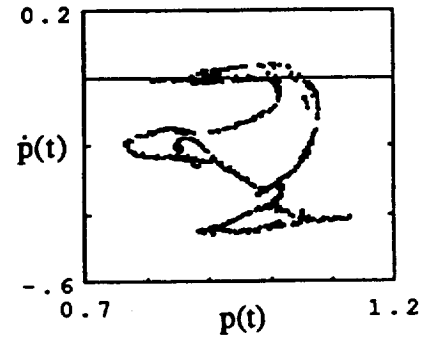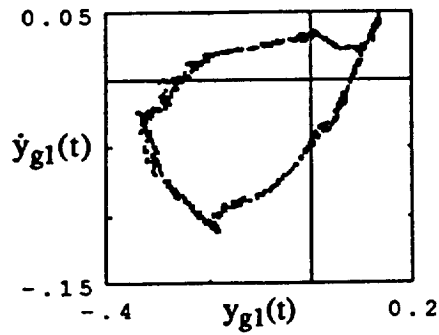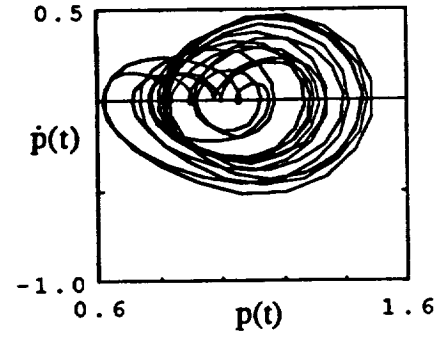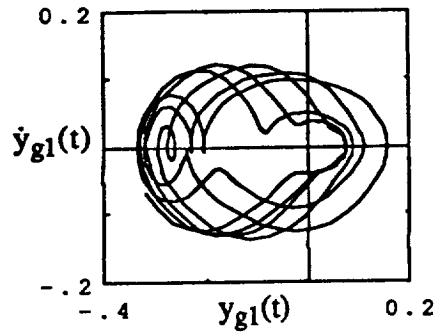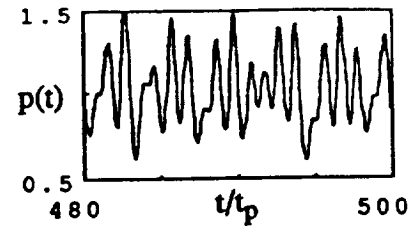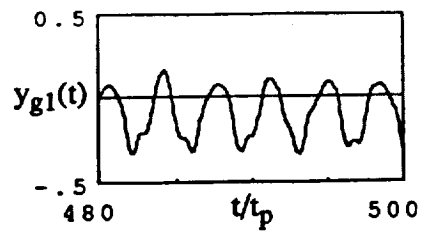
Figure 3.26. Quasi-periodic route to chaos; $F_m=0.1$, $F_{ah}=0.05$, $F_{b2}=0$, $b_h=b_c=0.1$, $b_{b2}=0$, $\zeta_{33}=0.05$, $\zeta_{13}=\zeta_{23}=0.0125$, $\zeta_{11}=\zeta_{22}=0.01$, $\hat{k}=1$; transition from quasi-periodic to chaotic response at $\Omega_h=1.3$.
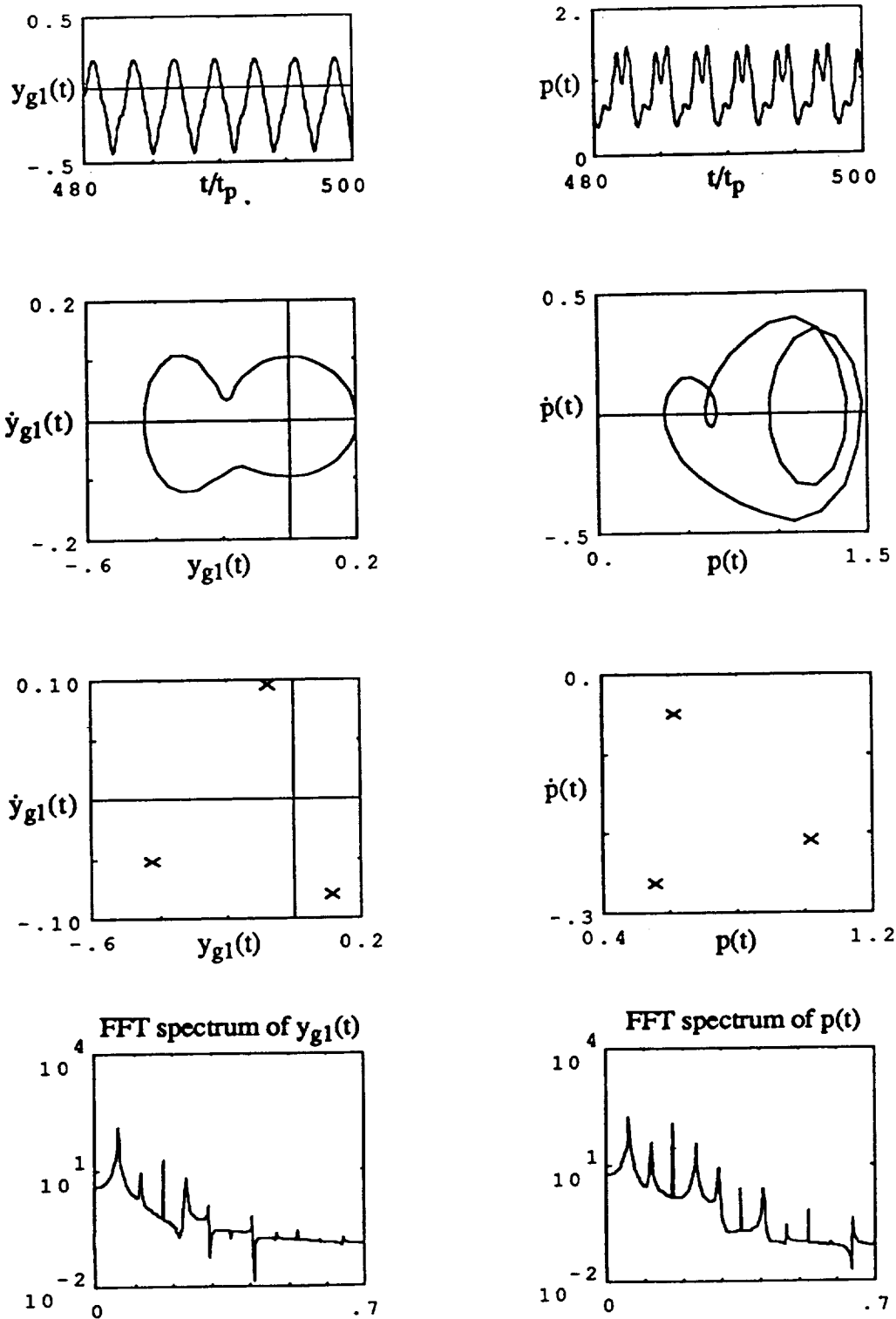
141
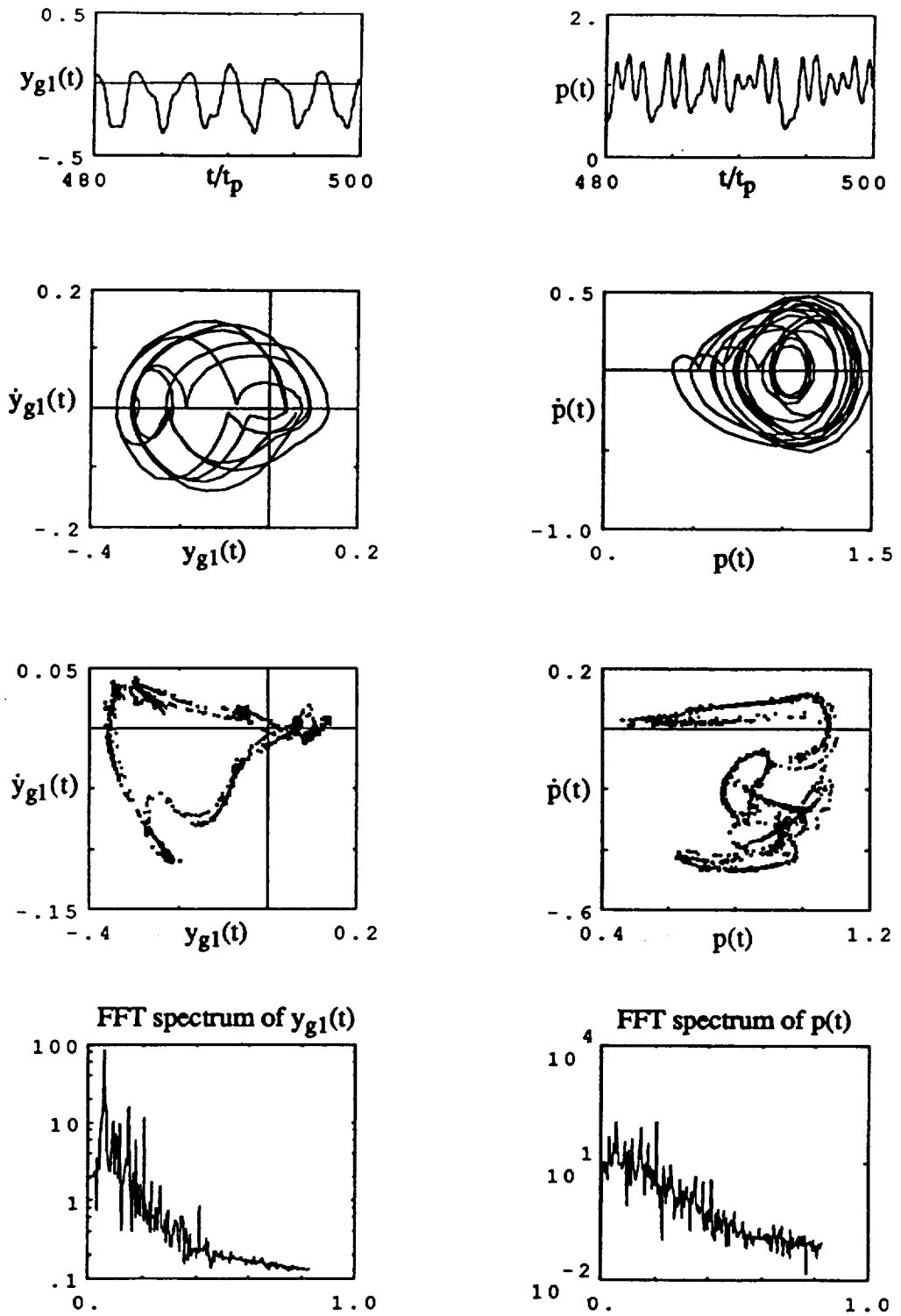
Figure 3.27. Quasi-periodic route to chaos; $F_m=0.1$, $F_{ah}=0.05$, $F_{b2}=0$, $b_h=b_c=0.1$, $b_{b2}=0$, $\zeta_{33}=0.05$, $\zeta_{13}=\zeta_{23}=0.0125$, $\zeta_{11}=\zeta_{22}=0.01$, $\hat{k}=1$; chaos at $\Omega_h=1.4$.

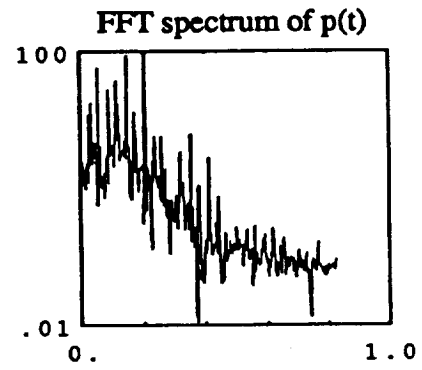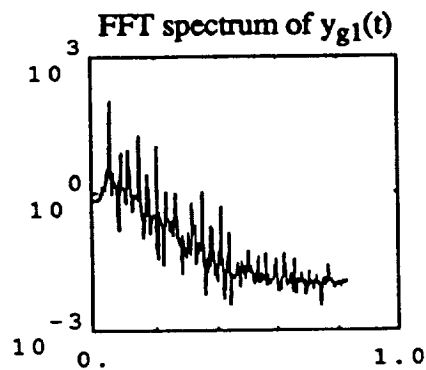backlash exist simultaneously is not considered here as it has already been examined in Section 3.4 using the two degree of freedom model.

A. Gear Backlash, Linear Bearings: For the non-linear model of Figure 3.2a with linear bearings ($b_{bi}=0$), b_h is used as the characteristic length b_c. Figures 3.28a and 3.29a show $y_{g1a}(\Omega_h)$ and $p_a(\Omega_h)$ spectra respectively for the soft bearings ($\hat{k}=1$) with $F_m=0.1$ and $F_{ah}/F_m=0.5$. Here y_{g2a} spectrum is not included since $y_{g1a}=y_{g2a}$ ($y_{g1}(t)=-y_{g2}(t)$) for a one-to-one gear ratio. As evident from Figures 3.28a and 3.29a, y_{g1a} at the first peak is larger than that seen at the second peak. Conversely, p_a is much lower at the first peak, implying that first mode is dominated by the transverse vibrations whereas the second mode is dictated by the torsional vibrations for soft bearings. This corresponds to a large dynamic bearing force $F_{dbi} \approx k_{bi}y_{gi}$, but a small dynamic transmission error ($p(t)+e(t)$) around the first natural frequency. Jump phenomenon is observed only at the second peak which is governed by the gear mesh where the excitation $e(t)$ is applied. This indicates that for $\hat{k}=1$ the modes are weakly coupled. Accordingly the gear mesh non-linearity, which forces the second peak to be non-linear, does not affect the linear characteristics of the first peak. However the modal coupling becomes stronger with an increase in $\hat{k}$ as evident from the jumps seen at both peaks in Figures 3.28b and 3.29b for $\hat{k}=5$ and Figures 3.28c and 3.29c for $\hat{k}=10$. Torsional vibrations start to dominate the first mode, and the second peak shifts upward and it may eventually move out of the operational speed range. Therefore, for a large $\hat{k}$ value associated with stiff shafts and bearings, a single degree of freedom torsional model as used in Chapter II should be sufficient. Another effect of a large $\hat{k}$ is that the nt_p subharmonic solutions replace some of the harmonic solutions as shown in Figures 3.28b,c and 3.29b,c.
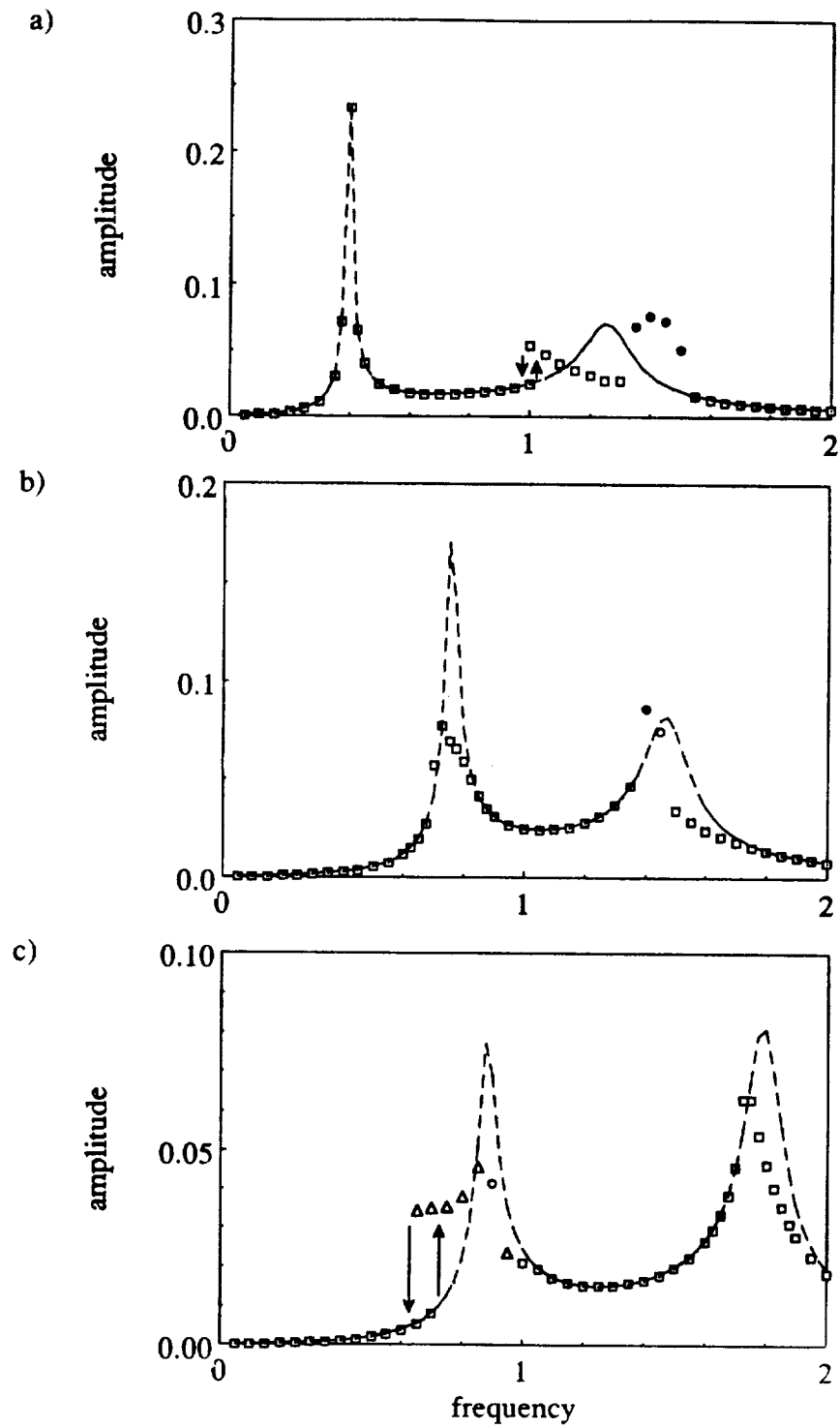
Figure 3.28. y_{gia} versus Ω_h, plots for $F_m=0.1$, $F_{ah}=0.05$, $F_{bi}=0$, $b_h=b_c=0.1$, $b_{bi}=0$, a) $k=1$, b) $k=5$, c) $k=10$; □ harmonic, △ period-one non-harmonic, o period-n subharmonic, • quasi-periodic or chaos, ————— corresponding linear response.
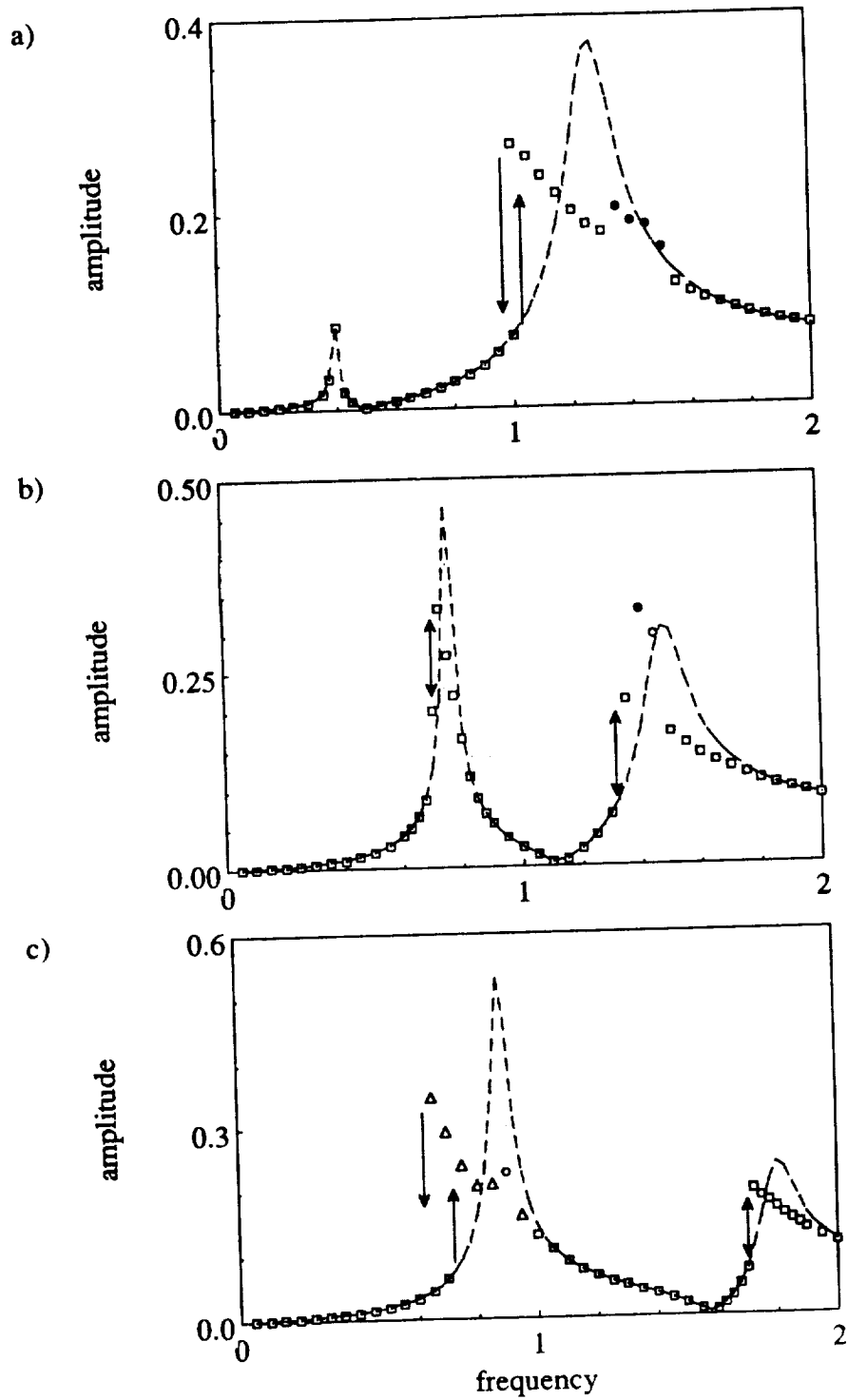
Figure 3.29. $\underset{\sim}{p}_a$ versus Ω_h, plots for $F_m=0.1$, $F_{ah}=0.05$, $F_{bi}=0$, $b_h=b_c=0.1$, $b_{bi}=0$, a) $k=1$, b) $k=5$, c) $k=10$; □ harmonic, Δ period-one non-harmonic, o period-n subharmonic, ● quasi-periodic or chaos, — — — — corresponding linear response.

145
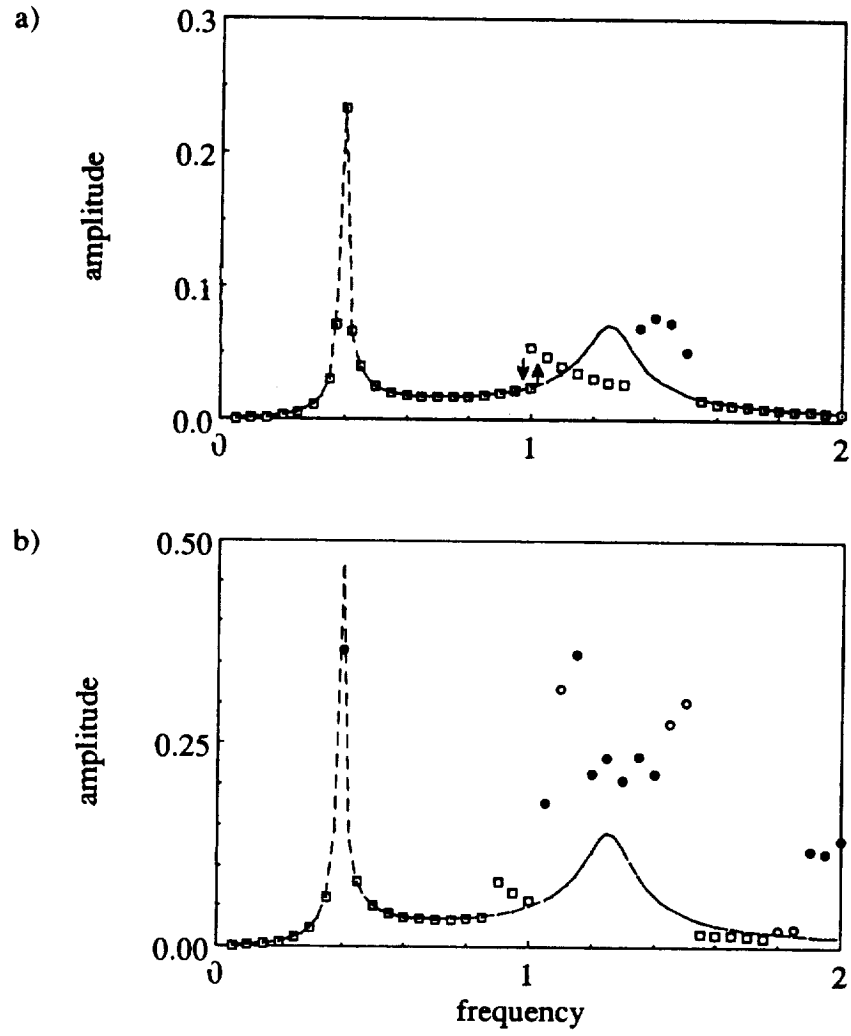
Figure 3.30. y_{gia} versus Ω_h plots for $F_m=0.1$, $F_{bi}=0$, $b_h=b_c=0.1$, $b_{bi}=0$, $\zeta_{33}=0.05$, $\zeta_{13}=\zeta_{23}=0.0125$, $\zeta_{11}=\zeta_{22}=0.01$, $k=1$; a) $F_{ah}=0.05$, b) $F_{ah}=1.0$; □ harmonic, ○ period-n subharmonic, ● quasi-periodic or chaos, – – – – corresponding linear response.

146
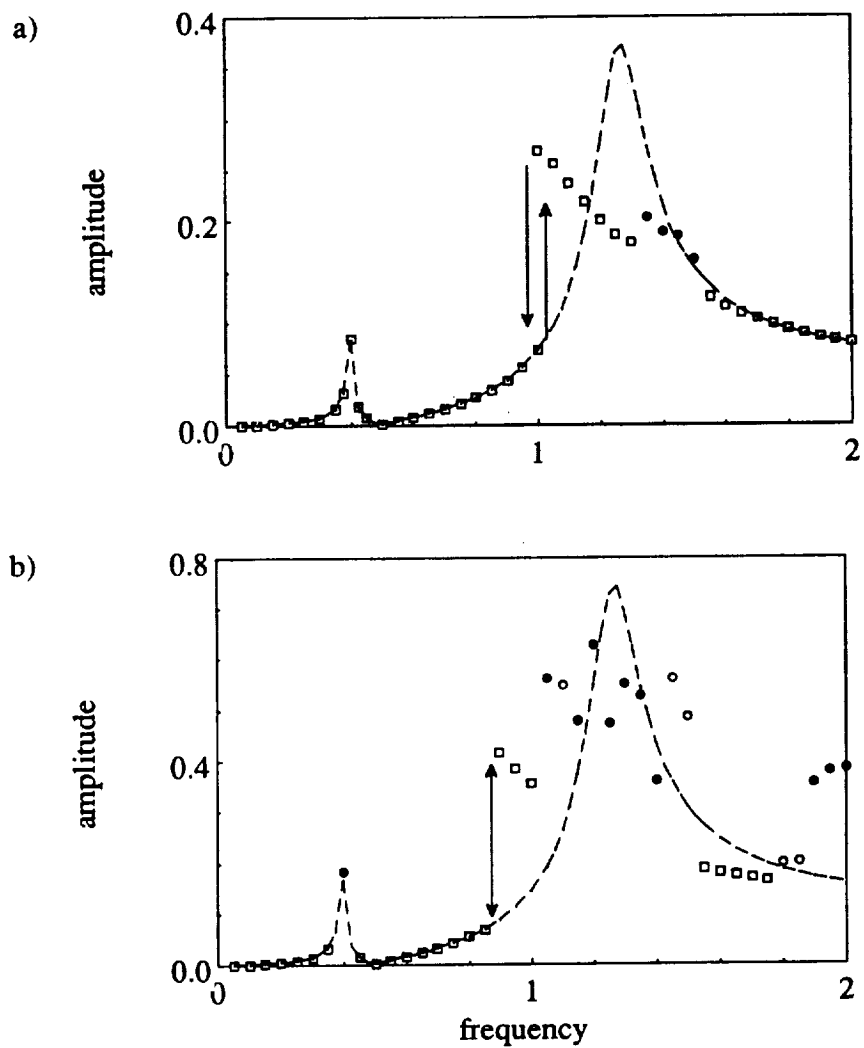
Figure 3.31. p_a versus Ω_h plots for F_m=0.1, F_{ah}=0.05, F_{bi}=0, b_h=b_c=0.1, b_{bi}=0, a) k=1, b) k=5, c) k=10; □ harmonic, o period-n subharmonic, ● quasi-periodic or chaos, −−−−− corresponding linear response.

Figures 3.30a, 3.31a and 3.30b, 3.31b examine the effect of load ratio for $F_{ah}/F_m=0.5$ and 1 respectively with $F_m=0.1$ and $\hat{k}=1$. The frequency response is well-defined and dominated by the harmonic solutions for $F_{ah}/F_m=0.5$. However when F_{ah}/F_m is increased to 1, the region beyond $\Omega_h=1.0$ becomes strongly non-linear consisting of subharmonic, quasi-periodic or chaotic responses. This was also seen for the gear pair model.

B. No Gear Backlash, Non-linear Bearings: Now consider the same system with $b_h=0$ and non-linear bearings described by the approximate model given in Sections 3.2.4. Results are presented for both roller and ball bearings separately since the radial clearance in a ball bearing is much smaller than that typically found in a roller bearing with the same inner and outer race diameters, say $b_{bi_{roller}} \approx 10 b_{bi_{ball}}$. For each case, b_{bi} is used as the characteristic length b_c.

Figures 3.32 and 3.33 show the steady state frequency response plots for the roller bearings of $b_{bi}=0.01$ mm (i=1,2), for three different $\hat{k}=k_{bi}/k_h$ values. As shown in Figures 3.32a and 3.33a for soft bearings ($\hat{k}=1$), two modes of interest are weakly coupled, and therefore the jump phenomenon is seen only at the first peak which is dictated by mostly transverse vibrations. Here, the bearing non-linearities affect the transverse displacements y_{g1} and y_{g2} which makes the first mode non-linear. The second peak is more dependent on the modal interactions. Here, again all of the solutions are purely harmonic and only no impact and single sided impact regimes exist. However, an increase in $\hat{k}$ introduces chaotic and subharmonic responses as shown in Figures 3.32b,c and 3.33b,c. For instance, all the solutions within the range $0.6<\Omega_h<1.7$ are non-harmonic for $\hat{k}=10$; the frequency response is no longer well defined and modal coupling is sufficiently strong so that jump discontinuities are

148

observed at both peaks.

A decrease in F_m/F_{ah} enhances the degree of the non-linearity as shown in Figures 3.34a,b and 3.35a,b. At $F_m/F_{ah}=1$ in Figures 3.34b and 3.35b, the responses within $0.5<\Omega_h<1.4$ are scattered and non-harmonic. However radial preloads F_{bi} on bearings should help the mean load F_m in limiting the effect of non-linearities. To prove this claim, we apply a high radial preload to both bearings, say $\overline{F}_m = \overline{F}_{bi}, i = 1,2$, corresponding to $F_{bi}=0.25$ for $F_m=1.0$ in the dimensionless form, and compare results with the previous case of $F_{bi}=0$ in Figures 3.34a,c and 3.35a,c. Figures 3.34c and 3.26c show that most of the subharmonic and chaotic solutions of Figures 3.34a and 3.35a are replaced by harmonic solutions. Hence a well defined frequency response curve with clear jump discontinuities is obtained by applying F_{bi}.

Now, replace roller bearings with ball bearings with $b_c=b_{bi}=0.001$ mm and again investigate the effect of $\hat{k} = k_{bi} / k_h$ in Figures 3.36 and 3.37. With soft bearings ($\hat{k} = 1$) the frequency response is linear (no jumps) which indicates that there are no impacts within the frequency range considered as shown in Figures 3.36a and 3.37a. However at a larger value of $\hat{k}$, double sided impact solutions appear since the clearance $2b_{bi}$ is very small. In Figures 3.36b and 3.37b for $\hat{k} = 5$, the frequency region of $0.65<\Omega_h<0.8$ consists of the double sided solutions. When $\hat{k}$ is increased to 10, the same behavior is also seen at the second peak as shown in Figure 3.36c and 3.37c. The earlier discussion on the effect of F_{ah}/F_m and F_{bi}/F_m for roller bearings is also applicable to the ball bearings as well.

3.6. EXPERIMENTAL VALIDATION

Munro's experimental dynamic transmission error results [27], which were acquired in 1962 using a four-square spur gear test rig, have been used earlier to
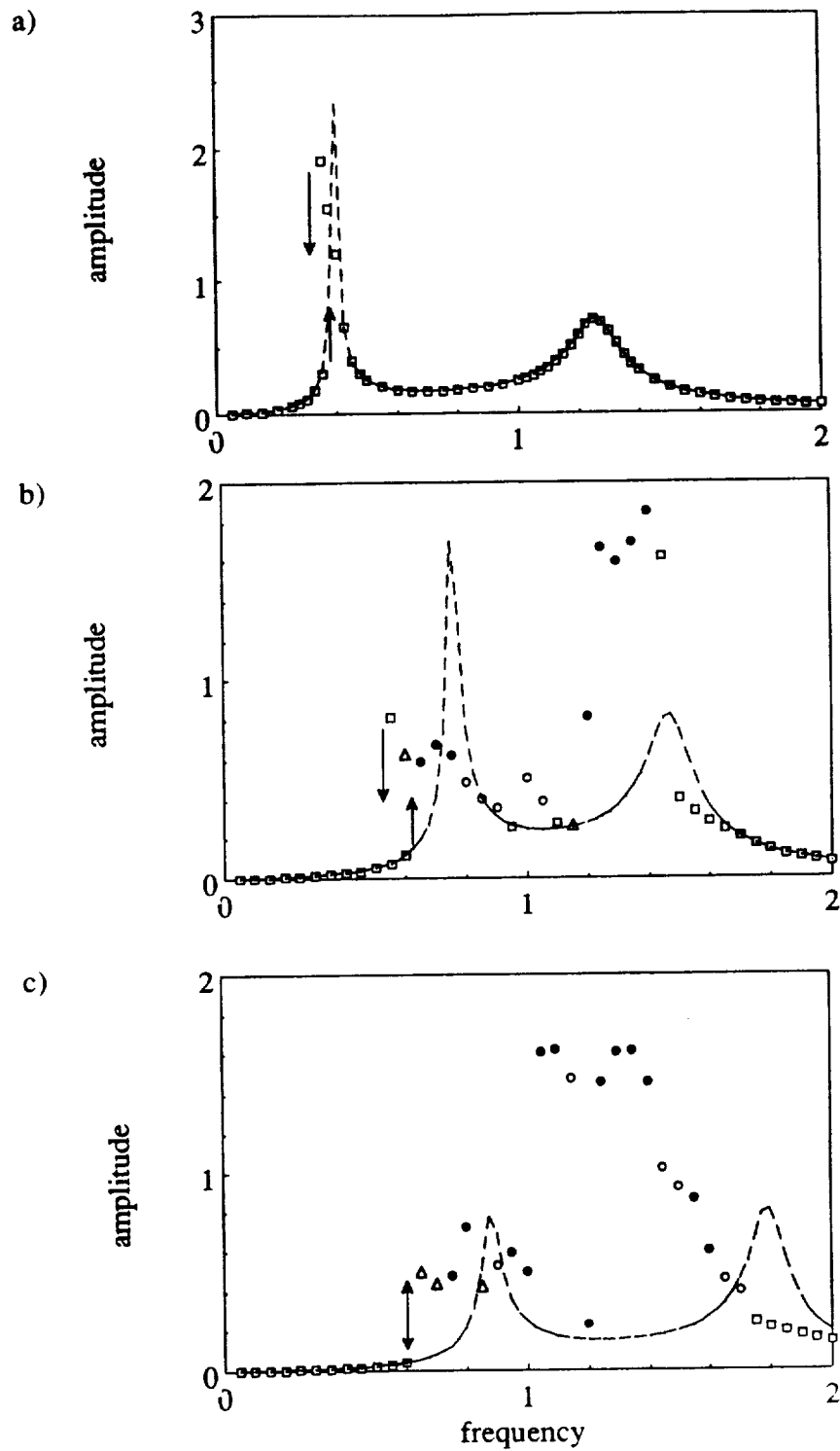
Figure 3.32. y_{gia} versus Ω_h plots for the case of roller bearings; $F_m=1.0$, $F_{ah}=0.5$, $F_{bi}=0$, $b_h=0$, $b_{bi}=b_c=0.01$mm, a) k=1, b) k=5, c) k=10; □ harmonic, △ period-one nonharmonic, o period-n subharmonic, ● quasi-periodic or chaos, −−−−− corresponding linear response.

150
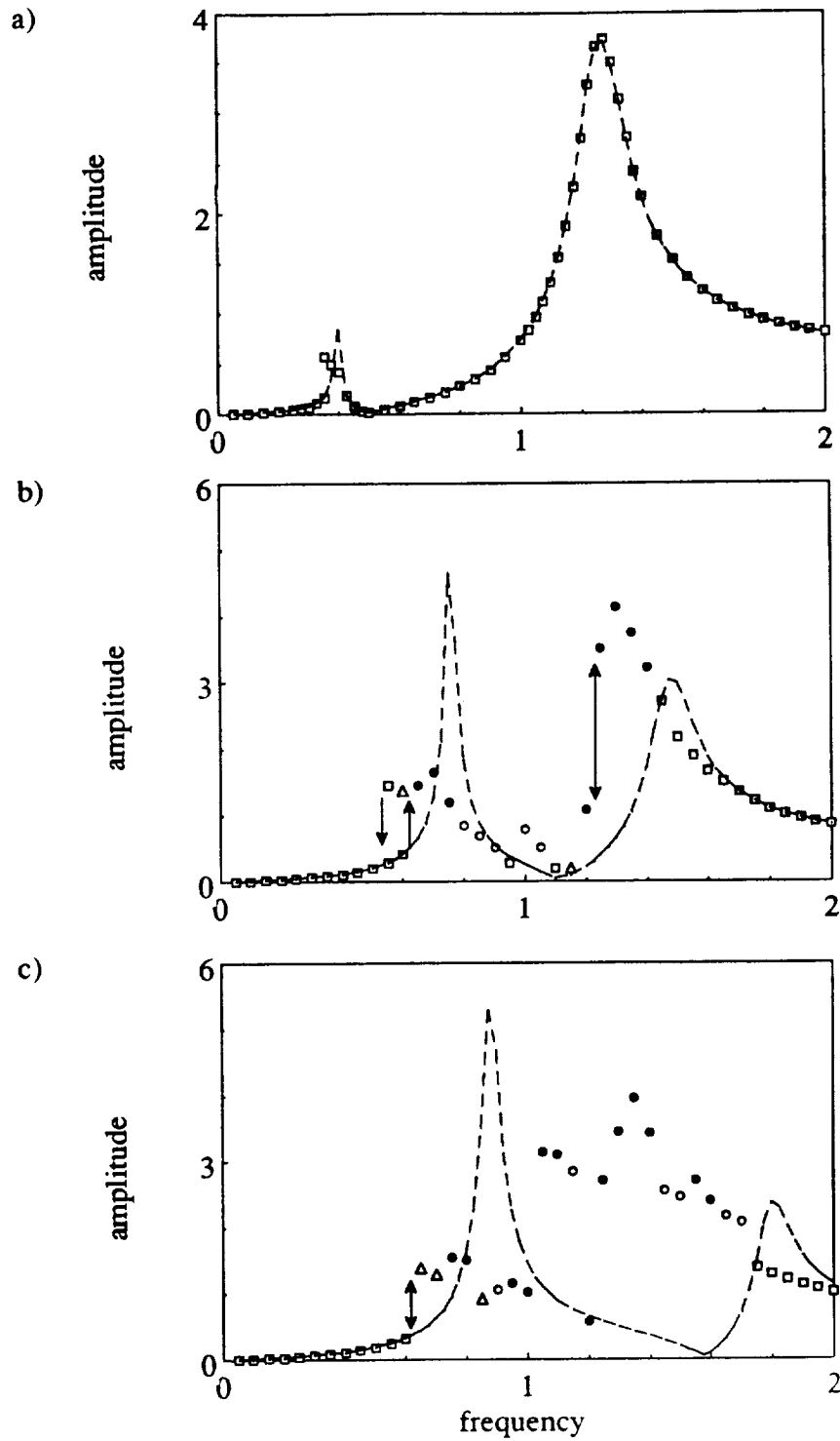
Figure 3.33. p_a versus Ω_h plots for the case of roller bearings; $F_m=1.0$, $F_{ah}=0.5$, $F_{bi}=0$, $b_h=0$, $b_{bi}=b_c=0.01$mm, a) $\hat{k}=1$, b) $\hat{k}=5$, c) $k=10$; □ harmonic, △ period-one nonharmonic, o period-n subharmonic, ● quasi-periodic or chaos, − − − − − corresponding linear response.

151

Figure 3.34. y_{gia} versus Ω_h plots for the case of roller bearings; $F_m = 1.0$, $b_h = 0$, $b_{bi} = b_c = 0.01$mm, $k = 5$; a) $F_{ah} = 0.5$, $F_{bi} = 0$, b) $F_{ah} = 0.5$, $F_{bi} = 0.25$, c) $F_{ah} = 1.0$, $F_{bi} = 0$; □ harmonic, △ period-one nonharmonic, o period-n subharmonic, ● quasi-periodic or chaos, – – – – corresponding linear response.

152

Figure 3.35. p_a versus Ω_h plots for the case of roller bearings; $F_m=1.0$, $b_h=0$, $b_{bi}=b_c=0.01\text{mm}$, $\hat{k}=5$; a) $F_{ah}=0.5$, $F_{bi}=0$, b) $F_{ah}=0.5$, $F_{bi}=0.25$, c) $F_{ah}=1.0$, $F_{bi}=0$; $\square$ harmonic, $\triangle$ period-one nonharmonic, $\circ$ period-n subharmonic, $\bullet$ quasi-periodic or chaos, —————— corresponding linear response.

153
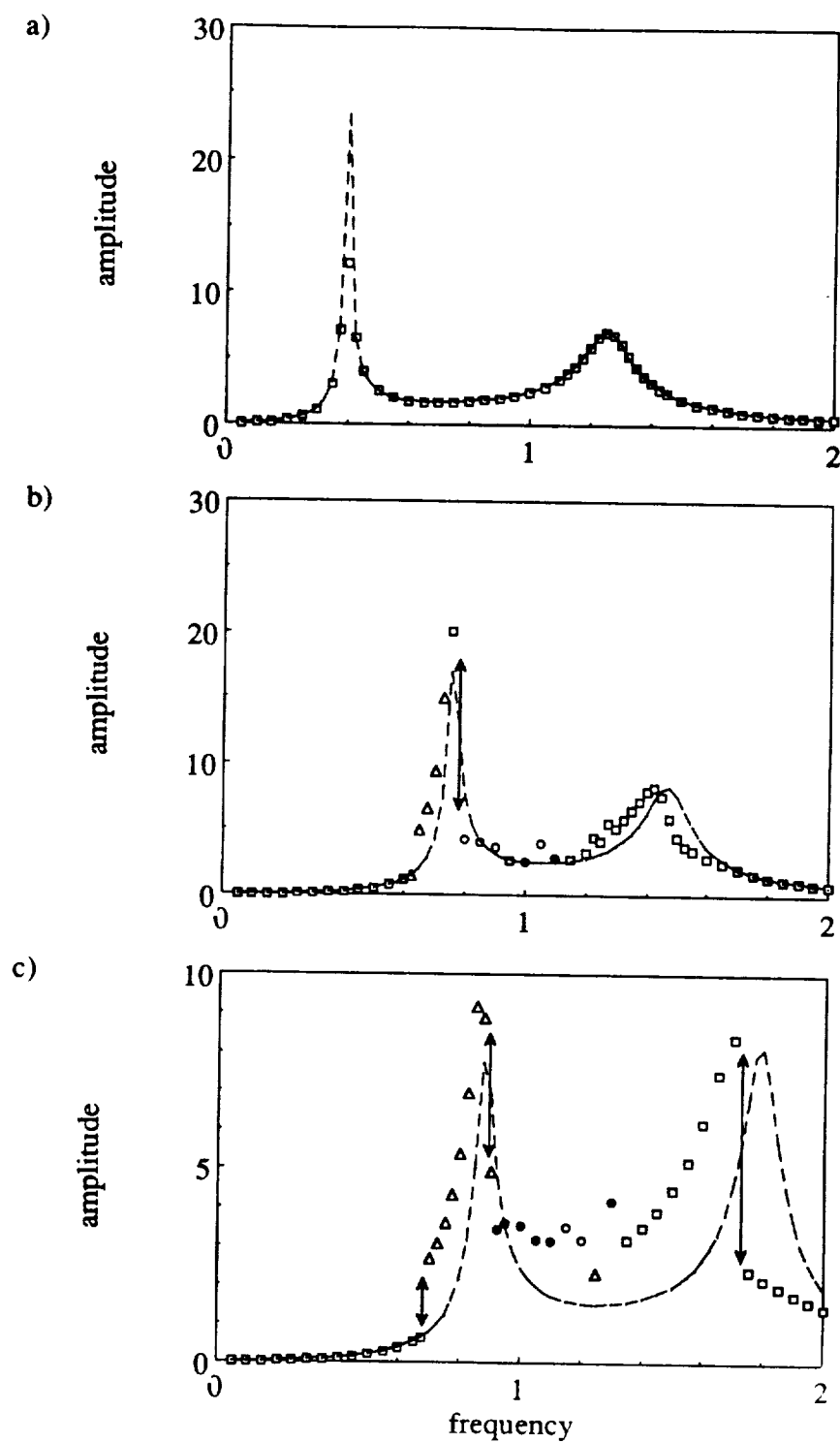
Figure 3.36. y_{gia} versus Ω_h plots for the case of deep-groove ball bearings; $F_m=10$, $F_{ah}=5$, $F_{bi}=0$, $b_h=0$, $b_{bi}=b_c=0.001mm$, a)$k=1$, b)$k=5$, c) $k=10$; $\square$ harmonic, Δ period-one nonharmonic, o period-n subharmonic, $\bullet$ quasi-periodic or chaos, $-----$ corresponding linear response.

154
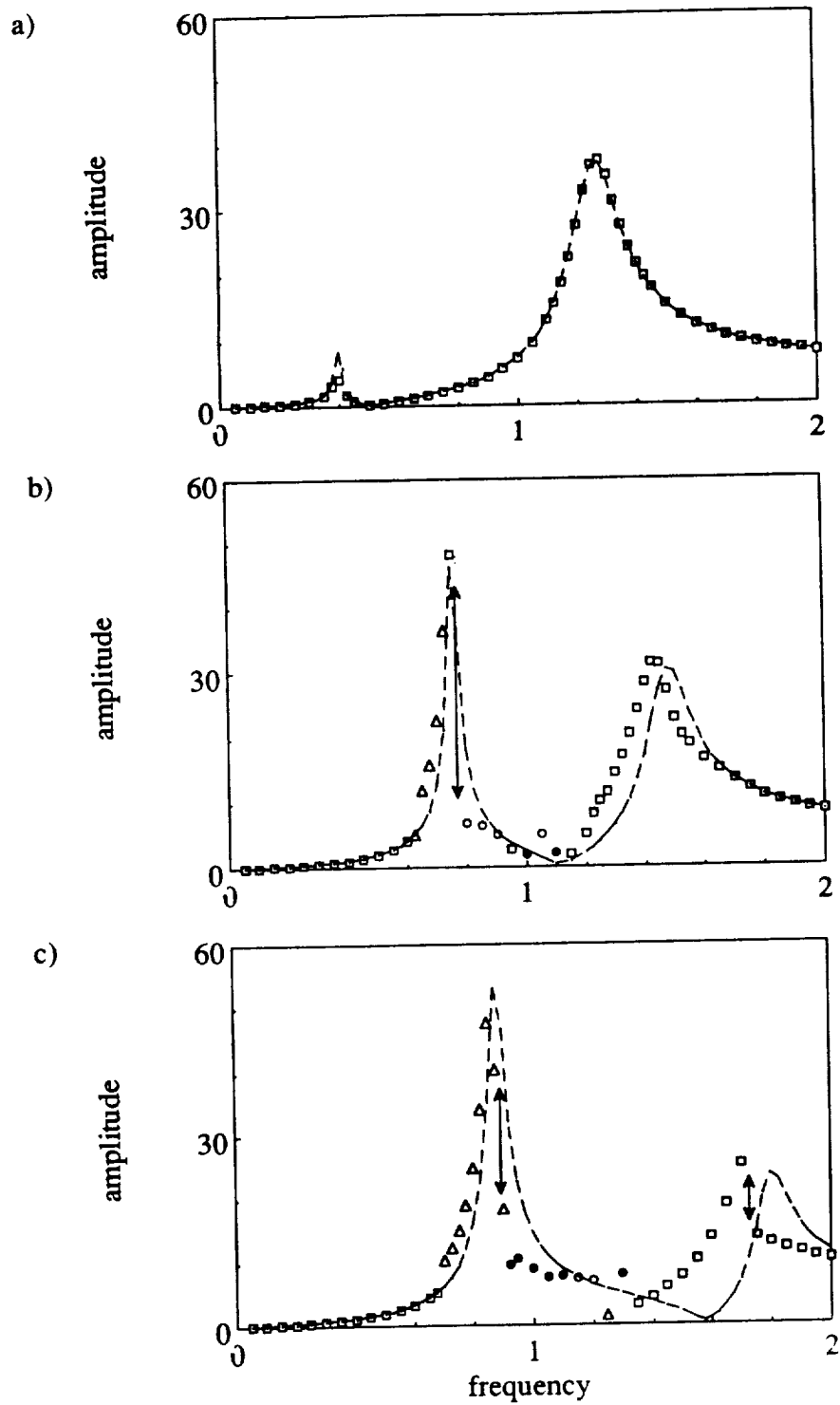
Figure 3.37. p_a versus Ω_h plots for the case of deep-groove ball bearings; $F_m=10$, $F_{ah}=5$, $F_{bi}=0$, $b_h=0$, $b_{bi}=b_c=0.001$mm, a) $\hat{k}=1$, b) $\hat{k}=5$, c) $\hat{k}=10$; harmonic, Δ period-one nonharmonic, o period-n subharmonic, • quasi-periodic or chaos, — — — — corresponding linear response.

validate the spur gear pair model of Chapter II assuming that the modes are weakly coupled with each other. Now, we use the three degree of freedom non-linear model of Figure 3.2a to analyze his test set-up [27]. In our analysis, bearings are assumed to be linear since they were highly preloaded; only gear backlash non-linearity is considered with $2b_h$=0.12 mm [74]. Table 3.2 lists the system parameters used in equation (3.3a) under four different mean loads. The system damping ratios are assumed to be uniform at each load. Average mesh stiffness k_h and alternating load F_{ah} values associated with each mean load F_m are also tabulated in Table 3.2.

Figures 3.38 through 3.42 compare dynamic transmission error predictions with the measurements [27]. At the design load (DL), which corresponds to the minimum static transmission error, good agreement is seen except for the jump discontinuity found experimentally at the second peak. In our model, we have increased F_{ah} slightly beyond the value given in Reference [27], so that the predicted amplitude of the first linear peak matches very well with the experiment. Such slight changes in critical system parameters such as F_{ah} and ζ, although they are varied within the experimental uncertainties, may alter the frequency response drastically as illustrated in Figures 3.39a and 3.39b. In Figure 3.39a we note that when we reduce the force ratio F_m/F_{ah} from 30 (the value given in Reference [27]) to 10, a jump discontinuity at the second peak is seen which is compatible with the experiment. Similarly, a small change in the damping values, which are not reported in Reference [27], also affects the frequency response as shown in Figure 3.39b. Figures 3.40 to 3.42 compare the dynamic transmission error spectra at 3/4, 1/2 and 1/4 of the design load. From these spectra we conclude that our proposed theory agrees well with the experimental results of Munro [27] both qualitatively and quantitatively, although amplitudes in the off-resonance regions are slightly off. Such amplitudes are close to the noise floor in the experiment.

Table 3.2. Parameters of the Munro's experimental set-up extracted from Reference [27].

	Mean load, F_m			
	design load(DL) 0.183	3/4 of DL 0.146	1/2 of DL 0.105	1/4 of DL 0.0579
F_{ah}	0.0058[†]	0.0178	0.0296	0.0393
k_b (N/m)	1.16×10^9	1.16×10^9	1.16×10^9	1.16×10^9
k_h (N/m)	3.44×10^8	3.22×10^8	3.01×10^8	2.72×10^8
κ_{11}, κ_{22}	0.950	0.966	0.983	1.007
κ_{13}, κ_{23}	0.242	0.242	0.242	0.242
ζ_{11}, ζ_{22}[††]	0.01	0.01	0.01	0.01
ζ_{13}, ζ_{23}[††]	0.00375	0.00375	0.00375	0.00375
ζ_{33}[††]	0.015	0.015	0.015	0.015

† modified so that the linear peak matches with the measured value.

†† estimated using the experimental data of Reference [27].
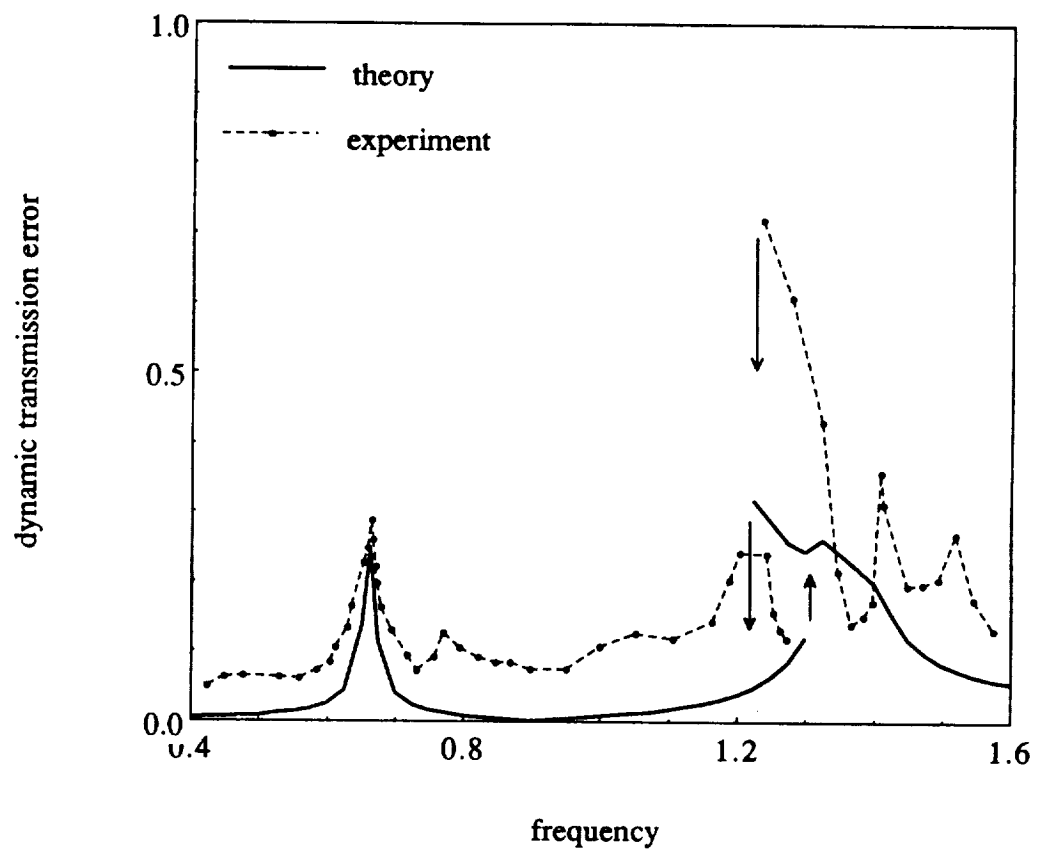
Figure 3.38.   Comparison of theory with Munro's [27] experiment at the design load.

158
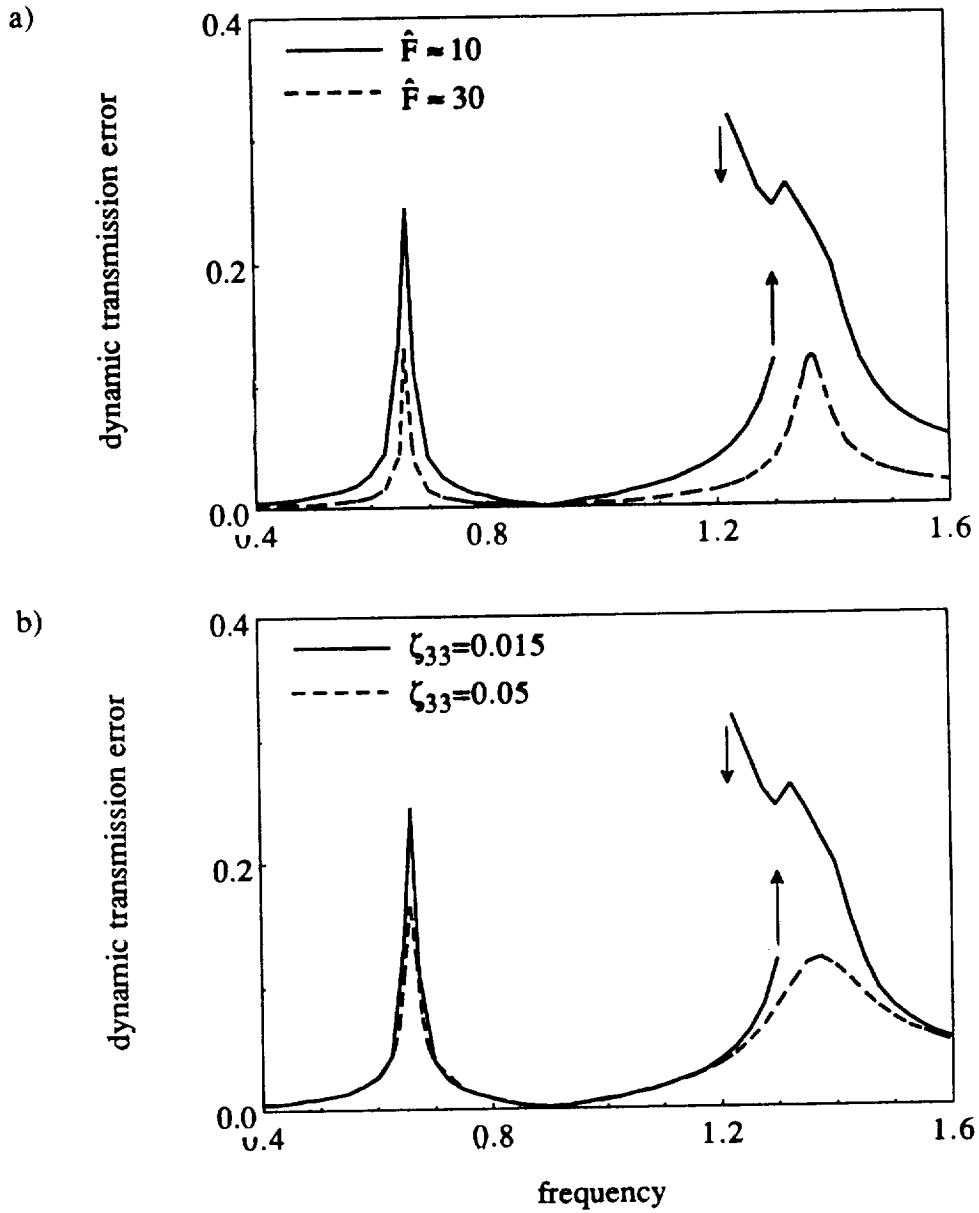
Figure 3.39. Effect of a) alternating load and b) damping on the dynamic transmission error spectrum at the design load.
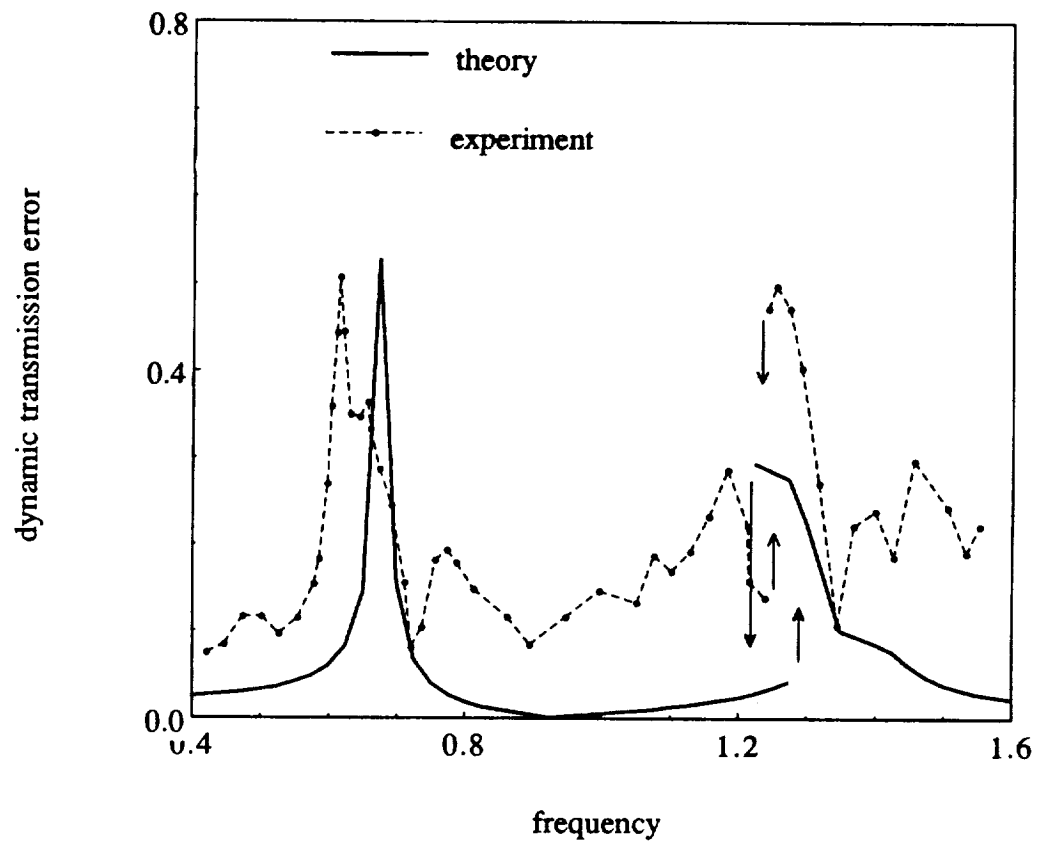
Figure 3.40. Comparison of theory with Munro's [27] experiment at 3/4 of the design load.

160
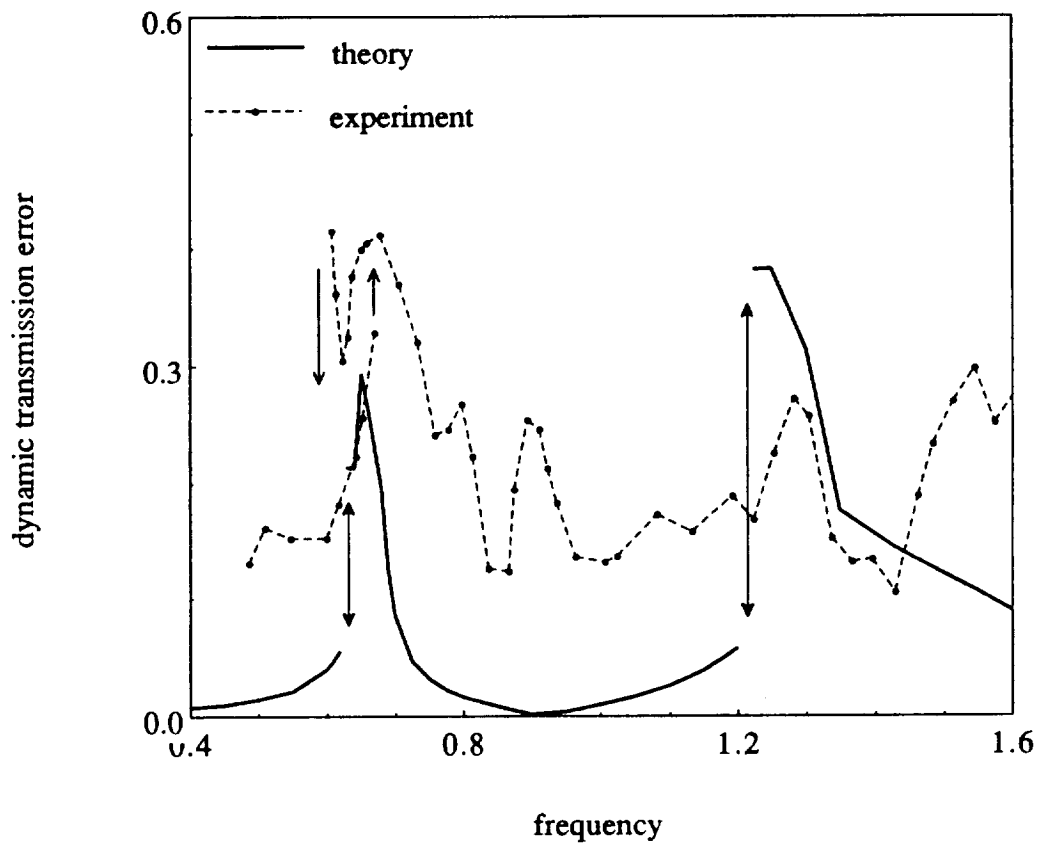
Figure 3.41. Comparison of theory with Munro's [27] experiment at 1/2 of the design load.

161
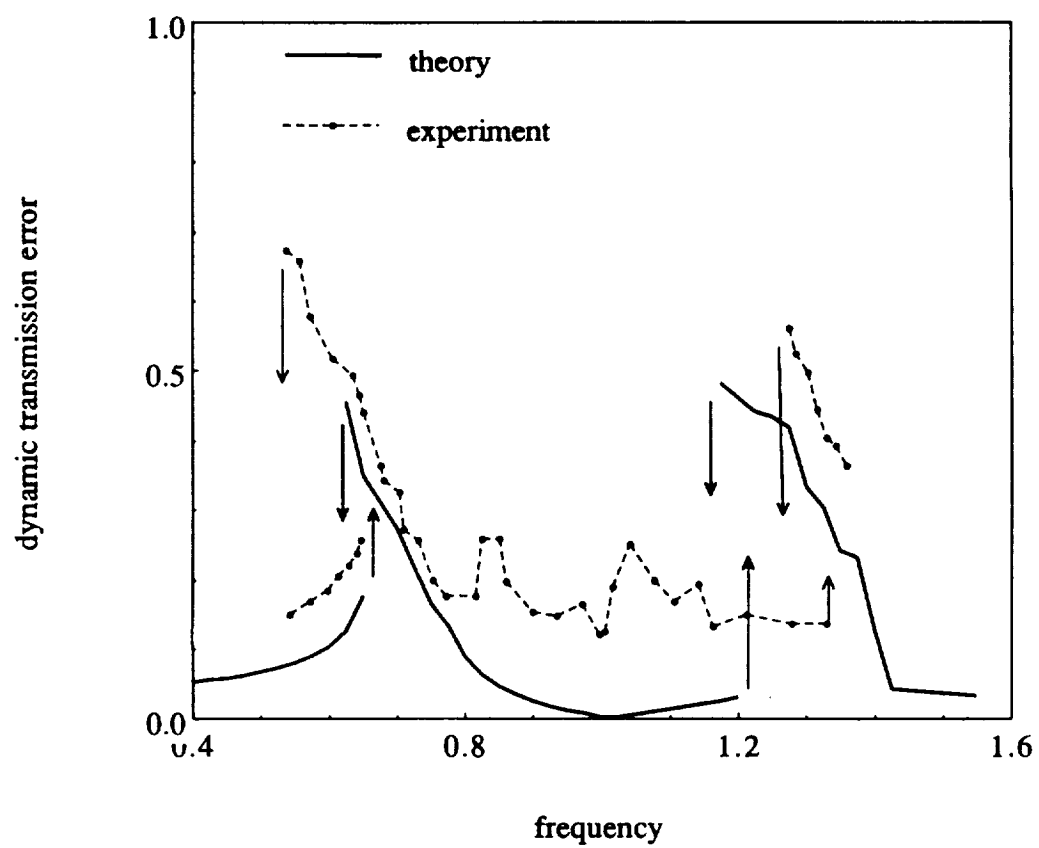
Figure 3.42. Comparison of theory with Munro's [27] experiment at 1/4 of the design load.

162

Further, discrepancies between the theory and the experiment may be due to the assumptions made in this study. It should however be pointed out that the experiment, even though it was very precise, was conducted almost three decades back before the advent of modern non-linear dynamics and chaos science [66-71]. Interestingly, Munro [27] had also reported subharmonic responses at 3/4, 1/2 and 1/4 of the design load, and "unrepeatable responses" (probably chaos) at 1/4 of the design load. Our results agree with such experimental observations as well. Both experiment and theory show that the chaotic solutions dictate the frequency response beyond the second resonance for 1/4 of the design load in Figure 3.42.

3.7. CONCLUSION

This analytical study on the non-linear dynamics of a geared rotor-bearing system with gear backlash and bearing clearances, as excited by the internal static transmission error and/or external torque pulsations, has made a number of contributions to the state of the art. First, an approximate non-linear model of the rolling element bearings with clearances has been developed and validated. Second, our mathematical model has been validated as it compares well with a previous experimental study, and several key parameters such as the mean load, mean to alternating force ratio, radial bearing preload, bearing stiffness and damping have been identified. Third, conditions for the chaotic and subharmonic resonances, and the routes to chaos have been identified. Forth, non-linear modal interactions have been examined. Finally, on a more fundamental note, our study enriches the current literature on coupled vibro-impact pairs [52,54,55].

163

CHAPTER IV

INTERACTIONS BETWEEN TIME-VARYING MESH STIFFNESS AND CLEARANCE NON-LINEARITIES

4.1. INTRODUCTION

Dynamic models of geared systems can be classified into four main groups. The first group includes linear time-invariant (LTI) models, as evident from an extensive review of the literature given in Reference [14]. The second group considers linear time-varying (LTV) mesh stiffness $k_h(\bar{t})$ in the analysis [27,29,62]. Periodic variation in $k_h(\bar{t})$ is due to the changing of the number of conjugate teeth pairs in contact during the convolute action. Accordingly, the system is excited parametrically as well as by the static transmission error $\bar{e}(\bar{t})$ introduced by kinematic errors and tooth deflections. In this case, the equation of motion of the gear pair essentially reduces to the Mathieu's or Hill's equation with a periodic external forcing function. The third group includes gear backlash in the models, but with time-invariant average mesh stiffness $k_h \neq k_h(\bar{t})$ [25,30,31,33,34,41,42]. It should be noted that backlash is bound to exist either by design or due to manufacturing errors and/or wear in any gear pair. Finally, the last group considers both gear backlash and mesh stiffness variation simultaneously [24,35-37,53]. However, none of these studies have addressed explicitly the effect of $k_h(\bar{t})$, including its interaction with the backlash non-linearity, on the steady state frequency response. Ozguven and Houser [24] have attempted to analyze this problem by replacing $k_h(\bar{t})$ with a constant mesh stiffness and by defining the "loaded static transmission error" excitation at the mesh point. But, Ozguven [75] has stated recently

that this approach may not work depending on the system parameters, and recommended a detailed investigation of this issue.

Numerous publications have analyzed LTV systems [76-78] and time-varying systems with quadratic and/or cubic non-linearities [79-82]. However, such studies are not directly applicable to the geared rotor systems which are the main focus of this chapter. This problem requires the solution to a set of time-varying differential equations with clearance-type non-linearities as excited by a periodic force generated at the gear mesh.

4.2. PROBLEM FORMULATION

A generic geared rotor-bearing system, which consists of a spur gear pair mounted on flexible shafts which are supported by rolling element bearings as shown in Figure 4.1a, is considered here. The gear box is assumed to be rigid. The effect of the prime mover or the load inertia is not considered assuming that such inertial elements are connected to the gear box through soft torsional couplings. Further, we assume that the system is symmetric about the plane of the gears and the axial motion (parallel to the shafts) is negligible. The governing equations of motion can be given in the matrix form as

$$\left[\overline{M}\right]\{\overline{q}''(\overline{t})\} + \left[\overline{C}\right]\{\overline{q}'(\overline{t})\} + \left[\overline{K}(\overline{t})\right]\{f(\overline{q}(\overline{t}))\} = \{\overline{F}(\overline{t})\} \tag{4.1}$$

where $\left[\overline{M}\right]$ is the time-invariant mass matrix and $\{\overline{q}(\overline{t})\}$ is the displacement vector. Here, damping matrix $\left[\overline{C}\right]$ is assumed to be time-invariant, as the effect of the tooth separation and time-varying mesh properties on mesh damping are considered negligible; validity of this assumption will be examined later. The stiffness matrix

165

rigid gear box

pinion

driving shaft

rolling element bearings

driven shaft

gear

(a)

Elastic force

slope: stiffness

1

Relative displacement

backlash or clearance
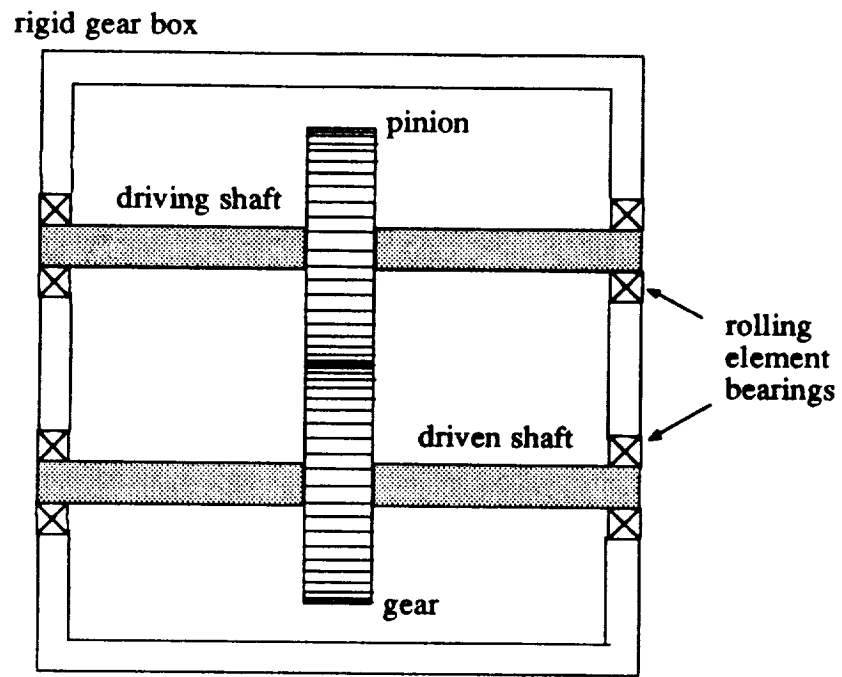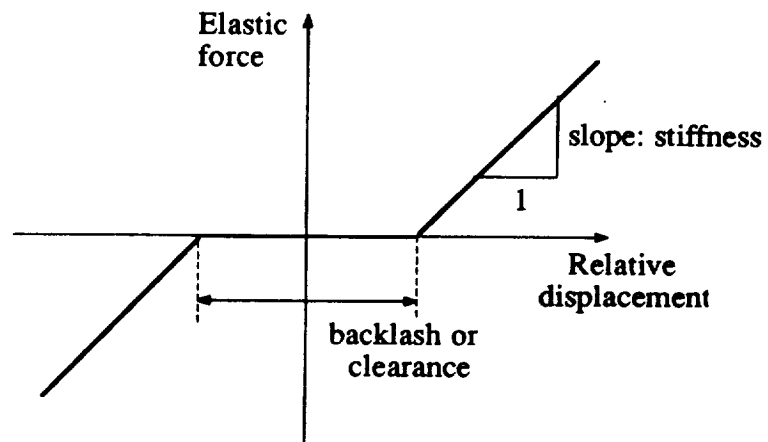
(b)

Figure 4.1   a) Generic geared rotor-bearing system, b) clearance non-linearity in gears and bearings.

$[\overline{K}(\bar{t})]$ is considered to be a periodically time-varying matrix given by $[\overline{K}(\bar{t})] = [\overline{K}(\bar{t} + 2\pi / \overline{\Omega}_h)]$ where $\overline{\Omega}_h$ is the fundamental gear mesh frequency. The non-linear displacement vector $\{f(\overline{q}(\bar{t}))\}$ includes the radial clearances in bearings and the gear backlash as shown in Figure 4.1b, and the forcing vector $\{\overline{F}(\bar{t})\}$ consists of both external torque and internal static transmission error excitations.

This chapter extends our previous non-linear single degree of freedom spur gear pair model of Chapter II and multi-degree of freedom geared rotor-bearing system model of Chapter III by including time-varying mesh stiffness $k_h(\bar{t})$, and investigates its effect on the frequency response of lightly and heavily loaded geared systems. Interactions between mesh stiffness variation and system non-linearities associated with gear backlash and radial clearances in rolling element bearings are also considered. Resonances of the corresponding LTV system associated with the parametric and external excitations are identified using the method of multiple scales. Our formulation will be validated by comparing predictions with available experimental results [27,28].

4.3. MATHEMATICAL MODEL

A reduced order form of the multi-degree of freedom system of equation (4.1), the three degree of freedom non-linear model of the geared rotor system, which has been used in Chapter III, is considered here. This includes gear inertias I_{g1} and I_{g2}, gear masses m_{g1} and m_{g2}, and base circle diameters d_{g1} and d_{g2}, as shown in Figure 4.2a. The gear mesh is described by a non-linear displacement function f_h with time varying stiffness $k_h(\bar{t})$ and linear viscous damping c_h. Bearings and the shafts that support the gears are modeled by equivalent elements with viscous damping coefficients c_{b1} and c_{b2} and non-linear springs defined by force-displacement functions f_{b1} and f_{b2} which are approximated by piece-wise linear, dead zone type non-linearities

as suggested in Chapter III. Both low frequency external excitation due to torque fluctuations and high frequency internal excitation due to the static transmission error $\bar{e}(\bar{t})$ are considered in the formulation. Input torque fluctuation is included, but the output torque is assumed to be constant, i.e. $\bar{T}_{g1}(\bar{t}) = \bar{T}_{g1m} + \bar{T}_{g1a}(\bar{t})$ and $\bar{T}_{g2}(\bar{t}) = \bar{T}_{g2m}$. External radial preloads $\bar{F}_{b1}$ and $\bar{F}_{b2}$ are also applied to both rolling element bearings.

4.3.1. Equations of Motion

Equations of coupled transverse-torsional motion of the geared rotor-bearing system shown in Figure 4.2a with the displacement vector $\{\bar{q}(\bar{t})\} = \{\bar{y}_{g1}(\bar{t}), \bar{y}_{g2}(\bar{t}), \bar{p}(\bar{t})\}$ are given in matrix form as follows:

$$
\begin{bmatrix} m_{g1} & 0 & 0 \\ 0 & m_{g2} & 0 \\ -m_{c1} & m_{c1} & m_{c1} \end{bmatrix} \begin{Bmatrix} \bar{y}''_{g1}(\bar{t}) \\ \bar{y}''_{g2}(\bar{t}) \\ \bar{p}''(\bar{t}) \end{Bmatrix} + \begin{bmatrix} c_{b1} & 0 & c_h \\ 0 & c_{b2} & -c_h \\ 0 & 0 & c_h \end{bmatrix} \begin{Bmatrix} \bar{y}'_{g1}(\bar{t}) \\ \bar{y}'_{g2}(\bar{t}) \\ \bar{p}'(\bar{t}) \end{Bmatrix}
$$

$$
+ \begin{bmatrix} k_{b1} & 0 & k_h(\bar{t}) \\ 0 & k_{b2} & -k_h(\bar{t}) \\ 0 & 0 & k_h(\bar{t}) \end{bmatrix} \begin{Bmatrix} f_{b1}(\bar{y}_{g1}(\bar{t})) \\ f_{b2}(\bar{y}_{g2}(\bar{t})) \\ f_h(\bar{p}(\bar{t})) \end{Bmatrix} = \begin{Bmatrix} -\bar{F}_{b1} \\ \bar{F}_{b2} \\ \bar{F}_m - m_{c1}\bar{e}''(\bar{t}) + \bar{F}_{aT}(\bar{t}) \end{Bmatrix}; \quad (4.2a)
$$

$$
\bar{p}(\bar{t}) = \frac{d_{g1}}{2}\theta_{g1}(\bar{t}) - \frac{d_{g2}}{2}\theta_{g2}(\bar{t}) + \bar{y}_{g1}(\bar{t}) - \bar{y}_{g2}(\bar{t}) - \bar{e}(\bar{t}); \quad (4.2b)
$$

$$
m_{c1} = \frac{1}{\left(\dfrac{d_{g1}^2}{4I_{g1}} + \dfrac{d_{g2}^2}{4I_{g2}} \right)}; \quad \bar{F}_m = \frac{2\bar{T}_{g1m}}{d_{g1}} = \frac{2\bar{T}_{g2m}}{d_{g2}}; \quad \bar{F}_{aT}(\bar{t}) = \frac{m_{c1}\bar{T}_{g1a}(\bar{t})}{2I_{g1}}; \quad (4.2c\text{-}e)
$$

168
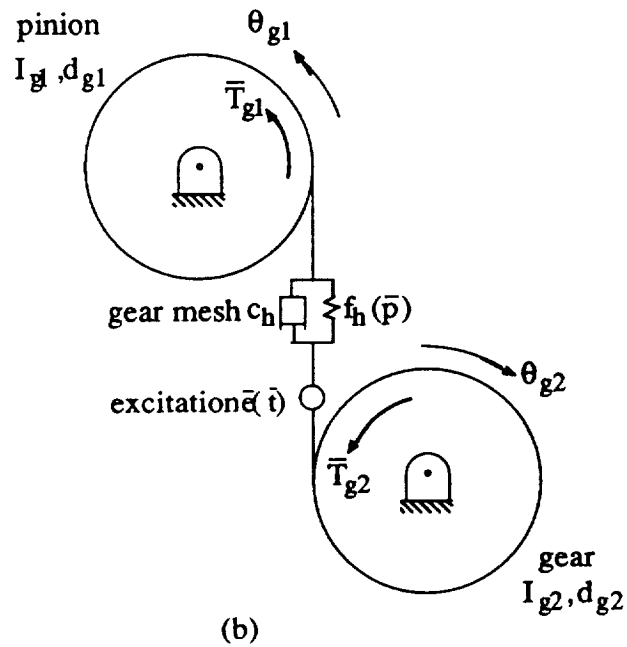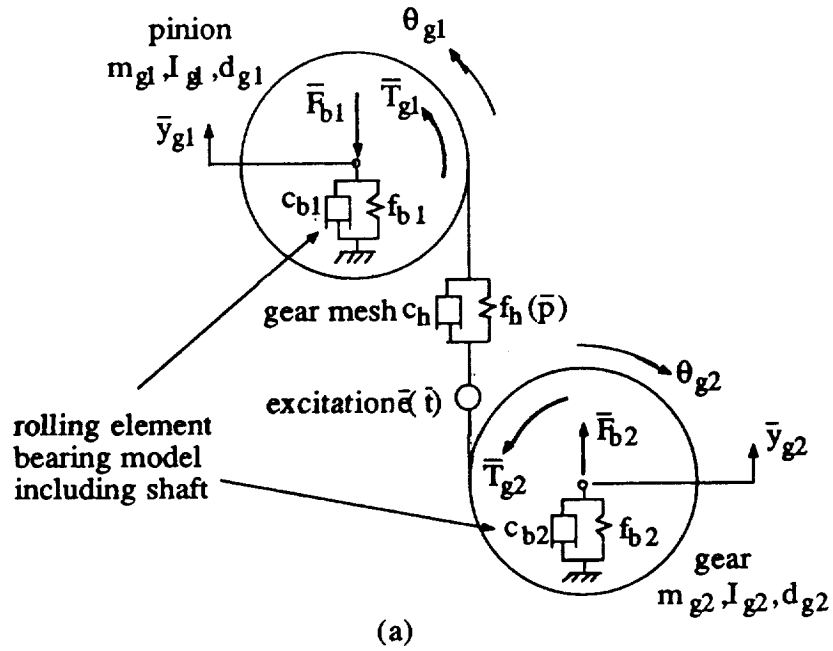
Figure 4.2. Non-linear models of the geared system of Figure 1; a) three degree of freedom system, b) gear pair model with a single degree of freedom.

169

$$k_h(\bar{t}) = k_h(\bar{t} + \frac{2\pi}{\overline{\Omega}_h}) = k_{hm} + \sum_{r=1}^{\infty} k_{har} \cos(r\overline{\Omega}_h \bar{t} + \phi_{hr}); \qquad (4.2f)$$

$$f_{bi}(\bar{y}_{gi}) = \begin{cases} \bar{y}_{gi} - b_{bi}; & \bar{y}_{gi} > b_{bi} \\ 0; & -b_{bi} < \bar{y}_{gi} < b_{bi} \\ \bar{y}_{gi} + b_{bi}; & \bar{y}_{gi} < -b_{bi} \end{cases}; \quad f_h(\bar{p}) = \begin{cases} (\bar{p} - b_h); & \bar{p} > b_h \\ 0; & -b_h < \bar{p} < b_h \\ (\bar{p} + b_h); & \bar{p} < -b_h \end{cases}. \quad (4.2g,h)$$

Here, $(\ )'$ donates derivative with respect to time $\bar{t}$, y_{gi} and θ_{gi} are the transverse and torsional displacements of the i-th gear (i=1,2), m_{c1} is the equivalent gear pair mass, $\overline{F}_m$ is the average force transmitted through the gear mesh, and $\overline{F}_{aT}(t)$ is the fluctuating force related to the external input torque excitation. Equations (4.2a-h) have been used previously in Chapter III except for $k_h(\bar{t})$ term, which is expanded in equations (4.2a-h) in the Fourier series form. Here $\bar{p}(\bar{t})$ is the difference between the dynamic transmission error and the static transmission error $\bar{e}(\bar{t})$. A dimensionless form of equation (4.2a) is obtained by letting $y_{gi}(\bar{t}) = \bar{y}_{gi}(\bar{t})/b_c$, $p(\bar{t}) = \bar{p}(\bar{t})/b_c$, $\omega_n = \sqrt{k_{hm}/m_{c1}}$, $\omega_{bi} = \sqrt{k_{bi}/m_{gi}}$ (i=1,2) and $t = \omega_n \bar{t}$ where b_c is the characteristic length. Here, we consider periodic excitation for both $\bar{e}(\bar{t})$ and $\overline{F}_{aT}(\bar{t})$ as $\bar{e}(\bar{t}) = \sum_{r=1}^{\infty} \bar{e}_r \cos(r\overline{\Omega}_h \bar{t} + \phi_{er})$, $\overline{F}_{aT}(\bar{t}) = \sum_{r=1}^{\infty} \overline{F}_{aTr} \cos(r\overline{\Omega}_T \bar{t} + \phi_{Tr})$ where $\overline{\Omega}_h$ and $\overline{\Omega}_T$ are the fundamental excitation frequencies of internal displacement and external torque fluctuations, respectively. Further, define dimensionless excitation frequencies $\Omega_h = \overline{\Omega}_h/\omega_n$ and $\Omega_T = \overline{\Omega}_T/\omega_n$ to yield the following governing equations of motion in the dimensionless form:

$$\begin{bmatrix} 1 & 0 & 0 \\ 0 & 1 & 0 \\ -1 & 1 & 1 \end{bmatrix} \begin{Bmatrix} \ddot{y}_{g1}(t) \\ \ddot{y}_{g2}(t) \\ \ddot{p}(t) \end{Bmatrix} + 2 \begin{bmatrix} \zeta_{11} & 0 & \zeta_{13} \\ 0 & \zeta_{22} & -\zeta_{23} \\ 0 & 0 & \zeta_{33} \end{bmatrix} \begin{Bmatrix} \dot{y}_{g1}(t) \\ \dot{y}_{g2}(t) \\ \dot{p}(t) \end{Bmatrix}$$

$$+ \begin{bmatrix} \kappa_{11} & 0 & \kappa_{13}(t) \\ 0 & \kappa_{22} & -\kappa_{23}(t) \\ 0 & 0 & \kappa_{33}(t) \end{bmatrix} \begin{Bmatrix} f_{b1}(y_{g1}) \\ f_{b2}(y_{g2}) \\ f_h(p) \end{Bmatrix} = \begin{Bmatrix} -F_{b1} \\ F_{b2} \\ F_m \end{Bmatrix} + \begin{Bmatrix} 0 \\ 0 \\ F_{ah}(t) \end{Bmatrix} + \begin{Bmatrix} 0 \\ 0 \\ F_{aT}(t) \end{Bmatrix}; \quad (4.3a)$$

$$F_{ah}(t) = \sum_{r=1}^{\infty} F_{ahr}(r\Omega_h)^2 \cos(r\Omega_h t + \phi_{er}); \quad F_{ahr} = \frac{\tilde{e}_r}{b_c}; \qquad (4.3b,c)$$

$$F_{aT}(t) = \sum_{r=1}^{\infty} F_{aTr} \cos(r\Omega_T t + \phi_{Tr}); \quad F_{aTr} = \frac{\tilde{F}_{aTr}}{m_{c1} b_c \omega_n^2}; \qquad (4.3d,e)$$

$$F_m = \frac{\overline{F}_m}{m_{c1} b_c \omega_n^2}; \quad F_{bi} = \frac{\overline{F}_{bi}}{m_{gi} b_c \omega_n^2}, \ i=1,2; \qquad (4.3f\text{-}g)$$

$$\zeta_{ii} = \frac{c_{bi}}{2m_{gi}\omega_n}; \quad \zeta_{i3} = \frac{c_h}{2m_{gi}\omega_n}, \ i=1,2; \quad \zeta_{33} = \frac{c_h}{2m_{c1}\omega_n}; \qquad (4.3h\text{-}j)$$

$$\kappa_{ii} = \frac{\omega_{bi}^2}{\omega_n^2}; \quad \kappa_{i3}(t) = \frac{k_h(t)}{m_{gi}\omega_n^2}, \ i=1,2; \qquad (4.3k\text{-}\ell)$$

$$\kappa_{33}(t) = \frac{k_h(t)}{k_{hm}} = 1 + \sum_{r=1}^{\infty} \varepsilon_r \cos(r\Omega_h t + \phi_{hr}); \qquad (4.3m)$$

171

$$f_{bi}(y_{gi}) = \begin{cases} y_{gi} - \dfrac{b_{bi}}{b_c}; & y_{gi} > \dfrac{b_{bi}}{b_c} \\ 0; & -\dfrac{b_{bi}}{b_c} < y_{gi} < \dfrac{b_{bi}}{b_c} \\ y_{gi} + \dfrac{b_{bi}}{b_c}; & y_{gi} < -\dfrac{b_{bi}}{b_c} \end{cases} \qquad f_h(p) = \begin{cases} p - \dfrac{b_h}{b_c}; & p > \dfrac{b_h}{b_c} \\ 0; & -\dfrac{b_h}{b_c} < p < \dfrac{b_h}{b_c} \\ p + \dfrac{b_h}{b_c}; & p < \dfrac{b_h}{b_c} \end{cases} \quad (4.3\text{n,o})$$

where F_{bi} (i=1,2) and F_m are the dimensionless components of the mean force vector $\{F\}_m$, and $F_{aT}(t)$ and $F_{ah}(t)$ pertain to the alternating external excitation $\{F(t)\}_e$ and internal excitation $\{F(t)\}_i$ force vectors, respectively.

4.4. GEAR PAIR STUDIES

First, we consider the spur gear pair model of Chapter II, as shown in Figure 4.2b, and investigate the effect of $k_h(t)$ on the steady state frequency response. The equation of motion of the gear pair is obtained from equation (4.3a) by substituting $y_{gi}(t)=0$ for fixed gear centers. Neglecting the input torque variations for the sake of convenience, $F_{aT}(t)=0$, we obtain the following equation of motion of a loaded gear pair with time-varying mesh stiffness and backlash, as excited by the static transmission error.

$$\ddot{p}(t) + 2\zeta_{33}\dot{p}(t) + \kappa_{33}(t)f_h(p(t)) = F_m + F_{ah}(t) \qquad (4.4)$$

where ζ_{33}, $\kappa_{33}(t)$, $f_h(p)$, F_m and F_{ah} are still given by equation (4.3). Since none of the existing analytical solution methods are found to be suitable for this problem, the digital simulation technique is used to solve equation (4.4). A 5th-6th order Runge-Kutta numerical integration algorithm with variable time step [50] is used here. This

172

technique has already been employed successfully in Chapter II for the gear pair problem with time-invariant mesh stiffness.

First consider only sinusoidally varying mesh stiffness and the static transmission error excitation, i.e. $\kappa_{33}(t) = 1 + \varepsilon_1 \cos(\Omega_h t + \phi_{h1})$ where $\varepsilon = \varepsilon_1$ and $F_{ah}(t) = F_{ah1}\Omega_h{}^2 \cos(\Omega_h t + \phi_{e1})$. The tooth deflection or $F_{ah}(t)$ is maximum under the applied mean load F_m when $\kappa_{33}(t)$ is minimum (i.e. minimum number of gear pair in contact). Similarly, minimum $F_{ah}(t)$ corresponds to maximum $\kappa_{33}(t)$. Therefore, there is an out of phase relationship between $F_{ah}(t)$ and $\kappa_{33}(t)$, i.e. $\phi_{h1} = \phi_{e1} + \pi$. Here, we set $\phi_{h1} = \pi$ and $\phi_{e1} = 0$ for the sake of convenience. Hence, equation (4.4) is modified to:

$$\ddot{p}(t) + 2\zeta_{33}\dot{p}(t) + [1 - \varepsilon\cos(\Omega_h t)]f_h(p(t)) = F_m + F_{ah}\Omega_h^2 \cos(\Omega_h t). \qquad (4.5)$$

4.4.1. Linear Time-varying (LTV) System

For zero gear backlash b_h, the gear mesh displacement function is $f_h(p) = p$. Hence equation (4.5) reduces to an LTV equation as follows:

$$\ddot{p}(t) + 2\zeta_{33}\dot{p}(t) + [1 - \varepsilon\cos(\Omega_h t)]p(t) = F_m + F_{ah}\Omega_h^2 \cos(\Omega_h t) \qquad (4.6)$$

Approximate analytical solutions of similar LTV differential equations with parametric and external excitations are already given in the literature [76,77,79-82]. Therefore, we will not attempt to solve equation (4.6) completely. Instead we identify the corresponding resonances using the method of multiple scales [76]. A first order uniform solution is given by an expansion having the following form where the scalar parameter ε is assumed to be very small.

173

$$p(t;\varepsilon) = p_o(T_o, T_1) + \varepsilon p_1(T_o, T_1) + O(\varepsilon^2) \tag{4.7}$$

where $T_n = \varepsilon^n t$ is the n-th time scale. Expansions for the derivatives with respect to t is obtained in terms of the partial derivatives with respect to time scales $D_n = \partial / \partial T_n$

$$d/dt = D_o + \varepsilon D_1 + O(\varepsilon^2); \quad d^2/dt^2 = D_o^2 + 2\varepsilon D_o D_1 + O(\varepsilon^2) \tag{4.8a,b}$$

Substituting equations (7) and (8) into equation (6) and equating like powers of ε, with the external force being applied at $O(\varepsilon^o)$, one obtains

$$D_o^2 p_o + p_o = F_m + F_{ah1}\Omega_h^2 \cos(\Omega_h T_o) \tag{4.9a}$$

$$D_o^2 p_1 + p_1 = -2D_o D_1 p_o - \mu D_o p_o + p_o \cos(\Omega_h T_o) \tag{4.9b}$$

where $\varepsilon\mu = 2\zeta_{33}$. The solution of equation (9a) is given in the complex domain as

$$p_o = A(T_1)e^{iT_o} + F_m + \Lambda e^{i\Omega_h T_o} + cc; \quad \Lambda = F_{ah1}\Omega_h^2 / 2(1 - \Omega_h^2) \tag{4.10a,b}$$

where cc represents the complex conjugate terms and $i = \sqrt{-1}$. At $\Omega_h \approx 1$, we note that $(1 - \Omega_h^2)^{-1}$ will make the amplitude of the response boundless; this is the primary resonance since it appears in the first order. Substituting equation (4.10) into equation (4.9b) we get

174

$$D_0^2 p_1 + p_1 = -2iD_1 A e^{iT_o} - i\mu A e^{iT_o} - i\mu \Lambda \Omega_h e^{i\Omega_h T_o} + \frac{1}{2} A e^{i(1+\Omega_h)T_o}$$

$$+ \frac{1}{2} A e^{i(1-\Omega_h)T_o} + \frac{1}{2} A e^{2i\Omega_h T_o} + \frac{1}{2} F_m e^{i\Omega_h T_o} + \Lambda + cc \quad (4.11)$$

Besides the primary resonance at $\Omega_h \approx 1$, the particular solution of equation (4.11) has other secular terms when $2\Omega_h \approx 1$ and $\Omega_h \approx 2$. At $2\Omega_h \approx 1$, summation of the external excitation frequency and the parametric excitation frequency is close to the dimensionless natural frequency which is unity. One could also observe resonances at $\Omega_h \approx n$, n>2 when higher scales are considered in equation (4.7). In summary, equation (4.6) has resonances at $\Omega_h \approx 0.5$ and n, where n=1,2,3....

Now, we solve equation (4.6) using digital simulation. Figure 4.3 shows the steady state frequency response curves $p_a(\Omega_h)$ and $p_m(\Omega_h)$ for a lightly loaded system with $F_m=0.1$, $F_{ah1}=0.05$, $\zeta_{33}=0.05$, $b_h=0$ and four different ε values. Note that $\varepsilon=0$ represents the LTI system. For $\varepsilon>0$, we do not observe any multi-valued regions and jump phenomenon, similar to those seen for the non-linear systems. Mesh stiffness variation ε has a negligible effect on the natural frequency which corresponds to the largest peak in Figure 4.3a; but an increase ε in amplifies p_a in both resonance and off-resonance regions. Here p_m is no longer uncoupled from p_a, and it varies substantially in the vicinity of primary resonance at $\Omega_h=1.0$, and the parametric resonance at $\Omega_h=0.5$, especially for a large ε confirming the analysis given earlier. Note that our study is limited to only these two resonances as an investigation of subharmonic resonances at $\Omega_h \approx n$, n>1 is beyond the scope of this study.

Figure 4.3. Frequency response spectra of a lightly loaded LTV gear pair with sinusoidal $\bar{e}(\bar{t})$ and $k_h(\bar{t})$, $F_m=0.1$, $F_{ah1}=0.05$, $\zeta_{33}=0.05$, $b_h=0$ and four different ε values; a)p_a versus Ω_h, b) p_m versus Ω_h.

176

4.4.2. Non-linear Time-varying System

Next we consider the time-varying non-linear system with backlash, given by equation (4.5). Figure 4.4 shows $p_a(\Omega_h)$ and $p_m(\Omega_h)$ spectra with $F_m=0.1$, $F_{a1}=0.05$, $\zeta_{33}=0.05$, and four ε values. In this case, we notice a jump discontinuity at the resonant frequency and a dual-valued region bounded by jump-up and jump-down transition frequencies. For $\varepsilon=0$, $p_m \neq p_m(\Omega_h)$ is evident in the no-impact regime, similar to the results given in Chapter II. But when $\varepsilon>0$, the transition frequencies which define the jump phenomenon become smaller, and p_a at the jump-down frequency grows with increasing ε. This indicates that $k_h(\bar{t})$ enhances the degree of non-linearity associated with the gear backlash. Similar to the results of LTV system in Figure 4.3, we again observe in Figure 4.4a a parametric resonance at $\Omega_h=0.5$, which is strong for $\varepsilon=0.2$ and 0.4 curves. Figure 4.5 compares the time histories p(t) for each ε values at the parametric resonance peak, $\Omega_h=0.5$. For the LTI system ($\varepsilon=0$), a harmonic no-impact type steady state solution exists as illustrated in Figure 4.5a. With increasing ε, this solution is transformed into a non-harmonic periodic solution with a larger peak to peak value as a result of the parametric mesh stiffness excitation, as shown in Figures 4.5b-d.

Now, consider a heavily loaded gear pair with $F_m=0.1$, $F_{a1}=0.01$ and $\zeta_{33}=0.05$. Figures 4.6a and 4.6b show $p_a(\Omega_h)$ and $p_m(\Omega_h)$ spectra, respectively. In this case, tooth separation does not occur for $\varepsilon=0$ which results in a linear frequency response curve with a constant p_m. A small jump is seen at $\varepsilon=0.1$, and this jump becomes larger for $\varepsilon=0.2$ and 0.4; overall alternating amplitudes p_a at resonance and within the off-resonance regions increase considerably. This suggests that the mesh stiffness variation is especially important for a heavily loaded gear pair with backlash.

177
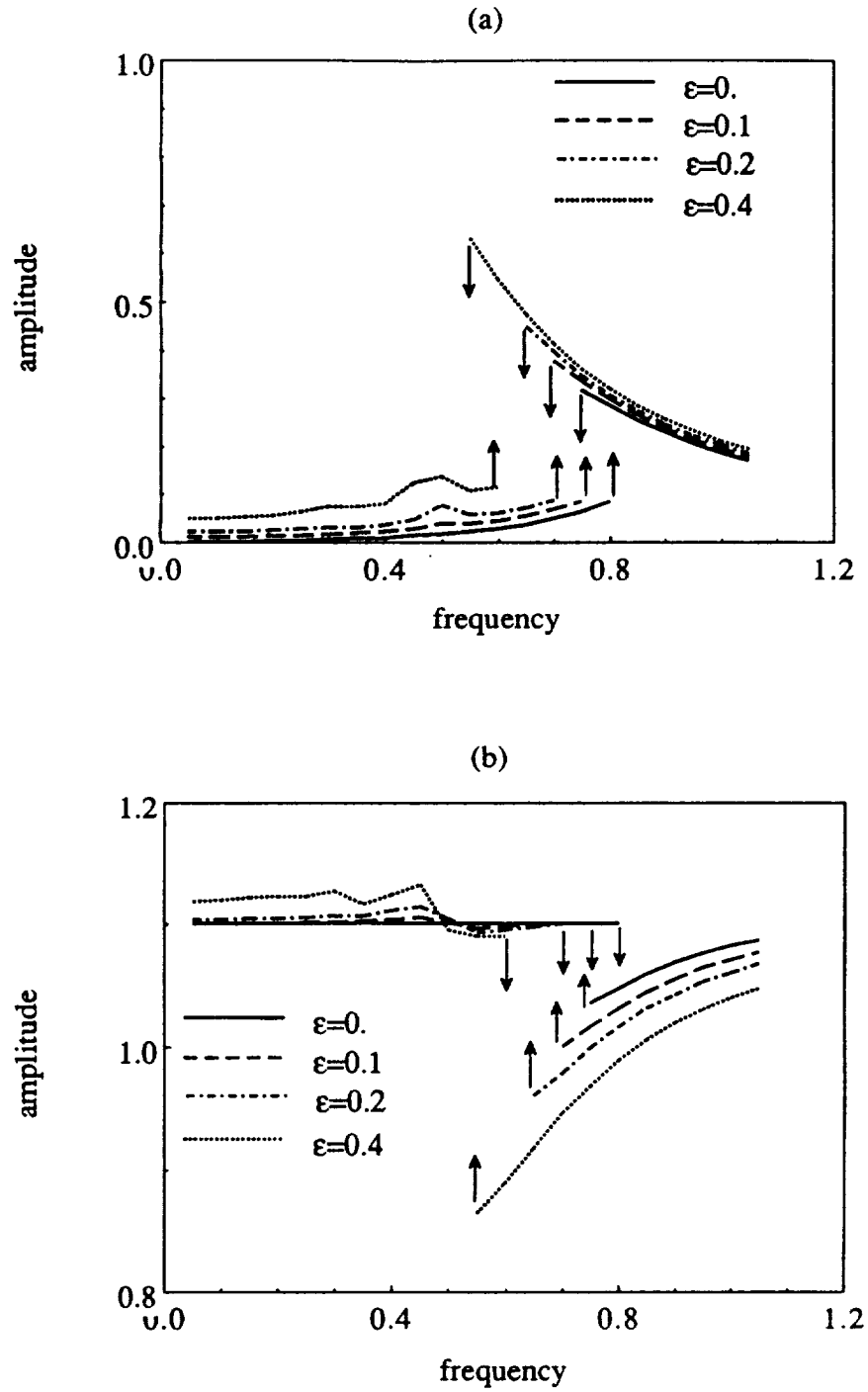
Figure 4.4. Frequency response spectra of a lightly loaded non-linear gear pair of Figure 2b with sinusoidal $\bar{e}(\bar{t})$ and $k_h(\bar{t})$, $F_m=0.1$, $F_{ah1}=0.05$, $\zeta_{33}=0.05$, $b_h=b_c$ and four different ε values; a)p_a versus Ω_h, b) p_m versus Ω_h.

178
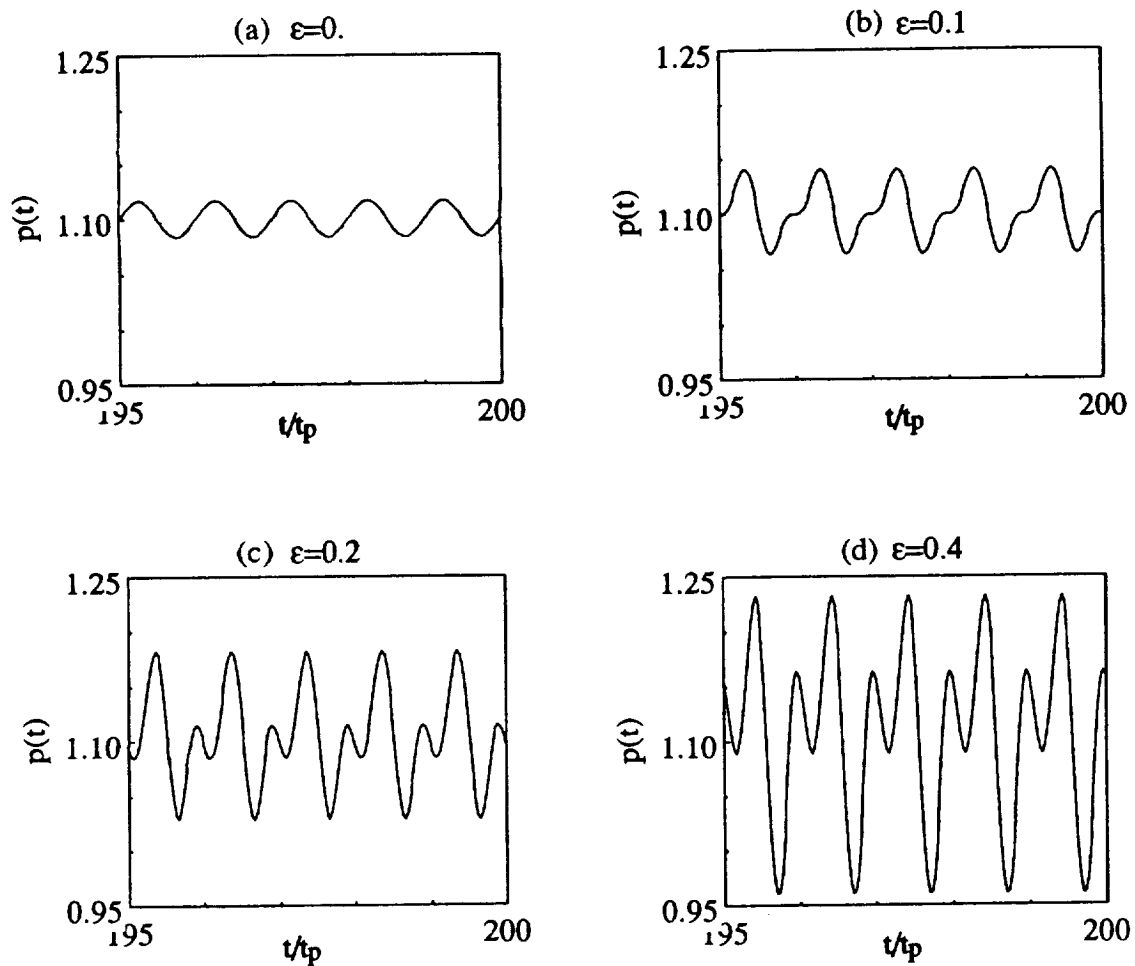
Figure 4.5. Steady state time histories corresponding to Ω_h=0.5 in Figure 4; a) ϵ=0 (LTI model), b) ϵ=0.1, c) ϵ=0.2, d) ϵ=0.4.
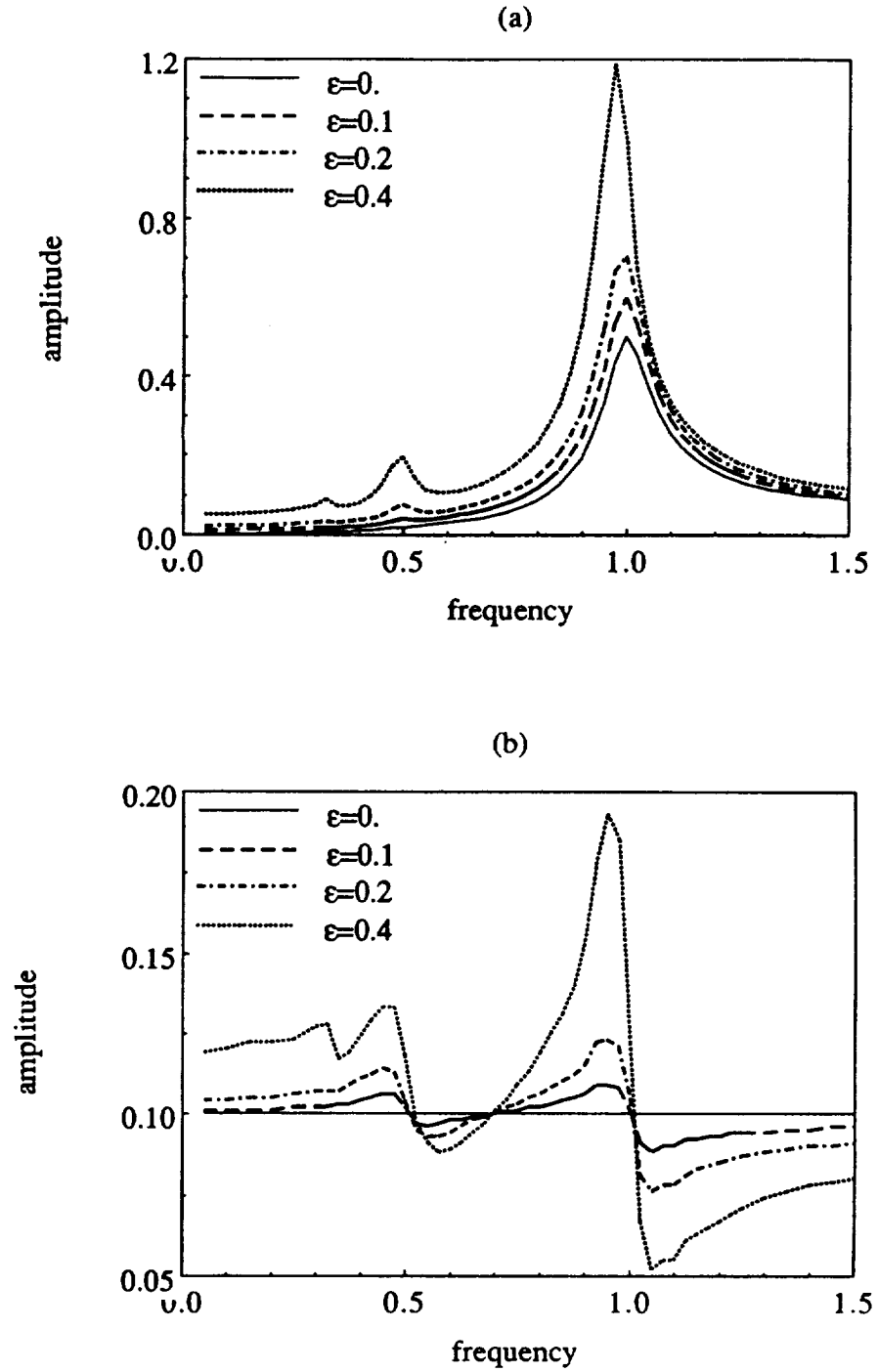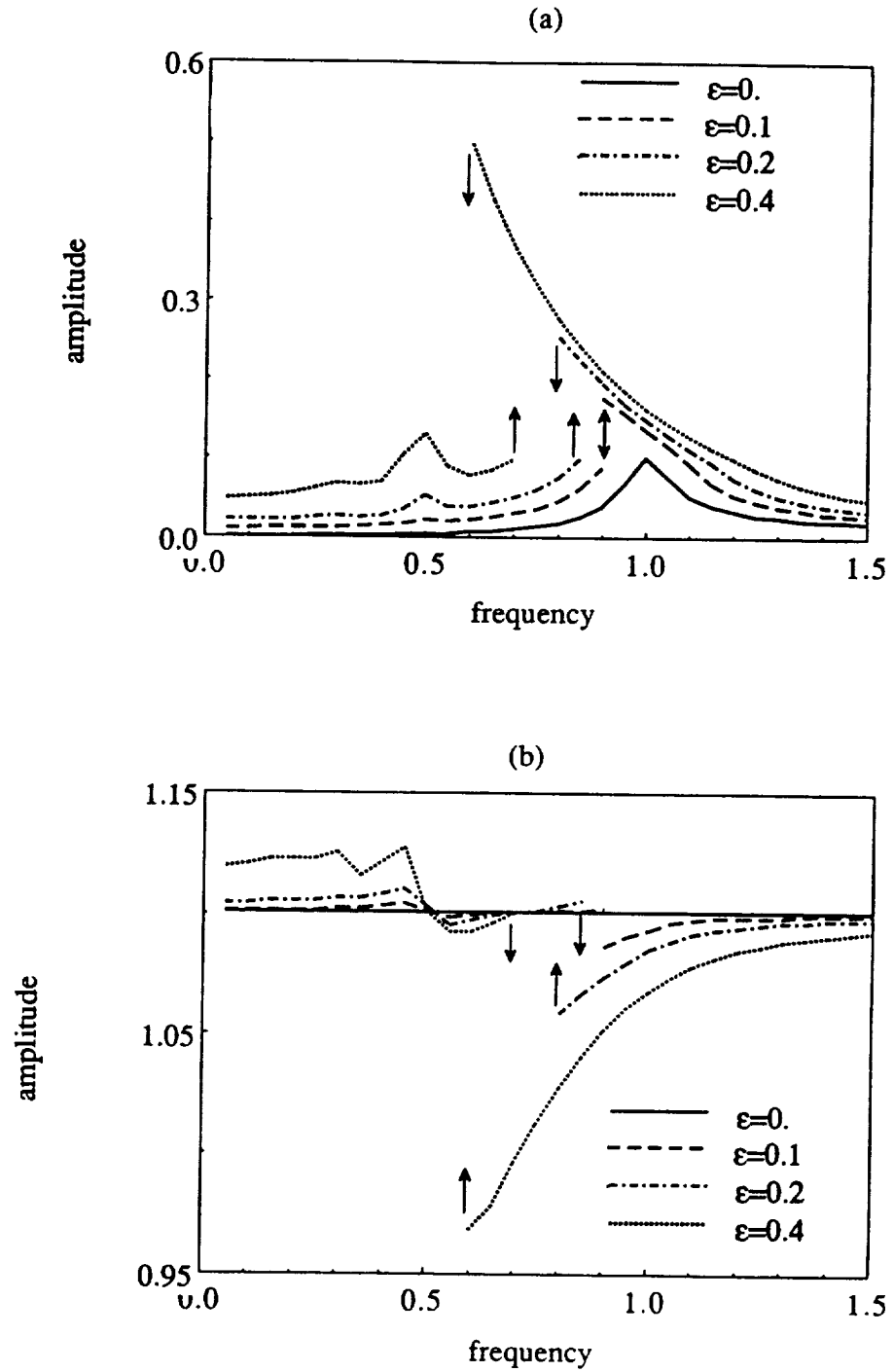
Figure 4.6. Frequency response spectra of a heavily loaded non-linear gear pair with sinusoidal $\bar{e}(\bar{t})$ and $k_h(\bar{t})$, $F_m=0.1$, $F_{ah1}=0.01$, $\zeta_{33}=0.05$, $b_h=b_c$ and four different ε values; a)p_a versus Ω_h, b) p_m versus Ω_h.

180

4.4.3. Non-linear Time-varying Mesh Damping

In order to investigate the effect of non-linear, time-varying gear mesh damping on the steady state frequency response, we consider a sinusoidally varying gear mesh damping $\zeta_{33}(t)$ which is assumed to be proportional to the mesh stiffness function $\kappa_{33}(t)$, and a non-linear velocity function g_h associated with tooth separation. Hence the governing equation of motion is

$$\ddot{p}(t) + 2\zeta_{33}(t)g_h(\dot{p}(t)) + [1 - \varepsilon\cos(\Omega_h t)]f_h(p(t)) = F_m + F_{ah}\Omega_h^2\cos(\Omega_h t); \quad (4.12a)$$

$$\zeta_{33}(t) = \zeta_{33}\kappa_{33}(t) = \zeta_{33}(1 + \varepsilon\cos(\Omega_h t + \phi_{h1})) ; \quad (4.12b)$$

$$g_h(\dot{p}(t)) = \begin{cases} 0; & -\dfrac{b_h}{b_c} < p < \dfrac{b_h}{b_c} \\ \dot{p}(t); & \text{else} \end{cases} \quad (4.12c)$$

Figure 4.7 compares frequency response spectra for the cases of a) non-linear time-varying gear mesh damping defined by equation (4.12), and b) linear time-invariant mesh damping, $\zeta_{33} \neq \zeta_{33}(t)$ with $g_h(\dot{p}(t)) = \dot{p}(t)$, as given by equation (4.5). As shown in Figure 4.7, both mesh damping models yield virtually the same spectra. Therefore a linear time-invariant gear mesh damping model can be used without losing any accuracy.

4.4.4. Periodic $\bar{e}(\bar{t})$ and $k_h(\bar{t})$

Up to now, we have only considered the sinusodally varying $k_h(\bar{t})$ and $\bar{e}(\bar{t})$. In real geared systems, however, both $k_h(\bar{t})$ and $\bar{e}(\bar{t})$ are periodic which can be

181
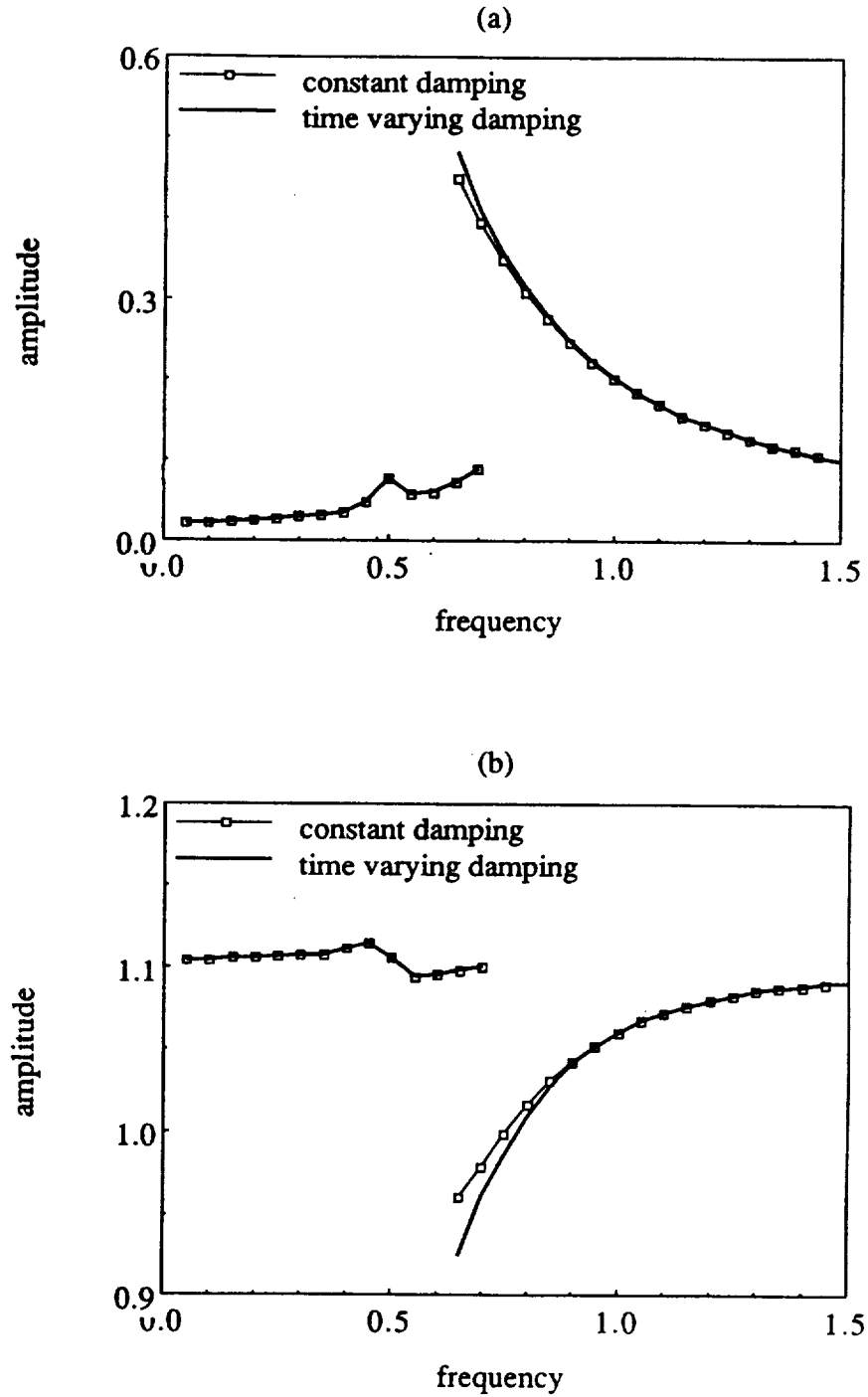
Figure 4.7. Frequency response spectra of gear pair corresponding to non-linear time varying and linear viscous damping models; a)p_a versus Ω_h, b) p_m versus Ω_h.

182

expressed in the Fourier series form. Figure 4.8 illustrates $k_h(\bar{t})$ and $\bar{e}(\bar{t})$ for a low contact ratio spur gear pair; these typical time histories are predicted using an existing spur gear tooth model [21]. The first six Fourier coefficients of $k_h(\bar{t})$ and $\bar{e}(\bar{t})$ are given in Table 4.1. Note that n-th harmonic of $\bar{e}(\bar{t})$ causes a resonance around $\Omega_h = 1/n$. Hence higher harmonics are important only at low frequencies. Accordingly, only the first three Fourier coefficients of $\bar{e}(\bar{t})$ are deemed sufficient here, given the nature of the practical gear noise and vibration problems. Similarly, $k_h(\bar{t})$ is also truncated for the sake of convenience, retaining the first three terms. Higher terms (n>3) could be easily included in the analysis if necessary. Therefore the governing equation with $F_{aT}(t)=0$ is

$$\ddot{p}(t) + 2\zeta_{33}(t)\dot{p}(t) + [1 - \sum_{r=1}^{3}\varepsilon_r \cos(r\Omega_h t)]f_h(p(t)) = F_m + \sum_{r=1}^{3}F_{ahr}(r\Omega_h)^2 \cos(r\Omega_h t)$$

(4.13)

Figures 4.9a and 4.9b show frequency response spectra for $F_m=0.1$, $F_{ah1}=0.05$, $F_{ah2}=0.02$, $F_{ah3}=0.01$, $\zeta_{33}=0.05$, $\varepsilon_1/\varepsilon_2=2$, $\varepsilon_1/\varepsilon_3=4$ and four different $\varepsilon_1=\varepsilon$ values. As shown in Figure 4.9, two other jump discontinuities, which are clearly associated with F_{ah2} and F_{ah3}, are found. These jumps are similar to the fundamental resonance peak except they have lower amplitudes. In order for these two jumps to exist, F_{ah2} and F_{ah3} excitations have to be large. Once again, it is evident that the periodic mesh stiffness enhances the extent of backlash non-linearity.
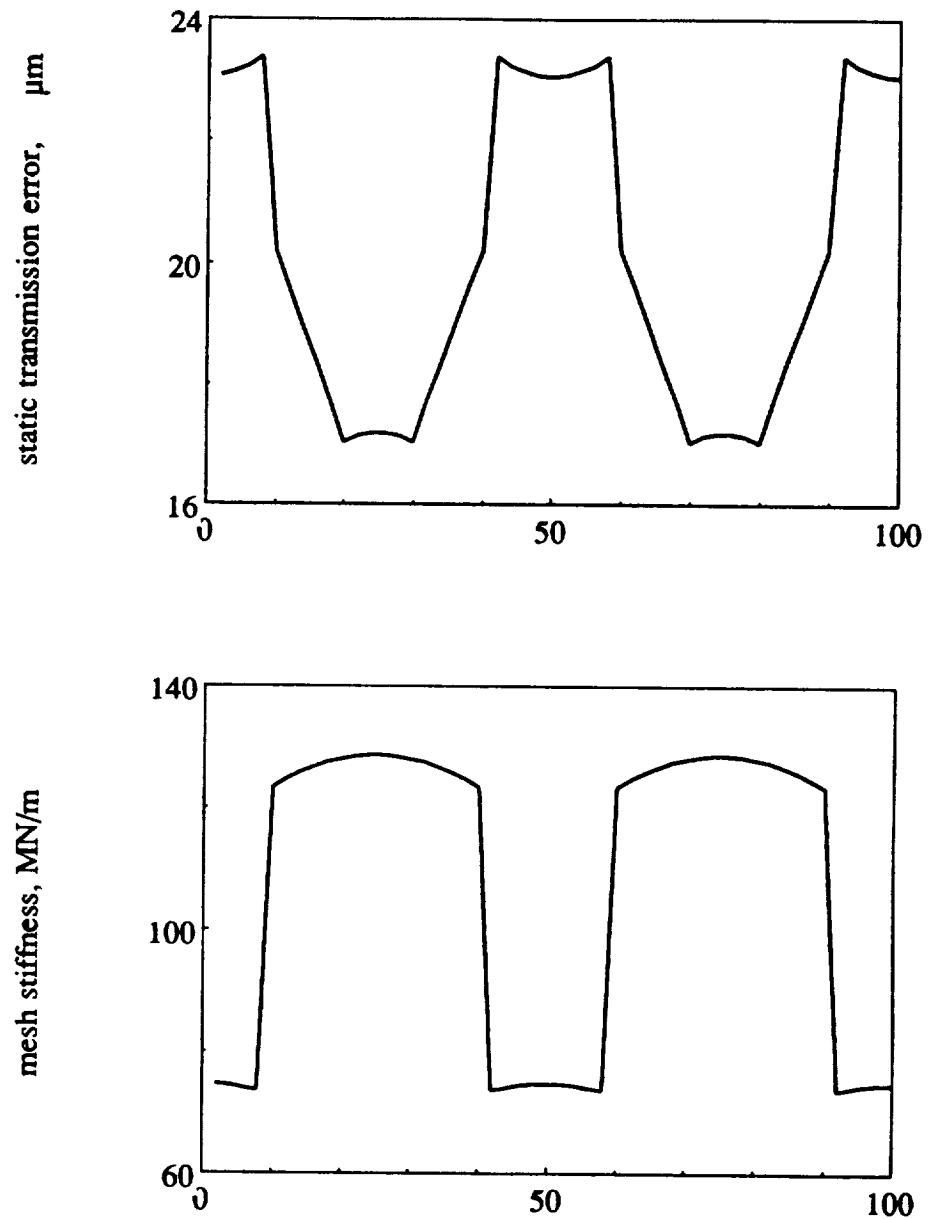
Figure 4.8 $\bar{e}(\bar{t})$ and $k_h(\bar{t})$ plots for a low contact ratio spur gear pair [21]. Here, number of teeth is 28, diametral pitch is 8, the pressure angle is 20 degrees, and a 6×10^{-4} in. tip modification starting at 26 degrees roll angle is applied.

184

Table 4.1   Fourier coefficients of $\bar{e}(\bar{t})$ and $k_h(\bar{t})$ given in Figure 4.8

| Harmonic n	Amplitude	
	$\bar{e}(\bar{t})$ (μm)	$k_h(\bar{t})$ (MN/m)
0	20.00	107.8
1	3.45	10.3
2	0.26	5.7
3	0.45	1.3
4	0.38	4.0
5	0.27	1.5
6	0.26	1.4
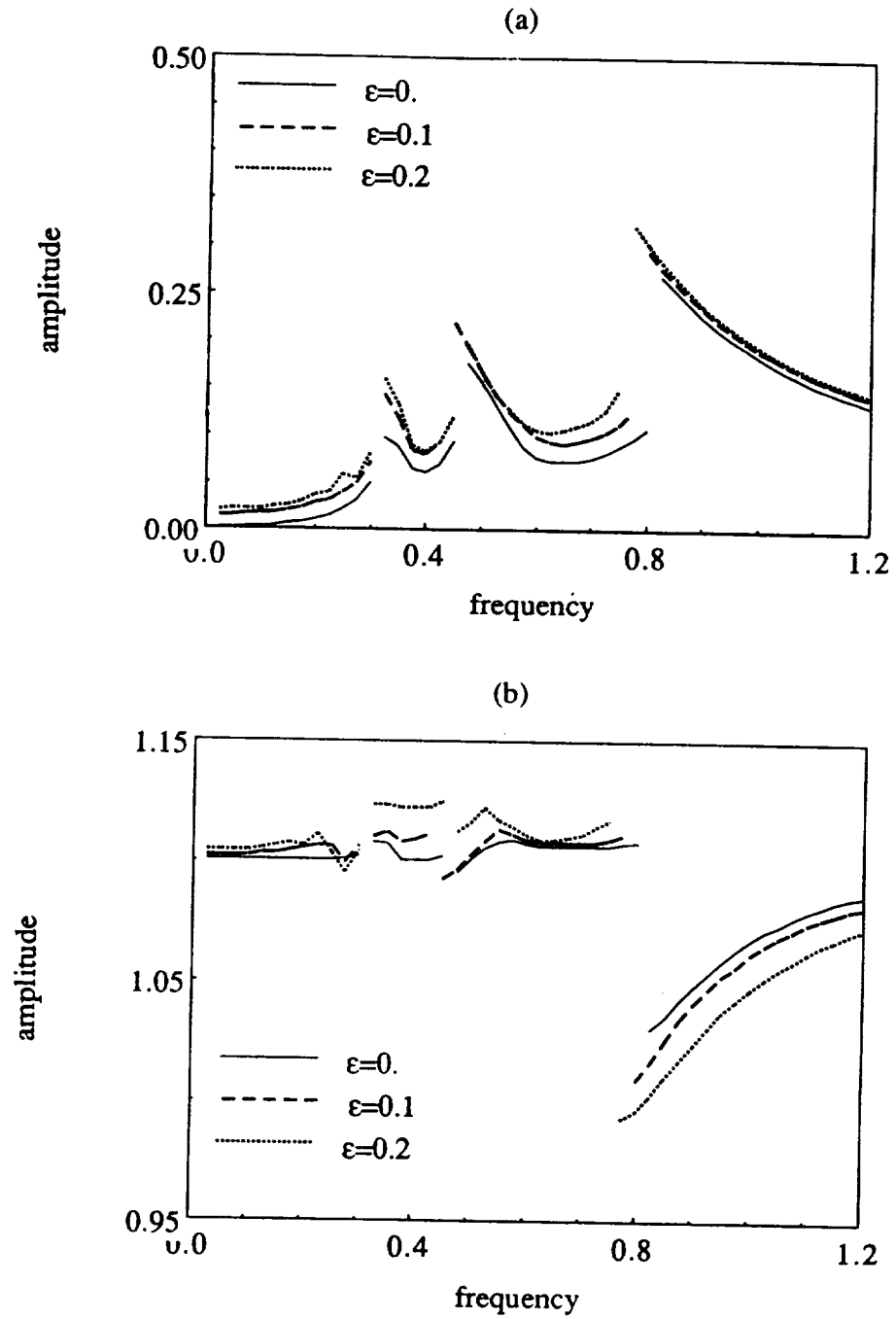
Figure 4.9. Frequency response spectra of a non-linear gear pair with periodic $\bar{e}(\bar{t})$ and $k_h(\bar{t})$, $F_m=0.1$, $F_{ah1}=0.05$, $F_{ah2}=0.02$, $F_{ah3}=0.01$, $\zeta_{33}=0.05$, $b_h=b_c$, $\varepsilon_1/\varepsilon_2=2$, $\varepsilon_1/\varepsilon_3=4$ and four different $\varepsilon_1=\varepsilon$ values; a)p_a versus Ω_h, b) p_m versus Ω_h.

4.5. GEARED ROTOR-BEARING SYSTEM STUDIES

Next, we solve the three degree of freedom non-linear model of Figure 4.2a and equation (4.3a) using the digital simulation technique for excitation $F_{ah}(t)$ with $F_{aT}(t)=0$.

4.5.1. Sinusoidal $\bar{e}(\bar{t})$ and $k_h(\bar{t})$

Similar to Section 4.4, assume sinusoidal forms: $\kappa_{33}(t) = 1 + \varepsilon \cos(\Omega_h t + \phi_{h1})$ and $F_{ah}(t) = F_{ah1}\Omega_h^2 \cos(\Omega_h t + \phi_{e1})$. Equation (4.3a) reduces to an LTV matrix equation when gear backlash and radial bearing clearances are set to zero, i.e. $f_h(p(t))=p(t)$ and $f_{bi}(y_{gi}(t))=y_{gi}(t)$, i=1,2. Figure 4.10 shows $p_a(\Omega_h)$ and $y_{g1a}(\Omega_h)$ spectra of this LTV system under heavily loaded conditions with $F_m=0.1$, $F_{ah1}=0.01$, $\zeta_{33}=0.05$, $\zeta_{i3}=0.0125$ and $\zeta_{ii}=0.01$, i=1, 2. Note that $y_{g1a}=y_{g2a}$ since the gear ratio is one. As shown in Figure 4.10, frequency response has peaks at $\Omega_h=\omega_I=0.4$ and $\Omega_h=\omega_{II}=1.25$ where ω_I and ω_{II} are the natural frequencies of the LTI system, corresponding to the first two coupled transverse-torsional modes. In Figure 10a, we observe a parametric resonance at $2\Omega_h=\omega_I$ similar to the gear pair model of Section 4.4 whereas the parametric resonance at $2\Omega_h=\omega_{II}$ is more obvious in $p_a(\Omega_h)$ spectrum of Figure 4.10b for a larger ε value. Again like the LTV gear pair results of Figure 4.3, y_{g1a} and p_a are amplified with increasing ε in both resonance and off-resonance regions.

Now introduce the gear backlash $b_h=b_c$ to this heavily loaded system; corresponding results are given in Figure 4.11. The most significant effect of $k_h(\bar{t})$ is that it interacts with the gear backlash non-linearity to develop a jump discontinuity at the second primary resonance peak. This is clearly evident from the fact that either backlash or $k_h(\bar{t})$ alone can not cause a jump for such a heavily loaded system.

(a)

(b)
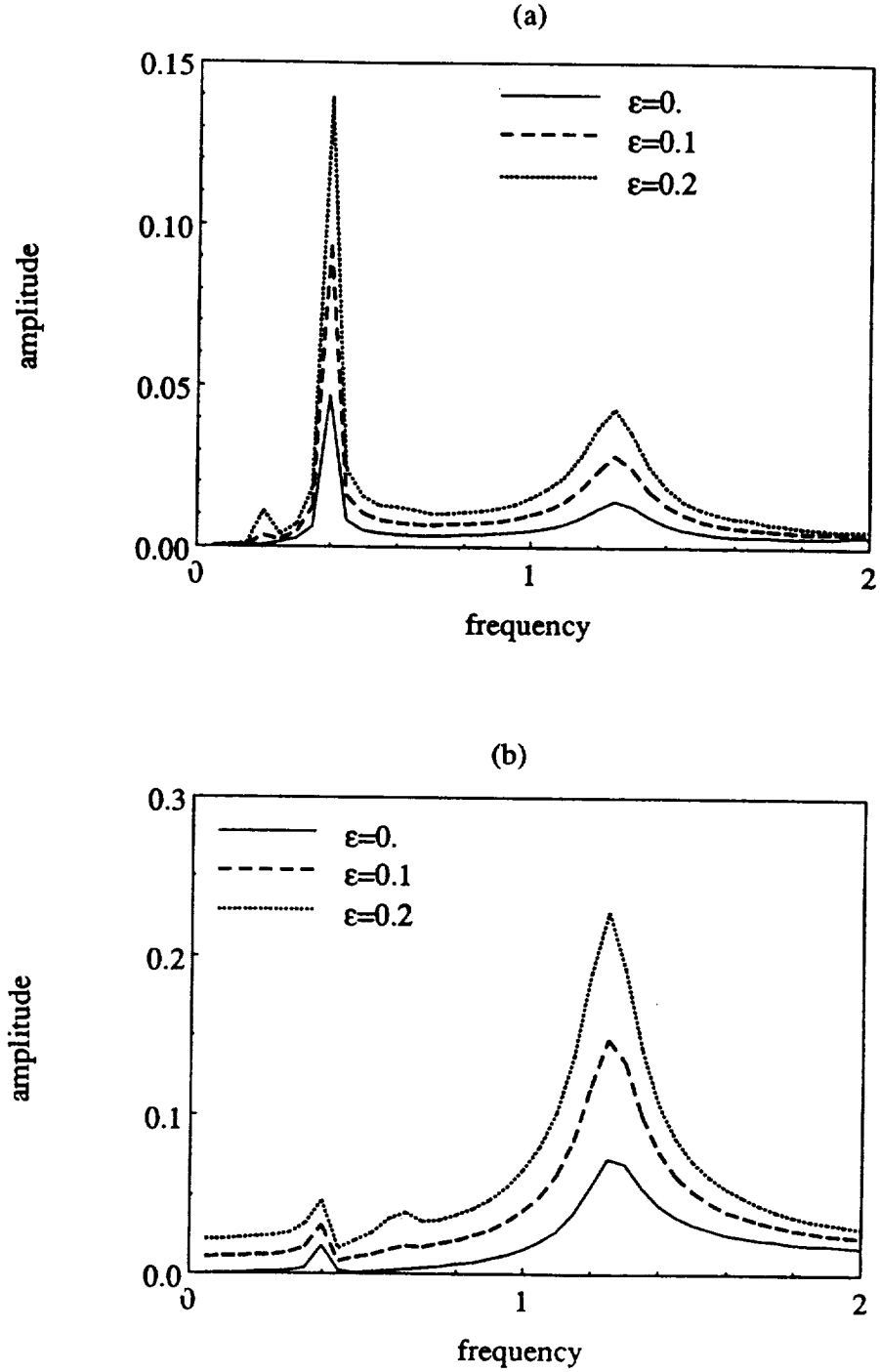
Figure 4.10. Frequency response spectra of a LTV geared rotor-bearing system of Figure 2a with sinusoidal $\bar{e}(\bar{t})$ and $k_h(\bar{t})$, $F_m=0.1$, $F_{ah1}=0.01$, $\zeta_{33}=0.05$, $\zeta_{33}=0.05$, $\zeta_{i3}=0.0125$ and $\zeta_{ii}=0.01$, $\kappa_{ii}=0.5$, $b_h=b_{hbi}=0$, i=1, 2, and four $\varepsilon_1=\varepsilon$ values; a) y_{gia} versus Ω_h, b) p_a versus Ω_h.

188

Besides an increase in amplitudes in Figures 4.11a and 4.11b, chaotic and/or quasi-periodic solutions, which do not exist in heavily loaded time-invariant systems as shown in Chapter III, are also predicted in the following regimes: $1.35 < \Omega_h < 1.65$ for $\varepsilon = 0.2$ and $1.25 < \Omega_h < 1.7$ for $\varepsilon = 0.4$. Similar to the LTV system of Figure 4.10, parametric resonances at $2\Omega_h = \omega_I$ and $2\Omega_h = \omega_{II}$ are again observed here.

Next, radial clearances in bearings $b_{bi} = b_c$ are considered for a heavily loaded system with zero gear backlash, $F_m = 1.0$, $F_{ah1} = 0.1$, $\zeta_{33} = 0.05$, $\zeta_{i3} = 0.0125$ and $\zeta_{ii} = 0.01$, $i=1$, 2. In this case, mesh stiffness variation and non-linearity exist in different components. As shown in Figure 4.12, ε again increases the amplitudes, but the spectrum shape is essentially the same. This is further evident from Figure 4.13, given for a lightly loaded drive with $F_m = 1.0$ and $F_{ah1} = 0.5$. This suggests a weak interaction between the gear mesh stiffness variation and bearing non-linearities.

4.5.2. Periodic $\bar{e}(\bar{t})$ and $k_h(\bar{t})$

Similar to the gear pair analysis of Section 4.4.4, we consider periodic $\kappa_{33}(t)$ and $F_{ah}(t)$ with three Fourier coefficients. Figure 4.14 shows spectra for $F_m = 0.1$, $F_{ah1} = 0.01$, $F_{ah2} = 0.004$, $F_{ah3} = 0.002$, $\zeta_{33} = 0.05$, $\zeta_{i3} = 0.0125$ and $\zeta_{ii} = 0.01$, $i=1$, 2; $\varepsilon_1/\varepsilon_2 = 2$, $\varepsilon_1/\varepsilon_2 = 4$, and $\varepsilon_1 = \varepsilon = 0$, 0.1 and 0.2. Here only the gear backlash non-linearity ($b_h = b_c$ and $b_{bi} = 0$) is considered. Peaks at $\Omega_h = \omega_I/n$ and $\Omega_h = \omega_{II}/n$, $n=1,2,3$ are predicted corresponding to excitation F_{ahr}. Periodic mesh stiffness enhances the alternating amplitudes over the values given by the time-invariant mesh stiffness case and introduces a jump discontinuity at the second primary resonance similar to the sinusoidal mesh stiffness case.
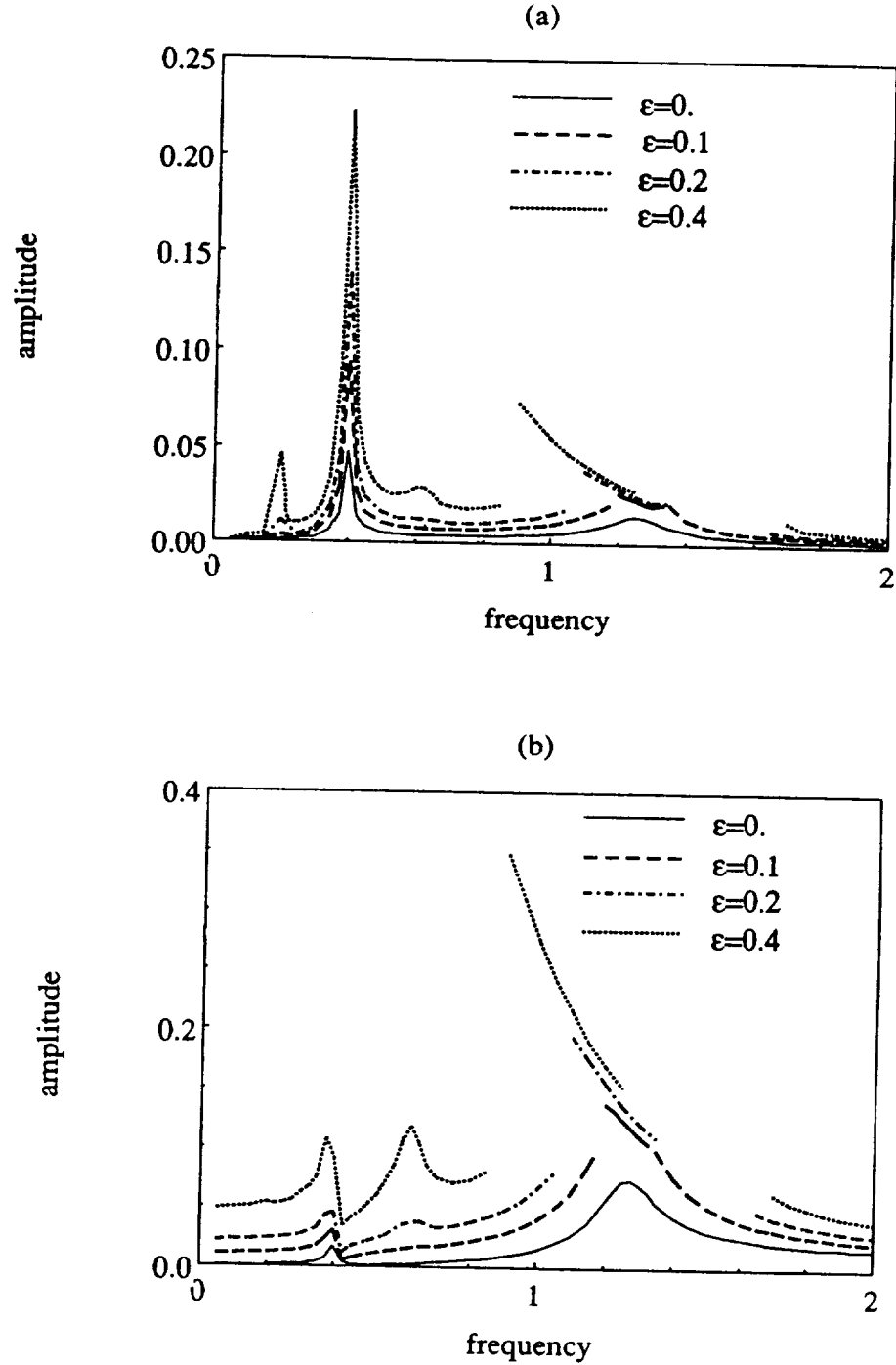
Figure 4.11. Frequency response spectra of a non-linear geared rotor-bearing system with sinusoidal $\bar{e}(\bar{t})$ and $k_h(\bar{t})$, $F_m=0.1$, $F_{ah1}=0.01$, $\zeta_{33}=0.05$, $\zeta_{33}=0.05$, $\zeta_{i3}=0.0125$ and $\zeta_{ii}=0.01$, $\kappa_{ii}=0.5$, $b_h=b_c$, $b_{bi}=0$, $i=1$, 2, and four $\varepsilon_1=\varepsilon$ values; a) y_{gia} versus Ω_h, b) p_a versus Ω_h.

190

(a)

(b)
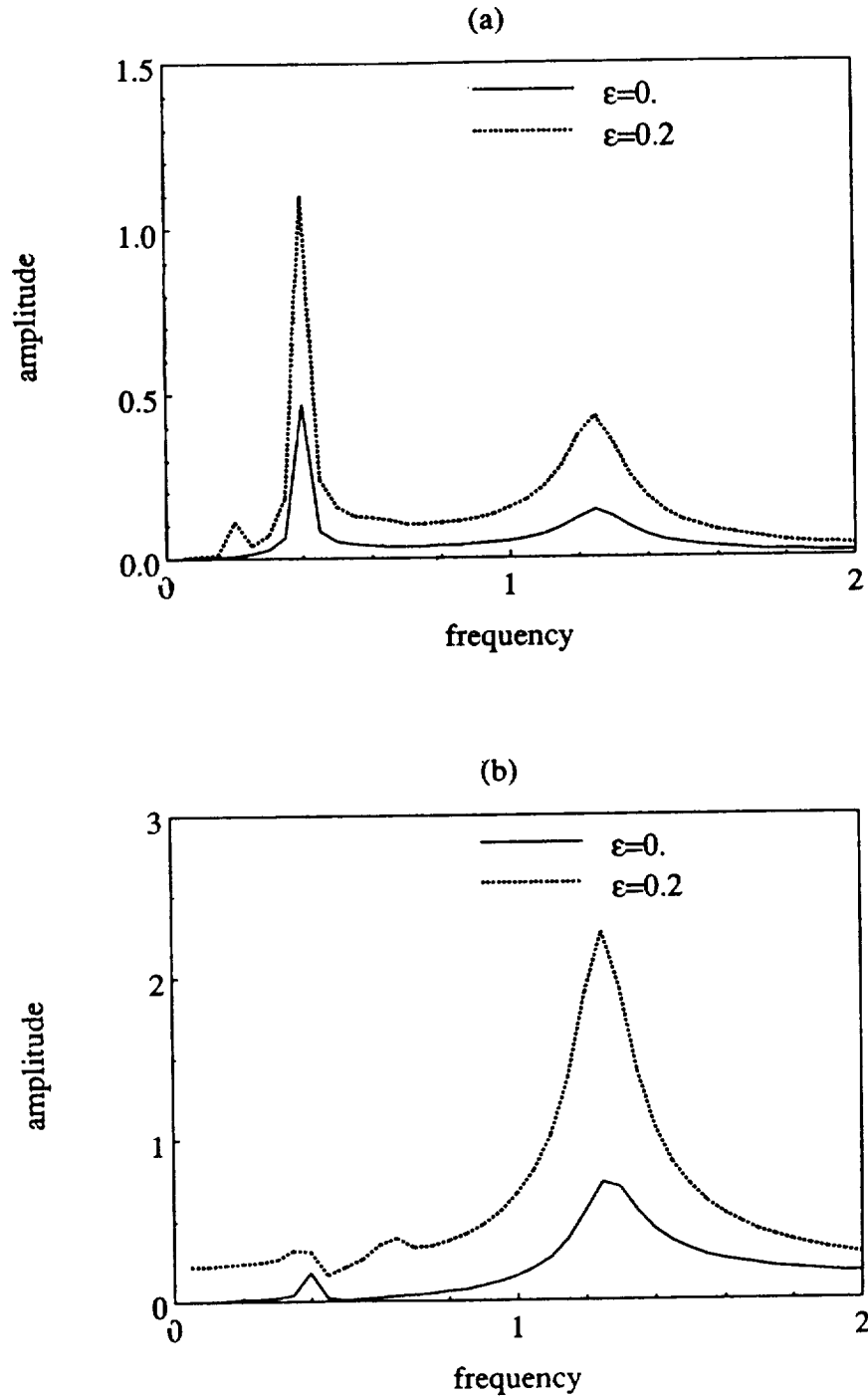
Figure 4.12. Frequency response spectra of a non-linear geared rotor-bearing system with sinusoidal $\bar{e}(\bar{t})$ and $k_h(\bar{t})$, $F_m=1.0$, $F_{ah1}=0.1$, $\zeta_{33}=0.05$, $\zeta_{33}=0.05$, $\zeta_{i3}=0.0125$ and $\zeta_{ii}=0.01$, $\kappa_{ii}=0.5$, $b_{bi}=b_c$, $b_h=0$, $i=1$, 2, and four $\varepsilon_1=\varepsilon$ values; a) y_{gia} versus Ω_h, b) p_a versus Ω_h.

(a)

(b)
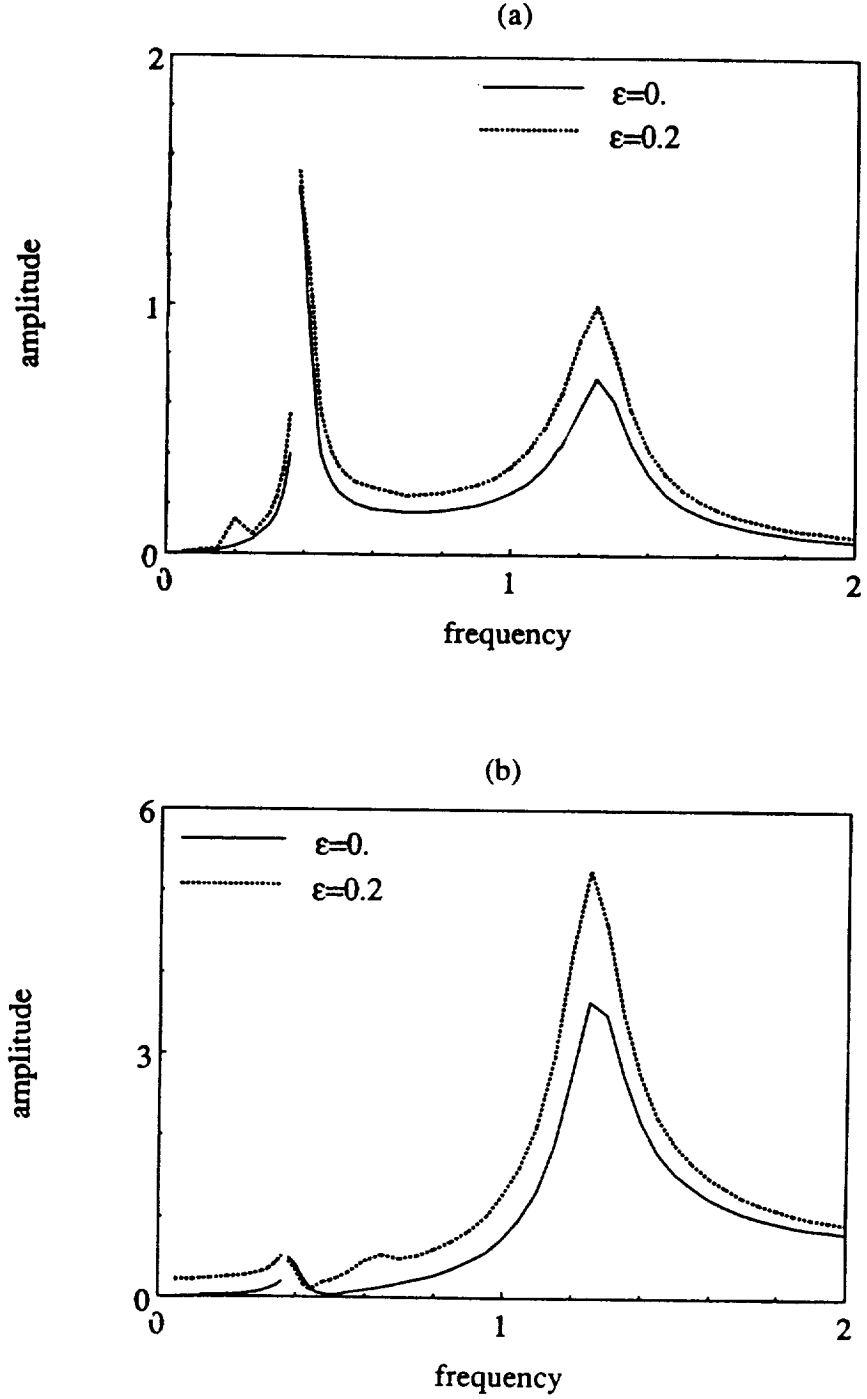
Figure 4.13. Frequency response spectra of a non-linear geared rotor-bearing system with sinusoidal $\bar{e}(\bar{t})$ and $k_h(\bar{t})$, $F_m=1.0$, $F_{ah1}=0.5$, $\zeta_{33}=0.05$, $\zeta_{33}=0.05$, $\zeta_{i3}=0.0125$ and $\zeta_{ii}=0.01$, $\kappa_{ii}=0.5$, $b_{bi}=b_c$, $b_h=0$, $i=1$, 2, and four $\varepsilon_1=\varepsilon$ values; a) y_{gia} versus Ω_h, b) p_a versus Ω_h.

192

(a)

(b)
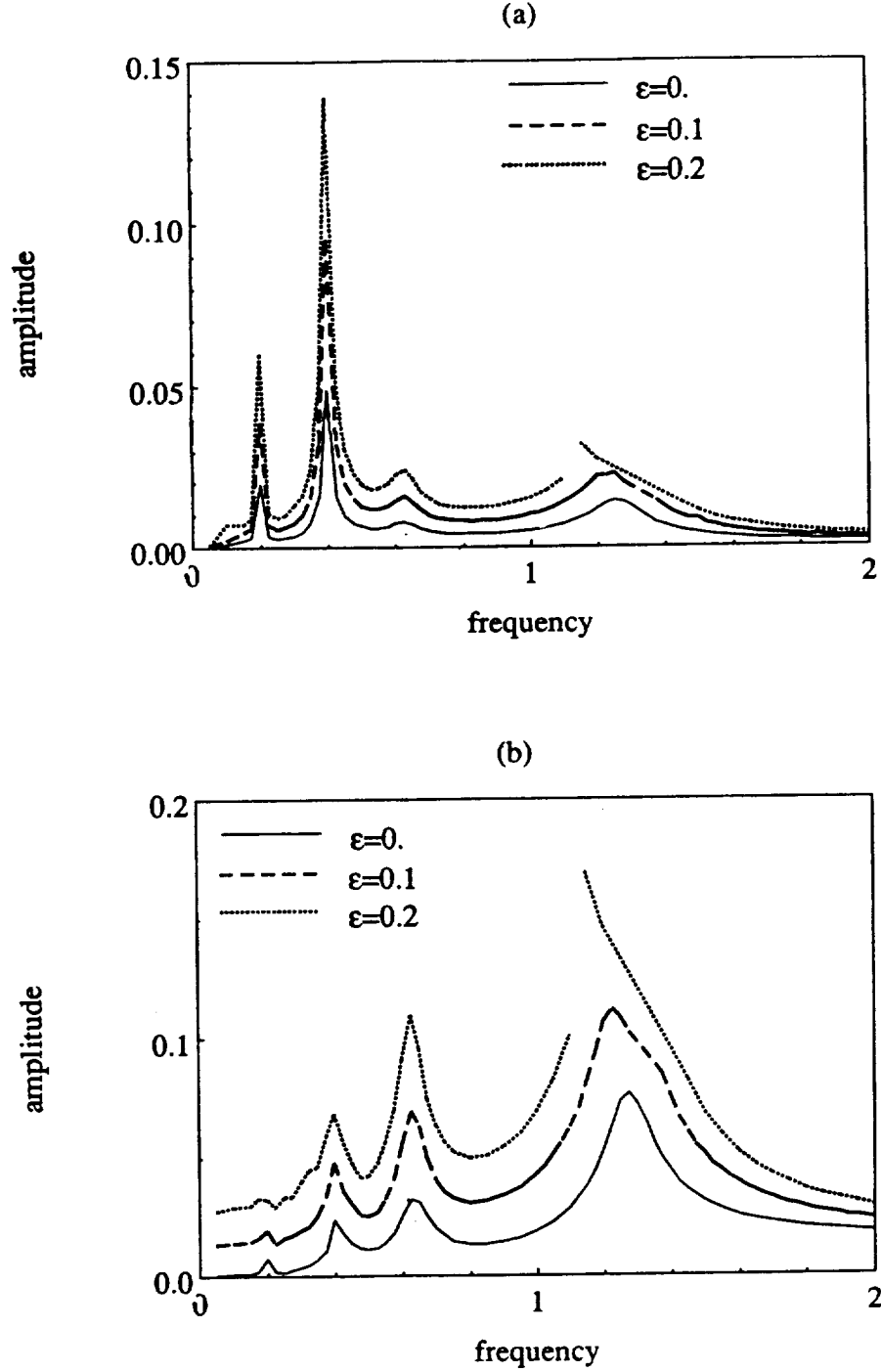
Figure 4.14. Frequency response spectra of a non-linear geared rotor-bearing system with periodic $\bar{e}(\bar{t})$ and $k_h(\bar{t})$, $F_m=0.1$, $F_{ah1}=0.01$, $F_{ah2}=0.004$, $F_{ah3}=0.002$, $\zeta_{33}=0.05$, $\zeta_{33}=0.05$, $\zeta_{i3}=0.0125$ and $\zeta_{ii}=0.01$, $\kappa_{ii}=0.5$, $b_h=b_c$, $b_{bi}=0$, $i=1$, 2, $\varepsilon_1/\varepsilon_2=2$, $\varepsilon_1/\varepsilon_3=4$ and three $\varepsilon_1=\varepsilon$ values; a)y_{gia} versus Ω_h, b) p_a versus Ω_h.

193

4.6. EXPERIMENTAL VALIDATION

4.6.1. Spur Gear Pair Dynamics

First we compare our theory with experimental results of Kubo [28], as extracted from Reference [24]. Kubo used a heavily damped (ζ_{33}=0.1) four-square spur gear test rig, and measured dynamic factor as the ratio of the dynamic to static tooth root stresses. The experimental set-up was designed to support a gear pair with very stiff shafts and bearings. Therefore our gear pair model can represent the test rig adequately, similar to Chapter II. The static transmission error $\bar{e}(\bar{t})$ and time-varying mesh stiffness $k_h(\bar{t})$ of the tested gear pair has been predicted using an existing elastic spur gear model [21] and then equation (4.4) is solved to predict the dynamic response. Here, we define the dynamic factor as the dynamic to static mesh force ratio which is equivalent to the dynamic factor calculation based on the stress analysis under the assumption that the change in the moment arm due to changes in the contact point is negligible. Figure 4.15 compares the envelope of measurements obtained by Kubo for several tooth pairs with our predictions. When the mesh stiffness $k_h(\bar{t})$ is assumed to be time-invariant, the predicted jump discontinuity is not as large as the jump seen in experimental data and the predicted transition frequency is higher than the measured value, as reported in Chapter II. However predictions improve significantly when sinusoidally varying $k_h(\bar{t})$ and $\bar{e}(\bar{t})$ at Ω_h are used, as given by equation (4.5). A sharp jump discontinuity is found which matches well with experiment, and the predicted dynamic factor is very close to measured envelope. Finally, prediction agrees with experiment even better when periodically varying $\overline{e(t)}$ and $\overline{kh(t)}$ with the first three Fourier coefficients considered. This figure clearly shows that the time-invariant linear or non-linear model can not predict the true dynamic behavior, as time-varying mesh stiffness must be included in the non-linear mathematical formulation.

194
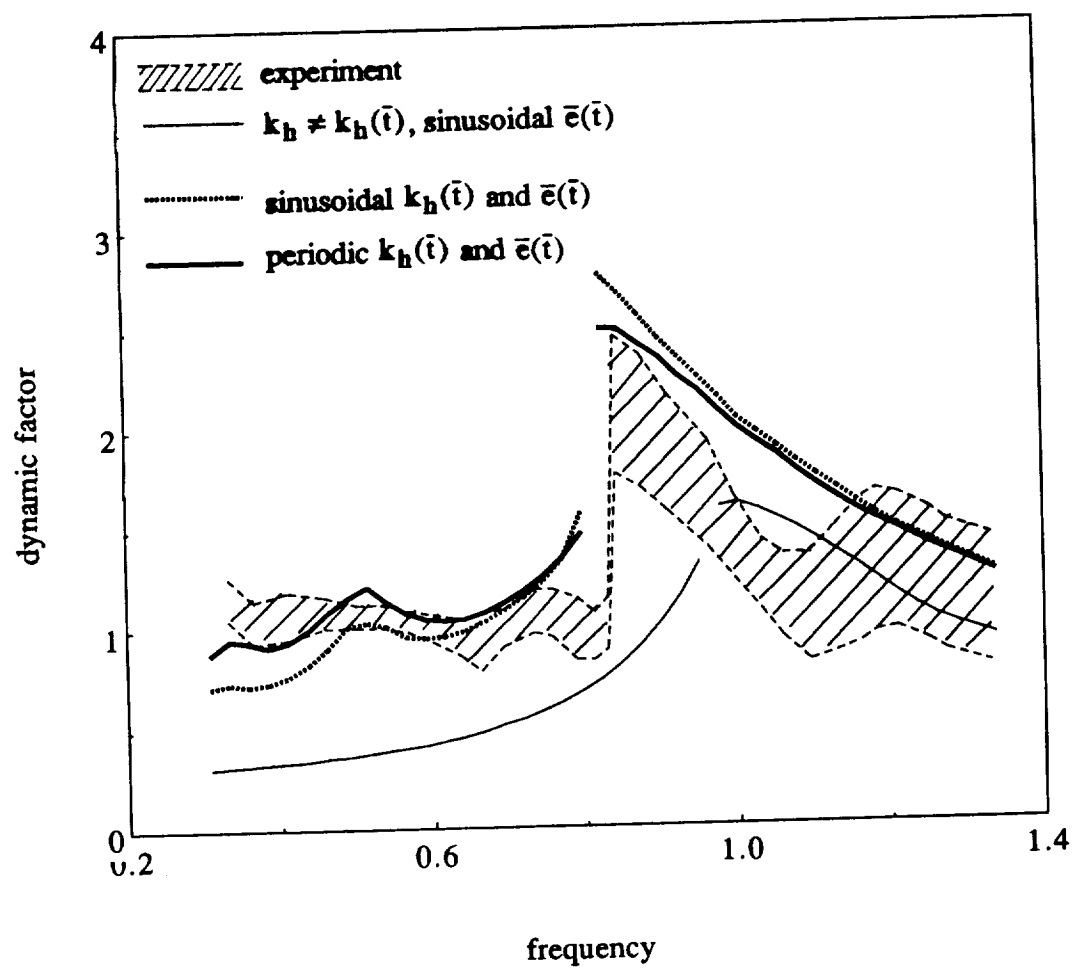
Figure 4.15   Comparison of theory with Kubo's [24,28] experimental results.

195

4.6.2. Geared Rotor-Bearing System

As the second example case, experimental results of Munro [27] are compared with our geared rotor-bearing model of Figure 4.2a and equation (4.3). These experimental results were used earlier to validate time-invariant multi-degree of freedom non-linear system of Chapter III in which we had to reduce the damping ratio and increase the excitation $\bar{e}(\bar{t})$ in order to correlate theory with experiment. Now we go back to the original system parameters given in References [27] and Chapter III, and predict the dynamic transmission error spectra using both time-varying and time-invariant gear mesh stiffness formulations for a three degree of freedom non-linear model with gear backlash and linear bearings. Figure 4.16 compares results at the design load which corresponds to the minimum excitation $\bar{e}(\bar{t})$. In this case, the mean load to alternating load ratio $\hat{F} = F_m / F_{ah1}$ is very large, say $\hat{F} \approx 30$. Time-invariant stiffness model prediction differs considerably from the experiment in Figure 4.16. Predicted amplitudes are considerably lower than the measurements, and a significant jump discontinuity found experimentally around the second natural frequency ω_{II} is not even predicted by this formulation. But when the periodically-varying mesh stiffness is considered, our model predicts the frequency response accurately including the jump discontinuity. The reason for a large jump around ω_{II} for a very heavily loaded system ($\hat{F} \approx 30$) is now clear. The second natural frequency ω_{II} of the corresponding LTI system is nearly twice the first natural frequency ω_I. This forces the second primary resonance at $\Omega_h \approx \omega_{II}$ to coincide with the parametric resonance at $\Omega_h \approx 2\omega_I$; consequently a very large jump discontinuity is developed.

At 3/4 of the design load with $\hat{F} \approx 10$, the effect of $k_h(\bar{t})$ is observed in Figure 4.17. Although the time-invariant model predicts the jump at ω_{II}, predicted amplitudes

196
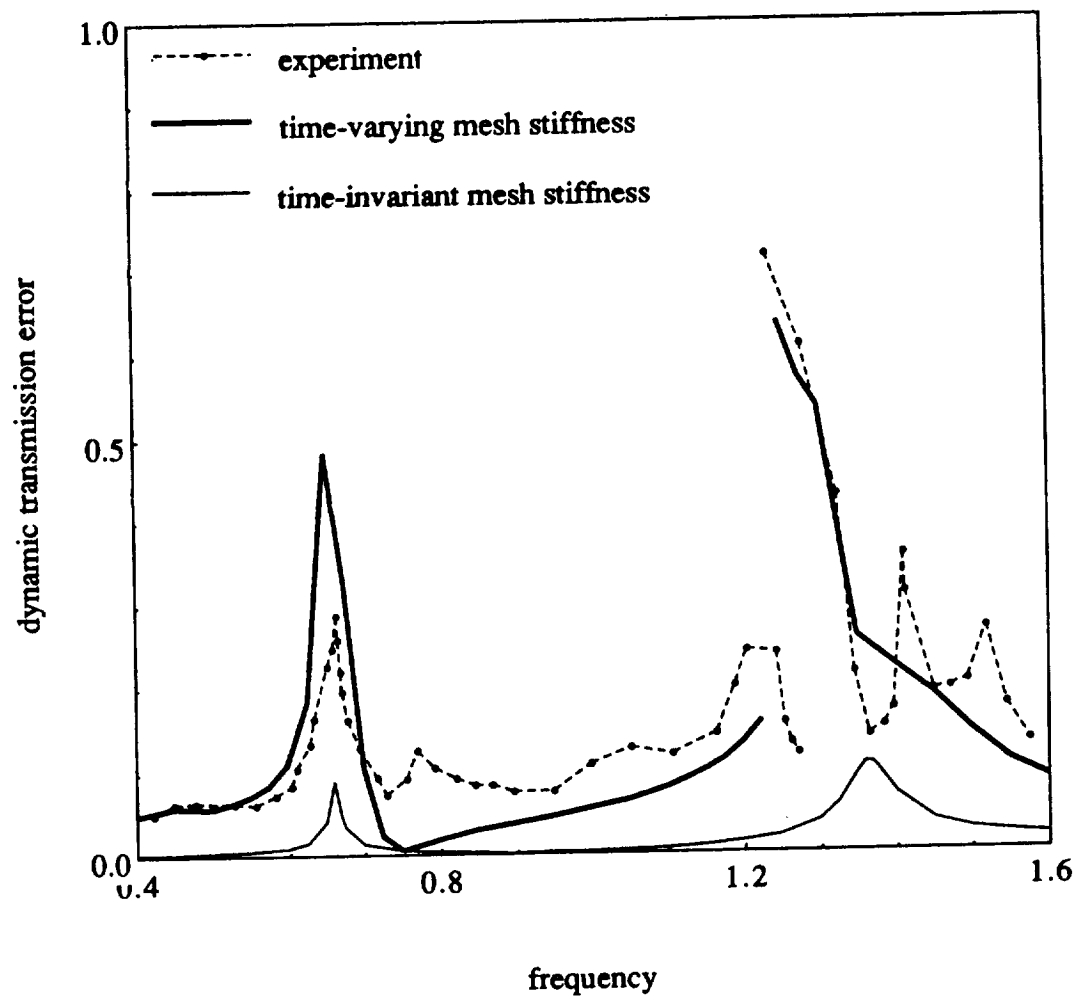
Figure 4.16   Comparison of theory with Munro's [27] experiment at the design load.
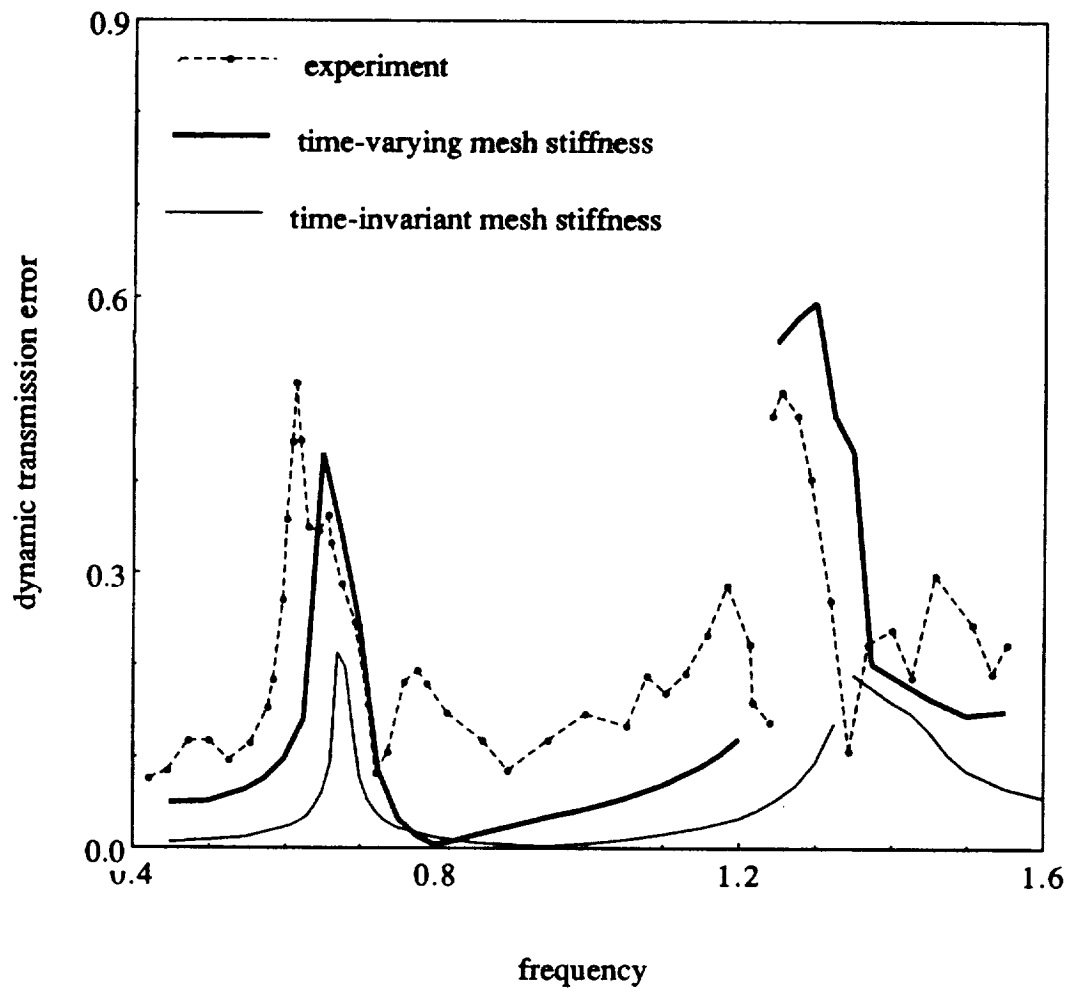
Figure 4.17   Comparison of theory with Munro's [27] experiment at 3/4 of the design load.

198
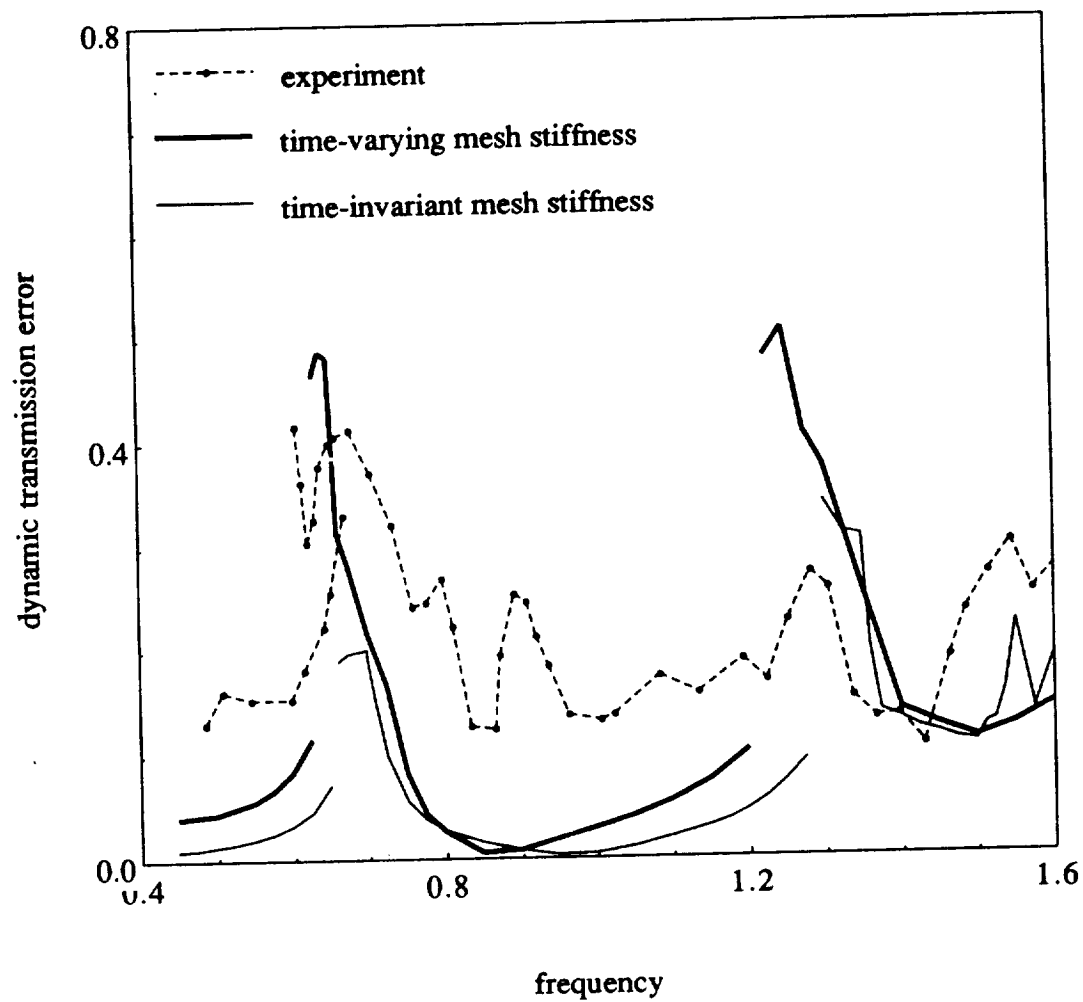
Figure 4.18   Comparison of theory with Munro's [27] experiment at 1/2 of the design load.
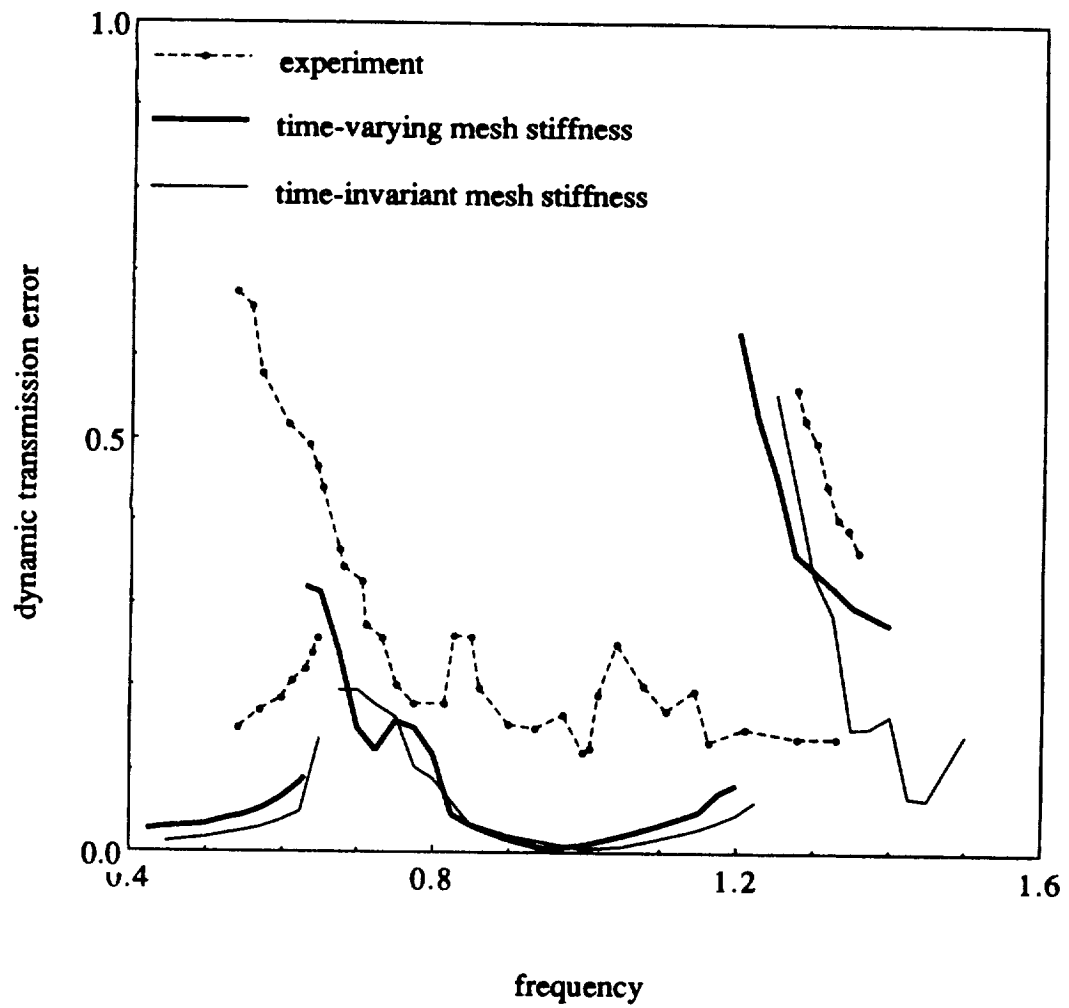
Figure 4.19   Comparison of theory with Munro's [27] experiment at 1/4 of the design load.

are far below the measurements. The inclusion of $k_h(\bar{t})$ improves predictions drastically. Similarly at 1/2 and 1/4 design loads, mesh stiffness variation as shown in Figures 4.18 and 4.19 respectively, affects the frequency response significantly and yields predictions closer to the measurements.

4.7. CONCLUDING REMARKS

This chapter on the non-linear dynamics of a geared rotor-bearing system with time-varying mesh stiffness $k_h(\bar{t})$, as excited by the static transmission error under a mean load, has resolved a number of fundamental issues. First, the interaction between time-varying mesh stiffness $k_h(\bar{t})$ and mean torque load has been understood. Second, frequency response of the corresponding LTV system has been studied, and the resonances associated with parametric and forced excitations have been identified. Third, dynamic interactions between $k_h(\bar{t})$ and system non-linearities associated with gear backlash and radial clearances in rolling element bearings have been investigated; a strong interaction between $k_h(\bar{t})$ and gear backlash is found where as the coupling between $k_h(\bar{t})$ and bearing non-linearities is weak. Finally, our time-varying non-linear formulation has yielded good predictions as compared with benchmark experiments.

CHAPTER V

CONCLUSION

5.1. SUMMARY

In this study, linear and non-linear mathematical models of a generic geared rotor-bearing system shown in Figure 1.1a are developed, and several modeling issues which have never been addressed previously in the literature are investigated in depth. In Chapter I, a dynamic finite element model of the system is developed. Effects of several system parameters such as torsional and transverse flexibilities of the shafts and prime mover/load inertias are investigated, and modes of interest are identified. Three reduced order linear time-invariant models are developed and the conditions under which such models are suitable are determined by comparing the eigen-solutions with the finite element model results.

In Chapter II, non-linear frequency response characteristics of a spur gear pair with backlash and time-invariant mesh stiffness are examined for both external and internal excitations. The internal excitation is of importance from the high frequency noise and vibration control view point and it represents the overall kinematic or static transmission error $\bar{e}(\bar{t})$. Such problems may be significantly different from the rattle problems associated with external, low frequency torque excitation. Two solution methods, namely the digital simulation technique and the method of harmonic balance have been used to develop the steady state solutions for the internal sinusoidal excitation. Difficulties associated with the determination of the multiple solutions at a given frequency in the digital simulation technique have been resolved as one must

search the entire initial conditions map. Such solutions and the transition frequencies for various impact situations are found analytically by the method of harmonic balance. Further, the principle of superposition can be employed to analyze the periodic transmission error excitation and/or combined excitation problems provided the excitation frequencies are sufficiently far apart from each other. Predictions compare reasonably well with the experimental data available in the literature.

In Chapter III, non-linear frequency response characteristics of a geared rotor-bearing system are examined. A three degree of freedom dynamic model is developed which includes non-linearities associated with radial clearances in the radial rolling element bearings and backlash between a spur gear pair; linear time-invariant gear meshing stiffness is assumed. Bearing non-linear stiffness function is approximated for convenience sake by a simple model which is identical to that used for the gear mesh. This approximate bearing model has been verified by comparing the steady state frequency spectra. Applicability of both analytical and numerical solution techniques to the multi-degree of freedom non-linear problem is investigated. Proposed theory is validated by comparing the results with available experimental data. Several key issues such as non-linear modal interactions and differences between internal static transmission error excitation and external torque excitation are discussed. Additionally, parametric studies are performed to understand the effect of system parameters such as bearing stiffness to gear mesh stiffness ratio, alternating to mean force ratio and radial bearing preload to mean force ratio on the non-linear dynamic behavior. A criterion used to classify the steady state solutions is presented, and the conditions for chaotic, quasi-periodic and subharmonic steady state solutions are determined. Two typical routes to chaos observed in this geared system are also identified.

Non-linear frequency response characteristics of a geared rotor-bearing system with time-varying mesh stiffness are examined in Chapter IV. The spur gear pair model of Chapters II and geared rotor-bearing system model of Chapter III are modified to include periodic mesh stiffness $k_h(\bar{t})$. Governing non-linear time-varying equations which include clearance non-linearities associated with gear backlash and rolling element bearings, as excited by the static transmission error $\bar{e}(\bar{t})$ under a mean torque load, are solved using digital simulation technique. Resonances of the corresponding linear time-varying (LTV) system associated with parametric and external excitations are identified using the method of multiple scales and digital simulation. Interactions between mesh stiffness variation and clearance non-linearities have been investigated; a strong interaction between time varying mesh stiffness $k_h(\bar{t})$ and gear backlash is found whereas the coupling between $k_h(\bar{t})$ and bearing non-linearities is weak. The predictions yielded by the proposed time-varying non-linear model agree well with the experimental results available in the literature.

5.2 FUTURE RESEARCH AREAS

The following topics are identified as areas of future research, based on the present study on non-linear dynamic analysis of geared rotor-bearing systems:

1. Extension of current models to study dynamics of helical and bevel gear drives, and multi-gear mesh systems such as planetary gear trains.

2. Iteration procedures for the transmission error input and inclusion of the interactions between external and internal kinematic error excitations. Also inclusion of side-bands in non-linear dynamic analysis.

3. Design of a passive vibration control strategy using squeeze film dampers. And, investigation of semi-active and active vibration and noise control schemes using piezoelectric actuators or hydraulic mounts.

4. Statistical energy analysis of non-linear geared systems.

REFERENCES

1. H. D. NELSON and J. M. MCVAUGH 1976 *Journal of Engineering for Industry, American Society of Mechanical Engineers* 98, 593-600. The dynamics of rotor-bearing systems using finite elements.

2. E. S. ZORZI and H. D. NELSON 1977 *Journal of Eng. for Power, American Society of Mechanical Engineers* 99, 71-76. Finite element simulation of rotor-bearing systems with internal damping.

3. H. D. NELSON 1980 *Journal of Mechanical Design, American Society of Mechanical Engineers* 102, 793-803. A finite rotating shaft element using Timoshenko beam theory.

4. H. N. OZGUVEN and Z. L. OZKAN 1983 *American Society of Mechanical Engineers Paper* 83-DET-89. Whirl speeds and unbalance response of multi-bearing rotors using finite elements.

5. L. D. MITCHELL and D. M. MELLEN 1975 *American Society of Mechanical Engineers Paper* 75-DET-75. Torsional-lateral coupling in a geared high-speed rotor system.

6. J. W. LUND 1978 *Journal of Mechanical Design, American Society of Mechanical Engineers* 100, 535-538. Critical speeds, stability and response of a geared train of rotors.

7. B. M. HAMAD and A. SEIREG 1980 *Journal of Engineering for Power, American Society of Mechanical Engineers* 102, 508-510. Simulation of whirl interaction in pinion-gear systems supported on oil film bearings.

8. H. IIDA, A. TAMURA, K. KIKUCHI and H. AGATA 1980 *Bulletin of Japanese Society of Mechanical Engineers* 23, 2111-2117. Coupled torsional-flexural vibration of a shaft in a geared system of rotors (1st report).

9. H. IIDA and A. TAMURA 1984 Proceedings, Conference on Vibration in Rotating Machinery, Institution of Mechanical Engineers, 67-72. Coupled torsional-flexural vibration of a shaft in a geared system.

10. H. IIDA, A. TAMURA and M. OONISHI 1985 *Bulletin of the Japanese Society of Mechanical Engineers* 28, 2694-2698. Coupled dynamic characteristics of a counter shaft in a gear train system.

11. H. IIDA, A. TAMURA and H. YAMAMOTO 1986 *Bulletin of the Japanese Society of Mechanical Engineers* 29, 1811-1816. Dynamic characteristics of a gear train system with softly supported shafts.

12. N. HAGIWARA, M. IDA and K. KIKUCHI 1981 Proceedings of International Symposium of Gearing and Power Transmissions (Tokyo), 85-90. Forced vibration of a pinion-gear system supported on journal bearings.

13. S. V. NERIYA, R. B. BHAT and T. S. SANKAR 1985 *The Shock and Vibration Bulletin* 55, 13-25. Coupled torsional flexural vibration of a geared shaft system using finite element method.

14. H. N. OZGUVEN and D. R. HOUSER 1988 *Journal of Sound and Vibration* 121, 383-411. Mathematical models used in gear dynamics - a review.

15. A. KAHRAMAN, H. N. OZGUVEN, D. R. HOUSER and J. J. ZAKRAJSEK 1989 Proceedings of the ASME 5th International Power Transmission and Gearing Conference, Chicago. Dynamic analysis of geared rotors by finite elements.

16. D. DUDLEY 1984 *Handbook of Practical Gear Design*. New York: McGraw-Hill.

17. D. B. WELBOURN 1979 *Proceedings of the Conference on Noise and Vibrations of Engines and Transmissions, Institution of Mechanical Engineers*, 9-14. Fundamental knowledge of gear noise-a survey.

18. D. R. HOUSER 1988 *Proceedings of Inter-Noise 88* 601-606 . Gear noise state of the art.

19. C. TROEDER, H. PEEKEN, A. LASCHET and K. TOOTEN 1983 *Proceedings of International Federation of the Theory of Machines and Mechanisms Sixth World Congress, New Delhi*, 2, 936-943. Causes and effect of torque change in hammering of toothed gears.

20. T. HAYASHI, N. NISHI, T. OHNO and F. R. E. CROSSLEY 1979 *Proceedings of the Forth World Congress on the Theory of Machines and Mechanisms* , 350-353. Multiple impacts of a cylinder between two planes and of a meshing teeth of a pair of gears.

21. M. S. TAVAKOLI and D. R. HOUSER 1986 *Journal of mechanisms, Transmissions and Automation in Design, Transactions of the American Society of Mechanical Engineers* 108, 86-95. Optimum profile modifications for the minimization of static transmission errors of spur gears.

22. R. G. MUNRO 1967 *The Aerospace Committee meeting of the American Gear Manufacturers Association* 1-11. Gear transmission error.

23. W. D. MARK 1987 *Journal of mechanisms, Transmissions and Automation in Design, Transactions of the American Society of Mechanical Engineers* 109, 283-291. Use of the generalized transmission error in the equations of motion of gear systems.

24. H, N. OZGUVEN and D. R. HOUSER 1988 *Journal of Sound and Vibration* **125**, 71-83. Dynamic analysis of high speed gears by using loaded static transmission error.

25. K ICHIMARU and F. HIRANO 1974 *Journal of Engineering for Industry, Transactions of the American Society of Mechanical Engineers* **96**, 373-381. Dynamic behavior of heavily-loaded spur gears.

26. E. P. REMMERS 1971 *American Society of Mechanical Engineers Paper* 71-DE-23. The dynamics of a gear pair system.

27. R. G. MUNRO 1962 *Ph. D. Dissertation, Cambridge University.* The dynamic behaviour of spur gears.

28. A. KUBO, K. YAMADA, T. AIDA and S. SATO 1972 *Transactions of Japanese Society of Mechanical Engineers* **38**, 2692-2715. Research on ultra high speed gear devices (reports 1-3).

29. K. UMEZAWA, T. SATA and J. ISHIKAWA 1984 *Bulletin of the Japanese Society of Mechanical Engineers* **38**, 102-109. Simulation of rotational vibration of spur gears.

30. T. SAKAI, Y. DOI, K. YAMATOMO, T. OGASAWARA and M. NARITA 1981 *SAE Paper* 810773. Theoretical and experimental analysis of rattling noise of automative gearbox.

31. S. OHNUMA, Y. SHIGETARO, I. MINEICHI and T. FUJIMOTO 1985 *SAE Paper* 850979. Research on the idling rattle of manual transmission.

32. D. C. H. YANG and J. Y. LIN 1987 *Journal of mechanisms, Transmissions and Automation in Design, Transactions of the American Society of Mechanical Engineers* **109**, 189-196. Hertzian damping, tooth friction and bending elasticity in gear impact dynamics.

33. R. J. COMPARIN and R. SINGH 1989 *Journal of Sound and Vibration* 133. Nonlinear frequency response characteristics of an impact pair.

34. R. SINGH, H. XIE and R. J. COMPARIN 1989 *Journal of Sound and Vibration* 130. Analysis of an automative neutral gear rattle.

35. F. KUCUKAY 1984 *Proceedings of the Third Conference on Vibrations of Rotating Machinery, Institution of Mechanical Engineers* 73-79. Dynamic loads in gear teeth.

36. R. C. AZAR and F. R. E. CROSSLEY 1977 *Journal of Engineering for Industry, Transactions of the American Society of Mechanical Engineers* 99, 792-798. Digital simulation of impact phenomenon in spur gear systems.

37. K. NAKAMURA 1967 *Bulletin of Japanese Society of Mechanical Engineers* 10, 846-854. Tooth separation and abnormal noise on power transmission gears.

38. H. H. LIN, R. L. HUSTON and J. J. COY 1987 *NASA Technical Memorandum* 100180. On dynamic loads in parallel shaft transmissions, I-modeling and analysis.

39. C. W. GEAR 1984 *Computer Aided Analysis and Optimization of Mechanical Systems, NATO ASI Series* F9, 323-334. Differential-algebraic equations.

40. C. W. GEAR 1984 *Computer Aided Analysis and Optimization of Mechanical Systems, NATO ASI Series* F9. 335-349. The numerical solution of problems which may have high frequency components.

41. C. C. WANG 1978 *Journal of Mechanical Design, Transactions of the American Society of Mechanical Engineers* 100, 363-373. Rotational vibration with backlash: Part 1.

42. C. C. WANG 1981 *Journal of Mechanical Design, Transactions of the American Society of Mechanical Engineers* **103**, 387-397. Rotational vibration with backlash: Part 2.

43. S. W. SHAW and P. J. HOLMES 1983 *Journal of Sound and Vibration* **90**, 129-155. A periodically forced piecewise linear oscillator.

44. F. C. MOON and S. W. SHAW 1983 International *Journal of Non-Linear Mechanics* **18**, 465-477. Chaotic vibrations of a beam with non-linear boundary conditions.

45. G. S. WHISTON 1979 *Journal of Sound and Vibration* **67**, 179-186. Impacting under harmonic excitation.

46. G. S. WHISTON 1987 *Journal of Sound and Vibration* **115**, 303-319. The vibro-impact response of a harmonically excited and preloaded one-dimensional linear oscillator.

47. G. S. WHISTON 1987 *Journal of Sound and Vibration* **118**, 395-429. Global dynamics of a vibro-impacting linear oscillator.

48. Y. UEDA 1980 *New Approaches to Nonlinear Problems in Dynamics*. SIAM: Philadelphia. 311-322. Steady motions exhibited by Duffing's equation: A picture book of regular and chaotic motion.

49. J. M. T. THOMPSON and H. B. STEWART 1986 *Nonlinear Dynamics and Chaos*. John Wiley and Sons: Chichester.

50. IMSL INC. 1986 *IMSL Users Manual*.

51. A. GELB and W. E. VANDER VELDE 1968 *Miltiple Input Describing Functions and Nonlinear System Design*. McGraw-Hill: New York.

52. L. E. GALHOUD, S. F. MASRI and J. C. ANDERSON 1987 *Journal of Applied Mechanics, Transactions of the American Society of Mechanical Engineers* 54, 215-225. Transfer function of a class of nonlinear multidegree of freedom oscillators.

53. H. WINTER and M. KOJIMA 1981 Proceedings of the International Symposium on Gearing & Power Transmissions, Tokyo c-12. A study on the dynamics of geared system - estimation of overload on gears in system.

54. R. J. COMPARIN and R. SINGH 1989 Submitted to *Journal of Sound and Vibration* . Frequency response characteristics of coupled impact pairs.

55. R. J. COMPARIN and R. SINGH 1989 *Journal of Mechanical Design, Transactions of the American Society of Mechanical Engineers* (in press). An analytical study of automotive neutral gear rattle.

56. A. H. NAYFEH 1983 *Journal of Sound and Vibration* 90, 237-244. The response of multidegree-of-freedom systems with quadratic non-linearities to a harmonic parametric resonance.

57. A. G. HADDOW, A. D. S. BARR and D. T. MOOK 1984 *Journal of Sound and Vibration* 97, 451-473. Theoretical and experimental study of modal interaction in a two-degree-of freedom structure.

58. D. T. MOOK, R. H. PLAUT and N. HAQUANG 1985 *Journal of Sound and Vibration* 102, 473-492. The influence of an internal resonance on non-linear structural vibrations under subharmonic resonance conditions.

59. D. T. MOOK, N. HAQUANG and R. H. PLAUT 1986 *Journal of Sound and Vibration* 104, 229-241. The influence of an internal resonance on non-linear structural vibrations under combined resonance conditions.

60. M. P. CARTMELL and J. W. ROBERTS 1988 *Journal of Sound and Vibration* **123**, 81-101. Simultaneous combination resonances in an autoparametric resonant system.

61. D. A. STREIT, A. K. BAJAJ and C. M. KROUSGRILL 1988 *Journal of Sound and Vibration* **124**, 297-314. Combination parametric resonance leading to periodic and chaotic response in two-degree-of freedom systems with quadratic non-linearities.

62. M. HORTEL 1967 Proceedings of the Fourth Conference on Non-linear Oscillations, 337-346. Forced damped vibrations in a nonlinear parametric system of gears with several degrees of freedom.

63. T. A. HARRIS 1966 *Rolling Bearing Analysis*. John Wiley and Sons: New York.

64. M. F. WHITE 1979 *Journal of Applied Mechanics, Transactions of the American Society of Mechanical Engineers* **46**, 677-684. Rolling element bearing vibration transfer characteristics: effect of stiffness.

65. T. C. LIM and R. SINGH 1989 Submitted to *Journal of Sound and Vibration*. Vibration transmission through rolling element bearings, part I: bearing stiffness formulation.

66. F. C. MOON 1987 *Chaotic Vibrations*. John Wiley & Sons: New York.

67. C. GREBOGI, E. OTT, S. PELIKAN and J. A. YORKE 1984 *Physica* 13D, 261-268. Strange attractors that are not chaotic.

68. J. M. T. THOMPSON and H. B. STEWART 1986 *Nonlinear Dynamics and Chaos*. John Wiley and Sons: Chichester.

69. J. D. CRAWFORD and S. OMOHUNDRO 1984 *Physica* 13D, 161-180. On the global structure of period doubling flows.

70. J. B. MCLAUGHLIN 1981 *Journal of Statistical Physics* 24, 375-388. Period-doubling bifurcations and chaotic motion for a parametrically forced pendulum.

71. H. G. SCHUSTER 1984 *Deterministic Chaos*. Physik-Verlag: Weinheim.

72. A. KUBO 1989 Private communication.

73. J. KRAUS, J. J. BLECH and S. G. BRAUN 1987 *Journal of Vibration, Acoustics, Stress, and Reliability in Design, Transactions of the American Society of Mechanical Engineers* 109, 235-240. In situ determination of rolling bearing stiffness and damping by modal analysis.

74. R. G. MUNRO 1989 Private communication.

75. H. N. OZGUVEN 1989 Research Report, the Ohio State University, Columbus, Ohio.

76. A. H. NAYFEH and D. T. MOOK 1979 *Nonlinear Oscillations*. Wiley-Interscience: New York.

77. A. H. NAYFEH 1985 *Problems in Perturbation*.Wiley-Interscience: New York.
78. J. A. RICHARDS 1983 *Analysis of Periodically Time-Varying Systems*. Springer-Verlag: New York.

79. H. TROGER and C. S. HSU 1977 *Journal of Applied Mechanics, Transactions of the American Society of Mechanical Engineers* 44, 179-181. Response of a nonlinear system under combined parametric and forcing excitation.

80. C. S. HSU and W. H. CHENG 1974 *Journal of Applied Mechanics, Transactions of the American Society of Mechanical Engineers* 41, 371-378.

Steady state response of a dynamical system under combined parametric and forcing excitation.

81. N. HAQUANG, D. T. MOOK and R. H. PLAUT 1987 *Journal of Sound and Vibrations* 118, 425-439. A non-linear analysis of the interactions between parametric and external excitations.

82. N. HAQUANG 1986 *Ph.D. Thesis, Virginia Polytechnic Institute and State University*. Response of non-linear structural systems to multifrequency excitations.

APPENDIX A

USER'S GUIDE FOR THE GEARED ROTOR DYNAMICS
PROGRAM - GRD

A.1. DESCRIPTION

Geared Rotor Dynamics Program "GRD" is a general purpose finite element computer program to analyze dynamics of a system consisting of two shafts supported on bearings and coupled by a gear mesh. It computes natural frequencies, mode shapes and the vibration response of the system to static transmission error excitation, mass unbalances and geometric eccentricities of gears. Many rigid disks, bearings, and hollow shafts can be considered by GRD. Since GRD uses finite elements method, the system should first be discretized to small rotor elements. It is also necessary to enter data for each element in sequence.

A.2. USING THE PROGRAM

There are two ways to input data in GRD. Data can be entered through a file or interactively. The first set of questions will give the user this option (the Primary Option). Display on screen:

```
ENTER DATA INTERACTIVELY OR FROM A DATA FILE?
OPTION (1) : ENTER DATA INTERACTIVELY
OPTION (2) : ENTER DATA FROM FILE
CHOOSE OPTION 1 OR 2 (NO DEFAULT)          >> __
```

A.2.1. OPTION I: Interactive Data Entry

By selecting this option, the user will be prompted to enter all the data that will be necessary to run this program. In the process, a new data file will be created from the user's input. The data entered will be reorganized in a format so that the program may read from it. For this reason, a new data file will be created and the user will be prompted to name this new file as follows:

```
DATA WILL BE INPUT INTERACTIVELY, AND IN THE PROCESS, YOUR INPUT
WILL BE ORGANIZED IN A NEW DATA FILE FOR THIS PROGRAM TO
READ FROM.
ENTER AN INPUT FILE NAME >> __
```

If an error should arise from opening this new file, the user will be given the option to try again:

```
*ERROR IN OPENING FILE* DO YOU WISH TO TRY AGAIN?
TYPE (1) FOR YES OR (2) FOR NO >>__
```

If YES, then the user will be asked the file name again. If NO, the program will return to the Primary Option.

2.1.1. Data Entry Groupings

In this section, the user will enter the necessary data. The questions will be grouped into the following categories.

```
1. GENERAL DATA
2. MATERIAL PROPERTIES
3. ELEMENT PROPERTIES
4. GEAR MESH PROPERTIES
5. FORCED RESPONSE DATA (If user chooses this option)
```

1. General Data:

In this section, the following general information about the overall system will be entered:

```
1) THE NUMBER OF ROTOR ELEMENTS IN THE FIRST SHAFT
2) THE NUMBER OF ROTOR ELEMENTS IN THE SECOND SHAFT
3) THE NUMBER OF ROTOR ELEMENTS BEFORE THE GEAR IN THE FIRST SHAFT
4) THE NUMBER OF ROTOR ELEMENTS BEFORE THE GEAR IN THE SECOND
   SHAFT
```

As an example, consider the system shown in Figure A1. The first step is to the divide rotors into small pieces (finite rotor elements) to obtain a finite element model of the system (as illustrated in Figure A2). The shorter the rotor elements, the higher the accuracy and the longer the computation time. In Figure A2, each shaft is divided into 4 pieces. The numbering can start at any end of the driving rotor and finish at any end

217
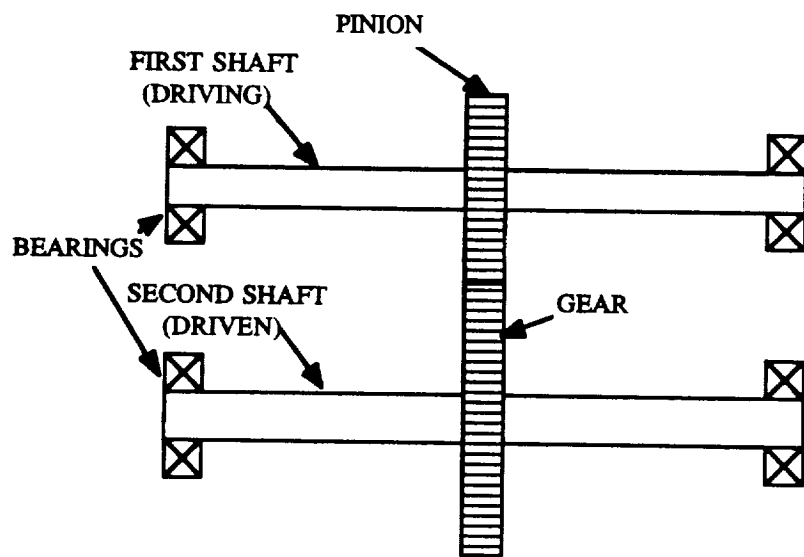
Figure A1. A Typical Geared Rotor System
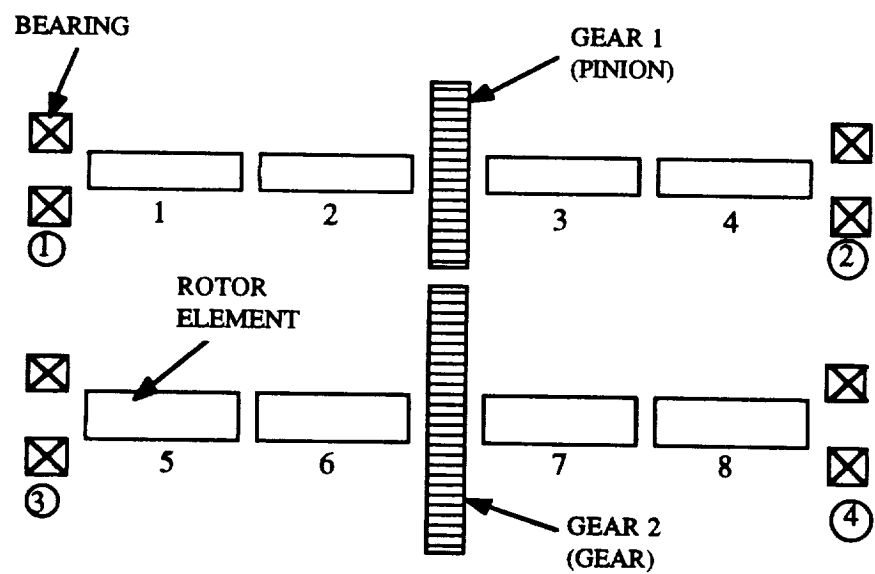
Figure A2. Finite Element Model

218

of the driven rotor. In Figure A2 for example, we start at the left end of the first shaft and finished numbering at the right end of the second shaft. According to this configuration (Figure A2), the number of rotor elements in the first and second shafts are both 4 and the number of rotor elements before the pinion and gear are 2 and 6, respectively.

2. Material Properties:

In this section, material properties of the shaft considered will be entered. The following will be required:

1) THE DENSITY OF THE SHAFT MATERIAL (kg/m^3) (DEFAULT=7800)
2) THE VISCOUS DAMPING COEFFICIENT (s)   (DEF=0)
3) THE HYSTERETIC DAMPING COEFFICIENT   (DEF=0)
4) THE MODULUS OF ELASTICITY (N/m^2) (DEF=.207E12)
5) SHEAR MODULUS OF ELASTICITY (N/m^2) (DEF=.0795E12)

3. Element Properties:

The main portion of data to be entered is in this section. The options given are the following:

1) DEFINING THE DISK ELEMENT
2) DEFINING THE BEARING ELEMENT
3) DEFINING THE ROTOR ELEMENT   (also the default selection)
4) DEFINING THE GEAR ELEMENT
5) FINISH WITH DATA INPUT FOR FIRST SHAFT
6) FINISH WITH DATA INPUT FOR SECOND SHAFT

The most important part in this section of questions is the order of data entry. The order is based on the numbered finite element model (see Figure A2). For the finite element model shown in Figure A2, the order of data input is as follows:

1) DEFINING BEARING #1
2) DEFINING ROTOR #1
3) DEFINING ROTOR #2
4) DEFINING GEAR#1
5) DEFINING ROTOR #3
6) DEFINING ROTOR #4
7) DEFINING BEARING #2
8) TYPE IN OPTION 5 (FINISHED WITH DATA INPUT FOR SHAFT #1)
9) DEFINING BEARING #3
10) DEFINING ROTOR #5
11) DEFINING ROTOR #6

219

12) DEFINING GEAR#2
13) DEFINING ROTOR #7
14) DEFINING ROTOR #8
15) DEFINING BEARING #4
16) TYPE IN OPTION 6 (FINISHED WITH DATA INPUT FOR SHAFT #2)

From the example above, one can see the ordering of data entry moving from the first element in shaft #1 to the last element in shaft #2. Ultimately, the program will also read from the data file in this order.

According to the option selected (disk, gear, rotor element or bearing), the following information is required:

The disk element - option 1:

1) DISK OUTER DIAMETER IN (m)
2) WIDTH OR THICKNESS OF DISK IN (m)
3) MATERIAL DENSITY OF DISK IN (kg/m^3) (DEF=7800)

The bearing element - option 2:

THE STIFFNESS (N/m)
1) K_{xx}
2) K_{xy}
3) K_{yx}
4) K_{yy}
THE DAMPING (N-s/m)
5) C_{xx}
6) C_{xy}
7) C_{yx}
8) C_{yy}

The rotor element - option 3:

1) LENGHT OF ROTOR ELEMENT IN (m)
2) OUTER DIAMETER OF ROTOR ELEMENT IN (m)
3) INNER DIAMETER OF ROTOR ELEMENT IN (m) (for hollow rotor) (DEF=0)
4) THE AXIAL LOAD IN (N) (DEF=0)

The gear element - option 4:

1) PITCH CIRCLE DIAMETER IN (m)
2) FACE WIDTH IN (m)

220

3) GEAR MATERIAL DENSITY IN (kg/m^3)   (DEF=7800)

Option 5 should be chosen when the elements of the first shaft have been defined. The user will then be given the material properties of the second shaft., and given the option to make changes to this set of data. Similarly, option 6 should be entered when all elements of the second shaft have been entered.

4. Gear Mesh Properties:

The following gear mesh properties will be entered in this section:

1) GEAR MESH STIFFNESS (N/m)
2) GEAR MESH DAMPING   (N-s/m)   (DEF=0)
3) BASE CIRCLE DIAMETER OF FIRST GEAR (m)
4) BASE CIRCLE DIAMETER OF SECOND GEAR (m)

Following the input of gear mesh data, the program will also ask the user for the number of natural frequencies wanted in the output.

5. Forced Response Data:

Here, the user is given the option to have forced response calculated. If the selection is NO, then interactive input will be complete. If the selection is YES, then the following options are given:

1) WHIRLING ORBIT AT A SPECIFIED NODE
2) DEFLECTIONS AT A SPECIFIED NODE
3) DYNAMIC LOAD TO STATIC LOAD RATIO AT THE MESHING POINT

Following the options menu, the general information for this section will be required:

1) GEOMETRIC ECCENTRICITY (RUNOUT) OF GEAR 1 (m)   (DEF=0)
2) GEOMETRIC ECCENTRICITY (RUNOUT) OF GEAR 2 (m)   (DEF=0)
3) PEAK TO PEAK VALUE OF STATIC TRANSMISSION ERROR (m)
4) MASS UNBALANCE OF GEAR 1 (kg-m)   (DEF=0)
5) MASS UNBALANCE OF GEAR 2 (kg-m)   (DEF=0)
6) NUMBER OF TEETH IN GEAR 1 (PINION)
7) AVERAGE FORCE TRANSMITTED (N)
8) VALUE OF MODAL DAMPING   (DEF=.01)

After the general information for this section has been completed, the program will require certain information based from the choice selected from the options menu :

Forced response option 1: Whirling orbit at a specified node, the following information will be required.

1) NUMBER OF NODE AT WHICH WHIRL ORBIT IS REQUIRED
2) ROTATIONAL SPEED OF SHAFT 1 (rad/s)

Forced response option 2: Deflections at a specified node will be required.

1) STARTING ROTATIONAL SPEED OF SHAFT 1   (rad/s)   (DEF=0)
2) UPPER LIMIT OF ROTATIONAL SPEED OF SHAFT 1   (rad/s)
3) INCREMENT FOR ROTATIONAL SPEED   (rad/s)   (DEF=5)
4) DIRECTION AT WHICH FORCED RESPONSE IS WANTED (1,2 OR 3) (DEF=1)
5) NUMBER OF NODE AT WHICH FORCED RESPONSE IS WANTED

In question (4), enter: 1 for deflection in pressure line direction; 2 for deflection in direction perpendicular to pressure line; 3 for torsional deflections

1) STARTING ROTATIONAL SPEED OF SHAFT 1   (rad/s)   (DEF=0)
2) UPPER LIMIT OF ROTATIONAL SPEED OF SHAFT 1   (rad/s)
3) INCREMENT FOR ROTATIONAL SPEED (rad/s)   (DEF=5)

Having completed this section on forced response, the program will then read from the new data file created from the interactive input. The output will be in an output data file named FOR001.DAT .

A.2.2. OPTION II: Enter Data From File

With this selection, the user is then requested to give the name of the file where the data is stored, instead of entering data interactively. The program will then proceed to read from the file. If an error should occur in opening the file, then the user will be given the option to try again. If the user opts to try again, then the user will be asked the file name again. If no, then the program will return to the primary option. After the program has read from the file the output will be found in an output data file.

A.4. SAMPLE OUTPUT FILE FOR001.DAT

```
*******************************************************************

                    GEARED ROTOR DYNAMICS PROGRAM

                               GRD

          GEAR DYNAMICS AND GEAR NOISE RESEARCH LABORATORY

                    THE OHIO STATE UNIVERSITY

*******************************************************************
```

THE FIRST SHAFT:

MATERIAL PROPERTIES OF THE SHAFT:

```
    DENSITY OF THE MATERIAL.....=   0.78000E+04 KG/M**3
    ELASTIC MODULUS.............=   0.20700E+12 N/M**2
    SHEAR MODULUS...............=   0.79500E+11 N/M**2
    VISCOUS DAMPING COEFFICIENT.=   0.00000E+00 S
    HYSTERETIC LOSS FACTOR......=   0.00000E+00
```

AT Z=   0.0000 M THERE EXISTS A BEARING WITH THE
FOLLOWING STIFFNESS AND DAMPING COEFFICIENTS:

```
    KXX=   0.10000E+10 N/M        KXY=   0.00000E+00 N/M
    KYX=   0.00000E+00 N/M        KYY=   0.10000E+10 N/M
    CXX=   0.00000E+00 N-S/M      CXY=   0.00000E+00 N-S/M
    CYX=   0.00000E+00 N-S/M      CYY=   0.00000E+00 N-S/M
```

AT Z=   0.0000 M THERE EXISTS A FINITE ROTOR ELEMENT WITH THE
FOLLOWING SPECIFICATIONS:

```
    LENGTH OF THE ELEMENT.......=   0.50000E-01 M
    OUTER DIAMETER..............=   0.30000E-01 M
    INNER DIAMETER..............=   0.00000E+00 M
    AXIAL LOAD..................=   0.00000E+00 N
```

AT Z=   0.0500 M THERE EXISTS A FINITE ROTOR ELEMENT WITH THE
FOLLOWING SPECIFICATIONS:

```
    LENGTH OF THE ELEMENT.......=   0.50000E-01 M
    OUTER DIAMETER..............=   0.30000E-01 M
    INNER DIAMETER..............=   0.00000E+00 M
    AXIAL LOAD..................=   0.00000E+00 N
```

AT Z=   0.1000 M THERE EXISTS A RIGID DISK WITH THE FOLLOWING
SPECIFICATIONS:

```
    OUTER DIAMETER......=   0.13500E+00 M
```

```
        WIDTH...............=   0.25400E-01 M
        MATERIAL DENSITY....=   0.78000E+04 KG/M**3


AT Z=    0.1000 M THERE EXISTS A FINITE ROTOR ELEMENT WITH THE
FOLLOWING SPECIFICATIONS:

        LENGTH OF THE ELEMENT.......=   0.50000E-01 M
        OUTER DIAMETER..............=   0.30000E-01 M
        INNER DIAMETER..............=   0.00000E+00 M
        AXIAL LOAD..................=   0.00000E+00 N


AT Z=    0.1500 M THERE EXISTS A FINITE ROTOR ELEMENT WITH THE
FOLLOWING SPECIFICATIONS:

        LENGTH OF THE ELEMENT.......=   0.50000E-01 M
        OUTER DIAMETER..............=   0.30000E-01 M
        INNER DIAMETER..............=   0.00000E+00 M
        AXIAL LOAD..................=   0.00000E+00 N


AT Z=    0.2000 M THERE EXISTS A BEARING WITH THE
FOLLOWING STIFFNESS AND DAMPING COEFFICIENTS:

        KXX=    0.10000E+10 N/M        KXY=    0.00000E+00 N/M
        KYX=    0.00000E+00 N/M        KYY=    0.10000E+10 N/M
        CXX=    0.00000E+00 N-S/M      CXY=    0.00000E+00 N-S/M
        CYX=    0.00000E+00 N-S/M      CYY=    0.00000E+00 N-S/M



THE SECOND SHAFT:
------------------


MATERIAL PROPERTIES OF THE SHAFT:

        DENSITY OF THE MATERIAL.....=   0.78000E+04 KG/M**3
        ELASTIC MODULUS.............=   0.20700E+12 N/M**2
        SHEAR MODULUS...............=   0.79500E+11 N/M**2
        VISCOUS DAMPING COEFFICIENT.=   0.00000E+00 S
        HYSTERETIC LOSS FACTOR......=   0.00000E+00


AT Z=    0.0000 M THERE EXISTS A BEARING WITH THE
FOLLOWING STIFFNESS AND DAMPING COEFFICIENTS:

        KXX=    0.10000E+10 N/M        KXY=    0.00000E+00 N/M
        KYX=    0.00000E+00 N/M        KYY=    0.10000E+10 N/M
        CXX=    0.00000E+00 N-S/M      CXY=    0.00000E+00 N-S/M
        CYX=    0.00000E+00 N-S/M      CYY=    0.00000E+00 N-S/M


AT Z=    0.0000 M THERE EXISTS A FINITE ROTOR ELEMENT WITH THE
FOLLOWING SPECIFICATIONS:

        LENGTH OF THE ELEMENT.......=   0.50000E-01 M
        OUTER DIAMETER..............=   0.40000E-01 M
        INNER DIAMETER..............=   0.00000E+00 M
        AXIAL LOAD..................=   0.00000E+00 N
```

AT Z= 0.0500 M THERE EXISTS A FINITE ROTOR ELEMENT WITH THE
FOLLOWING SPECIFICATIONS:

    LENGTH OF THE ELEMENT.......= 0.50000E-01 M
    OUTER DIAMETER..............= 0.40000E-01 M
    INNER DIAMETER..............= 0.00000E+00 M
    AXIAL LOAD..................= 0.00000E+00 N

AT Z= 0.1000 M THERE EXISTS A RIGID DISK WITH THE FOLLOWING
SPECIFICATIONS:

    OUTER DIAMETER......= 0.24500E+00 M
    WIDTH...............= 0.25400E-01 M
    MATERIAL DENSITY....= 0.78000E+04 KG/M**3

AT Z= 0.1000 M THERE EXISTS A FINITE ROTOR ELEMENT WITH THE
FOLLOWING SPECIFICATIONS:

    LENGTH OF THE ELEMENT.......= 0.50000E-01 M
    OUTER DIAMETER..............= 0.40000E-01 M
    INNER DIAMETER..............= 0.00000E+00 M
    AXIAL LOAD..................= 0.00000E+00 N

AT Z= 0.1500 M THERE EXISTS A FINITE ROTOR ELEMENT WITH THE
FOLLOWING SPECIFICATIONS:

    LENGTH OF THE ELEMENT.......= 0.50000E-01 M
    OUTER DIAMETER..............= 0.40000E-01 M
    INNER DIAMETER..............= 0.00000E+00 M
    AXIAL LOAD..................= 0.00000E+00 N

AT Z= 0.2000 M THERE EXISTS A BEARING WITH THE
FOLLOWING STIFFNESS AND DAMPING COEFFICIENTS:

    KXX= 0.10000E+10 N/M   KXY= 0.00000E+00 N/M
    KYX= 0.00000E+00 N/M   KYY= 0.10000E+10 N/M
    CXX= 0.00000E+00 N-S/M   CXY= 0.00000E+00 N-S/M
    CYX= 0.00000E+00 N-S/M   CYY= 0.00000E+00 N-S/M

GEAR MESH PROPERTIES:

    BASE CIRCLE DIAMETER OF GEAR 1...= 0.1270 M
    BASE CIRCLE DIAMETER OF GEAR 2...= 0.2310 M
    AVERAGE MESH STIFFNESS...........= 0.20000E+09 N/M
    AVERAGE MESH DAMPING.............= 0.00000E+00 N-S/M

****

A. FREE VIBRATION ANALYSIS:

FOLLOWING NATURAL FREQUENCIES AND MODESHAPES ARE CALCULATED
FOR THE ABOVE SPECIFIED SYSTEM:

225

MODE 1

NATURAL FREQUENCY=   0.0002 (HZ.)

CORRESPONDING MODESHAPES:

DISP. IN Y	DISP. IN X	ROT. ABOUT Y	ROT. ABOUT X	ROT. ABOUT Z
-.260E-08	0.000E+00	0.000E+00	-.105E-06	0.599E+01
-.358E-08	0.000E+00	0.000E+00	0.108E-06	0.599E+01
0.119E-08	0.000E+00	0.000E+00	-.411E-07	0.599E+01
-.524E-08	0.000E+00	0.000E+00	-.983E-07	0.599E+01
-.299E-08	0.000E+00	0.000E+00	0.136E-06	0.599E+01
0.771E-08	0.000E+00	0.000E+00	0.499E-06	0.329E+01
0.253E-07	0.000E+00	0.000E+00	0.535E-07	0.329E+01
-.188E-09	0.000E+00	0.000E+00	-.118E-05	0.329E+01
-.256E-07	0.000E+00	0.000E+00	0.557E-07	0.329E+01
-.781E-08	0.000E+00	0.000E+00	0.505E-06	0.329E+01

****

MODE 2

NATURAL FREQUENCY=   486.0262 (HZ.)

CORRESPONDING MODESHAPES:

DISP. IN Y	DISP. IN X	ROT. ABOUT Y	ROT. ABOUT X	ROT. ABOUT Z
0.929E-02	0.000E+00	0.000E+00	0.551E+01	-.646E+01
0.261E+00	0.000E+00	0.000E+00	0.410E+01	-.645E+01
0.375E+00	0.000E+00	0.000E+00	-.119E-06	-.643E+01
0.261E+00	0.000E+00	0.000E+00	-.410E+01	-.645E+01
0.929E-02	0.000E+00	0.000E+00	-.551E+01	-.646E+01
-.950E-02	0.000E+00	0.000E+00	-.180E+01	0.110E+01
-.918E-01	0.000E+00	0.000E+00	-.134E+01	0.110E+01
-.129E+00	0.000E+00	0.000E+00	0.995E-09	0.109E+01
-.918E-01	0.000E+00	0.000E+00	0.134E+01	0.110E+01
-.950E-02	0.000E+00	0.000E+00	0.180E+01	0.110E+01

****
.
.
.
.
.
.

MODE 10

NATURAL FREQUENCY= 2479.9504 (HZ.)

CORRESPONDING MODESHAPES:

DISP. IN Y	DISP. IN X	ROT. ABOUT Y	ROT. ABOUT X	ROT. ABOUT Z
0.124E-01	0.000E+00	0.000E+00	0.459E+01	0.978E+01
0.212E+00	0.000E+00	0.000E+00	0.288E+01	0.950E+01
0.279E+00	0.000E+00	0.000E+00	-.897E-10	0.865E+01
0.212E+00	0.000E+00	0.000E+00	-.288E+01	0.950E+01
0.124E-01	0.000E+00	0.000E+00	-.459E+01	0.978E+01
-.990E-02	0.000E+00	0.000E+00	-.134E+01	-.166E+01
-.691E-01	0.000E+00	0.000E+00	-.897E+00	-.162E+01
-.917E-01	0.000E+00	0.000E+00	-.562E-10	-.147E+01
-.691E-01	0.000E+00	0.000E+00	0.897E+00	-.162E+01
-.990E-02	0.000E+00	0.000E+00	0.134E+01	-.166E+01

****

B. FORCED VIBRATION ANALYSIS:

FORCED RESPONSE AT THE SPECIFIED FREQUENCY RANGE:

    0.591142E-04
    0.675386E-04

APPENDIX B

DIMENSIONAL AND NON-DIMENSIONAL QUANTITIES

FOR THE EXPERIMENTAL TEST RIGS

Table B1. Dimensionless and dimensional parameters for Kubo's test rig [28].

DIMENSIONAL QUANTITIES	
Number of teeth	25/25
I_{g1}, I_{g2} [kg-m^2 (lb-ft^2)]	0.00115 (0.0278)
m_{c1} [kg]	0.23
d_{g1}, d_{g2} [m (in)]	0.094 (3.7)
k_b	rigid
k_h [N/m (lbf/in)]	3.8E8 (2.17E6)
$\bar{F}_m$ [N (lbf)]	2295 (1030)
$\tilde{e}$ [m (in)]	1.92E-6 (7.56E-5)
b_h [m (in)]	0.1E-3 (0.0039)

DIMENSIONLESS QUANTITIES	
ζ (page 44)	0.1
F_m (page 44)	0.06
F_{ah} (page 44)	0.0192
F_m/F_{ah}	3.12

228

Table B2. Dimensionless and dimensional parameters for Munro's test rig [27].

DIMENSIONAL QUANTITIES

number of teeth	32/32
I_{g1}, I_{g2} [kg-m^2 (lb-ft^2)]	0.136 (3.29)
m_{g1}, m_{g2} [kg (lb)]	31.1 (68.5)
d_{g1}, d_{g2} [m (in)]	0.2 (8)
b_h [m (in)]	0.12E-3 (4.7E-3)

	Design Load (DL)	3/4 DL	1/2 DL	1/4 DL
$\bar{F}_m$ [N (lbf/in FW)]	3782 (1700)	2836 (1275)	1891 (850)	947 (425)
k_h [N/m]	3.44E8	3.22E8	3.01E8	2.72E8
$\tilde{e}$ [m]	3.5E-7	1.06E-6	1.78E-6	2.36E-6

DIMENSIONLESS QUANTITIES

	Design Load (DL)	3/4 DL	1/2 DL	1/4 DL
F_m (equation 3.3i)	0.183	0.146	0.105	0.058
F_{ah} (equation 3.3j)	0.0058	0.0178	0.0296	0.0393
κ_{11}, κ_{22} (equation 3.3f)	0.950	0.966	0.983	1.007
κ_{13}, κ_{23} (equation 3.3g)	0.242	0.242	0.242	0.242
ζ_{11}, ζ_{22} (equation 3.3c)	0.01	0.01	0.01	0.01
ζ_{13}, ζ_{23} (equation 3.3d)	0.00375	0.00375	0.00375	0.00375
ζ_{33} (equation 3.3e)	0.015	0.015	0.015	0.015

APPENDIX C

LENGTH OF TRANSIENT SOLUTION AND CPU TIME

C.1. Length of Transient Solution

It is necessary to run the digital simulation routines for many cycles in order to reach the steady state solution. This can easily be detected by a time history repeating itself and a phase plane trajectory followed at each period of the steady state solution. Following are found to be the major factors which determine the length of the transient region of the time history:

1. Damping Ratio: Damping ratio is inversely proportional to the time needed to reach steady state solution. Larger the damping, shorter the transients. Figure B1 shows this relationship for the single degree of freedom model of gear pair. A similar trend is observed in Multi-degree of freedom model also.

2. Excitation Frequency: The transient solution is found to be longer in the vicinity of the resonance frequency than the off-resonance region. Figure B1 compares length of transient solution versus damping ratio curves corresponding to resonance and off-resonance excitation frequencies.

3. Initial Conditions: Transients are longer when the initial displacement and velocity are away from the mean values of the steady state solution sought.

C.2. CPU Times

CPU time needed in digital simulation depends on: i. the number of increments per period of forcing function (20-40 points per period is good enough), ii. the
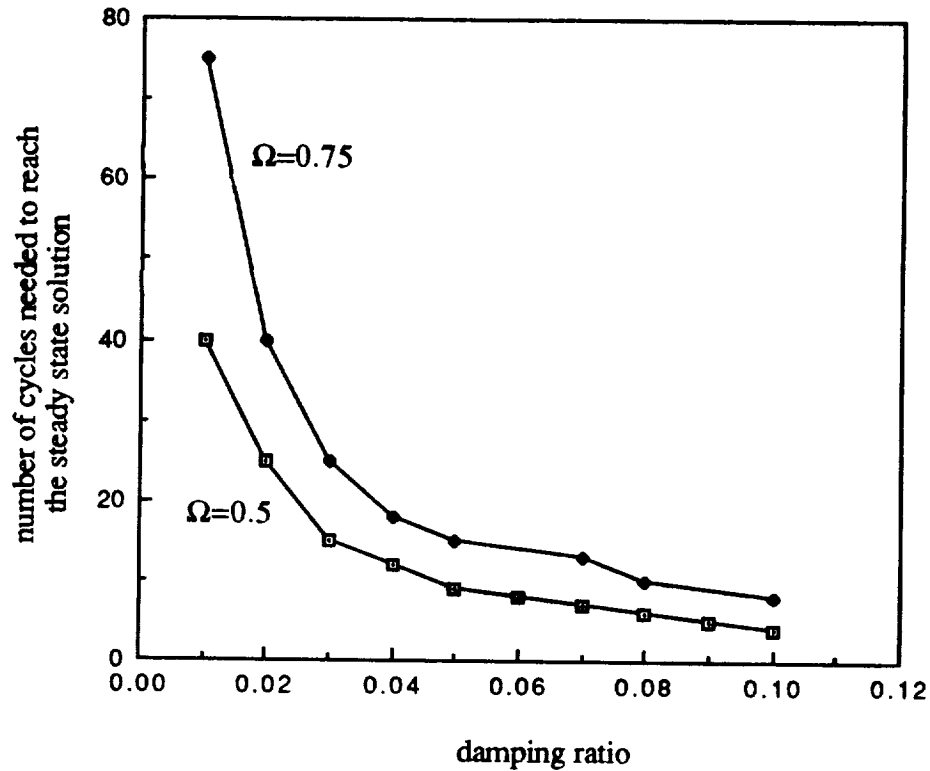
230

Figure C1. Length of the transient solution in a gear pair as a function of damping ratio for off-resonance (Ω=0.5) and resonance (Ω=0.7) frequencies

tolerance of the solution accuracy (1×10^{-5} to 1×10^{-9} is acceptable), and iii. number of degrees of freedom. For the single degree of freedom model with a tolerance of 1×10^{-9} and an increment of 20 points/period, nearly 10 sec. of CPU time is required to run for 100 cycles. The three degree of freedom model with same parameters uses 1.2 min. of CPU time for 100 cycles.

231

APPENDIX D

COMPARISON OF PREDICTIONS WITH NASA MEASUREMENTS

In this section, a comparison of the FEM predictions of the NASA Gear Noise Test Rig shown in Figure D1 with the measurements of NASA is given. System parameters and the predicted natural modes of the system have already been given in Tables 1.1 and 1.2, respectively. The static transmission error and mesh stiffness variation predictions are also shown in Figure 4.8. Here, the comparison of the predicted frequency response spectrum with measurements of NASA is limited to torsional (angular acceleration) vibrations since the set-up was not equipped for transverse vibration measurements. Only a qualitative agreement is observed between the predictions and measurements as shown in Figure D2 due to the uncertainties associated with the sensitivities of instruments and due to the errors involved in measurement such as resonance and calibration problems of angular transducers.
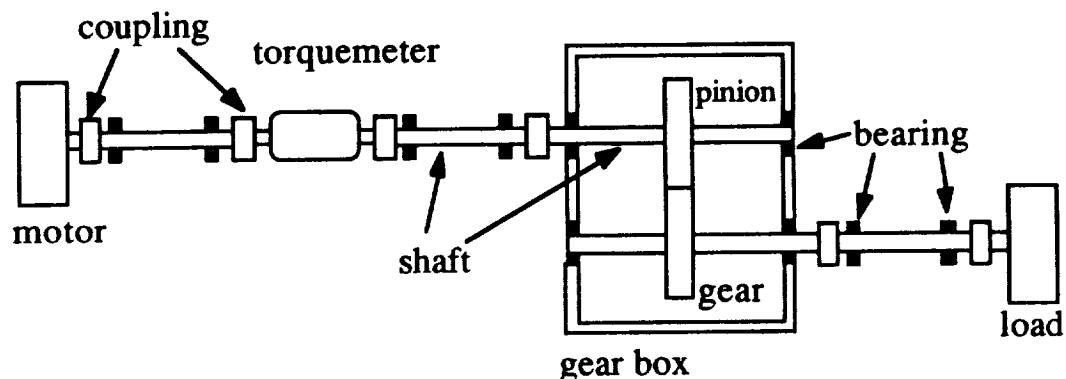
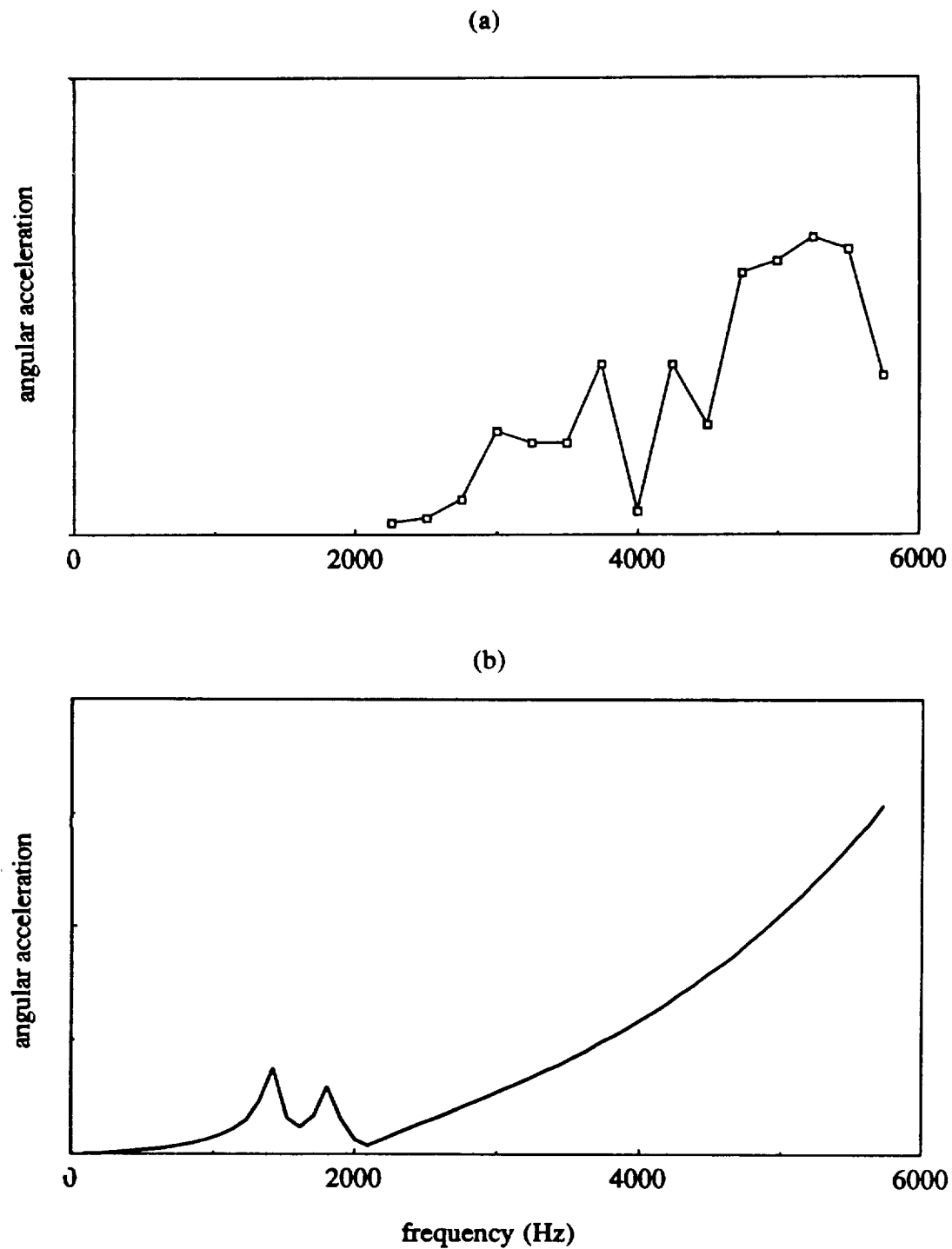

Figure D1. NASA Gear Noise Test Rig.

(a)

(b)

frequency (Hz)

Figure D2. Angular acceleration spectrum of the NASA Gear Noise Test Rig at pinion

location; a) measurements b) FEM predictions.

APPENDIX D

COMPARISON OF PREDICTIONS WITH NASA MEASUREMENTS

In this section, a comparison of the FEM predictions of the NASA Gear Noise Test Rig shown in Figure D1 with the measurements by NASA is given. System parameters and the predicted natureal modes of the system have already been given in Tables 1.1 and 1.2, respectively. The static transmission error and mesh stiffness variation predictions are also shown in Figure 4.8. Here, the comparison of the predicted frequency response spectrum with measurements by NASA is limited to torsional (angular acceleration) vibrations. Only a qualitative agreement is observed between the predictions and measurements as shown in Figure D2. Quantitative discrepancies are attributed to the resonance problems experienced with the angular transducers.
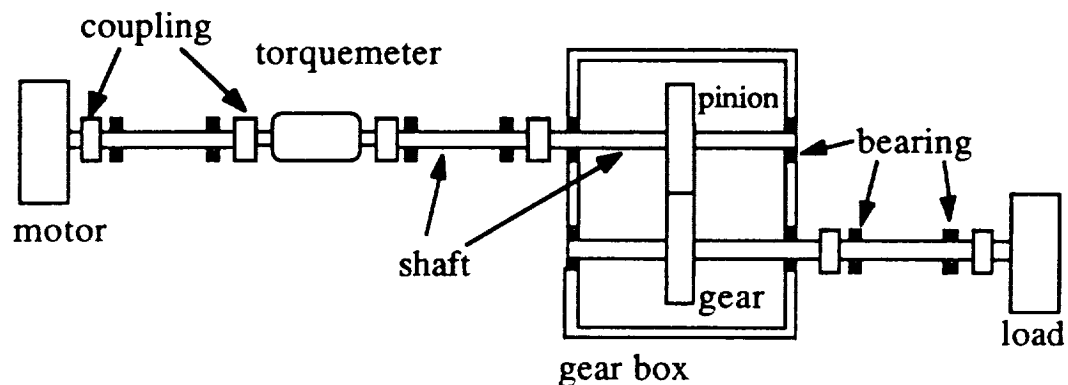
Figure D1. NASA Gear Noise Test Rig.

234

1. Report No. NASA CR-4338 AVSCOM TR-90-C-020	2. Government Accession No.	3. Recipient's Catalog No.
4. Title and Subtitle Non-Linear Dynamic Analysis of Geared Systems		5. Report Date November 1990
		6. Performing Organization Code
7. Author(s) Rajendra Singh, Donald R. Houser, and Ahmet Kahraman		8. Performing Organization Report No. None (E-5718)
		10. Work Unit No. 505-63-51
9. Performing Organization Name and Address Ohio State University Department of Mechanical Engineering Columbus, Ohio 43210		
		11. Contract or Grant No. NAG3-773
12. Sponsoring Agency Name and Address Propulsion Directorate U.S. Army Aviation Systems Command Cleveland, Ohio 44135-3191 and NASA Lewis Research Center Cleveland, Ohio 44135-3191		13. Type of Report and Period Covered Contractor Report Final
		14. Sponsoring Agency Code

16. Abstract

Under the driving conditions, a typical geared system may be subjected to large dynamic loads. Also, the vibration level of the geared system is directly related to the noise radiated from the gear box. Accordingly, a good understanding of the steady state dynamic behavior of the system is required in order to design reliable and quiet transmissions. It is the main focus of this study with the scope limited to a system containing a spur gear pair with backlash and periodically time-varying mesh stiffness, and rolling element bearings with clearance type non-linearities. The internal static transmission error excitation at the gear mesh, which is of importance from high frequency noise and vibration control view point, is considered in the formulation in sinusoidal or periodic form. A dynamic finite element model of the linear time-invariant (LTI) system is developed. Effects of several system parameters, such as torsional and transverse flexibilities of the shafts and prime mover/load inertias, on free and forced vibration characteristics are investigated. Several reduced order LTI models are developed and validated by comparing their eigen solutions with the finite element model results. Using the reduced order formulations, a three-degree of freedom dynamic model is developed which includes non-linearities associated with radial clearances in the radial rolling element bearings, backlash between a spur gear pair and periodically varying gear meshing stiffness. As a limiting case, a single degree of freedom model of the spur gear pair with backlash is considered and mathematical conditions for tooth separation and back collision are defined. Both digital simulation technique and analytical methods such as method of harmonic balance and the method of multiple scales have been used to develop the steady state frequency response characteristics for various non-linear and/or time-varying cases. Difficulties associated with the determination of the multiple solutions at a given frequency in the digital simulation technique have been resolved. The proposed formulation has been validated by comparing the predictions with the results of two benchmark experiments reported in the literature. Several key system parameters such as mean load and damping ratio are identified and their effects on the non-linear frequency response are evaluated quantitatively. Other fundamental issues such as the dynamic coupling between non-linear modes, dynamic interactions between component non-linearities and time-varying mesh stiffness, and the existence of subharmonic and chaotic solutions including routes to chaos have also been examined in depth.

17. Key Words (Suggested by Author(s)) Bearings Gears Vibrations Machine design	18. Distribution Statement Unclassified – Unlimited Subject Category 37		
19. Security Classif. (of this report) Unclassified	20. Security Classif. (of this page) Unclassified	21. No. of pages 248	22. Price* A11

NASA

National Aeronautics and
Space Administration

Washington, D.C.
20546

SPECIAL FOURTH CLASS MAIL
BOOK